A new perspective on volcanic particle sedimentation and aggregation

Rossi, Eduardo

UNIVERSITÉ DE GENÈVE
Départment des Sciences de la Terre

FACULTÉ DES SCIENCES
Professeur Costanza Bonadonna

A new perspective on volcanic particle sedimentation and aggregation

THÈSE

présentée à la Faculté des sciences de l'Université de Genève
pour obtenir le grade de Docteur ès sciences, mention Sciences de la Terre

par

Eduardo Rossi

de Empoli (Italie)

Thèse N° 5260

Genève
Atelier de reprographie ReproMail
2018

UNIVERSITÉ DE GENÈVE

FACULTÉ DES SCIENCES

DOCTORAT ÈS SCIENCES, MENTION SCIENCES DE LA TERRE

Thèse de Monsieur Eduardo ROSSI

intitulée :

«A New Perspective on Volcanic Particle Sedimentation and Aggregation»

La Faculté des sciences, sur le préavis de Madame C. BONADONNA, professeure associée et directrice de thèse (Département des sciences de la Terre), Monsieur L. MASTIN, docteur (David Johnston Cascades Volcano Oberservatory, United States Geological Survey, Vancouver, Washington State, USA) et Monsieur S. LANE, professeur (Lancaster Environnment Center, University of Lancaster, United Kingdom), autorise l'impression de la présente thèse, sans exprimer d'opinion sur les propositions qui y sont énoncées.

Genève, le 14 septembre 2018

Thèse - 5260 -

Le Doyen

N.B. - La thèse doit porter la déclaration précédente et remplir les conditions énumérées dans les "Informations relatives aux thèses de doctorat à l'Université de Genève".

Acknowledgments

First, I would like to thank my thesis director prof. Costanza Bonadonna for her enthusiasm, support, and help during all these years of PhD. She has been a precious guide for the project and a priceless example of how scientific research should be. The resilience I showed after all the difficulties I had during my third year has been possible only with her support. No doubt about it. I will be always grateful to her for this.

Second, I would like to thank the entire NEMOH network, under which my project was born. Being awarded of an ITN Marie Curie fellowship has been a privilege and a unique occasion to meet people, share knowledge and grow up as scientist and as a man. NEMOH has been a real family. The best environment to start new friendships and to have unique experiences. I am particularly grateful to the "mind behind the project": Paolo Papale. And to all the people involved in this great adventure.

Third, how to forget the closest companions of my adventure? Starting from the "problem-solver" Gholamhossein Bagheri, Sebastien Biass, Federico Brogi, Stefano Pollastri, Lucia Dominguez (which I would like to thank also for her assistance when I needed…), Valerie Baumann, Allan Fries, Jonathan Lemus, Paul Jarvis, Matthew John Edwards, Laura Pioli, Irene Manzella, Corine Frischknecht.

Last, but not least, I would like to thank my family for all the support they gave me during all these years. They have been really precious in helping when I needed their hand and assistance.

A special "thank" goes to Martina, who has always been by my side in all my schools, conferences, adventures around the world. I have never felt alone: her words, in many circumstances, have changed my nights in day. I will be always grateful to her.

The research leading to these results has received funding from the European Union Seventh Framework Programme (FP7/2007-2013) under the project NEMOH, grant agreement n° 289976.

Table of Contents

List of Figures

List of Tables

Summary

Recent volcanic crises (2010 Eyjafjallajökull, Grimsvotn 2011, Iceland; Puyehue-Cordon Caulle 2011, Chile) have demonstrated the widespread impact that even small-moderate explosive volcanic eruptions can have on our society. The air traffic closure occurred in large parts of Europe as a result of the 2010 Eyjafjallajökull eruption is still a vivid memory of how a moderate eruption can result in a total or partial closure of 300 airports and cost about 1.300.000.000 € to the airline industry. During the last decade, several efforts have been made to improve Volcanic Ash Transport and Dispersal Models (VTADMs) and their predictions in order to better respond to volcanic crisis and mitigate associated volcanic risk. However, the long range prediction of volcanic ash is still affected by our poor understanding of size-selective sedimentation processes (e.g. particle aggregation, gravitational instabilities) in reducing the residence time of particles in the atmosphere. If this processes are not adequately described and parameterized, VATDMs tend to overestimate the atmospheric concentration of fine ash in the far field. Main objectives of this thesis include to: i) develop a robust mathematical framework to theoretically describe ash aggregation, based on field, theoretical and experimental constraints; ii) better characterize the physics of ash aggregation, providing a coherent formalization of the most important physical parameters involved in the process; and iii) implement the resultant theoretical framework into VATDMs. First, a one-dimensional scheme for the of coagulation of particles has been developed and applied to a thermal plume model using the 3rd August 2013 Vulcanian eruption of Mount Sakurajima, Japan, as a case study. This scheme, based on the so-called Fixed Pivot Technique, where the variable mass is supposed to be discrete, has also been tested and implemented within NAME, the VATDM in use at MetOffice, UK. Second, the mathematical framework has been extended towards the use of arbitrary multidimensional parameters. In this novel approach, the relationships that govern the resulting products of a collision are arbitrary and not restricted to additive properties as in previous approaches. This new theoretical framework, namely the

Generalized Fixed Pivot Technique (GFPT), can be applied in different contexts and disciplines. Third, the GFPT was couple with specific parameterisations for volcanic as in order to develop a new methodology for the investigation of the role of aggregation in volcanic plumes. This resulted in a new parameterization of crucial physical processes, such as the collision rate and the sticking efficiency of collisional processes. To the other end of the spectrum of particle fallout during volcanic explosive eruptions, sedimentation of large clasts has also been addressed both to derive critical eruption source parameters, such as plume height, and to assess the associated hazard. In particular, existing methods for the study of clast sedimentation have been extended in order to incorporate important eruptive and sedimentation processes, with a special focus on the effect of atmospheric winds on plume rise. A comprehensive software package was developed that is capable to describe real topography and three-dimensional atmospheric profiles. The method has been thoroughly validated with eruptions of varying intensity and applied to compile a new set of nomograms for the determination of plume height and wind intensity at the time of the eruption in various eruptive conditions (including weak and transitional plumes) based on clast distribution on the ground. Such a model can also be used to compile probability maps for the assessment of proximal hazard associated with the sedimentation of large clasts.

Résumé

Les crises volcaniques récentes (2010 Eyjafjallajökull, Grimsvotn 2011, Iceland; Puyehue-Cordon Caulle 2011, Chile) nous ont montré le grand impact que peuvent avoir les éruptions volcaniques de petite ou moyenne ampleur sur notre société. La fermeture du trafic aérien dans une grande partie de l'Europe suite à l'éruption de l´Eyjafjallajökull en 2010 est encore présente dans notre mémoire et nous a montré comment une éruption d'ampleur modérée peut provoquer la fermeture totale ou partiale de 300 aéroports et coûter environ 1.300.000.000 € à l'industrie aéronautique. Durant ces dix dernières années de nombreux efforts ont été réalisés pour perfectionner les modèles de transport et de dispersion des cendres volcaniques (Volcanic Ash Transport and Dispersal Models, VTADMs) et leur prédiction, qui serviront à mieux gérer les crises volcaniques et réduire les risques volcaniques associés. Néanmoins il existe encore un manque de connaissances sur les processus de sélection des particules par sédimentation (ej. Agrégation des particules, instabilités gravitationnelles) qui réduisent le temps de résidence des particules dans l'atmosphère, qui constituent des données primordiales pour les prédictions à long terme des cendres volcaniques. Lorsque ces processus ne sont pas correctement décrits et paramétrés, le VATDMs a tendance à surestimer la concentration de particules de cendres fines dans les régions lointaines. Les principaux objectifs de cette thèse comprennent : i) Le développement d'un cadre mathématique solide pour décrire de manière théorique l'agrégation des cendres, sur la base d'observations sur le terrain, tout en considérant les contraintes théoriques et expérimentales. ii) Définir de manière précise la physique de l'agrégation des cendres, en fournissant une formalisation cohérente des principaux paramètres impliqués dans le processus ; et iii) Appliquer le cadre théorique qui en résulte dans les VATDMs. Premièrement, un système unidimensionnel pour la coagulation des particules a été créé et appliqué à un modèle thermique de panache, qui est basé sur le cas d'étude de l'éruption vulcanienne du 3 août 2013 du Mont Sakurajima au Japon. Ce système, basé sur la soi-disant technique de pivot fixe « Fixed Pivot Technique », où la variable masse

est censée être discrète, a été testé et appliqué avec les modèles NAME et VATDM, actuellement utilisés au MetOffice au Royaume-Uni. Deuxièmement, le cadre mathématique a été étendu vers l'utilisation de paramètres multidimensionnels arbitraires. Dans le cadre de cette nouvelle approche, les liens qui gouvernent les produits provenant d'une collision sont arbitraires, contrairement aux approches précédentes où ils étaient limités aux propriétés additives. Ce nouveau cadre théorique, nommé la technique de pivot fixe généralisée (Generalized Fixed Pivot Technique, GFPT), peut être appliqué dans différents contextes et disciplines. Troisièmement, une nouvelle méthodologie a été développée pour étudier le rôle de l'agrégation dans les panaches volcaniques, par la technique de GFPT couplé avec des paramètres spécifiques pour les cendres volcaniques. Cela a permis d'avoir de nouveaux paramètres liés à des processus physiques cruciaux, comme la vitesse de collision et l'efficacité de l'adhérence dans les processus de collision. La sédimentation de grands clastes, qui représentent l'autre bout du spectre des retombées de particules qui ont lieu lors d'une éruption volcanique explosive, a aussi été abordée dans cette étude, dans le but d'obtenir les paramètres de source critiques des éruptions, comme la hauteur du panache, et d'évaluer les dangers associés. Entre autres, les méthodes existantes pour l'étude de la sédimentation des clastes ont été développées pour incorporer de nouveaux processus sur la sédimentation et l'éruption, focalisées en particulier sur la croissance du panache volcanique. Un progiciel (software package) complet qui s'avère capable de décrire la topographie réelle et des profils atmosphériques tridimensionnels a été développé. Une validation complète de la méthode basée sur la distribution des clastes sur le sol a été réalisée avec des éruptions de différentes intensités. Cette validation a permis de compiler un nouveau set d'abaques (nomograms) pour la détermination de la hauteur du panache et l'intensité du vent au moment de l'éruption, ainsi que dans différentes conditions éruptives (comprenant des types de panaches faibles et transitionnels). Un modèle de ce type peut aussi être utilisé pour compiler des cartes de probabilité qui seront employées pour l'évaluation du danger proximal associé à la sédimentation de grands clastes.

Chapter 1

Introduction

Volcanic eruptions are one of the most violent and fascinating phenomena on our planet, responsible for a wide range of hazards and risks on a local and global scale. Among all the possible consequences involved in an eruptive event, tephra dispersion in the atmosphere represents an open challenge for the scientific community and a vulnerable aspect of the society. The air space closures occurred in large parts of Europe as a result of the 2010 Eyjafjallajökull eruption (Iceland) is still a vivid example of how a moderate eruption can affect multiple countries around the world and cost about 1.300.000.000 € to the airline industry. Most of the criticalities associated with volcanic tephra derive from its capability of acting at different spatial scales, as a consequence of the large spectrum of sizes of the ejected objects. *Bombs and blocks* ($size \geq 64\ mm$) are usually confined within few kilometres from the vent; *lapilli* ($2\ mm - 64\ mm$) can sediment up to some tens of kilometres from the crater; *coarse ash* ($63\ \mu m - 2\ mm$) and *fine ash* ($< 63\ \mu m$) travel for hundreds or thousands of kilometres. Major events can literally impact from a local region up to the global scale. The risk associated with tephra dispersal goes from the damage of buildings, infrastructures, and airplanes engines to the effects on health of humans and animals, the contamination of plants and crops. It is thus evident how an improved understanding of the mechanisms connected with tephra dispersal and sedimentation represents a key aspect of our capacity to predict possible consequences of a volcanic eruption and reduce the associated impact.

Once that lapilli and volcanic ash are injected in the atmosphere, an important role for the fate of these objects is driven by their vertical terminal velocity, i.e. the constant falling speed which is a consequence of the balance between gravity and drag force. Larger terminal velocities result in a reduced residence time in the atmosphere and a smaller travel distance. Two main aspects are needed to constrain the terminal velocity of an object: the characterization of i) its shape and of ii) the associated drag coefficient. It is thus not surprising that after the 2010 Eyjafjallajökull eruption a great effort has

been dedicated to the improvement of the parameterisation of the shape of volcanic ash and lapilli (Bagheri et al., 2015; Liu et al., 2015) and their drag coefficient (Bagheri and Bonadonna, 2016; Dioguardi et al., 2018; Ganser, 1993; Haider and Levenspiel, 1989; James et al., 2003). However, field observations over a large time frame have demonstrated that in a great amount of volcanic explosions ash does not sediment as a single object but in an aggregated form (Brown et al., 2012). In other words, the final object that impacts the ground is often constituted of a cluster of separated particles, differently packed. This aspect affects enormously both the ash dispersal forecasting and the studies of shape and drag. Moreover, the fact that most ash aggregates are poorly preserved in the field makes their study even more complicated. Several attempts have been dedicated in the last decades to the characterisation of ash properties (Burns et al., 2017; Durant et al., 2009; Gilbert and Lane, 1994; James et al., 2003; Lane et al., 1993; Schumacher and Schmincke, 1995; Sorem, 1982; Van Eaton et al., 2015; Van Eaton et al., 2012) and their theoretical modelling (Cornell et al., 1983; Costa et al., 2010; Veitch and Woods, 2001). However recent field observations show that the high degree of complexity of their structures requires major efforts and new tools (Bagheri et al., 2016).

Few words on the terminology used in the present work: in our context "*particle*" refers to a single tephra, regardless the size of the object; "*aggregate*" refers to an object formed by more than one particle. "*Cluster*" and "*aggregate*" are considered as synonyms.

Another important aspect of tephra dispersal is the study of lapilli sedimentation. In size, lapilli are in between ash and large bombs (Fisher, 1961). The former are fully coupled dynamics with the plume flow, the latter form ballistic trajectories driven by the initial momentum of the eruption. Intermediate sizes between these two classes results for lapilli in partially coupled dynamics with plume flow that cannot be completely considered as a ballistic. Carey and Sparks (1986) introduced a methodology to quantify the sedimentation process of centimetric clast sizes and relate the maximum downwind and crosswind distances of the associated isopleth contours to the height of the eruptive column. This method has been later improved by Burden et al. (2011). However this approach still presents major limitations and drawbacks in case of weak and transitional plumes, i.e. plume dominated by the external atmospheric winds.

1.1 Field observation of ash aggregation in nature

The presence of aggregation in volcanic deposits has been probably documented for the first time by Scrope (1829). Several historical observations of one specific type of aggregates, the so-called *accretionary lapilli*, are reported in Moore and Peck (1962). It is not surprising that this kind of aggregate has always assumed a great importance in the community, since it is usually quite well preserved in the deposits. However several other typologies of aggregates have been observed in modern times, such as the loosely bound structures collected after the 1980 eruption at Mount Saint Helens, US (Hobbs et al., 1981; Sorem, 1982) and also observed at Sakurajima Volcano, Japan (Bagheri et al., 2016; Gilbert et al., 1991) and during the 2010 Eyjafjallajökull eruption, Iceland (Bonadonna et al., 2011; Taddeucci et al., 2011). We refer to these objects as *ash clusters*. A complete classification of the different aggregate morphologies are presented in Brown et al. (2012) and summarised here for convenience. Two main families are identified: *Particle Clusters* (PC) and *Accretionary Pellets* (AP). The first group is subdivided in: PC1, ash clusters, and PC2, coated particles. The second group is formed of: AP1, poorly structured pellets; AP2, pellets with concentric structure (i.e. what we generally refer to as "accretionary lapilli"); AP3, liquid pellets. PC1 objects are ash clusters, characterised by low densities around $60 - 200\ kg/m^3$ and a typical size of the components less than $40\ \mu m$. PC2 clusters are characterized by the presence of a large coated particle at the center of the geometry. The size of the inner particle is usually much greater than $200\ \mu m$ and recent observations suggest that PC1 objects may be sometimes related to the coating part of PC2 aggregates (Bagheri et al., 2016). AP1 are poorly structured aggregates with median size of the population between $\approx 30 - 90\ \mu m$ and overall size between $100\ \mu m$ and few millimetres. AP2 are pellet with concentric structure, a typical overall size between $2 - 15\ mm$, which reveal the presence of inner components of $\approx 25 - 50\ \mu m$. Finally, AP3 are liquid pellets with a wide range on inner particles size ($\approx 1\ \mu m - 1\ mm$), a relevant presence of liquid water and a generally poor conservation after the impact. It is worth noticing that field observations and theoretical investigations suggest that iced water could play a primary role in the formation of AP1 and AP2 clusters (Van Eaton et al., 2015). A complementary scheme of definitions is based on the sticking mechanism responsible for their conglomeration. Usually two main groups are defined: *wet aggregates* and *dry*

aggregates. In the first group are historically included those clusters where a macroscopic role of water is present (accretionary lapilli or accretionary pellets). In the second group are included the PC, where other sticking mechanisms are considered dominant, such as the electrostatic forces. However this classification is still debated and sometimes misleading since the role of water in form of condensed humidity may be crucial as dissipation mechanism. Recent observations suggest that the family of ash pellets (AP) is probably associated with a dominant role of liquid water and/or salt bridges in their bounds (Burns et al., 2017). On the other side, particle clusters are formed in absence of a macroscopic external source of water. For this reason their presence is expected to be more common with respect to AP family. Unfortunately their original structure is poorly preserved soon after the impact on the ground and the residual part left on the sticky papers or other supports can be erroneously interpreted without the use of appropriate techniques. The use of advanced methodologies, such as the contemporary use of the High-Speed camera (HS) and the collection on a sticky paper, helps in reconstructing the original geometry and dynamical properties of aggregates before the collision. Bagheri et al. (2016) reveal the presence of large inner particles in a vast majority of the observed PC aggregates at Sakurajima Volcano, during the eruptions of July-August 2013. For the same volcano Gilbert and Lane (1994) reported the presence of large cores, even if inside the accretionary lapilli. An important fact of the observations of Bagheri et al. (2016) is that the inner particle did not stick to the collector, e.g. the sticky paper, as the coating part did. The remaining part of the cluster could have been erroneously interpreted as PC1 object, similar in shape. The same phenomenon has been observed a posteriori using the videos obtained by Taddeucci et al. (2011) during the 2010 Eyjafjallajökull eruption. Field observations reveal a high degree of complexity in volcanic ash aggregation: different geometries, different sizes and degrees of preservation, different bounding mechanisms.

1.2 Laboratory characterization of ash aggregation

In the last two decades field and theoretical observations have stimulated a large amount of experimental investigations on volcanic ash aggregation. The seminal work of Gilbert and Lane (1994) represents one of the first complete attempts to recreate the

accretionary lapilli in a laboratory apparatus. In particular, the authors report for the first time an experimental curve of the aggregation efficiency. In their experiment they used a vertical wind tunnel to inject ash over the surface different suspended targets: water droplets or polystyrene spheres. Pure water or sodium chloride solutions were injected together with the ash flow or deposited on the surface of the target sphere. At the end of the process the authors managed to recreate similar structures to those observed in the accretionary lapilli. In particular they suggested that sodium-chloride crystals could act as a strong binding medium and explain the compactness of the samples observed in nature. This hypothesis has been supported by recent laboratory experiments (Mueller et al., 2016) and field observations (Burns et al., 2017). Concerning the dynamical properties of ash clusters, Lane et al. (1993) experimentally investigated the terminal velocity of roughly spheroidal aggregates, with variable porosity and structure. Gilbert et al. (1991) conducted field experiments with real ash fallouts at Sakurajima using parallel charged plates and a Faraday cage. The authors estimated a surface charged density almost equal to the saturation limit, indicating an enormous presence of electrostatic charges. These results are confirmed from experiments on the role of electrostatic charges conducted by Schumacher (1994), who dispersed samples of ash in a strong external electrostatic field. He observed a transport of part of the material along the horizontal direction, along the force lines of the

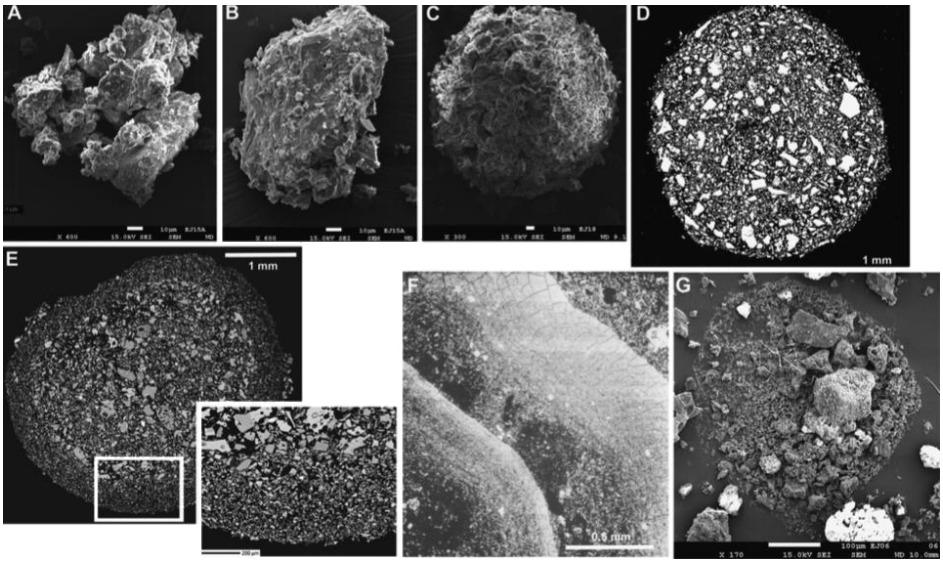

Figure 1.1 Image taken from Brown et al. (2011). a) PC1 particle clusters; b) PC2 coated particle; c) AP1 particle, all taken from 2010 eruption of Eyjafjallajokull volcano, Iceland. (Bonadonna et al., 2011b). d) AP1 from Soufriere Hills volcano, Montserrat (Bonnadonna et al., 2002b); e) AP2 from Upper Scoria deposits, Santorini; f) Close-up image of rims of an AP2 concentrically structured accretionary pellet from Poris PDC deposit, Tenerife (Brown and Branney, 2004); g) Evaporated mud rain droplet (AP3) from 2010 eruption of Eyjafjallajokull volcano, Iceland (Bonadonna et al., 2011b).

electrostatic field. This experiment confirms the high degree of electrification of volcanic ash. Similar experiments are conducted by James et al. (2002) in order to estimate the role of electrostatic charge on freely falling dry aggregates. Fragmentation of 1980 Mount Saint Helens samples of pumices created the electrostatic charge on the surfaces of the particles (*fracto-emission*). The authors measured terminal sizes, densities and terminal velocities of their laboratory products. An interesting observation is that the measured fall velocities for clusters can be modelled as equivalent spheres of low density ($100 - 200\ kg/m^3$). These results are also confirmed by a second series of experiments with a similar apparatus (James et al., 2003). Telling and Dufek (2012) conducted experiments of ash aggregation in an enclosed tank where humidity can be varied and the motion of particles monitored by the combination of Particle Image Velocimetry (PIV) and HS cameras. The authors focused on the crucial aspect of relative kinetic energy of a collision. In particular they reported the aggregation efficiency, i.e. the probability of a successful sticking, as a function of the collision kinetic energy for a few dozen of points. Van Eaton et al. (2012) instead used a vibratory pan in order to investigate aggregation growth patterns under a wide range of temperatures and water conditions. A remarkable aspect of this experiment is the importance given to the specific role of ice in volcanic aggregates, further extended from a theoretical point of view in Van Eaton et al. (2015). A final interesting and recent experiment by Mueller et al. (2017) focuses the attention on the stability of ash pellets structures. In their apparatus the author analyses the impact of artificial aggregates against flat surfaces. The main bond between single particles consists of Na-Cl bridges that result in a stable cementation process. The authors find that coarse-grained aggregates (i.e. the size of primary particles $\geq 50\mu m$) are remarkably more stable than fine-grained aggregates.

1.3 Theoretical models for ash aggregation

In the last thirty years great effort has been dedicated to the development and improvement of Volcanic Ash Transport and Dispersal Models (VATDMs) (Folch, 2012). Their role became crucial to the operational community when the air space of central Europe was closed during the 2010 Eyjafjallajökull eruption. Given the location of the

eruption, ash advisories were mostly compiled by the London Volcanic Ash Advisory Center (VAAC), describing the presence of ash over large parts of Europe. During the period 15-21 April 2010 more than 300 airports were closed and 7 million passengers were affected in more than twenty countries. It became evident to the overall society how the capacity of predicting volcanic ash trajectories and concentrations had severe consequences on various economic sectors. In this scenario volcanic ash aggregation played a primary role. As a matter of fact, the terminal velocity of clustered particles is usually higher than the components (Lane et al., 1993). Neglecting aggregation results in overestimation of fine ash in the atmosphere in the far-field, with a consequent increase of the predicted concentrations. Most aggregates break soon after the impact on the ground and evidence of their aggregated configuration is lost (Bagheri et al., 2016). Given that the Total Grain Size Distribution (TGSD) is a key input parameter for VATDMs and it describes the initial "disaggreagated" ejected particle population, if particle aggregation is not considered, model outcomes cannot be accurate.

Unfortunately, the nature of aggregation presents several complications that make its modelling complex, challenging and often inefficient. First, aggregation may involve a large number of objects (particles concentration$\sim 10^7 - 10^{11} \frac{\#}{m^3}$). Secondly, aggregation in a volcanic context frequently occurs in highly turbulent environments with Reynolds number up to $Re \sim 10^{11}$ (Kieffer and Sturtevant, 1984). Thirdly, the physics of the collision and the sticking processes is quite far from being well understood for ash. It is thus not surprising that different modelling approaches, with different degrees of compromise, have been developed throughout the years. Two main families of models can be defined: the *empirical* and the *theoretical models*. All those methods that empirically modify the initial TGSD according to the best fits with field observations belong to the first family (Biass et al., 2014; Bonadonna and Phillips, 2003; Cornell et al., 1983). The second family identifies those methods that obtain a modified TGSD according to a pre defined theoretical framework (Costa et al., 2010; Textor et al., 2006; Veitch and Woods, 2001). The great majority of the existing models take into account aggregation as a modified TGSD for the initial dispersal part (Folch et al., 2016; Mastin et al., 2016). This method somehow derives from the observation that a better fit between observed data and predicted results can be obtained modifying the terminal velocity of pre-determined classes of particles (Armienti et al., 1988; Carey and Sigurdsson, 1982).

One of the first historical attempts to fully incorporate the effects of agglomeration processes in an empirical prediction model dates back to Cornell et al. (1983). The authors assume that all aggregates appear as a unique effective aggregated class with diameter d_{agg}^{C} and density ρ_{agg}^{C}. To this class are attributed the 50% of ash with diameter $44 - 63\ \mu m$, the 75% of ash between $31 - 44\ \mu m$, and the 90% of ash smaller than $31\ \mu m$. These percentages derive from a best fit with predicted and observed quantities for the Campanian tuff ash layer (Y-5), correlated with the 38,000 y.b.p. Campanian ignimbrite. Bonadonna et al. (2002) and Bonadonna and Phillips (2003) extended this approach to wet aggregates, modifying empirically the initial TGSD according on the experimental results of Gilbert and Lane (1994). Sulpizio et al. (2012) attributed to a single aggregate size d_{agg}^{S} the constant percentages removed from smaller sizes involved in aggregation processes. The value of the percentages is derived from a best fit. An extended application of the previous approaches is reported in Mastin et al. (2016). The authors investigated four deposits and a total of 192 simulations, holding fixed the ash density ($\rho_{agg}^{M} = 600\ kg/m^3$) and investigating the variance of aggregates size d_{agg}^{M} (i.e. the mean value of the distribution of aggregates) as a function of different eruptive conditions. Despite the great variability of the initial conditions they found that d_{agg}^{M} ranged in a narrow interval ($0.15\ mm \leq d_{agg}^{M} \leq 0.20\ mm$). This result is somehow relevant, since it demonstrated common and invariant features of ash aggregation regardless the eruptive scenario. All the previous methods are based on the modification of the TGSD in order to obtain a good fit with field data. A completely different approach starts from the physical equations that govern aggregation and try to reconstruct the observed scenarios. However, this methodology is often challenging and sometimes intractable, unless some approximations are made. The reason of this complexity is directly linked to the physics of the phenomenon: if we limit our attention to the volcanic plume, it is not rare to find peaks in particles concentration of $\sim 10^7 - 10^{11}\ \frac{\#}{m^3}$. It is thus clear that even the most complete theory needs an initial simplification of the problem. In his seminal work Smoluchowski (1916) introduced the so-called *mean field approximation* to treat coagulation problems. In this approximation the population of particles is fully described with a density function $f(m)$ [units: $\frac{\#}{kg \cdot m^3}$], which is characterized by the following property:

$$N_k = \int_{m_{k-1/2}}^{m_{k+1/2}} f(m)\, dm \tag{2.1}$$

Where N_k is the number of particles per unit volume with mass comprised between $[m_{k-\frac{1}{2}}, m_{k+\frac{1}{2}}]$. According to Smoluchowski, the creation of particles with mass m is given by the conservation equation:

$$\frac{df(m)}{dt} = \frac{1}{2}\int_0^m K(m-\varepsilon,\varepsilon)\; n(m-\varepsilon)\, n(\varepsilon)\, d\varepsilon \; - n(m)\int_0^\infty K(m,\varepsilon)\, n(\varepsilon)\, d\varepsilon \tag{2.2}$$

The first term indicates the creation of particles with mass m due to collision of smaller sizes. The second term describes the loss of particles of size m due to the interaction with all the other sizes. The physics of the interactions is condensed inside the quantities $K(m_1, m_2)$, usually considered as the product of a collision rate β and a sticking efficiency α. The density function $f(m)$ can be mathematically related to the TGSD commonly used in volcanology.

One of the first application of the complete Smoluchowski theory in a volcanic context appeared in Veitch and Woods (2001). In their work the authors introduced mass balance equations inside plume transport equations. The final result is a TGSD that changes along the curvilinear coordinate of the central axis of an erupted column. Despite the simplifications assumed on the definition of the quantities $K(m_1, m_2)$, this first attempt of coupling of aggregation and plume equations still represents an important milestone, later followed by other authors.

A more sophisticated approach, but still based on the Smoluchowski equations, is represented by the aggregation scheme implemented in ATHAM (Active Tracer High resolution Atmospheric Model) (Textor et al., 2006). In their work the authors improved the microphysics of the processes and adopted a set of generalized gamma functions as initial conditions for the TGSD. This aspect allows having analytical solutions of different integrals. They distinguish between intermodal and intramodal aggregation. Intermodal aggregation involves gravitational capture of particles of different sizes. This process leads to a gain of particles in the larger mode and a loss of smaller ones. Intramodal aggregation happens within a single fixed class.

A hybrid and alternative method to the Smoluchowski coagulation equations has been presented by Costa et al. (2010) and recently implemented in a volcanic plume by Folch et al. (2016). In their model the authors increased the efficiency of their numerical scheme using the a priori assumption that ash aggregates follow fractal geometry. This hypothesis implies that the number of particles N_p with size d_p contained in an aggregate of overall size d_A are:

$$N_p \approx \left(\frac{d_A}{d_p}\right)^{D_f} \tag{2.3}$$

Where $D_f \leq 3$ denotes the fractal dimension of the geometry. The use of this relationship simplifies the equations, but its ude in volcanology is still matter of debate. However it has been observed and experimented in several different scientific fields (Kostoglou and Konstandopoulos, 2001; Matthews and Hyde, 2004; Richardson, 1995). Similarly to Cornell et al. (1983), Costa et al. (2010) assume that all the aggregates appear in one single class d_{agg}^{CO} with unique density ρ_{agg}^{CO}. In this sense this model is in between the empirical and the theoretical approach.

1.4 Reconstruction of the erupted plume heights from clast positions on the ground

One of the crucial aspects related with clasts sedimentation is the hidden information contained in their spatial distribution. As a matter of fact, tephra are frequently the only "witnesses" remained of many ancient or not observed eruptions. Carey and Sparks (1986) developed a well know method, here named as *CS method*, that allows associating the height of an eruptive column and wind intensity at the time of the eruption with the maximum downwind and crosswind distances on the ground of centimetric clast sizes. The theoretical background behind this method relies on the so-called *clast support envelopes*. The underlying idea is that clast sizes can be transported in a volcanic plume until the drag of the rising gas mixture is strong enough to counter balance the gravity force. When the velocity of the gas decreases, the resulting drag is not sufficient anymore and clasts start their sedimentation process. Converting the drag coefficients in terms of velocities, the authors derive a simple relation to define the exact

position where particle start to sediment: this threshold is represented by the point where the terminal velocity of a clast equals the upward plume velocity. Assuming a Gaussian profile for the radial component of the gas mixture velocity, we can define a region inside the eruptive column where clasts will be released: the *clast support envelope*. Particles are then released from this region and sedimented on the ground under the action of pre-defined atmospheric wind profiles. For a given clast and eruption, the maximum positions on the ground along the wind axis and its orthogonal direction constitute the downwind and crosswind distances.

Carey and Sparks (1986) use the plume model presented in Sparks (1986) in the *forward process* of relating final unknown distances with known column heights. For each eruption and wind condition investigated in their work, they associated a plume height to a couple of maximum downwind and crosswind distances. The final dataset collected at the end of this sensitivity process is then used in a backward process, i.e. to relate known clast distances to unknown plume heights. Their methodology provides a set of plots, called *nomograms*, that allows relating a combination of maximum downwind and crosswind distances with the unknown height and wind intensity of the eruption that generated that specific sedimentation event. Nomograms work for fixed clast size and density combination, in a total range of $250\,\frac{kg}{m^3} \leq \rho \leq 2500\,\frac{kg}{m^3}$ and $0.8\,cm \leq d \leq 32\,cm$. More recently, Burden et al. (2011) revised the CS method, improving some aspects related to the plume dynamics and the detail of the atmospheric winds. Moreover they introduced a probabilistic use of the procedure that allows quantifying the uncertainties associated with the method. The probabilistic approach relies on the execution of many repetitions of the same eruption, with initial conditions confined in a predetermined range. The final outcome of the procedure is a distribution of values from which the statistical parameters of interest for the definition of uncertainty can be deduced (mean, variance, etc.).

Nonetheless, both the CS method and the model of Burden et al. (2011) do not consider the effect of wind on eruptive columns, i.e. the CS method can be strictly applied only to strong eruptions, where the central axis of the plume is supposed to be vertical.

1.5 Objectives of this work

The previous sections emphasize that the study of volcanic particle sedimentation poses a series of open questions that still need to be fully addressed.

In particular:

1. When and where does aggregation of ash occur? What are its kinematic and dynamic properties?
2. How is it possible to fully describe the formation of solid agglomerates from a theoretical point of view?
3. What is the actual geometry of volcanic ash aggregates before their impact on the ground? How does it affect the theoretical description?
4. How can we practically parameterize and study the structure of an aggregate?
5. What are the leading processes that lead ash to stick?
6. How can plume height be derived based on clast distribution associated with weak and transitional plumes? Can we use the same model to assess the associated hazard?

This thesis consists of four main chapters. **Chapter 2** presents the paper written as part of the NEMOH special volume (Rossi E., Bonadonna C. "*Field and theoretical investigations of volcanic ash aggregation: the case of the eruption of 3rd of August 2013 at Sakurajima Volcano (Japan)*", In: P. Papale et al., Numerical, Experimental and Stochastic Modelling of Volcanic Processes and Volcanic Hazards, (INGV Pisa, in press)). It this chapter, the 1-D aggregation equations are coupled within a thermal plume model. The main goal is to compare the computed aggregation timescales with those observed during weak Vulcanian explosions that occurred on the 3rd of August 2013 at Sakuarajima Volcano (Japan). This work is characterized by the first application of the *fixed-pivot technique* to a volcanic problem.

Chapter 3 describes the Generalized Fixed Pivot Technique (GFPT), a new methodology that extends the fixed-pivot technique towards arbitrary multidimensional spaces. The aim of this work is to provide a general mathematical tool capable to solve complex aggregation problems. In particular this technique attempts to overcome the limitations existing in the old descriptions derived from coagulation problems of water droplets. As

a matter of fact, volcanic ash, proto-planetary dust and particulate matter are all composed by solid objects that require a more advanced theoretical framework (Rossi E., Patterson R., Bonadonna C., "*Aggregation of multidimensional arbitrary properties: the Generalized Fixed Pivot Technique*", submitted to "Physical Review E").

Chapter 4 introduces a way to combine the GFPT into a steady-state volcanic plume. This work represents the first application of a multidimensional population balance in a volcanic problem. In particular two internal parameters are proposed to fully characterize volcanic aggregates: mass and porosity, i.e. mass and density. The whole population of particles is thus tracked as it rises within the column. The main outcome of the model is a Total Grain Size Distribution (TGSD) that accounts for particle clusters. Moreover several aspects related to ash aggregation are presented in detail: a numerical computation of coated aggregate porosities; an exhaustive dissertation on the collision kernels that should be used in a volcanic plume; sticking efficiencies for wet and dry aggregation; quantification of the dissipative mechanisms present on the surface of volcanic ash, with the exclusion of electrostatic forces, net or induced (Rossi, Pollastri, Bonadonna , *in prep*).

In **Chapter 5** we propose a new model for the determination of plume height of volcanic eruptions based on the maximum downwind and crosswind distances of isopleth contours. This model is based on the approach of Carey and Sparks, 1986, but it introduces tilted clast support envelopes and new implementations of gravity current, 3D meteorological data and topography. The main results of this work are twofold: the possibility to use this model for forward predictions and the production of a new series of *nomograms* that take into account the effect of the wind on the shape of the clast support envelopes. The last point extends the use of the Carey and Sparks methodology for weak and transitional plumes (Rossi E., Bonadonna C., Degruyter W., "*A new strategy for the estimation of plume height from clast dispersal in various atmospheric and eruptive conditions*", submitted to Earth and Planetary Science Letters).

Chapter 2

Sectional methods in volcanology: the case of the eruption of 3rd of August 2013 at Sakurajima Volcano (Japan)[1]

2.1 Introduction

Volcanoes are a source of multiple hazards, e.g. lava flows, pyroclastic density currents, tephra fallout and lahars. Among all the possible hazards, tephra fallout has the potential to affect the surrounding environment from short to very large distances, with disruptive consequences on local communities and both land and aviation transport. The spatial and temporal scales of tephra fallout strongly depend on how single particles interact among themselves and with all the gas phases involved in the eruption. Here we will focus on a particular aspect that has large consequences on tephra fallout: volcanic ash aggregation. Field evidence from the Sakurajima campaign of August 2013 are discussed from a theoretical point of view. These results are presented exhaustively in the work of (Bagheri et al., 2016) and more details can be found there. The main purpose of this work is to show how these two different and independent approaches, theoretical and field-based, may be connected to complete our understanding of the problem. Aggregation processes are known to affect sedimentation of fine ash (< 63 μm) by considerably reducing its residence time in the atmosphere (Brown et al., 2012; Lane et al., 1993). If particle aggregation is not taken into account, volcanic ash transport and dispersal models fail to accurately describe both particle deposition in proximal areas and atmospheric concentrations in the far field, with important implications for hazard assessment and real-time ash forecasting (Folch et al., 2010; Rose and Durant, 2011). From a physical perspective, aggregation is essentially the interaction of single particles, or clusters, to generate larger agglomerates. It can be seen as a process where two main

[1] Rossi E., Bonadonna C. "*Field and theoretical investigations of volcanic ash aggregation: the case of the eruption of 3rd of August 2013 at Sakurajima Volcano (Japan)*", In: P. Papale et al., Numerical, Experimental and Stochastic Modelling of Volcanic Processes and Volcanic Hazards

and distinct conditions must occur: collision and sticking. Volcanic particles mainly collide due to their different motions within the fluid. In fact, the degree of coupling of a particle with the flow inside a volcanic environment (Stokes number) may cover a wide number of ranges. This practically means that some particles will follow instantaneously the fluid changes and some others not. As a consequence, particles will experience different relative velocities and so they will collide if their cross sections are large enough. A given collision results in aggregation if the relative kinetic energies of colliding particles are depleted by some dissipative mechanisms. The final clustering depends on complex interactions of surface liquid layers, electrostatic forces or shape factors. Depending on the water content, particle aggregation results in the formation of particle clusters if water is absent and accretionary pellets in all the other cases (including poorly-structured pellets AP1, pellets with concentric structures AP2, and liquid pellets AP3 in the nomenclature of Brown et al. 2012). During the last two decades several experimental, numerical and field investigations have been carried out to describe aggregation processes in terms of particle grain-size distribution, terminal velocity, structure, density and porosity (e.g. (Lane et al., 1993; Gilbert and Lane, 1994; Schumacher, 1994; Schumacher and Schmincke, 1995; James et al., 2002; Bonadonna et al., 2011a; Taddeucci et al., 2011; Telling et al., 2013; Van Eaton, Harper, & Wilson, 2013)). However, due to the low preservation potential of particle clusters in the deposits, most studies focused on the characterization of the more resistant well-structured pellets (i.e. AP2 most commonly known as accretionary lapilli; (Gilbert and Lane, 1994; James et al., 2003)). In the first part of this paper we will introduce new field techniques especially designed for the study of particle clusters (also known as dry aggregates), which include ash clusters (PC1) and coated particles (PC2) according to the classification of (Brown et al., (2011). Ash clusters, PC1, are defined as fragile irregular shaped aggregates composed of particles < 40 μm, whereas coated particles, PC2, are defined as fragile aggregates comprised of a crystal, crystal fragment, pumice or lithic clast partially covered in fine ash. The traditional terminology “dry aggregates” can be somewhat misleading. In fact, dry aggregation implies an aggregation process where there is no evidence of macroscopic liquid droplets inside the clusters. This does not exclude the presence of water vapour in the mixture or even condensed humidity upon particle surfaces. In this case the layer of water on the surfaces, if present, is much thinner than the size of the particles involved. Field investigations of real-time volcanic

ash aggregation may count on studies that cover several decades: the 1980 eruption of Mount St. Helens, USA (Sorem, 1982), 1990-1994 eruptions of Sakurajima volcano, Japan ([Gilbert et al., 1991; Sparks et al., 1997]), the 1997 eruption phase of Soufrière Hills volcano, Montserrat (Bonadonna, et al., 2002) and the 2010 eruption of Eyjafjallajökull volcano, Iceland (Bonadonna et al., 2011; Taddeucci et al., 2011). Sorem, (1982) observed ash clusters with diameters between 250-500 μm about 390 km from the vent that were composed of particles <40 μm. (Gilbert et al., 1991) and (Sparks et al., 1997) reported ash clusters at Sakurajima volcano with diameters <3 mm, which consisted of particles <200 μm, whereas coated particles had diameters >200 μm and were covered with particles <20 μm. (Bonadonna, et al., 2002) observed both types of particle clusters resulting from either dome collapse or Vulcanian explosions at Soufrière Hills volcano. Finally, at Eyjafjallajökull volcano Bonadonna et al. (2011) observed both types of particle clusters between 10 and 55 km from vent. Ash clusters had diameters up to 600 μm and consisted of particles < 90 μm, while coated particles were composed of large particles up to 760 μm that were coated with particles < 100 μm. For the same eruption, High-Speed (HS) videos recorded by Taddeucci et al. (2011) show how most particle clusters fell with terminal velocities between 1 - 4 m/s at ground level. In this work we have introduced a multi-technique approach for field investigations applied to a specific volcanic explosion of Sakurajima volcano (Japan), which includes field High-Speed-High-Resolution (HS-HR) imaging and analyses of in-situ collected particle clusters. The advantage of this technique relies on its capability to describe completely aggregates as they form and fall in a real environment, without any a priori assumption or bias. Aggregates are so described in terms of their terminal velocity, density, population and structure. This work represents the first step done under my fellowship within the NEMOH ITN to go towards a more detailed and physical-based approach to the unsolved problem of ash aggregation. The novel contribution of this work is twofold: first, we provide strong field constrains on timescales and shapes of dry aggregates before their impact on the ground; second, discrete methods to the numerical solution of aggregation equations are introduced. The main objective of this study is to underline how modern observations can be linked to a general theoretical description, which can start from the physics of the processes to retrieve some measured evidences from the field, like sizes or timescales for observed aggregates. In

order to do this, the second part of this work will be dedicated to the development of a volcanic plume theory which may take into account the aggregation of volcanic particles.

2.2 Field observations: methods

Dry aggregation of volcanic particles is frequently observed in those eruptions where fine ash is present (<63 μm) and meteorological conditions are favourable (high relative humidity). Electrostatic forces are also supposed to play a key role at these sizes. Direct observations of falling aggregates are not rare: some well-studied examples are the eruptions of Sakurajima Volcano in Japan (Gilbert et al., 1991) and Eyjafjallajökull eruption of 2011 in Iceland (Bonadonna et al., 2011; Taddeucci et al., 2011). Despite their importance, an exhaustive description of particle clusters is not always easy due to their fragile structure leading to poor preservation in the deposits. For this reason, field techniques mainly involve the collection of tephra samples directly during fallout using sticky paper (e.g. Bonadonna et al., 2011). This simple technique permits analysis of the population of each single aggregate with a Scanning Electron Microscope (SEM). Recently, more sophisticated tools based on the use of high speed cameras have been applied to analyze major properties of aggregates, like terminal velocity, size and density (Taddeucci et al., 2011). Both techniques have advantages and disadvantages: direct collection of samples permits us to reconstruct a posteriori the grain-size of aggregates and characterize the internal structure but it fails to capture the associated sedimentation dynamic. On the other hand, HS movies allow us to see fundamental details of cluster sedimentation and impact with the ground, but the information on particles population inside aggregates is mostly missing. Only their combination can give a complete overview on dynamical and morphological properties of particle clusters without a-priori assumptions. Therefore, in order to fully characterize particle aggregation, we developed a multi-technique approach. Each aggregate is recorded during its falling and impact on the sticky paper. The part that sticks to the paper – which, in our experience, is rarely the entire aggregate - is further analyzed under the SEM.

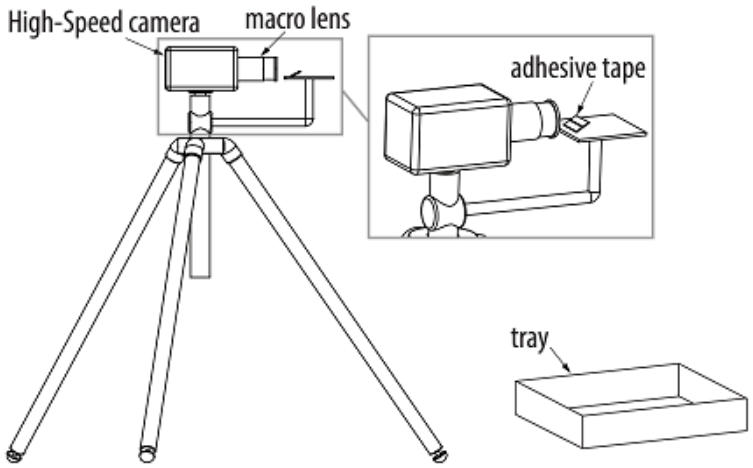

Fig. 2.1 Setup optimized for field recording of falling aggregates. Particles that land on the adhesive tape are filmed through the macro-lens of the High-Speed camera. The adhesive tape is usually strong enough to stick the coating part of the falling aggregates but not the internal core. Meanwhile a tray placed next to the tripod of the camera collects the falling tephra at that position.

In Fig. 2.1 a schematic diagram of the field setup is reported: a High-Speed (HS) camera on a tripod focused on a thin-glass support covered with a specific double-sided tape allowing for further analyses with a Scanning Electron Microscope (SEM). The HS camera with a resolution of 1200×800 pixels at 800 fps mounted with a Nikon 60 mm f/2.8D AF Micro-Nikkor lens was used at the ground-based observation site in order to capture HS-HR movies with a pixel size of 40 μm. In addition, tephra samples are collected in dedicated trays at sequential time steps in order to monitor time variations in grain-size distribution. Ash from the trays was analyzed for grain-size using a Laser Diffraction (LD) particle-size analyzer (CILAS 1180). This technique allows measuring, directly or indirectly, the following quantities: i) terminal velocity; ii) aggregate population; iii) density; and iv) internal structure. This multi-approach was applied during the field campaign at Sakurajima Volcano (Japan) of July-August 2013. Detailed measurements were acquired for one particular eruption that occurred at 17:47 Japanese Standard Time (JST) on the 3rd of August 2013, which reached a maximum plume height of 2.8 km a.s.l. The eruption consisted of three major single explosions that produced an ash cloud that reached the maximum height after about 240 seconds after the onset. The ash cloud spread toward south-east with a velocity of ~5.5 m/s as inferred from wide angle HD movies. Our ground-observation site was located about 3.7 km downwind from the vent along the dispersal axis. Ash fallout was sampled at two

time intervals in order to characterize sedimentation in time: i) between 18:00 and 18:07 JST, associated with the arrival of individual particles followed by sub-spherical aggregates (Phase I), and ii) between 18:07 and 18:12 JST mostly associated with sub-spherical aggregates (Phase II). Individual particles were recognized as non-vesiculated fragments with diameters between ~300-1200 μm and density of ~2500 kg/m^3 (measured by water pycnometer).

2.2.1 Field observations: results and discussion

Aggregate cores: evidence from observations

As shown in Fig 2.2, all aggregates broke at impact with the adhesive tapes, leaving behind an ensemble of fine ash and a significantly larger particle (from now on defined as *core*), which in most of the cases bounced off of the sticky paper. Sizes of cores (~ 200-500 μm) are comparable with the sizes of the entire aggregates before the impact (~ 400-800 μm) and correspond well to the mode of the coarse population of ground deposit for aggregates sedimented during both fallout phases (i.e. 500 μm and 250 μm, respectively; red arrows in Fig. 2.2). Ash coating mostly consists of particles < 90 μm and it is clear from Fig. 2.2b that this image on the sticky paper recalls the idea of what we typically interpreted as a fragile particle cluster in Brown et al. (2012) (i.e. PC1). The whole aggregate - core plus coating - is more similar to a coated particle (i.e. PC2). However, Bagheri et al. (2016) introduced a new category of particle clusters (PC3; *cored clusters*) to better describe these aggregates that have a larger coating than PC2. In fact,

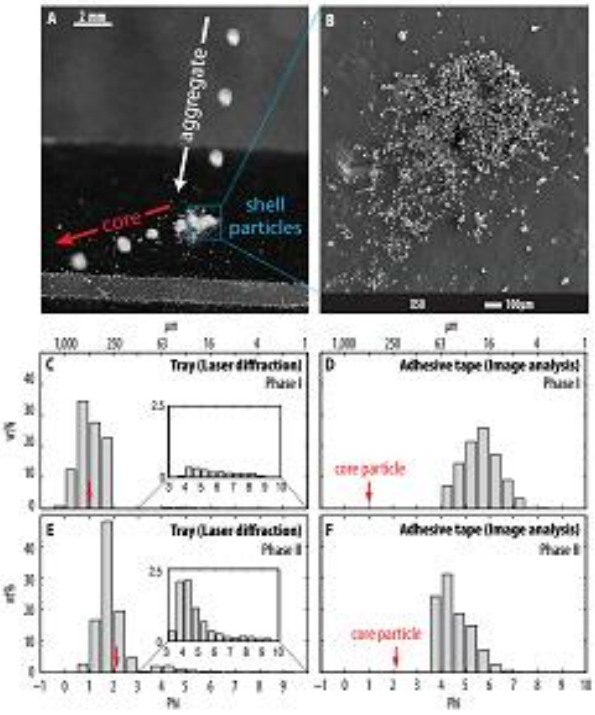

Figure 2.2 (a) Recorded image of a falling aggregate upon a sticky paper that shows the escape of a larger particle inside the whole cluster. (b) Scanning Electron Microscope image of particles of the shell. These small particles represent all what remains on the adhesive tape of the original aggregate. Without the recorded image, the shell particles could be erroneously misinterpreted as the whole aggregate (i.e. PC1). (c-e) Grain size analyses of ash collected in the tray during the first (18.00-18.07 JLT) and the second fallout phase (18.07-18.12 JLT). (d-f) Grain size analyses of particles contained inside two different aggregates sedimented respectively in the first (d) and second fallout phase (f).

cored clusters (PC3) are mostly sub-spherical fragile aggregates that have never been observed in the deposits nor on adhesive tape as they typically break at impact with the ground. They consist of a core particle (coarse ash to fine lapilli size) fully covered by a thick shell of particles < 90 microns.

Aggregate cores: consequences on aggregation

The difference is not just a matter of nomenclature, but it has deep consequences on the dynamics of sedimentation and modelling in general. First, if aggregates are thought to be created from fine ash only, as previously thought based on SEM analysis alone (Sorem, 1982; Lane et al., 1993; Brown et al., 2012), they should be categorized as ash clusters, for which the main collision mechanisms are very weak. However, we suspect that most PC1 described in literature originally deposited as cored aggregates (i.e. PC3), as it can also be seen in the HS videos recorded during the Eyjafjallajökull 2010 eruption (e.g. VIDEO #2 of Taddeucci et al., (2011)). Cored aggregates can form much faster and at much lower particle concentrations than PC1 because their collision mechanisms, i.e. the so-called *differential settling*, are several orders of magnitude more efficient than Brownian motion and turbulence (Elimelech et al., 1998), (Pruppacher & Klett, 2004), (Costa et al., 2010). Additionally, it is widely accepted that the grain-size of fallout deposits affected by particle aggregation are bimodal because they consist of simultaneous sedimentation of individual lapilli and/or coarse ash particles together with fine ash particles aggregated in clusters (Carey and Sigurdsson, 1982; Brazier et al., 1983). Although this theory can account for the deposition distance of individual particles, which in some cases matches the deposition distance of aggregate cores, it fails to explain the proximal deposition of aggregates only composed of fine ash unless unrealistic aggregate densities are considered (Carey and Sigurdsson, 1982). In fact, premature fallout of fine ash can be more easily explained if most aggregates are considered to consist of coarse-ash particles coated a thick layer of particles <100 μm (PC3) instead of consisting of only particles <100 μm (PC1).

Aggregate dynamical features

The measured quantities from our HS videos are basically the terminal velocities and sizes of falling aggregates and internal cores (Tab. 2.1). The densities of the whole aggregates are evaluated inverting the formula for the terminal velocity. On the other

side densities of central cores are estimated under the hypothesis that these particles are part of the population of those collected in the trays. A first interesting point is the clear variation in the characteristics of aggregates deposited during Phase I and Phase II. Aggregates of Phase I are characterized by larger cores than aggregates of Phase II. Second, the ash coating of Phase I is thinner than the ash coating of Phase II aggregates compared to their core diameter. The ash fraction involved in the coating of individual aggregates, ϕ_{agg}, for Phase I is about 10% whereas for Phase II it is 17% (Bagheri et al., 2016). This indicates that Phase I aggregates were associated with thinner ash coating than Phase II aggregates compared to their core diameter.

		Aggregates				**Core particles**	
Fallout phase	**Sed. Time**	**Diameter [μm]**	**Density [$kg\ m^{-3}$]**	**Velocity [ms^{-1}]**	**Porosity [%]**	**Diameter [μm]**	**Density [$kg\ m^{-3}$]**
I	18:02-18:07	718 – 807	806 – 1009	2.7 – 2.9	60 – 68	500 – 525	2500-2700
II	18:07-18:12	440 – 630	357 – 864	1.2 – 1.8	67 – 83	200 – 330	2500-2700

Table 2.1 Observed aggregates at Sakurajima Volcano during the eruption of 3rd of August 2013.

Timing of aggregation

Given that Phase II clusters are characterized by thicker shells and most likely needed more time to form than Phase I clusters, it can be concluded from numerical inversions (Bagheri et al., 2016) that particle clusters can be formed within 180 seconds after the onset of the eruption. As a comparison, accretionary lapilli and frozen accretionary pellets were reported to be formed within 300 and 600 seconds after the onset of 1990 eruption of Sakurajima volcano (Japan) and the March 2009 eruption of Redoubt volcano (Alaska), respectively (Gilbert and Lane, 1994; Brown et al., 2012). It cannot be excluded in our case that aggregation continued to occur beyond 175 s simply because our observation is just based on a single proximal location in the field.

2.3 Theoretical investigations

One of the main challenges in the characterization of particle aggregation includes the capability to describe field observations from a theoretical point of view. In this section a mathematical model for ash aggregation is introduced. As outlined in the introduction, aggregation is the result of the sticking of single particles (or agglomerates) once they have collided together. It is evident that a theoretical description of aggregation processes should be dependent on, at least, three main quantities: i) concentration of particles; ii) collision rate and; iii) sticking efficiency. If at least one of these quantities is zero, aggregation can simply not occur. The equation that relates these three quantities is the so-called "Smoluchowski Coagulation Equation" (SCE) (Jacobson, 2005), which describes the evolution in time of a population of particles of mass m in a control volume where no other physical processes occur (diffusion, advection, etc.):

$$\frac{dn(t,m)}{dt} = \frac{1}{2}\int_0^m K(t, m-\varepsilon, \varepsilon)\ n(t, m-\varepsilon)\ n(t,\varepsilon)\ d\varepsilon\ - n(t,m)\int_0^\infty K(t,m,\varepsilon)\ n(t,\varepsilon)\ d\varepsilon \tag{2.4}$$

Key quantities that appear inside the equation are:

- $n(t,m)$: distribution function of the number of particles per unit volume with a mass equal to m at a certain time t (units: $[\frac{\#}{kg \cdot m^3}]$)
- $K(t,m,\varepsilon)$: Aggregation kernel, which contains all the information about collision rates and sticking efficiencies of particles of masses m and ε (units: $[\frac{m^3}{s}]$). For clarity, this term is usually split in to two different contributions to enhance the different roles of sticking and collision: $K(t,m,\varepsilon) = \alpha(t,m,\varepsilon)\ \cdot \beta(t,m,\varepsilon)$, where $\alpha(t,m,\varepsilon)$ is the sticking efficiency (units: [#]) and $\beta(t,m,\varepsilon)$ is the collision rate (units: $[\frac{m^3}{s}]$).

The Smoluchowski coagulation equation is a particular case of a more general and comprehensive theory, which is called "Population Balance Equations" (PBE) (Ramkrishna, 2000). The underlying assumption in this theory is that there is a density function that describes the number of elements (particles) inside a population with a

given selected property, such as "mass" in this case. This density function is described by the quantity $n(t,m)$, which represents the number of particles with a mass inside the interval $[m, m+dm]$. For clarity, it must be outlined that the aggregation equation is just a part of the General Dynamic Equation (GDE), which studies how the distribution function $n(t,m)$ evolves in presence of other physical processes, like for instance advection and diffusion, just to mention the more common ones in volcanology. The complete transport equation for an "advection-diffusion-aggregation" process characterised by a constant of diffusion D $[m^2/s]$ is (Gelbard & Seinfeld, 1979):

$$\frac{\partial n(t,m)}{\partial t} + \nabla \cdot (n(t,m)\,\vec{v}) - \nabla \cdot (D\,\nabla n(t,m)) = \frac{1}{2}\int_0^m K(t, m-\varepsilon, \varepsilon)\; n(t,m-\varepsilon)\, n(t,\varepsilon)\, d\varepsilon \; - n(t,m)\int_0^\infty K(t,m,\varepsilon)\, n(t,\varepsilon)\, d\varepsilon \tag{2.5}$$

The solution of the aggregation equations is not trivial and analytical solutions exist only for simple cases. There are several methods for the numerical solution of Eq. (2.1), but generally they can be grouped in three major families (Vanni, 2000): method of moments (Standard Moment Method, Quadrature Method of Moments), stochastic methods (Monte-Carlo) and sectional methods (Fixed-Pivot, Cell-Average, Finite-Volume). Each of these approaches has different pros and cons: moment methods are usually faster than others, since they focus on some integral quantities of interest – i.e. moments. Sectional methods - also called "discrete methods" - are computationally more expensive, but they provide a direct description of the evolution of populations (Kumar & Ramkrishna, 1996). In the following, we will focus on sectional methods with a specific attention to the fixed-pivot technique and how it can be applied inside a thermal plume model. The purpose is to see how well this theoretical approach reproduces the main features observed during the Sakurajima campaign of July 2013.

2.3.1 Sectional methods: the fixed-pivot technique

In the sectional methods the continuous density function $n(t,m)$ is discretized over a total number of bins (N_c) and each bin (section) evolves in time. The discretization is done by substituting the density function $n(t,m)$ with the so-called "Dirac-comb", which

samples the continuous function at fixed positions m_k, as shown in Fig. 2.3 (Kumar & Ramkrishna, 1996):

$$n(t,m) = \sum_{k=1}^{N_c} N_k(t)\ \delta(m - m_k) \tag{2.6}$$

The quantities N_k are the number of particles per unit volume with mass inside each interval $[m_{k-1/2}, m_{k+1/2}]$:

$$N_k = \int_{m_{k-1/2}}^{m_{k+1/2}} n(m)dm = \int_{m_{k-1/2}}^{m_{k+1/2}} \left(\frac{dN}{dm}\right) dm \tag{2.7}$$

A common problem to all the sectional methods arises when the fixed positions m_k are not aligned on a linear grid. In fact, for arbitrary grids, the collision of two different particles of masses m_k and m_j rarely correspond to an existent mass m_i. For linear grids this problem is implicitly avoided since it is always true that $m_k + m_j = m_i$. Unfortunately the use of a linear gridding does not permit us to investigate a large number of diameters, due to the mathematical relation between mass, density and diameter. This is clear looking at the following relations:

$$d_1 \approx (m_1)^{1/3}\ ;\ d_{100} \approx (100\ m_1)^{1/3} \rightarrow \frac{d_{100}}{d_1} = (100)^{1/3} \approx\ 4.6 \tag{2.8}$$

That is, assuming spherical particles with the same density, one hundred linear bins in mass would cover just a factor 4.6 in diameter. This suggests that we replace a linear gridding with a logarithmic one, capable to cover the larger interval of particle diameters. For this, one needs to re-distribute mass between the available grid points (bins) in order to conserve the total mass. All the different sectional methods differ basically in the way they establish this rule to redistribute the mass. Among all the different sectional methods we discuss here the so-called “fixed-pivot” technique. The fixed-pivot technique is described exhaustively in (Kumar & Ramkrishna, 1996) and (Jacobson, 2005) and for a given bin labelled as m_i it redistributes the mass between the two closer bins m_{i-1} and m_{i+1} conserving the zeroth and first moment of the distribution, i.e. the number of particles and the total mass. If we refer to the scheme of Fig 2.3b this implies the following systems of equations:

$$\begin{cases} w_1(m, m_i)\ 1 + w_3(m, m_{i+1})\ 1 = 1 \\ w_1(m, m_i)\ m_i + w_3(m, m_{i+1})\ m_{i+1} = m \end{cases} \tag{2.9}$$

$$\begin{cases} w_2(m, m_i)\ 1 + w_4(m, m_{i-1})\ 1 = 1 \\ w_2(m, m_i)\ m_i + w_4(m, m_{i-1})\ m_{i-1} = m \end{cases} \tag{2.10}$$

For a given bin m_i the mass conservation is assured by the two quantities of interest $w_1$and w_2:

$$S = \begin{cases} w_1(m, m_i) = \dfrac{m_{i+1} - m}{m_{i+1} - m_i} \\ w_2(m, m_i) = \dfrac{m_{i-1} - m}{m_{i-1} - m_i} \end{cases} \tag{2.11}$$

The integration of Eq. (2.1) over the interval $[m_{i-1/2}, m_{i+1/2}]$, combined with the mass conservation assured by Eq. (2.8), leads to the fixed-pivot equations that rule the change in time of particles per unit volume of mass *i* due to aggregation (Kumar et al., 2006)

$$\frac{d\ N_i}{dt} = \ B_i - \ D_i \tag{2.12}$$

Where:

$$\begin{aligned} B_i = & \sum_{m_i \le (m_k + m_j) < m_{i+1}} \left(1 - \frac{1}{2}\ \delta_{kj}\right) \left(\frac{m_{i+1} - m}{m_{i+1} - \ m_i}\right) K(m_k, m_j)\ \ N_k\ N_j \\ & + \sum_{m_{i-1} \le (m_k + m_j) < m_i} \left(1 - \frac{1}{2}\ \delta_{kj}\right) \left(\frac{m - m_{i-1}}{m_i - \ m_{i-1}}\right) K(m_k, m_j)\ \ N_k\ N_j \end{aligned} \tag{2.13}$$

$$D_i = \sum_{j=1}^{N_c} \ K(m_i, m_j)\, N_i N_j \tag{2.14}$$

δ_{kj} is the so-called "Kronecker delta function" :

$$\delta_{kj} = \begin{cases} 0\ if\ k \neq j \\ 1\ if\ k = j \end{cases} \tag{2.15}$$

Equations (2.9), (2.10) and (2.11) represent the fixed pivot equivalent to (Eq.2.1). This means that the initial continuous problem has been transformed into a set of Ordinary Differential Equations (ODEs), one for each bin representing the *i*-th mass.

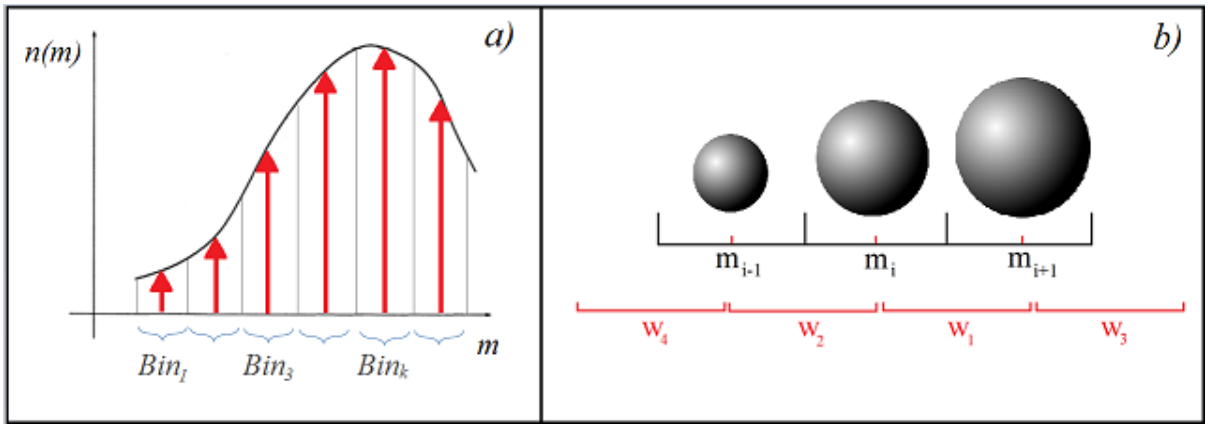

Fig. 2.3 (a) Discretization of a continuous curve n(m) using a sum of Dirac deltas. (b) Notation used in the fixed pivot technique, defined in order to conserve the first two moments of the distribution (number of particles and mass)

Aggregation kernels

Next step is to clarify the importance and meaning of quantities $K(m_i, m_j)$, which basically contain all the physics of the process. Aggregation kernels are basic quantities to study the evolution in time of populations since they describe the collision rate of particles of mass m_i and m_j that give rise to a new aggregate. This implicitly means that $K(m_i, m_j)$ contains the information about "successful" collisions, i.e. collisions that bring two particles to be stuck together. If, for example, the collision rate inside a volume is really high (e.g. billions of collisions per second), but no sticking processes have been occurring, $K(m_i, m_j)$ will be zero. This suggests to split the kernel matrix $K(m_i, m_j) = \alpha(m_i, m_j) \cdot \beta(m_i, m_j)$in two different parts: a dimensionless coefficient $\alpha(m_i, m_j)$, which describes the probability of sticking, and a dimensional parameter $\beta(m_i, m_j)$, which contains all the information about the collision rates (Jacobson, 2005). The dimensions of $\beta(m_i, m_j)$ are similar to a volumetric flow rate $[\frac{m^3}{s}]$. A complete discussion about collisional kernels and their derivation can be found in (Jacobson, 2005). In volcanology (e.g. Costa et al., 2010), the main processes taken into account for collision rates are turbulent-related kernels (turbulent-inertial (TI) and turbulent shear (TS)), laminar shear (LS), differential sedimentation (DS) and the Brownian motion (BM), which is negligible for the sizes involved.

$$\beta_{ij}^{TI} = \left(\frac{\epsilon^{3/4}}{g\nu^{1/4}}\right)\frac{\pi}{4}(d_i + d_j)^2\left|u_{ti} - u_{tj}\right| \tag{2.16}$$

$$\beta_{ij}^{TS} = \left(\frac{\pi\epsilon}{15\,\nu}\right)^{1/2}(d_i + d_j)^3 \tag{2.17}$$

$$\beta_{ij}^{LS} = \frac{\Gamma_L}{6}(d_i + d_j)^3 \tag{2.18}$$

$$\beta_{ij}^{DS} = \frac{\pi}{4}(d_i + d_j)^2\left|u_{si} - u_{sj}\right| \tag{2.19}$$

$$\beta_{ij}^{BM} = \frac{2\,K_B T}{3\mu}\cdot\frac{(d_i + d_j)^2}{d_i d_j} \tag{2.20}$$

where ϵ is the dissipation rate of turbulent kinetic energy, g is the gravitational acceleration, μ and ν are the fluid dynamic and kinematic viscosities, Γ_L is the laminar shear coefficient, u_s is the terminal velocity and u_t is velocity provided to particles trapped inside turbulent eddies. Some of these expressions depend on quantities difficult to quantify, especially for turbulent flows, like ϵ, Γ_L or u_t. Some approximations or assumptions must be taken in these cases. For example, according to (Textor & Ernst, 2004), the value of ϵ is related to the plume velocity u_p and the sizes of the largest eddies inside the plume (which we consider equivalent to the plume radius):

$$\epsilon \approx 0.1\,\frac{{u_p}^3}{L} \tag{2.21}$$

The laminar shear coefficient is theoretically given by:

$$\Gamma_L = \left|\frac{du_p}{dr}\right| \tag{2.22}$$

A key point is which kernels are relevant inside the volcanic environment. Here some basic concepts contained in (Textor & Ernst, 2004) and (Marshall & Li, 2014) are summarized:

1) The turbulent kernels β_{ij}^{TI} and β_{ij}^{TS} are valid within the Saffman-Turner limit, that is, for particles smaller than a characteristic spatial scale (called the "Kolmogorov length") and with Stokes numbers $St < 1$. In order to be inside the Saffman-Turner limit, particles have to be smaller than the turbulent eddies, which

implies having well correlated velocities between them. The Kolmogorov micro-scale is proportional to $\gamma_K \approx (\frac{{\nu_a}^3}{\epsilon})^{1/4}$, where ν_a is the air kinematic viscosity and ϵ is the dissipation rate of turbulent kinetic energy. For a plausible range of ϵ between $0.1 - 100\frac{m^2}{s^3}$, and for $\nu_a \approx 10^{-5} - 10^{-4}\frac{m^2}{s}$ we get $\gamma_K \approx 10^{-3} - 10^{-4}m$. This means that particles larger than some hundred microns will not be in the Saffman-Turner limit. In addition, as outlined by (Textor & Ernst, 2004) , the Stokes number of volcanic particles spans a huge number or values, roughly from 10^3 for bigger particles to 10^{-3} for the smaller ones. Also in this case is not easy to establish if the Saffman-Turner condition is valid.

2) Particles laying outside the Saffman-Turner limit show uncorrelated velocities among them, which basically means that they are not trapped inside the fluid turbulent eddies. This extreme is often called "the accelerative-independent regime" and it has been treated by Abrahamson (Marshall & Li, 2014), who introduced to the following expression for collisions among two particles with Stokes number $St > 1$:

$$\beta_{ij}^{AI} = \left(\frac{\pi}{6}\right)^{\frac{1}{2}} (d_1 + d_2)^2 \sqrt{\langle u_{mi}^2 \rangle + \langle u_{mj}^2 \rangle} \tag{2.23}$$

In this expression $\langle u_{mi}^2 \rangle$ stands for the mean-square velocity magnitude for a *i*-th particle due to an isotropic turbulence. It is worth-mentioning that u_{mi} is obviously different from u_{ti} used in [Eq. 2.13] since u_{ti} contains info related to the small eddies above the Kolmogorov scale. u_{mi} is a mean velocity given by the bulk turbulence which of course depends also on the particles involved, how they interact with different eddies and how they keep their inertia passing through them. Abrahamson kernel [Eq. 2.20] remains undefined so far for a volcanic plume, due to its dependency from the unknown quantities u_{mi}. Complete CFD simulations of turbulent plumes coupled with particles could provide a better understanding of this collisional kernel in future.

3) Sedimentation kernel β_{ij}^{DS} is due to differences in particle terminal velocity because of size, density, and shape. (Textor & Ernst, 2004) suggest to compare gravitational and turbulent effects using their respective accelerations as a term

for comparison. (Pruppacher & Klett, 2004) provide an expression for turbulent acceleration for particles with $St < 1$: $a_T = \frac{\epsilon^{3/4}}{\nu^{1/4}}$. In this case $g < a_T$ for $\geq 0.1\ \frac{m^2}{s^3}$. For larger particles with $St \gg 1$ the acceleration due to turbulent eddies with size γ_m between the largest one ($\approx$ plume radius) and the smallest one before viscosity terms become dominant (i.e. the Kolmogorov micro-scale γ_K) is: $a_m = \frac{(\epsilon\,\gamma_m)^{2/3}}{\gamma_m}$. Textor shows that using reasonable numbers for γ_m of 10, 100 and 1000 meters, $g > a_m$ for a wide range of values of the dissipation rate of turbulent kinetic energy ($\epsilon < 100\ \frac{m^2}{s^3}$). In practice this means that gravitational collection should be the dominant process for larger sizes in most of the volcanic plume and cloud. Nevertheless this comparison is true under the assumption that particles are under sedimentation: but volcanic particles are dragged upwards by the rising plume and as a rule of thumb sedimentation does not occur if upward velocity is higher than particles terminal velocities. From the comparison of Gaussian profiles of plume velocity and terminal velocities (Carey & Sparks, 1986) derive that relevant parts of the volcanic plume are not affected by sedimentation for particles with sizes less than 1 mm. This suggests that the role of the sedimentation kernel β_{ij}^{DS} inside a volcanic plume may be over-estimated if the role of the drag due to the upward velocity is neglected.

To sum up the previous analyses, the common leading parameters among all the different kernels concern the relative velocities and projected areas of two colliding particles. The source of uncertainty is the knowledge of the velocities assumed by different sizes in different fluid-dynamical conditions. In this report the collisional kernels of (Folch et al., 2016) will be used. They represent a good compromise between general features of particles inside the volcanic plume and simplicity. After clarifying the collisional part, we focus on the sticking efficiency $\alpha(m_i, m_j)$. This parameter is a dimensionless number that expresses the probability to have a given number N_s of stuck particles over the total number of collisions N_T for each pair of particles with masses m_i and m_j. The implicit assumption here is that the sticking efficiency is an ensemble average $\langle\alpha(m_i, m_j)\rangle$ over different collisions, involving pairs of particles with the same physical and chemical features. In order to have the sticking, the relative kinetic energies of the two colliding particles must be depleted by dissipative mechanisms.

Several processes are responsible for this, including viscous dissipation due to the presence of liquid layers upon the surfaces, presence of adhesion forces (electrostatic, chemical, etc.), work spent to rearrange the internal structure of aggregates, etc. A complete and exhaustive experimental investigation of all these processes is still far from being achieved, but theoretical expressions for specific cases are reported in literature. In this work the formulation of (Costa et al., 2010) for wet sticking is applied. This model is a recalibration for the volcanic environments of what is contained in the work of (Liu & Litster, 2002). The expression used for the sticking efficiency is a function of the viscous Stokes number St_{ij}:

$$\alpha_{ij} = c_1 \frac{1}{(St_{ij}/St_{cr})^q + 1} \tag{2.24}$$

Where $St_{cr} = 1.3$, $q = 0.8$, $St_{ij} = \frac{8\,\rho_p|v_i - v_j|}{9\mu_l} \cdot \frac{d_i d_j}{d_i + d_j}$ and c_1 is a multiplicative constant ($c_1 = 1$ in the original work). It is important to note that the sticking efficiency depends on the relative velocities of particles, which is one of the major sources of uncertainties affecting the collisional kernels. Here we follow the simplified approach of (Costa et al., 2010) and set the relative velocities equal to the terminal velocities $|v_i - v_j| \approx |v_{si} - v_{sj}|$. The formulation of (Eq. 2.21) should be used in all the situations where the pressure of water vapor inside the plume overcomes the saturation pressure of humid air respect to a liquid surface. In fact, in this condition the vapor contained inside the plume can condense and deposit upon the surfaces of interacting particles. One-dimensional plume models can provide general indications about this condition, but on the other hand they may neglect important details due to turbulence and humid air entrainment that can lead to a local exceedance of the saturation pressure. In this work we make the assumption that the shape of the sticking matrix is given by (Eq. 2.24) throughout the rising plume, but different values will be investigated both for the parameters q and c_1. The idea is that, in general, the mathematical form of any sticking process should describe the tendency to have a decrease in the efficiency as the sizes of the particles involved increase, as shown from the plot of (Eq. 2.24) in Fig. 2.7 .

2.3.2 Thermal model

Explosions at Sakurajima Volcano are very similar to an instantaneous release of ash. This observation justifies the idea of coupling the fixed-pivot equations with a non-sustained plume model, like the thermal-co-ignimbrite model of (Woods & Kienle, 1994). To do that, the mass conservation equation is split into the mass fraction n_d of the dry gas phase, the mass fraction n_v of the humid gas phase (vapor), the mass fraction n_w of the liquid water and, finally, the mass fraction n_s of the solid phase, introducing the equivalence for the bulk density $\rho_B = \rho_B n_d + \rho_B n_v + \rho_B n_w + \rho_B n_s$. In turn, the solid phase is divided among each *bin* according to the mass fractions x_i in order to assure $\sum_{i=1}^{N_{bin}} x_i = 1$.

We introduce some basic definitions to describe the contributions of dry air and vapor from the atmosphere to the model. Defining the atmospheric mixing ratio q_x as the ratio of the mass fraction of vapor n_{av} relative to the mass fraction of dry air n_{ad}, the following relations hold for atmospheric values (Degruyter & Bonadonna, 2012):

$$\rho_a = \rho_a n_{ad} + \rho_a n_{av} \tag{2.25}$$

$$\rho_a n_{ad} = \frac{P}{R_v T_a} \cdot \frac{(1+q_x)}{q_x + \frac{R_d}{R_v}} \cdot \left(\frac{1}{1+q_x}\right) \tag{2.26}$$

$$\rho_a n_{av} = \frac{P}{R_v T_a} \cdot \frac{(1+q_x)}{q_x + \frac{R_d}{R_v}} \cdot \left(\frac{q_x}{1+q_x}\right) \tag{2.27}$$

The expressions above are all functions of known environmental quantities except for the mixing ratio q_x. This quantity can be expressed in terms of the saturation vapor pressure e_s, the relative humidity r_h, and the gas constants for vapour and dry air, respectively R_v and R_d:

$$q_x = r_h \cdot \frac{R_v}{R_d} \cdot \frac{e_s}{P - e_s} \tag{2.28}$$

The modified conservation equations for mass yield to a new set of relations describing the thermal model in terms of a dry air gas phase, a vapor gas phase and, more

important, a set of equations equal to the number of size bins available for the solid phase:

Dry air phase:
$$\frac{d}{dt}\left[\frac{4}{3}\pi r^3 \rho_B n_d\right] = 4\pi\, r^2 k_\varepsilon u_p \rho_a n_{ad} \tag{2.26}$$

Vapor:
$$\frac{d}{dt}\left[\frac{4}{3}\pi r^3 \rho_B n_v\right] = 4\pi\, r^2 k_\varepsilon u_p \rho_a n_{av} - \frac{4}{3}\pi r^3 \rho_B n_v \lambda \tag{2.27}$$

Liquid water:
$$\frac{d}{dt}\left[\frac{4}{3}\pi r^3 \rho_B n_w\right] = \frac{4}{3}\pi r^3 \rho_B n_v \lambda \tag{2.28}$$

Solid phase (size i):
$$\frac{d}{dt}\left[\frac{4}{3}\pi r^3 \rho_B n_s x_i\right] = \frac{4}{3}\pi\, r^3 m_i (B_i - D_i) \tag{2.29}$$

Momentum:
$$\frac{d}{dt}\left[\frac{4}{3}\pi r^3 \rho_B u_p\right] = g\,(\rho_a - \rho_B)\,\frac{4}{3}\pi r^3 \tag{2.30}$$

Enthalpy:
$$\frac{d}{dt}\left[\frac{4}{3}\pi r^3 \rho_B \left(C_p T_p + gh + \frac{u_p^2}{2}\right)\right] = 4\pi r^2 \rho_a k_\varepsilon u_p (C_a T_e + gh) + L\frac{d}{dt}\left[\frac{4}{3}\pi r^3 \rho_B n_w\right] \tag{2.31}$$

Z-coordinate:
$$\frac{d}{dt} z = u_p \tag{2.32}$$

The fixed-pivot equations (Eq. 2.10-2.11) enter on the right-hand side of (Eq. 2.29). This implementation is a simplified description of the problem from several points of view, but it shows clearly how the discrete equations for aggregation can be embedded inside a more complete transport model for plume dynamics. This set of ODEs is solved explicitly with the ODE45 Runge-Kutta solver of Matlab. The typical outputs from the thermal model are shown in (Fig. 2.4).

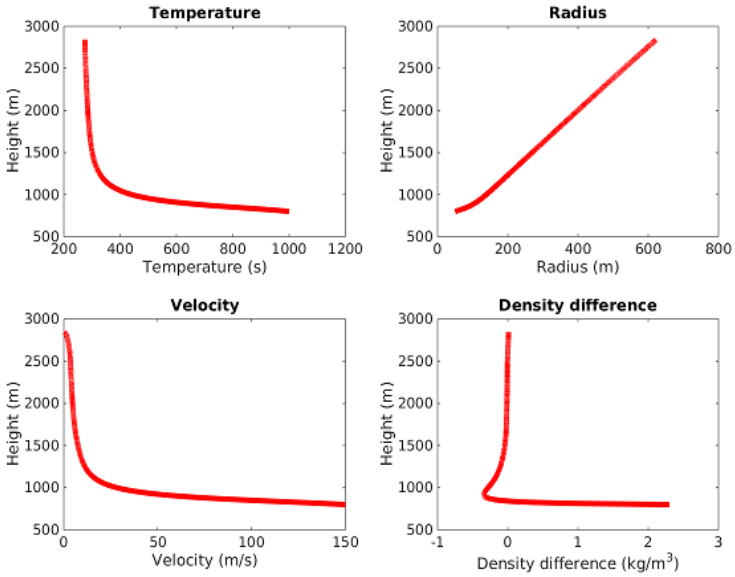

Figure 2.4 Eruption with v_{p0}=150 m/s, r_0 = 50 m, n_{d0}= 0.02, n_{v0} = 0.02, n_{s0} = 0.96, n_{w0} = 0. Temperature, radius, velocity and density differences displayed as a function of the height of the thermal

2.3.3 Results and discussion

Sensitivity investigations

Despite its simplifications, equations (2.26)-(2.32) represent a good testbed to analyze the dependence of the Smoluchowski equations on some key parameters implicit in the theoretical formulation. Three fundamental aspects of the thermal model are briefly analyzed here: i) the role of particle breaking (disaggregation) and its importance to not overestimate particle aggregation; ii) the importance of the initial conditions on the gas mixture; iii) the sensitivity of the outputs to changes in the sticking efficiencies. For all the simulations shown in this section an initial distribution of particles equal to a Gaussian with mean of 5 ϕ and variance of 2 ϕ is used. It is sampled every 0.5 ϕ.

1. A complete approach describing collisions between particles and aggregates should also describe their tendency to break if their relative kinetic energies are high enough to destroy their bonds or internal structures. Disaggregation somehow reduces the number of aggregates and keeps the grain size distribution similar to the initial one, or even finer. Progressively, as the relative kinetic energies decrease, aggregation prevails over breakings and equations (2.26)-(2.32) become reasonable to describe the population balance inside the thermal plume. We assume different initial areas above the vent where aggregation is forbidden in order to test the final TGSD (Fig. 2.5): these areas are parameterized respect to the vent, from a null region (red bars) to 10 times the initial radius (blue bars). Results of Fig. 2.5 show that neglecting the effect of particle disaggregation near the vent has severe consequences on the final distribution. Unfortunately, it is not easy to define quantitatively the region where aggregation can be considered as the leading process, since it depends on the relative velocities of particles and on the strength of the bonds. This deserves further investigation in a future.

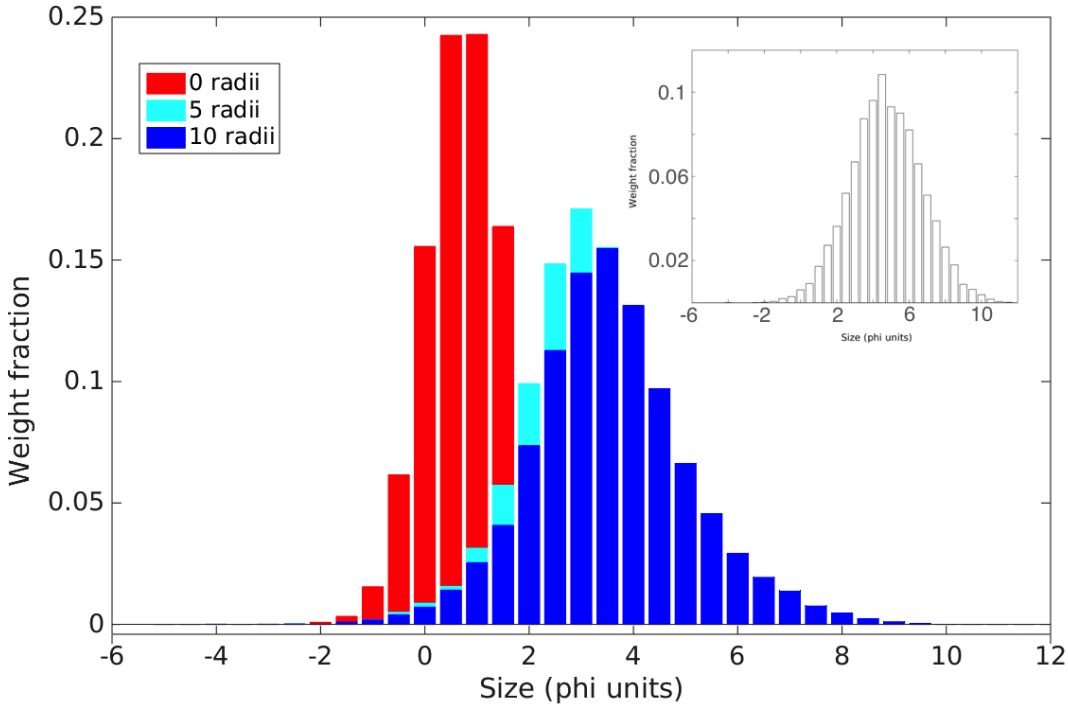

Fig. 2.5 Sensitivity test to investigate the effects of a "no aggregation zone" close to the vent, in order to account for the effects of disaggregation on the final distribution. The width of this region is parameterized with respect to the vent radius (equal to 50 meters). Colored bars are relative to the final grainsize distribution at the top of the plume. Red bars show a plume model where aggregation is considered from the beginning of the eruption. The initial grain-size distribution (Gaussian with mean = 5, variance = 2) is shown inside the small box

2. Fig. 2.6 shows that small changes in the initial conditions of mass fractions for the four different phases may lead to significant differences in the final grain size distribution. In fact, these parameters directly affect the concentration of solid fraction inside the plume and, consequently, the number of particles per unit volume. Fig. 2.6 reports different runs with different initial conditions for phases in the dusty gas mixture.

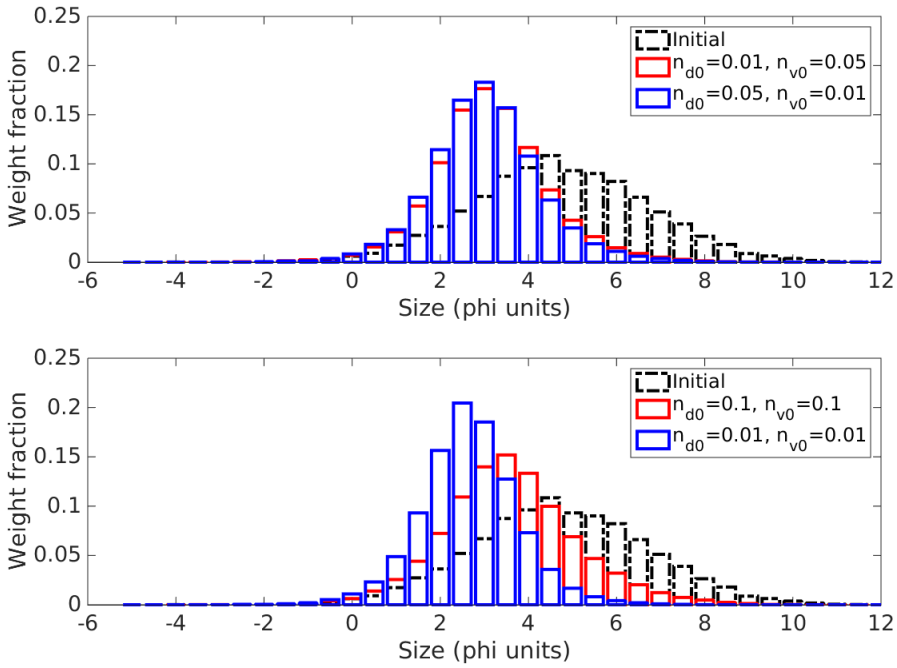

Fig. 2.6 Sensitivity test to investigate how different initial gas fractions in the mixture can affect particle aggregation. n_d0 indicates the mass fraction of initial dry air in the mixture, and n_v0 indicates the mass fraction of vapor.

3. The role of modifications in the sticking efficiency is studied. This is particularly relevant since the sticking efficiency is a quantity poorly constrained, especially in volcanology. We focused on two different aspects of (Eq. 2.21): the role of two parameters c_1 and q. c_1 is simply a multiplicative constant, on the other hand q alters the global shape of (Eq. 2.21) as shown in Fig. 2.7.

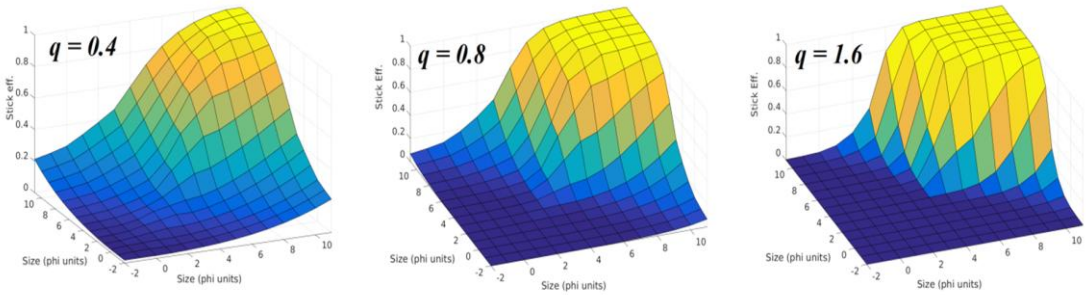

Fig. 2.7 Effect of the q parameter on the sticking efficiency (Eq. 2.21). Smaller values of q produce larger sizes in aggregation processes.

In Fig. 2.8a it is interesting to notice that if we consider correct the original value of $c_1 = 1$, a difference in 10% in c_1 (red line) produces negligible differences among the particles classes. Instead a difference in 50% in c_1(blue line) can produce in this case a difference for a single class up to 30%. Deeper consequences on aggregation are related to the parameter q, that basically alters the shape of the sticking matrix and modifies the threshold where the sticking is zero between different particle sizes. The higher the values of q the slower will be the efficiency among larger sizes. In Fig. 2.8b it is evident how q really influences the final outputs, since it basically modifies the role of different collisional mechanisms inside the equations. In fact the sticking efficiency can be seen as a weight applied to the collisional kernel that can inhibit some sizes from being aggregated. This short analysis shows how dramatically important a good knowledge of the sticking processes is, since small changes in the parameters can deeply affect the aggregation. Future laboratory experiments, specifically designed for volcanic ash and aggregates, could fill the gap between quantities required by the theory and our present knowledge.

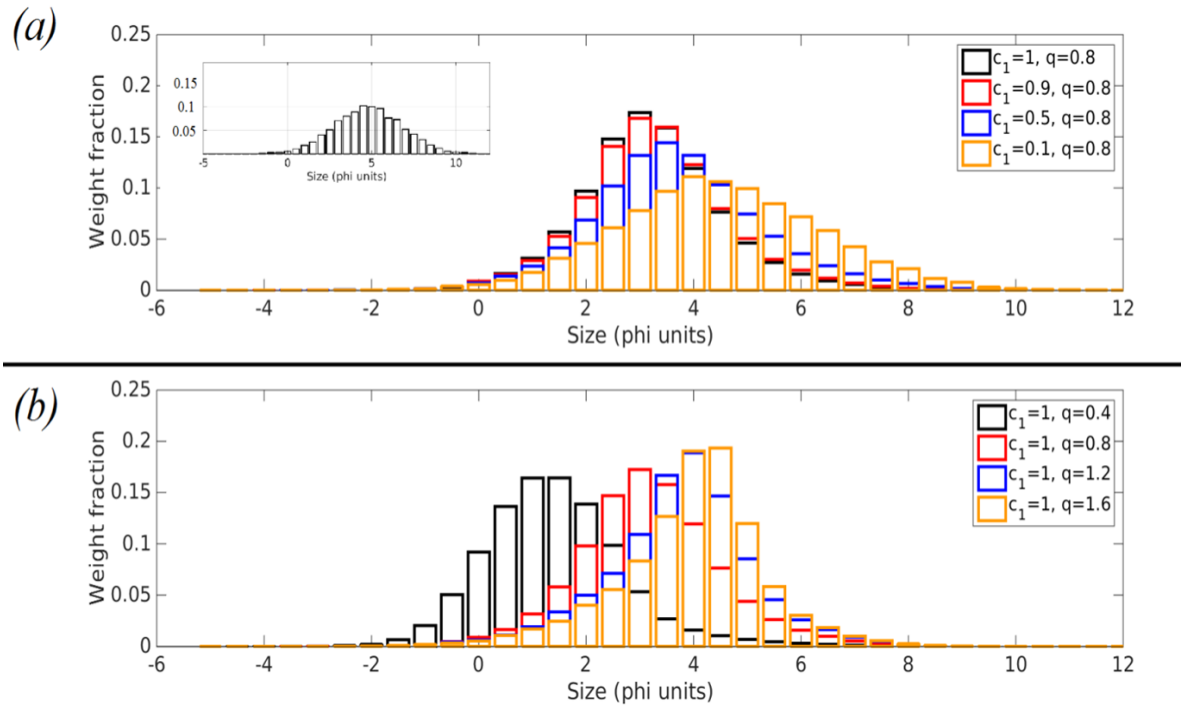

Fig. 2.8 Sensitivity of on the sticking efficiency. (a) The parameterization of Costa et al. (2010) is reduced by 90%, 50% and 10%. The small box describes the initial grainsize distribution. The q parameter is kept equal to the original (i.e. q = 0.8). (b) Effects of the influence of a modified parameter q. The higher the value of q, the less the sticking for larger sizes.

Application to the Sakurajima eruption of the 3rd of August 2013

In this work the main goal is to capture general aspects of ash aggregation in a real context avoiding complexity. As already mentioned, some basic information is missing for the eruption of 3rd of August at Sakurajima volcano (Japan), like the Total Grain Size Distribution (TGSD) and details on the initial conditions for the gas-solid mixture at the vent. Nevertheless field observations for this particular eruption provide alternative ways of comparison with models, such as the timescales of aggregation. As mentioned in the previous paragraphs, numerical inversions and direct observations at Sakurajima Volcano indicate that the observed aggregates formed within a time-window of 180 seconds after the eruption (Bagheri et al., 2016). This time threshold is used here as a point of comparison.

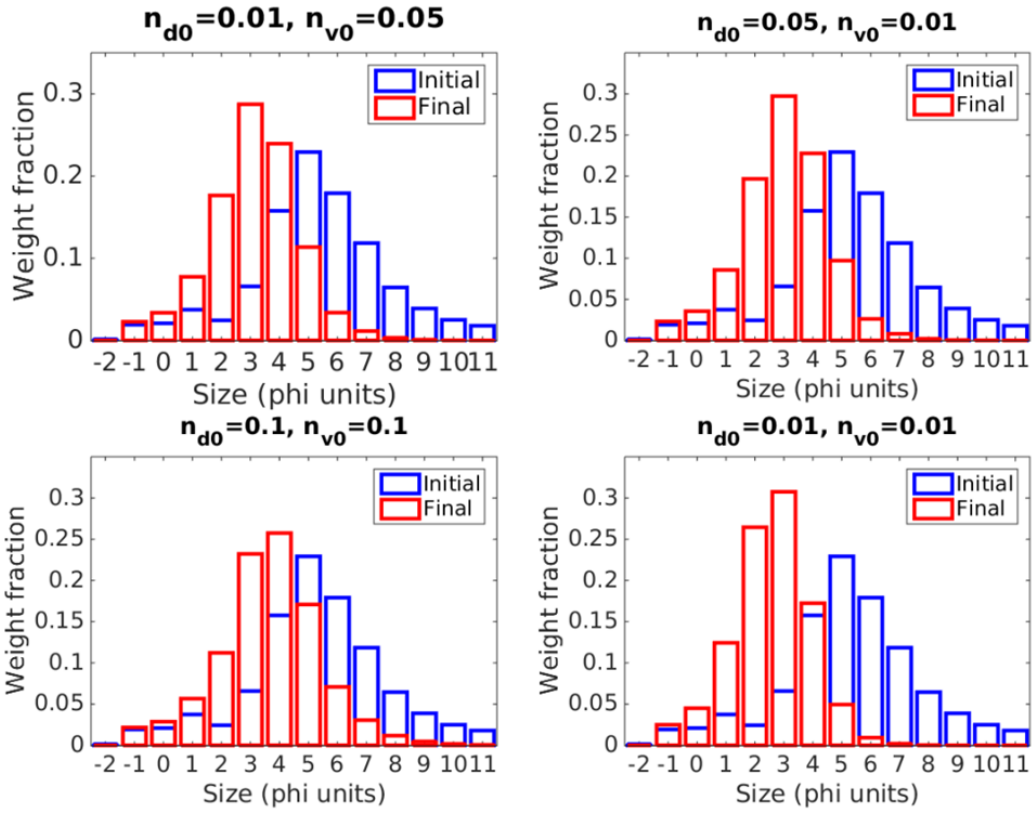

Fig. 2.9 Final TGSD for a Vulcanian-type eruption. The initial grainsize distribution is taken from the eruption of 18 July 2008 at Montserrat Volcano (Cole et al., 2014). Different gas fractions are evaluated as initial conditions for the thermal (n_{d0}, initial mass fraction of dry air; n_{v0}, initial mass fraction of vapor).

The initial TGSD of a weak Vulcanian eruption that occurred at Monserrat on the 18 of July 2005 (Fig. 2.9 – blue lines) is considered as initial condition. From direct observations we know that the eruption consisted of at least three main explosions, where the second and the third happened around 20 seconds and 50 seconds after the first one. The three thermals merged in a single large cloud which reached the maximum height of $\approx 2800\ m$ a.s.l. after 240 seconds. In Fig. 2.9 the expected TGSD at the top of the plume is reported for four different initial scenarios (details in Tab.2.2). In all these four scenarios aggregation is not allowed within five initial radii above the vent, which correspond to 35 s in time after the eruption. Five final TGSDs show that the expected maxima of weight fractions are all around $3\ \phi$. All the four scenarios produce plume heights that are in good agreement with ground observations, but the third scenario ($n_{d0} = n_{v0} = 0.1$) seems to be quite unrealistic for the rising time of the thermal. Ash aggregation is expected to reduce the total number of particles inside the volume, conserving the mass. The rate at which this happens is a function of the particle concentration inside the plume. At a specific time t_s aggregation will be not more effective and the total number of particles will converge to a plateau. A good indication of t_s is given from the analysis of the decay curve shown in Fig. 2.10a. It shows that aggregation never stops completely but that its efficiency drops dramatically as the concentration reduces: we can define t_s as the time where the drop happens. This reveals that $150\ s < t_s < 380\ s$ for all the different scenarios under analysis (see Tab. 2.2 for details). The theoretical time window is thus in good agreement with the observed value of 200 s. However the sensitivity test on the region above the vent with no aggregation (see previous section) suggests investigating how the timescales change if we modify the extension of this region. Considering aggregation from the beginning of the eruption (vent height) leads to extremely short timescales which are quite unrealistic if compared with what we observed in the field. An increase of the no-aggregation region up to ten initial radii (which corresponds to a maximum time of 35 s after the eruption, depending on different mass fractions concentrations – see Fig. 2.10) leads to a time window of high efficiency for aggregation between $220\ s < t_s < 450\ s$. This confirms that pure aggregation models, i.e. without breaking of particles, tend to seriously overestimate the effects of particles aggregation if run immediately above the vent.

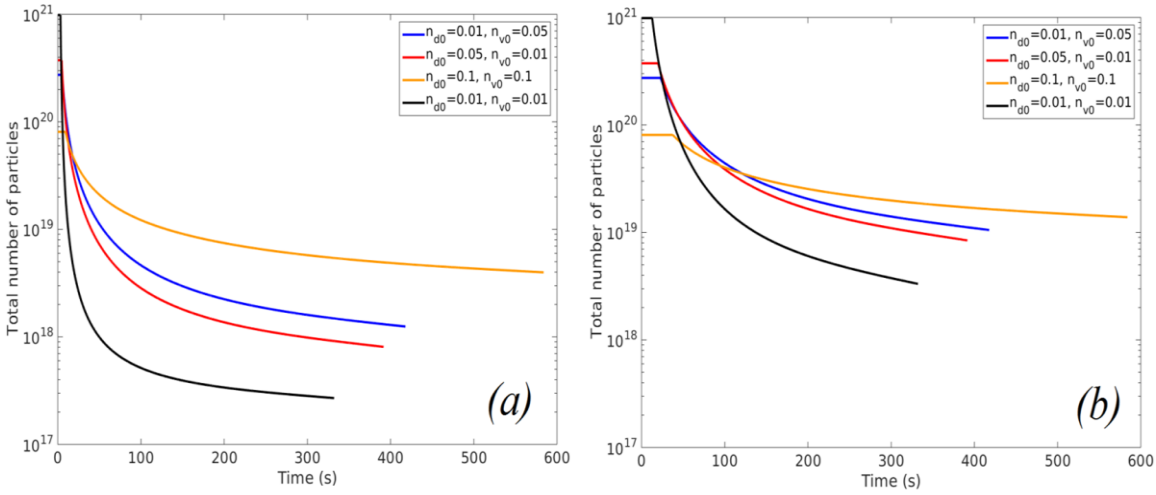

Figure 2.10 Total number of particles inside the thermal volume as a function of time. Time stops when the plume velocity approaches zero. In a pure aggregation model, the total number of particles is expected to decrease continuously until the plateau, where aggregation is no more effective due to the reduced concentration of particles. Two initial conditions for the forbidden zone for aggregation are analysed: five times the initial radius, i.e. 250 m (a) ten times the initial radius, i.e. 500 m (b).

	n_{d0}	n_{v0}	$r_0\ (m)$	$v_0\ (m/s)$	k_ε	$t_s(s)$
Scenario 1	0.01	0.05	50	150	0.25	250
Scenario 2	0.05	0.01	50	150	0.25	230
Scenario 3	0.1	0.1	50	150	0.25	400
Scenario 4	0.01	0.01	50	150	0.25	150

Table 2.2 Initial conditions and computed timescales t_s for all the different simulated scenarios.

2.4 Conclusions

In this work we have combined two different aspects of volcanic ash aggregation: field observations and theoretical description. Field data presented in this paper come from the eruption of 3rd of August at Sakurajima Volcano and they are based on combination of High-Speed movies and particle collection on sticky papers. Observations show the presence of large particles ($\approx 300 - 700\ \mu m$) inside the aggregates and a maximum time of formation of $180\ s$. This means that ash aggregation is a fast process, at least

within the observed conditions. The theoretical perspective starts from the so-called Smoluchowski Coagulation Equation, which describes the change in mass of a population of particles interacting with given collision frequencies and sticking efficiencies. Several quantities and initial conditions are not easy to constrain and this represents a weak point for predictions. Nevertheless we showed that the way we combined aggregation and volcanic plume theory produces scenarios that are comparable to the observations. The main outcome of this work is the application of the Smoluchowski theory and the validation with field data that was never attempted before. Regardless of the many main assumptions used in the theory, the main aspects of collisions between particles are considered: death and birth term for a pure aggregative process, the most important collisional kernels and the size dependent sticking efficiency. The combination of transport processes inside volcanic plumes and aggregation equations produces timescales that are reasonable with the observed data. This is a key result that should not be taken for granted a priori. Our promising outcomes confirm that the Smoluchowski Coagulation Equation and our theoretical approach are appropriate and relevant to the description of particle aggregation in volcanic plumes and clouds.

2.5 Acknowledgements

The research leading to these results has received funding from the European Union Seventh Framework Programme (FP7/2007-2013) under the project NEMOH, grant agreement n° 289976.

2.6 Author's contribution

E. Rossi, G. Bagheri, S. Biass and C. Bonadonna contributed to the field observations with the HS camera and the sticky paper at Mount Sakurajima, Japan. E. Rossi performed the SEM analysis of aggregates. E. Rossi developed the theoretical description of the problem.

Chapter 3

Aggregation of multidimensional arbitrary properties: the Generalized Fixed Pivot Technique[2]

3.1 Introduction

Particle aggregation is a common process of many different natural systems including: planetary formation, dispersal and sedimentation of volcanic ash, food industry, biology, atmosphere, aerosol sciences, polymerization and blood circulation. The reason of this generality is that in principle all those fluids involving particles may lead to the formation of agglomerates. The theoretical description of aggregation is a particular subset of the more general Population Balance Theory (PBT). The PBT treats the population under analysis in terms of selected properties $\boldsymbol{p}$, called *internal parameters*, and a density function $f(\boldsymbol{p})$. The density function provides the number of elements per unit volume with properties between two specific values $\boldsymbol{p_d}$ and $\boldsymbol{p_u}$:

$$\int_{\boldsymbol{p_d}}^{\boldsymbol{p_u}} d\boldsymbol{p}\, f(\boldsymbol{p}) = N_{du} \tag{3.1}$$

For many decades the study of aggregation processes has uniquely been based on a one-dimensional description of the problem, the so-called Smoluchowski Coagulation Equations (SCE) (Smoluchowski, 1916) This set of equations describes the growth of aggregates using one internal parameter: mass or volume. However this approach is strictly exhaustive for just few cases, such as the coagulation of pure water droplets, or the interaction of monomeric spheres in a suspension. For a large number of other events the SCE are not capable to describe comprehensively an aggregation event.

The reason for this lack of completeness is that in many cases one single internal parameter is not sufficient to describe how solid particles aggregate. In many cases a

[2] Submitted to Physical Review E as : Rossi E., Patterson R. Bonadonna C. "*Aggregation of multidimensional arbitrary properties: the Generalized Fixed Pivot Technique*"

more exhaustive description is obtained increasing the dimensionality of the equations. However it is just in the last fifteen years that the increasing availability of computational power has made the numerical solution of multidimensional problems feasible (Vale and McKenna, 2005). Several techniques currently exist to solve aggregation in multidimensional spaces. One of those that mainly took advantage of the increasing computing power is the so-called fixed pivot technique (Chakraborty and Kumar, 2007; Chiney and Kumar, 2012; Kumar and Ramkrishna, 1996; Kumar and Ramkrishna, 1997; Marchisio and Fox, 2005; Pollack et al., 2016; Vanni, 2000). The key aspect of the fixed pivot technique is that it works with a discretized density function $f(\boldsymbol{p})$. The solution is evaluated at fixed positions in the multidimensional space of the internal parameters (*pivots*). The main advantage is that a large number of pivots provide an accurate description of the evolution of the entire population. The drawback is that for a large number of pivots the computational time can be unmanageable.

In the present work we will discuss and demonstrate how this technique can be extended to the solution of aggregation problems with arbitrary internal properties introducing the Generalized Fixed Pivot Technique (GFPT). The term *arbitrary* in this context emphasises the use of internal properties that are not necessarily additive. This point represents a crucial difference respect to previous works, since in many problems the most useful internal properties are not additive (Johansen et al., 2008; Marchisio and Barresi, 2009; Matthews and Hyde, 2004).

3.2 The Generalized Fixed Pivot Technique (GFPT)

A rigorous formalisation of the fixed pivot technique has been introduced by the seminal work of Kumar and Ramkrishna (1996). In this paragraph we will discuss how the principles of the fixed pivot technique can be extended to the study of multidimensional arbitrary spaces. This new approach is called the Generalized Fixed Pivot Technique (GFPT) and it is strictly valid under the assumption of binary collisions. The starting point of the discussion is represented by the multidimensional aggregation equation with no explicit relations between the internal properties (Eq. 3.2) (Okuzumi et al., 2009).

$$\frac{\partial f(\boldsymbol{p},t)}{\partial t} = B(\boldsymbol{p},t) - D(\boldsymbol{p},t)$$
$$= \frac{1}{2}\int d\boldsymbol{p}' \int d\boldsymbol{p}'' K(\boldsymbol{p}';\boldsymbol{p}'',t) f(\boldsymbol{p}',t) f(\boldsymbol{p}'',t) \delta[\boldsymbol{p}_{1+2}(\boldsymbol{p}',\boldsymbol{p}'') - \boldsymbol{p}]$$
$$- f(\boldsymbol{p},t) \int d\boldsymbol{p}' K(\boldsymbol{p};\boldsymbol{p}') f(\boldsymbol{p}',t) \qquad (3.2)$$

Aggregation equations can always be split in a *birth* and a *death* term, regardless of the dimensionality of the problem. The first term on the right hand side of Eq.3.2, $B(\boldsymbol{p},t)$, represents the creation of particles with property $\boldsymbol{p}$ (*birth*), while the second term, $D(\boldsymbol{p},t)$, represents the loss (*death*). In Eq. (3.2) $f(\boldsymbol{p}',t)$ and $f(\boldsymbol{p}'',t)$ represent the density function for two colliding particles evaluated at two specific points in the multidimensional space, selected using the condition on the Dirac delta functions $\delta[\boldsymbol{p_{1+2}}(\boldsymbol{p}',\boldsymbol{p}'') - \boldsymbol{p}]$. For a set of properties $\boldsymbol{p} = [a, b, \dots]$:

$$\delta[\boldsymbol{p}_{1+2}(\boldsymbol{p}',\boldsymbol{p}'') - \boldsymbol{p}] = \delta[a_{1+2}(a',a'') - a] \cdot \delta[b_{1+2}(b',b'') - b] \dots \qquad (3.3)$$

The distribution function $f(\boldsymbol{p})$ is supposed to be continuous over the region of interest. The symbol $\boldsymbol{p}_{1+2}$ indicates the resulting property born from the interaction of $\boldsymbol{p}'$ and $\boldsymbol{p}''$. In this context the symbol of integration must be considered on a space of dimension equal to p, where bold letters indicate a vector. It is worth mentioning that the physics of the process is entirely contained inside the aggregation kernels $K(\boldsymbol{p}';\boldsymbol{p}'',t)$. The quantities $K(\boldsymbol{p}';\boldsymbol{p}'',t)$ provide a global information of the collision rate for two particles with properties $\boldsymbol{p}$ and their sticking probability. For a multidimensional problem the evaluation of these functions represents a challenging task. The higher the number of internal parameters, the higher the information required describing completely the evolution of the population. One-dimensional kernels have been derived theoretically in the past to describe specific conditions, such as the collision rates due to the Brownian motion or the sedimentation collisions between free falling particles. However the major complexity of multidimensional kernels requires future studies and specific experimental investigations to be understood. In the present work we will mostly use constant kernels or quantities derived from the previous one-dimensional approaches. For the particular condition of one internal additive property, $p = V$ and $\delta[V' + V'' - V]$, Eq. (3.2) is formally identical to the Smoluchowski Coagulation Equation (SCE):

$$\frac{\partial f(V,t)}{\partial t} = \frac{1}{2}\int_0^V dV' K(V';V-V',t) f(V',t) f(V-V',t) - f(V,t)\int_0^\infty dV' K(V;V',t) f(V',t) \tag{3.4}$$

The extension of Eq. (3.2) to account for arbitrary internal parameters generates some complications that must be analysed in detail. Two aspects are of particular interest: the limits of integration and the number of roots contained in the Dirac delta functions.

• **Limits of integration**: The choice of the limits for the integration usually concerns the birth term uniquely. The loss term is always evaluated over the entire space of definition of parameters, since particles disappear interacting with all the others. The key point is that limits of integration for the birth term are strongly related to the definition of the internal parameters and how they aggregate. For example, in the SCE particles volume is the internal parameter. The lowest extreme is constrained by the condition that volumes are always positive and their interaction can produce uniquely larger particles. Therefore, the minimum volume, zero, is also the lowest bound of the integral. The upper extreme is determined by the fact that a particle of volume V can be formed solely by smaller particles. In the case limit in which one of the two particles is an infinitesimal object, the extreme bound is exactly the volume of the particle itself. This justifies value of the upper limit in Eq.4. In general each problem that uses the Eq.2 requires a specific analysis of the extremes of integration. In the fixed pivot technique this is not very important, since all the integrals are supposed to cover the region of interest. The discretization of the entire domain produces a set of multidimensional cells, in which the population will evolve according to the conditions contained in the Dirac delta functions. A particular caution must be taken in defining the region of interest. Aggregation can produce particles with properties outside the domain, resulting in a leakage of information.

• **Number of roots**: The Dirac delta functions in Eq. (3.2) determine how aggregates with property $\boldsymbol{p}$ are generated from the interaction of two particles with properties $\boldsymbol{p}'$ and $\boldsymbol{p}''$. The Dirac deltas contain one equation to be solved for each internal parameter as shown in Eq. (3.3). The equalities to be solved for the internal properties $\boldsymbol{p} = [a, b, c, \dots]$ are:

$$\boldsymbol{p}_{1+2}(\boldsymbol{p}', \boldsymbol{p}'') - \boldsymbol{p} = 0 \rightarrow \begin{cases} a = a_{1+2}(a', a'') \\ b = b_{1+2}(b', b'') \\ c = c_{1+2}(c', c'') \end{cases} \quad (3.5)$$

In this work we consider uniquely acceptable solutions of Eq. (3.5) that provide single values in the final region of interest, but injective functions are not mandatory. The study of multiple roots will be considered in a future work.

3.2.1 Discrete equations in the GFPT

The common feature to all the Fixed Pivot Methods (FPM), such as the GFPT, is to discretize the space of the internal parameters p and then solve a set of Ordinary Differential Equations (ODEs) for each cell of the discrete domain. The first step in this process is to divide the space of the internal parameters in a set of smaller regions, called cells. According to Eq. (3.1) the distribution function will be integrated over these cells to provide the number of particles per unit volume within each region. The discretization of the space creates a *n*-dimensional grid where each cell is represented with an internal fixed value, the pivot. In the present work we refer to this grid as the primary grid. One of the main problems in the discretization has always been how to deal with new aggregated particles that appear in a different position respect to the pivots. This happens in the great majority of cases since the product of an aggregation will not coincide with our discrete points, unless the number of pivots is extremely high and the computational time prohibitive. From its first appearance (Kumar and Ramkrishna, 1996), the solution of this problem has represented one of the most important features of the fixed pivot technique. The criterion used in the FPM is to split each single new aggregate within the closest cell in order to conserve some specific quantities. According to Chakraborty and Kumar (2007), for n internal parameters the minimum number of cells used in this allocation is n+1. The way in which aggregates are redistributed in the space requires an additional grid, as shown in Fig. 3.1. We refer to this grid as secondary grid and usually there is no need to use additional points to define it. Pivots from the primary grid will define the vertexes of the cells. In general for a bidimensional problem the secondary grid is composed of squares or triangles; cubes

and tetrahedra for a tridimensional one. As a rule of thumb the higher the number of points used for the redistribution the higher the numerical diffusion. A specific description of the secondary grid will be done in one of the following paragraphs.

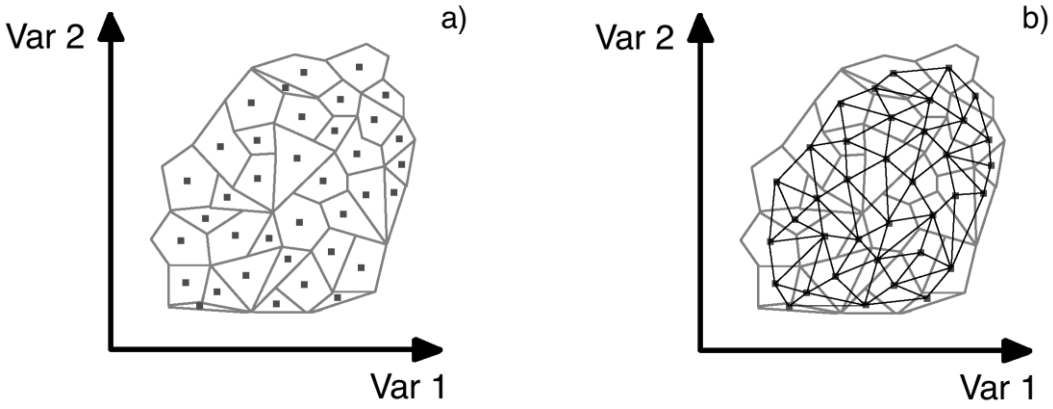

Figure 3.1 Representation of the primary and secondary grids for a bidimensional problem. On the x and y axes are reported the two internal parameters Var_1 and Var_2. The primary grid (a) divides the space of the internal variables in a set of arbitrary cells where the continuous distribution function is integrated. Each node of the grid is thus associated with a number of particles per unit volume. The secondary grid (b) defines which cells are involved in the redistribution of non pivotal aggregates. It is generated following a specific criterion that depends on the problem under analysis. In this work the secondary grid is generated following the Delaunay criterion.

Two main steps are required in order to discretize the aggregation equations in the GFPT: first, to replace the distribution function with a sum of Dirac delta functions centered at the pivots positions; second, to integrate Eq. (3.2) over each cell. For a set of internal properties $\boldsymbol{p} = [a, b, c, \dots]$ the first step means to substitute $f(\boldsymbol{p})$ with Eq. (3.6) inside the aggregation equations:

$$f(\boldsymbol{p}, t) = \sum_{i=1}^{N_c} N_i(t)\delta(\boldsymbol{p} - \boldsymbol{p}_i) = \sum_{i=1}^{N_c} N_i(t)\delta(a - a_i)\delta(b - b_i)\delta(c - c_i) \dots \tag{3.6}$$

In Eq. (3.6) the quantity $N_i(t)$ is the number of particles per unit volume contained in each cell i as a function of the indipendent variable t. N_c is the number of cells in the primary grid. The second step is achieved integrating Eq. (3.2) over each multidimensional cell. For the left hand side of Eq. (3.2), over the i-esim cell, we have:

$$\frac{dN_i(t)}{dt} = \int_{\odot_i} \frac{\partial f(\boldsymbol{p},t)}{\partial t} d\boldsymbol{p} \tag{3.7}$$

Therefore the evolution of the number of particles per unit volume in the i-esim cell is given by:

$$\frac{dN_i(t)}{dt} = \underbrace{\int_{\odot_i} d\boldsymbol{p}\, B(\boldsymbol{p},t)}_{B_i^d} - \underbrace{\int_{\odot_i} d\boldsymbol{p}\, D(\boldsymbol{p},t)}_{D_i^d} \tag{3.8}$$

The continuous problem described in Eq. (3.2) is thus transformed in the solution of a set of ODEs where the unique dependent variable is time t. In this work we will use a progressive index from $i = 1$ to N_c to identify each cell, and the symbol $\odot_i$ to identify the relative multidimensional region in the primary grid. Cells of the secondary grid will be instead identified with the symbol Δ_s. B_i^d and D_i^d are the discrete birth and death terms for the cell i. The following sections are dedicated to the research of explicit expressions for quantities B_i^d and D_i^d.

The birth term

The discretization of the birth term B_i^d represents the main difference between the GFPT and the FPT. In the GFPT the relationships between the internal parameters are not explicit and this involves the presence of a multidimensional Dirac delta, as reported in Eq. (3.3). This term is not present in the FPT. The relationships between the internal parameters will be defined at the end of the discretization and not at the beginning, as in the FPT. For convenience we report the birth term B_i^d entirely:

$$B_i^d = \int_{\odot_i} d\boldsymbol{p}\, \frac{1}{2} \int d\boldsymbol{p}' \int d\boldsymbol{p}'' K(\boldsymbol{p}', t; \boldsymbol{p}'', t) f(\boldsymbol{p}', t) f(\boldsymbol{p}'', t) \delta[p_{1+2}(\boldsymbol{p}', \boldsymbol{p}'') - \boldsymbol{p}] \tag{3.9}$$

The first step in the discretization is to replace the population density $f(\boldsymbol{p})$ with a series of Dirac delta functions. Substituting Eq. (3.6) in Eq. (3.9) we have:

$$B_i^d = \int_{\odot_i} d\boldsymbol{p}\ \frac{1}{2}\int d\boldsymbol{p}'\ \times$$

$$\times \int d\boldsymbol{p}''K(\boldsymbol{p}';\boldsymbol{p}'')\left(\sum_{l=1}^{N_c} N_l\delta(\boldsymbol{p}'-\boldsymbol{p}_l)\right)\left(\sum_{m=1}^{N_c} N_m\delta(\boldsymbol{p}''-\boldsymbol{p}_m)\right)\delta[p_{1+2}(\boldsymbol{p}',\boldsymbol{p}'')-\boldsymbol{p}] \tag{3.10}$$

For a given cell i in the primary grid, there will be s cells in the secondary grid involved in the creation of aggregates. Each aggregate that appears in one of the s cells will contribute to the term B_i^d, according to a relative weight $W_s(\boldsymbol{p},\boldsymbol{p_i})$ that will be discussed in detail later.

$$B_i^d = \sum_s \int_{\Delta_s} dp\ W_s(\boldsymbol{p},\boldsymbol{p}_i)\frac{1}{2}\int d\boldsymbol{p}'\int d\boldsymbol{p}''K(\boldsymbol{p}';\boldsymbol{p}'')\left(\sum_{l=1}^{N_c} N_l\delta(\boldsymbol{p}'\right.$$
$$\left.-\boldsymbol{p}_l)\right)\left(\sum_{m=1}^{N_c} N_m\delta(\boldsymbol{p}''-\boldsymbol{p}_m)\right)\times\ \delta[\boldsymbol{p}_{1+2}(\boldsymbol{p}',\boldsymbol{p}'')-\boldsymbol{p}] \tag{3.11}$$

The multidimensional integral over $d\boldsymbol{p}''$ can be rewritten as the sum of N_c integrals over each cell of the primary grid.

$$B_i^d = \sum_s \int_{\Delta_s} d\boldsymbol{p}\ W_s(\boldsymbol{p},\boldsymbol{p}_i)\frac{1}{2}\int d\boldsymbol{p}'\sum_{k=1}^{N_c}\int_{\odot_k} d\boldsymbol{p}''K(\boldsymbol{p}';\boldsymbol{p}'')\left(\sum_{l=1}^{N_c} N_l\delta(\boldsymbol{p}'\right.$$
$$\left.-\boldsymbol{p}_l)\right)\left(\sum_{m=1}^{N_c} N_m\delta(\boldsymbol{p}''-\boldsymbol{p}_m)\right)\times\ \delta[\boldsymbol{p}_{1+2}(\boldsymbol{p}',p_k)-\boldsymbol{p}] \tag{3.12}$$

The integration over $\boldsymbol{p}''$ is conditioned by the presence of $\sum_{m=1}^{N_c} N_m\,\delta(\boldsymbol{p}''-\boldsymbol{p_m})$ The Dirac deltas are different from zero only if the index m and k are equal. Therefore the integral becomes:

$$B_i^d = \sum_s \int_{\Delta_s} d\boldsymbol{p}\ W_s(\boldsymbol{p},\boldsymbol{p}_i)\frac{1}{2}\int d\boldsymbol{p}'\sum_{k=1}^{N_c} K(\boldsymbol{p}';\boldsymbol{p}'')\left(\sum_{l=1}^{N_c} N_l\delta(\boldsymbol{p}'-\boldsymbol{p}_l)\right)N_k\ \times$$
$$\times\ \delta[\boldsymbol{p}_{1+2}(\boldsymbol{p}',\boldsymbol{p_k})-\boldsymbol{p}] \tag{3.13}$$

The integration over $\boldsymbol{p}'$ follows the same procedure used for $\boldsymbol{p}''$. After same manipulations we have:

$$B_i^d = \sum_s \int_{\Delta_s} d\boldsymbol{p}\, W_s(\boldsymbol{p}, \boldsymbol{p}_i) \frac{1}{2} \sum_{j=1}^{N_c} \sum_{k=1}^{N_c} K(\boldsymbol{p_j}; p_k) N_j N_k\, \delta\left[\boldsymbol{p}_{1+2}(\boldsymbol{p}_j, \boldsymbol{p}_k) - \boldsymbol{p}\right] \tag{3.14}$$

Eq. (3.14) can be interpreted as follows: the birth term B_i^d is given by the weighted sum of s couples of particles j and k that satisfy the condition $\delta\left[\boldsymbol{p}_{1+2}(\boldsymbol{p}_j, \boldsymbol{p}_k) - \boldsymbol{p}\right]$ on the variable $\boldsymbol{p}$. This condition is equivalent to consider those couples of particles that produce an aggregate with properties $\boldsymbol{p}$ in one of the s regions Δ_s. The final expression for the birth term in the GFPT becomes

$$B_i^d = \frac{1}{2} \sum_{j=1}^{N_c} \sum_{k=1}^{N_c} \sum_{\boldsymbol{p}_{1+2}(\boldsymbol{p}_j, \boldsymbol{p}_k) \subseteq \Delta_s} W_s(\boldsymbol{p}_{1+2}(\boldsymbol{p}_j, \boldsymbol{p}_k), \boldsymbol{p}_i) K(\boldsymbol{p}_j, \boldsymbol{p}_k) N_j N_k \tag{3.15}$$

The death term

The discretization of the death term in the GFPT is completely equivalent to other techniques, such as the fixed pivot or the cell average (Kumar et al., 2006; Kumar and Ramkrishna, 1996). The loss of particles is not dependent on the internal properties $\boldsymbol{p}$, since each particle can interact with all the others without any limitation. The details of the discretization for the sink term can be found in (Vale and McKenna, 2005). The death term for the continuous aggregation Eq. (4.2) is discretized as follows:

$$D(\boldsymbol{p}, t) = f(\boldsymbol{p}, t) \int d\boldsymbol{p}' K(\boldsymbol{p}, \boldsymbol{p}') f(\boldsymbol{p}', t) \rightarrow D_i^d = N_i \sum_{k=i}^{N_c} K(\boldsymbol{p}_j, \boldsymbol{p}_k) N_k \tag{3.16}$$

Evaluation of weights

One of the main advantages introduced in the fixed pivot technique is the possibility to choose arbitrary steps for the primary grids. The use of weights W_s allows redistributing non-pivotal new aggregates on a selected number of existing points, in order to conserve

specific quantities. The advantage of this procedure is the decrease of the number of pivots for the primary grid. The drawback is that the numerical diffusion grows with a decreasing number of pivots. In this paragraph we examine how this procedure can be applied for the GFPT. As a matter of fact the use of non-additive internal parameters does not change the way in which particles are redistributed. Particle redistribution is just dependent on how the newborn aggregate is shared with existing pivots. The following discussion is based on the work of Chakraborty and Kumar (2007) and adapted to the GFPT.

As introduced in section 3.2.1 the GFPT uses a primary and a secondary grid. The primary grid is defined as the set of cells that divides the space of the internal parameters. Each cell is characterised by an internal point, the pivot. The secondary grid is instead defined as a set of pivots where non-pivotal particles are redistributed. The number of points involved in the redistribution of non-pivotal aggregates is not uniquely defined. Chakraborty and Kumar (2007) show that for a n-dimensional problem the minimum number of points used in the redistribution is n + 1. So far the common approaches used in literature vary with the dimensions of the problem: for a 1D problem, lines are the unique choices; for a 2D problem triangles or rectangles can be a solution; for a 3D problem we can select tetrahedrons or parallelepipeds. For a secondary grid with the minimum number of elements, consistency is obtained preserving $n+1$ properties Q over j points of each cell of the secondary grid involved in the redistribution of the particle $\boldsymbol{p}_{1+2}$. We identify these N_p points with the indexes vector $\boldsymbol{id} = [\alpha, \beta, \gamma, \dots]$.

$$\sum_{i=1}^{N_p} W_{Id(i)}\left(\boldsymbol{p}_{1+2}, \boldsymbol{p}_{id(i)}\right) \cdot Q_j\left(\boldsymbol{p}_{Id(i)}\right) = Q(\boldsymbol{p}_{1+2}) \tag{3.17}$$

Usually the quantities to be conserved involve specific moments of the distribution, like the zeroth and the first for the 1-dimensional problem. The extension to *n*-dimensions is done similarly, conserving the number of particles and the *n* internal properties $\boldsymbol{p}$. This process is not affected from the non-addictiveness of the internal properties. It is just dependent on the position of the new aggregate in the multidimensional space. In other words the weights $W_{Id(i)}$ are a measure of how far the products of an aggregation are from existing pivots. It is now clear why a reduced number of pivots will generate

numerical diffusion: if the secondary grid is sparse, new aggregates are allocated among pivots far in space that in reality are not involved in the physical process. The meaning of Eq. (3.17) can be explained with an example. Let us consider a 3-dimensional problem where tetrahedrons constitute the secondary grid. The internal properties $\boldsymbol{p}$ are: $[M, S, C]$. Tetrahedrons vertexes involved in the single redistribution are: $\boldsymbol{id} = [2, 5, 8, 18]$.

$$\begin{cases} W_2 + W_5 + W_8 + W_{18} = 1 \\ W_2 \cdot M_2 + W_5 \cdot M_5 + W_8 \cdot M_8 + W_{18} \cdot M_{18} = M_{1+2} \\ W_2 \cdot S_2 + W_5 \cdot S_5 + W_8 \cdot S_8 + W_{18} \cdot S_{18} = S_{1+2} \\ W_2 \cdot C_2 + W_5 \cdot C_5 + W_8 \cdot C_8 + W_{18} \cdot C_{18} = C_{1+2} \end{cases} \tag{3.18}$$

For each couple of particles j and k the quantities $W_{Id(i)}\left(\boldsymbol{p}_{1+2}, \boldsymbol{p}_{id(i)}\right)$ are determined uniquely. In the GFPT this process is done once, just before the computation of the ODEs. The calculus of $W_{Id(i)}$ can be speeded up noticing that the problem is symmetrical for a permutation of the indexes j and k. Weights evaluation completes the discrete equations for a multidimensional cell i in the GFPT is:

$$\begin{aligned} \frac{\partial N_i(t)}{\partial t} = \frac{1}{2} \sum_{j=1}^{N_c} \sum_{k=1}^{N_c} \sum_{\boldsymbol{p}_{1+2}\left(\boldsymbol{p}_j, \boldsymbol{p}_k\right) \subseteq \Delta_s} & W_s\left(\boldsymbol{p}_{1+2}\left(\boldsymbol{p}_j, \boldsymbol{p}_k\right), \boldsymbol{p}_i\right) K\left(\boldsymbol{p}_j, \boldsymbol{p}_k\right) N_j N_k \\ & - N_i \sum_{k=1}^{N_c} K(\boldsymbol{p}_i; \boldsymbol{p}_k) N_k \end{aligned} \tag{3.19}$$

3.2.2 Implementation of the GFPT

The GFPT provides a set of ODEs that represents the most general expression for aggregation on a discrete space. This generality allows a high degree of freedom in the implementation of the solution. The cells of the primary grid $(\odot_i)$ and those of the secondary (Δ_s) are not uniquely defined and they can vary according to the needs or the requirements of the user. In this section the implementation of the GFPT in a dedicated algorithm is described in detail. Historically the first grids have been made by rectangular elements on a bidimensional space and parallelepipeds on a tridimensional one. Both for the primary and the secondary grid. This choice for the secondary grid allows to express W_s directly, without any use of search algorithms to evaluate the

condition $\boldsymbol{p}_{1+2}(\boldsymbol{p}_j, \boldsymbol{p}_k) \subseteq \Delta_s$. However the use of rectangles and parallelepipeds for the secondary grid is not easily adaptable for all those situations where a particular accuracy is required in specific regions of the space. A more flexible grid is composed of triangles and tetrahedrons as introduced in Chakraborty and Kumar (2007). These elements can be generated from an arbitrary set of points, once established a criterium for the triangulation. In terms of adaptablity this represents a great advantage since a denser number of pivots can be assigned where it is needed, without any complication. It is important to stress that the use of these grids for dimensions greater than three can be demanding. In this work all the examples proposed are described in terms of two internal variables. Thus the secondary grid is composed of triangles.

The GFPT is written in Matlab. This software provides useful built-in functions to perform *n*-dimensional Delaunay triangulations or point localisation over a set of triangles or tetrahedrons. Of course any other language can be used but it requires additional work to implement the previous functions. In this case useful references to implement a Delaunay triangulation and spatial localisations over a set of tetrahedrons can be found in Liu et al. (2015). The algorithm is structured as follows:

1. Definition of the cells of the primary grid and the relative fixed pivots.

2. Evaluation of the initial conditions on the number of particles per unit volume contained in each multidimensional cell.

3. Definition of the cells of the secondary grid by means of a triangulation between the fixed pivots. In this work the Delaunay criterion is used to create triangles and tetrahedrons. Other criteria may be chosen. At the end of the triangulation each pivot i will belong to s elements of the grid. Each aggregate that appears in one of the s elements will contribute to the formation of particles in i.

4. For each couple of pivots j and k we evaluate which cell of the secondary grid contains the resultant aggregate $\boldsymbol{p}_{1+2}(\boldsymbol{p}_j, \boldsymbol{p}_k)$. This search can be speeded up noticing that the collision of j and k is equivalent to k and j. A fraction of the quantity $\boldsymbol{p}_{1+2}$ is attributed to each single vertex of the cell according to Eq. (4.17).

5. Step 4 is repeated for all the couples of points. This allows to relate the creation of aggregates in the pivot i to specific couples of points *j* and *k* that contribute with a specific fraction $W_s(\boldsymbol{p}_{1+2}(\boldsymbol{p}_j, \boldsymbol{p}_k), \boldsymbol{p}_i)$. This process is computed only once.

6. Solution of the ODEs present in Eq. (4.19). An explicit Runge-Kutta solver (ODE45) of the fourth-fifth order is used for non-stiff problems. However stiffness can arise for particular initial conditions. In this case we use a variable backward differentiation formula (ODE15s). In both cases the positiveness of the solutions is imposed by default in the ODE solver.

3.3 Numerical results and discussion

The GFPT can be applied to different classes of problems. In this paragraph several examples are shown and discussed to demonstrate its versatility: the verification of the algorithm and one test case. In the verification process the numerical scheme is compared with analytical solutions, although these are available only for additive properties. The test-case is an ideal experiment where micrometer paint droplets interact together to form new colours that depend on masses and initial colours of colliding droplets. Particles are supposed to be in a box where no net motion through the boundaries is present. The internal variable *colour* can be defined as a unique quantity or it can be decomposed along three primary axes. Resultant colours after a collision are expressed as the average of the colliding colours weighted over the respective masses. With this example we want to emphasise the use of the GFPT for a variety of different and unusual applications.

3.3.1 Verification: additive properties

The Generalized Fixed Pivot Technique is compared with analytical solutions in order to test the accuracy. Analytical solutions of Eq. (3.2) are possible only for the specific condition of additive internal properties and constant aggregation kernels $K(\boldsymbol{p}'; \boldsymbol{p}'') = K$. In this work we use the set of solutions reported in Vale and McKenna (2005) for a *n*-dimensional problem. The initial conditions are:

$$f_{analitical}(p_1, p_2, \dots, p_n, t = 0) = N_0 \cdot \prod_{i=i}^{n} \frac{(a_i + 1)^{(a_i+1)} p_i^{a_i}}{\Gamma(a_i + 1) p_{i0}^{a_{i+1}}} \cdot exp\left[-(a_i + 1)\frac{p_i}{p_{i0}}\right] \tag{3.20}$$

Where the parameters a_i define the shape of the initial distribution of particles. A value of $a_i = 0$ gives an exponential distribution, $a_i = 1$ a Gamma distribution. The validation is done analyzing two different cases: $a_i = 0$ and $a_i = 1$ with two internal parameters p_1, p_2. The general solutions for Eq. (3.20) are:

$$f_{analitical}(\boldsymbol{p}_1, \boldsymbol{p}_2, \dots, \boldsymbol{p}_n, t = \tau) = \frac{4N_0}{(\tau + 2)^2} \prod_{i=i}^{n} \frac{(a_i + 1)^{(a_i+1)} p_i^{a_i}}{p_{i0}} \cdot exp\left[-\frac{(a_i + 1)\,\boldsymbol{p}_i}{p_{i0}}\right] \cdot \sum_{k=0}^{\infty} \left(\frac{\tau}{\tau + 2}\right)^k \times \prod_{i=i}^{n} \frac{\left[(a_i + 1)(a_j + 1)\right]^k \left(\boldsymbol{p}_j / \boldsymbol{p}_{j0}\right)^{\left[(k+1)(a_j+1)-1\right]}}{\Gamma[(a_i + 1)(k + 1)]} \tag{3.21}$$

Where the non dimensional time τ is defined as $\tau = N_0 K_0 t$. The discrete results of the GFPT are compared with the continuous functions of Eq. (3.21) according to Vale and McKenna (2005). The quantities used for the comparison are the averaged density function $f_{analytical}$ and the numerical density function $\bar{f}_{num}$, defined as follows:

$$\bar{f}_{analitical} = \frac{1}{area_{\odot_i}} \int_{\odot_i} f(\boldsymbol{p}) d\boldsymbol{p} \tag{3.22}$$

$$\bar{f}_{num} = \frac{N_i}{area_{\odot_i}} \tag{3.23}$$

We start our analysis from the numerical solution of Eq. (3.20) for a bidimensional case with two different values of a_i. The results are shown as a contour plot in Fig. (3.2) for an initial exponential distribution (a_i) and a Gamma distribution ($a_i = 1$). The primary grid is composed of 2500 rectangular cells (50 x 50) distributed uniformly over the log-log space. The secondary grid of triangles is defined with a Delaunay triangulation. Fig. (3.2) shows a good agreement between numerical predictions and theoretical values for both cases. In addition these results are in line with what reported in Vale and McKenna, (2005) for similar initial conditions.

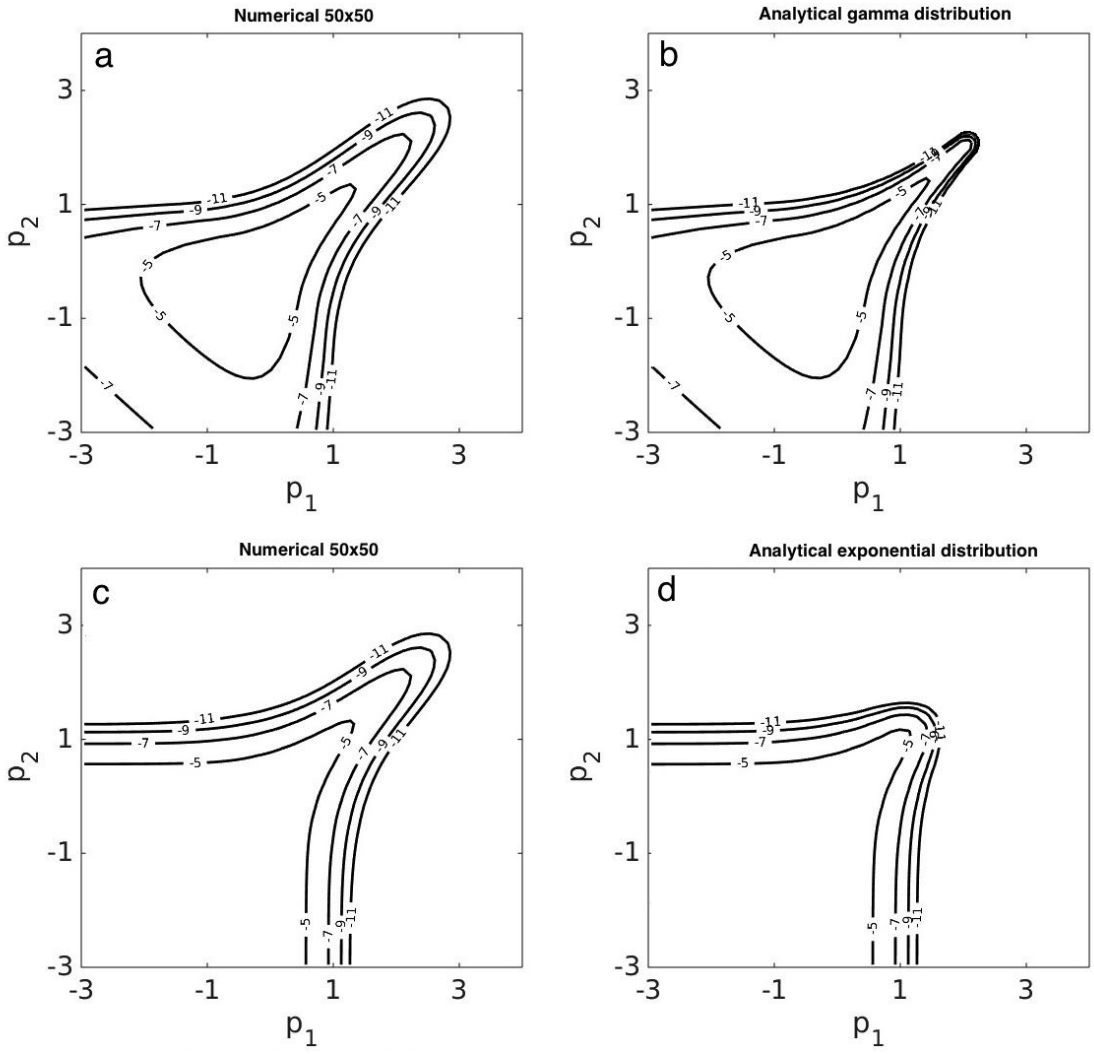

Figure 3.2 Numerical and analytical solutions for two additive parameters p_1 and p_2 for the initial conditions of Eq.3.20 with $p_{10} = p_{20} = 1, N_0 = 1, \tau = 100$: $a_i = 0$ (a, b) and $a_i = 1$ (c, d) respectevely. The primary grid is made of 50 x 50 cells.

As expected, larger sizes are affected by numerical diffusion that provokes decay in the performances of the algorithm. Numerical diffusion is generated from the allocation of new particles among pivots that are far in space. This is due to the use of a constant number of pivots over a logarithmic scale, which produces a reduced number of points for large sizes. It is worth mentioning that the GFPT predicts correctly the first $n + 1$ moments (Fig. 3.3). However the accuracy of higher moments is strictly dependent on the number of pivots used as demonstrated in Fig. (3.4).

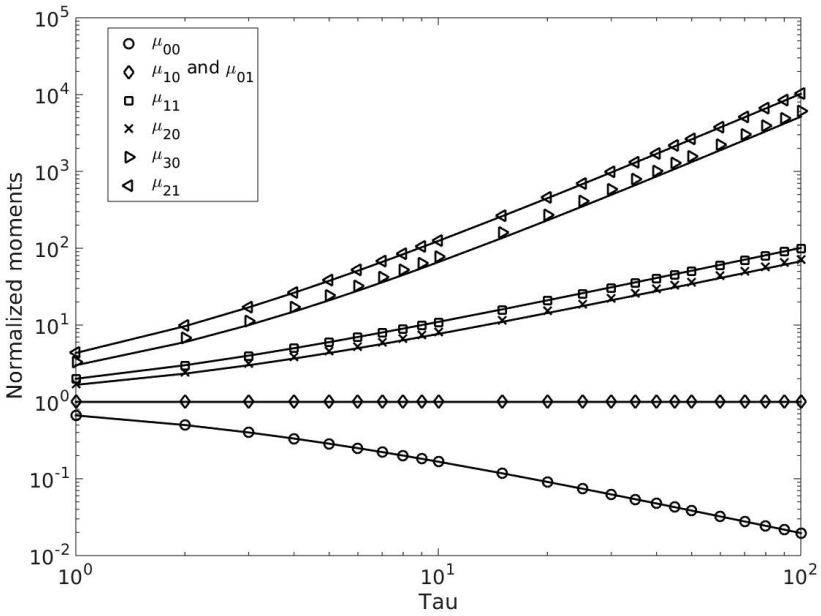

Figure 3.3 Comparison between the first moments of the distribution evaluated numerically for 2500 points (50 x 50) and the relative exact analytical values for Eq. 3.20 with $a_i = 1$ (black lines) as a function of the adimensional time τ.

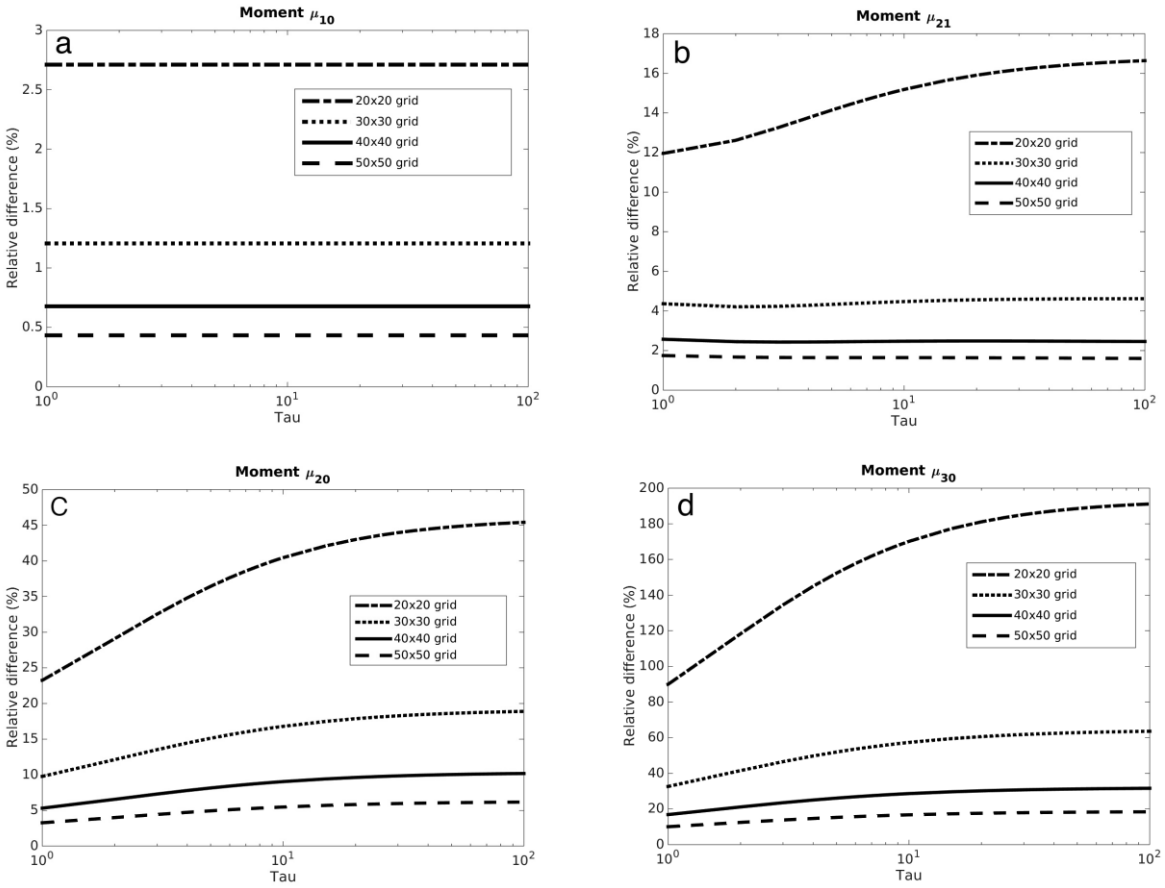

Figure 3.4 Differences between moments $\mu_{00}, \mu_{21}, \mu_{20}$ and μ_{30} evaluated numerically for different grid steps and the relative exact analytical values for Eq. 20 with $p_{10} = p_{20} = 1, N_0 = 1$ and $a_i = 1$.

3.3.2 Collisions of micrometer paint droplets in a box

In this example we apply the GFPT to an ideal experiment where liquid droplets of coloured paints interact in a box to create larger droplets with new colours. This is a typical example of coagulation where the volume of the final object is the sum of the interacting particles. In this context the interest is focused on the study of how colours evolve within the population and what are the prevalent shades after a given time tend. We assume micrometer size particles and an instantaneous blending process among them. This implies that the product of a collision can be always labelled with a unique colour. A more realistic description could be obtained introducing a third parameter to describe the degree of mixing between colours. The mixing of paints, pigments and inks is explained with the subtractive colours theory (Pridmore, 2011), but a detailed analysis of the resultant colour is strictly dependent on the chemistry of the paints used. The subtractive theory relates the colour of an object to the frequencies of the light it can absorb. A given dye is described in terms of three numbers from 0 to 1, representing the normalised fractions of primary colours inside the dye. The normalisation factor used depends on the number of bits allocated to define the colour depth. The absence of any pigment, represented with the triplet [0 0 0], produces a white shade in the subtractive theory. Viceversa, a full intensity for each channel defines the black colour ([1 1 1]). Primary colours are defined as those triplets that absorb completely all frequencies if blended in equal proportions. In this example the Cyan-Magenta-Yellow (CMY) triplet is used as a base for primary colours. At least two strategies can be adopted to treat this ideal experiment within the framework of population balances. The parameter "colour" can be treated as a unique variable, or it can be decomposed in three components. The first approach results in a two dimensional problem, where mass and colour are the two internal parameters; the second option in a four-dimensional one, where the internal parameters are mass, cyan (C), magenta (M) and yellow (Y). The mathematical expression that governs the resultant dye is the average of the three primary components, weighted over the respective masses. This formula is commonly used in managing colours in computer graphics and it can be expressed as follows:

$$\boldsymbol{p}_{1+2}\begin{cases} m_{1+2} = m' + m'' \\ C_{1+2} = \dfrac{1}{m' + m''} \cdot (m'C' + m''C'') \\ M_{1+2} = \dfrac{1}{m' + m''} \cdot (m'M' + m''M'') \\ Y_{1+2} = \dfrac{1}{m' + m''} \cdot (m'Y' + m''Y'') \end{cases} \tag{3.24}$$

Here we discuss the solution of the GFPT using relations Eq. (3.24). Droplets are supposed to be in an idealized box where the collision rate of droplets is described by a constant aggregation kernel of $K = 10^{-10} m^3 s^{-1}$. The range of sizes analysed spans from 1 to 10 μm. The variable *colour* can be treated both as a unique parameter or a three dimensional quantity in the CMY space. In the second case the application of the GFPT is straight-forward but it results in a four-dimensional problem $(C, M, Y, mass)$ with consequent drawbacks on searching algorithms. On the contrary, the first case has the advantage of being a bidimensional problem $(Colour, mass)$. But the reassignments of new aggregates to existing pivotal positions requires more effort, since each CMY newborn combination must be converted in defined values on the colour axis. We adopted the second strategy, i.e. the colour axis is represented with a mono-dimensional vector of CMY combinations, sorted according to their relative hue from violet to red as in the electromagnetic spectrum (CMY values must be converted in HSL to do a rainbow-like sorting). This sorting converts the variable colour into a quantity that increases along the axis, as a common variable like the mass. In other words the HSL sorting guarantees that consecutive pivots along the colour axis have similar hues. The advantage is evident when particles are generated in non-pivotal positions, i.e. the majority of the cases. As a matter of fact, a non-pivotal particle will be shared between colours of similar hue with respect to the newborn droplet, as it always happens in the fixed pivot technique.

Droplets collide and the resultant colour on a CMY scale is determined according to Eq. (3.24). The CMY value is then converted in a point on the secondary plane using a linear interpolation between the two closest pivotal colours. Finally, the searching algorithm finds the triangular element on the secondary grid that contains the point and the quantity is shared between the three vertexes according to Eq. (3.17). Each CMY channel I represented with 2 bits resulting in a total of 64 different combinations. We apply the

GFPT with several different initial conditions. Figure 3.5 shows the time evolution of two binary combinations of initial colours: cyan and yellow, red and blue.

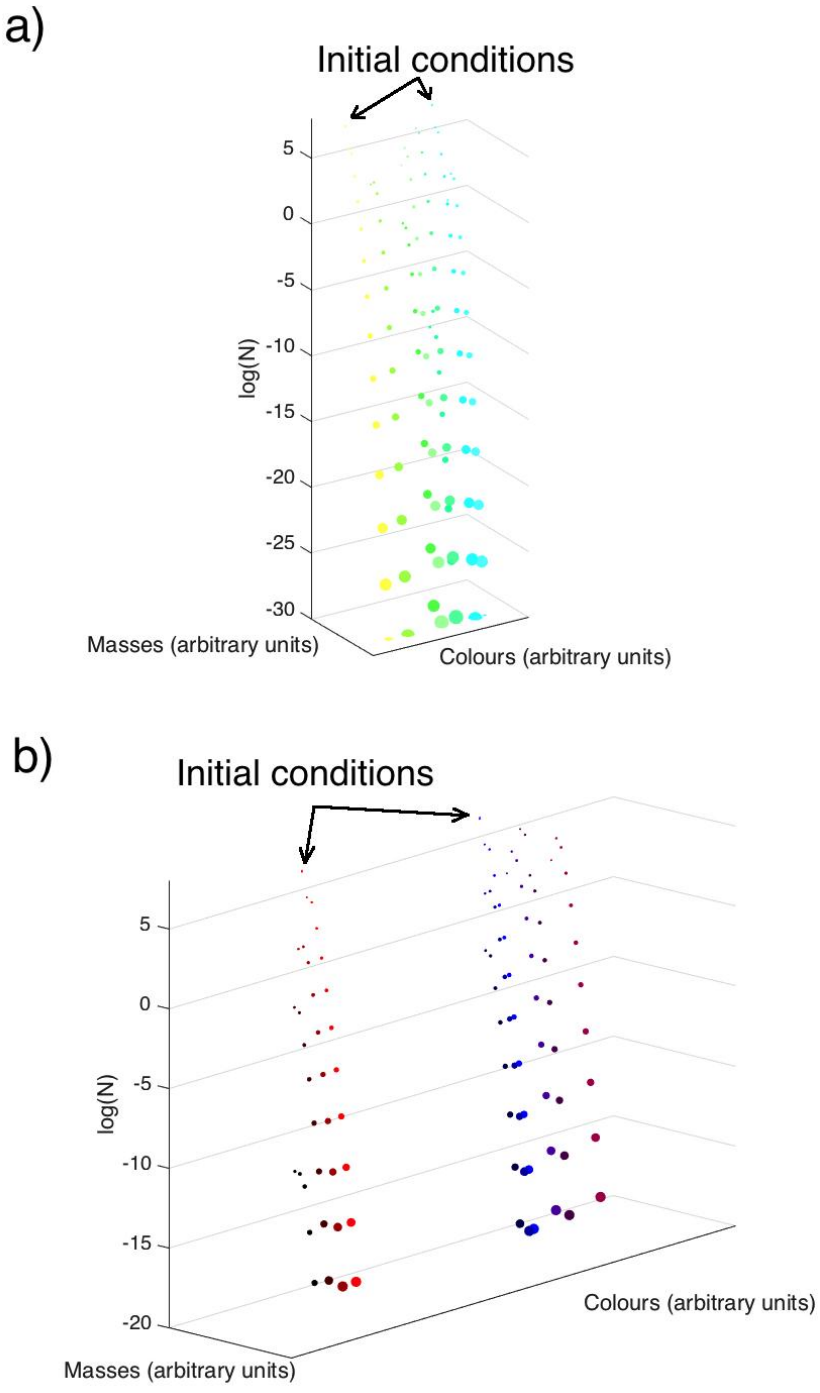

Figure 3.5 Chromatic evolution after 100 s of two initial distributions composed of just two colours. An initial concentration of $10^7 m^{-3}$ droplets is used for both the examples. a) Initial colours are cyan and yellow b) Initial colours are red and blue. Both figures represent the final population, i.e. after 100 s.

Initial concentrations for both examples are fixed at $10^7 m^{-3}$ with a size of 1 μm. The system starts with two tones but after a while the generation of a third colour creates the conditions for a cascade effect. However the propagation of the colours is bounded within the limits contained within Eq. (3.24). In the case of cyan and yellow, two primary colours in the CMY codifications, there is no way to activate the third channel (magenta). Red and blue, allows a wider spectrum of combinations. A different test is reported in Figure 3.6. Here all the 64 colours available are blended together, starting with a concentration of $10^7 m^{-3}$ droplets with a size of 1 μm. The output after 100 s shows that for each family of colours, the maximum of the distribution is associated with the darkest tone. This is due to the mixing: as a matter of fact in the subtraction theory the higher the number of colours mixed, the higher will be the number of wavelengths absorbed.

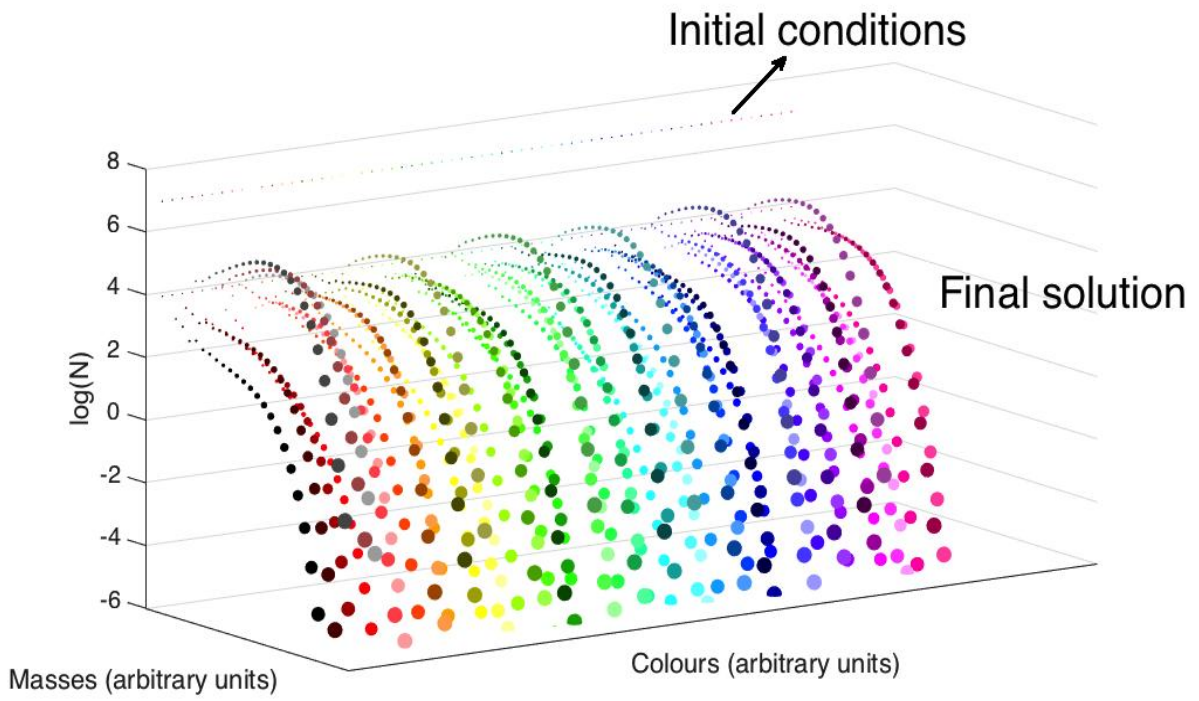

Figure 3.6 Colour evolution for an initial concentration of $10^7\ m^{-3}$ droplets for each of the 64 colours available (2 bits). A constant kernel of $10^{-10}\ m^3 s^{-1}$ is applied to every collision. The total simulation time is 100 s. Size distribution evolves towards larger sizes as expected for a pure coagulation problem. Darker shades becomes dominant with time due to the increasing absorption of light consequent to the superimposition of different colours.

3.4 Conclusions

We demonstrated how the fixed pivot technique (Kumar and Ramkrishna, 1996) can be successfully applied to the solution of aggregation processes of multidimensional arbitrary properties. This new approach is called the Generalized Fixed Pivot Technique (GFPT). In population balances, members of a population are described in terms of pre-defined internal properties. In the past, additive relations have been proposed for multidimensional problems as a natural extension of the one dimensional Smoluchowski Coagulation Equations (SCE). The GFPT expands what was achieved in previous works to the use of arbitrary properties. As a matter of fact, in many circumstances the complexity of particle interactions can be fully described only with non-additive properties. This usually happens with the packing of solid objects, but can also affect coagulation problems. In this work the GFPT is rigorously derived from the continuous aggregation equations under specific, but quite general, assumptions. We have also shown the great versatility of the new technique with an example where previous techniques would be ineffective. The GFPT inherits all the advantages and disadvantages of the fixed pivot technique, such as the accuracy and the underlying simplicity of the method. On the contrary a large number of pivots is required to avoid numerical diffusion, as discussed in the verification section of this paper. In fact this limits the applicability of the GFPT for those situations where a great number of internal parameters is required. In conclusion this work represents our effort to extend the common method of the fixed pivot technique towards more general scenarios. An effort that is required to describe accurately the complexity of the aggregation in natural systems.

3.5 Acknowledgements

The research leading to these results has received funding from the European Union Seventh Framework Programme (FP7/2007-2013) under the project NEMOH, grant agreement n° 289976.

3.6 Author's contribution

E. Rossi contributed to the complete formalization of the theoretical framework and the codes that perform the computations contained in this chapter.

Chapter 4

A new theoretical method for the study of ash aggregation[3]

4.1 Introduction

During volcanic explosive eruptions the fraction of fine ($< 63\,\mu m$) and coarse ($63\,\mu m - 2mm$) ash injected in the atmosphere frequently sediments in the form of aggregates as evidenced by numerous field observations (Bagheri et al., 2016; Brown et al., 2012; Carey and Sigurdsson, 1982; Gilbert et al., 1991; Sorem, 1982; Taddeucci et al., 2011; Van Eaton et al., 2015). Volcanic aggregates usually show larger terminal velocities and a smaller permanence time in the atmosphere than their single components. As a result, particle aggregation efficiently removes fine ash from the atmosphere, increasing the amount of proximal sedimentation. However, despite its importance, ash aggregation is not easily implemented in Volcanic Ash Transport and Dispersal Models (VATDMs) and its full description still remains a challenging task in the scientific community. A main consequence of neglecting ash aggregation in forecast models is the overestimation of fine particles in the far field and the underestimation of tephra fallout in the proximal and medial regions (< a few tens to a few hundreds of kilometres depending on plume height). The air traffic closure occurred in large parts of Europe as a result of the 2010 Eyjafjallajökull eruption (Iceland) is still a vivid example of the importance of having accurate predictions from VATDMs. In the last three decades many efforts have been made to describe the effects of ash aggregation on tephra fallout. One of the first approaches is based on the empirical redistribution of ash from fine to coarser classes in order to emulate the action of aggregation (Bonadonna et al., 2002; Bonadonna and Phillips, 2003; Cornell et al., 1983). Empirical models are calibrated on the comparison between field observations and model results. Recently, Mastin et al. (2016) has demonstrated that the lognormal distribution describing the best fit for aggregates in empirical models is quite general and scenario independent. However, despite their advantages in terms of computational efficiency, empirical methods lack a

[3] Rossi E., Pollastri S., Bonadonna C. (paper part I, paper part II, *to be submitted*).

physical description of the process, which reduces enormously the range of applicability. In particular, they still represent a reasonable alternative for probabilistic long-term hazard assessments requiring fast computation times where aggregation processes are calibrated on past field observations and treated statistically. Nonetheless, empirical descriptions are of more complex application when used to forecast ash dispersal from individual eruptions in real time. Approaches based on more accurate physical models are possible, but the associated theoretical framework is more complex and its solution computationally inefficient. The main complications in describing volcanic ash aggregation are related to the large number of particles involved in the process and the poor constraint on the physical processes involved. Typical values for particle concentration in volcanic plumes are of the order of $\sim 10^{7-12}\ m^{-3}$ (Veitch and Woods, 2001), a number that makes a statistical approach necessary, e.g. the so-called Smoluchowski Coagulation Equation (SCE) (Smoluchowski, 1916):

$$\frac{dn(V)}{dt} = \frac{1}{2}\int_0^V K(V-\varepsilon,\varepsilon)\ n(V-\varepsilon)\, n(\varepsilon)\, d\varepsilon\ - n(V)\int_0^\infty K(V,\varepsilon)\, n(\varepsilon)\, d\varepsilon \tag{4.29}$$

In the SCE the creation of droplets/particles with volume V is governed by the aggregation kernel K and a density distribution function $n(\varepsilon)$ that gives the number of particles with volume comprised between $[V, V+dV]$. The aggregation kernel is usually expressed as the product of two different quantities ($K = \alpha \cdot \beta$): the sticking efficiency α and the collision rate β. All the physics of the process is condensed in these two numbers, on which depends the possibility of solving Eq. (4.1). The collision rate β quantifies the flow rate of particles impacting on each other and it is dependent on the particular physical phenomenon under analysis (Brownian motion, turbulence, sedimentation, thermophoresis, etc.). The sticking efficiency α describes the probability that a collision results in an aggregation process, i.e. the particle is not rebounded. It depends on the capability of the system to dissipate the relative kinetic energy of the impact. One of the first uses in volcanology of the SCE appeared in Veitch and Woods (2001), followed by Textor et al. (2006). Costa et al. (2010) has provided an approximated solution to Eq. (4.1) based on the assumption of fractal geometry within the aggregates. Recently Folch et al. (2016) applied this framework to the study of ash aggregation in a volcanic plume. However, a large number of observations suggest that ash aggregates have complex and irregular structures and do not follow a fractal

packing. According to the classification of Brown et al. (2012), two main families of objects are identified: *Particle Clusters* (PC) and *Accretionary Pellets* (AP). The first group is subdivided in: PC1, ash clusters, and PC2, coated particles. The second group is formed of: AP1, poorly structured pellets; AP2, pellets with concentric structure; AP3, liquid pellets. PC1 are ash clusters, characterised by low densities around $60 - 200\ kg/m^3$ and typical size of the components less than $40\ \mu m$. PC2 clusters are characterized by the presence of a large coated particle at the centre with sizes> $200\ \mu m$. AP1 are poorly structured aggregates with median size of the population between $\approx 30 - 90\ \mu m$ and overall size between $100\ \mu m$ and few millimetres. AP2 are pellets with concentric structure and a typical overall size between $2 - 15\ mm$. Finally, AP3 are liquid pellets with a wide range on inner particle size ($\approx 1\ \mu m - 1\ mm$), a significant presence of liquid water and a generally poor conservation after the impact. Bagheri et al. (2016) have also introduced an additional class of cored particle clusters (PC3) that consist of a core particle (200–500microns) fully covered by a thick shell of particles < 90microns. PC2 and PC3 mostly differ due to the thicker coating of PC3. Such a large variety of shapes and structures are poorly described by the one-dimensional description of the SCE. As a matter of fact, objects with the same mass may have different densities or porosities, which results in a completely different sedimentation process. Moreover, recent observations of falling aggregates during the 2010 Eyjafjallajökull eruption, Iceland, and the July-August 2013 eruptions at Mount Sakurajima, Japan, have suggested a primary role of coated particles in aggregates formation for PC objects (Bagheri et al., 2016; Taddeucci et al., 2011).

This chapter proposes an innovative perspective of the theoretical description of ash aggregation, which avoids most of the limitations of the one-dimensional approach of the SCE. The new methodology is derived from the Generalized Fixed Pivot Technique (GFPT) presented in chapter 3 applied to the study of ash aggregation in volcanic plumes. For this purpose, the mass balance equations of a one-dimensional steady state plume model have been modified in order to take into account several classes of solid aggregates and their evolution. The choice of limiting the attention only to the eruptive plume is motivated both by a need for computational efficiency and by the fact that aggregation occurs where particles concentration is higher (Veitch and Woods, 2001). Moreover, field observations of aggregation timescales suggest relatively fast processes that are compatible with an occurrence in the volcanic plume (Bagheri et al., 2016).

According to the GFPT, aggregates are studied tracking the evolution of two internal properties: mass and porosity. The initial Total Grain Size Distribution (TGSD) is thus modified along the central axis of the plume on the base of the physics of collisional and sticking processes. The final TGSD at the top of the volcanic plume will be composed of classes of different size, density and mass with respect to the original distribution at source. A major attention is posed on the definition of the collisional processes occurring in the highly turbulent volcanic environment. An alternative parameterisation of the sticking efficiency for wet and dry environments has been rigorously presented. All these aspects will be discussed in the following sections.

4.2 Equations of particle aggregation

The Generalized Fixed Pivot Technique (GFPT) developed in chapter 3 is applied here to the study of ash aggregation in a volcanic plume. The final software package is written in Matlab. In the GFPT n internal parameters p_n are chosen in order to fully characterize the evolution of a population under analysis. In our notation superscript quantities p_n' and p_n'' denote the internal properties of two aggregating particles, the symbol p_{1+2} is referred to the final product of their interaction, bold type quantities $\boldsymbol{p}$ are vectors. The unique limitation posed by the theory concerns the form of the mathematical function that relates p_n' and p_n'' to p_{1+2}. This relationship must be a single-valued function of the interacting properties, i.e. the final product of the collision is described by a single value in the final space of the internal variables. No constrains are posed on the number of internal properties involved in the process.

As discussed in the introduction to this chapter, major attention is devoted to the role of density in the final aggregates. Density is fully characterized by a length scale and a mass scale. It seems thus reasonable to limit the use of the GFPT to two internal parameters. Moreover, two parameters are a good compromise between the accuracy of the theoretical description and the computational efficiency of the numerical solution. The definition of the first internal parameter is straightforward, considering that *mass* (m) is conserved for solid particles as *volume* is in the original Smoluchowski equation (Smoluchowski, 1916). Moreover, mass is responsible for the dynamics of the object. The role of the second internal parameter is instead to capture the complex packing of

the aggregate structure. In this work we chose *porosity* (ϕ) as the second descriptor. This quantity can be easily translated into an equivalent density or a volume. According to this choice, each particle is labelled with a bi-dimensional vector in the space of the internal parameters, $\vec{p} = (m, \phi)$. The mathematical function g that relates the initial and final porosities of the two colliding objects will be made explicit in the next section.

$$\begin{cases} M_{1+2} = M' + M'' \\ \phi_{1+2} = g(\phi', \phi'', M', M'') \end{cases} \tag{4.2}$$

In the GFPT the space of the internal parameters is subdivided in two different grids (Fig. 4.1). The *primary grid* defines N_c cells where the actual particle concentration ($\frac{\#}{m^3}$) is evaluated. To each cell is associated a fixed point, called *pivot*, labelled with letter i. The shape of the i-esim cell of the primary grid is arbitrary. The *secondary grid* defines the way in which non-pivotal particles are redistributed within the existing pivots. According to Chakraborty and Kumar (2007), using triangular elements for the secondary grid in a 2-D problem minimizes the numerical diffusion.

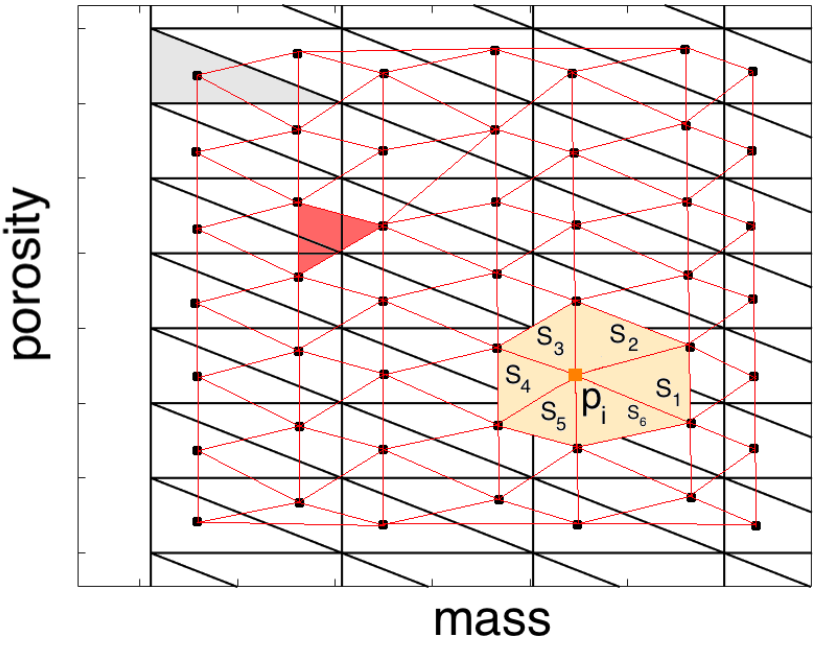

Figure 4.1 Example of gridding used in the GFPT. The primary grid is formed of triangular elements (black lines) with a series of fixed pivots at their barycentre (dots). In light grey the area of one cell of the primary grid. The secondary grid is as well formed of triangular elements (red lines). It is derived from a Delaunay triangulation between the positions of the fixed pivots. Triangles in orange identify the cells of the secondary grid involved in the process of redistribution relatively to the pivot p_i.

The secondary grid is thus composed of t triangular cells, denoted with the symbol $\triangle$, obtained with a Delaunay triangulation between the fixed pivots of the primary grid. Our code takes advantages of the Matlab built-in function for Delaunay triangulations, but efficient algorithms can be implemented in every computing language (Liu et al., 2015). It is worth stressing that in general the number of cells of the primary and secondary grid is not the same. The evolution of particle concentration in the i-esim cell is governed by an Ordinary Differential Equation (ODE) defined as follows:

$$\frac{\partial N_i(t)}{\partial t} = B_i - D_i \tag{4.3}$$

The two terms B_i and D_i are responsible respectively for the creation and destruction of objects belonging to the i-esim cell. If we denote with $\triangle_s$ the triangles of the secondary grid that have one vertex that coincides with the pivot i, we have:

$$B_i = \frac{1}{2}\sum_{j=1}^{N_c}\sum_{k=1}^{N_c}\sum_{\boldsymbol{p_{1+2}}(\boldsymbol{p_j},\boldsymbol{p_k})\subseteq\triangle_s} W_s(\boldsymbol{p_{1+2}}(\boldsymbol{p_j},\boldsymbol{p_k}),\boldsymbol{p_i})\ K(\boldsymbol{p_j},\boldsymbol{p_k})\ N_j N_k \tag{4.4}$$

$$D_i = N_i\sum_{k=1}^{N_c} K(\boldsymbol{p_i},\boldsymbol{p_k})\ N_k \tag{4.5}$$

Where the aggregation kernel $K(\boldsymbol{p_j},\boldsymbol{p_k}) = \alpha_{jk}\cdot\beta_{jk}^P$ is expressed as a function of the sticking efficiency α_{jk} and the collision rate β_{jk}^P for a couple of objects j and k involved in a collision process P (i.e. Brownian motion, turbulence, sedimentation, etc.). The birth term B_i states that between all the possible combinations of collisions, the ones that produce an effect in the i-esim cell are those that satisfy the condition $\boldsymbol{p_{1+2}}(\boldsymbol{p_j},\boldsymbol{p_k})\subseteq\triangle_s$. In other words, only aggregates generated in triangles of the secondary grid that involve the i-esim cell are considered in the birth term B_i. The weight terms $W_s(\boldsymbol{p_{1+2}}(\boldsymbol{p_j},\boldsymbol{p_k}),\boldsymbol{p_i})$ take in charge the redistribution of non-pivotal objects within the vertexes of the triangular cell. It is important to notice that the main appealing part of the GFPT respect to other theories is that the relationship $\boldsymbol{p_{1+2}}(\boldsymbol{p_j},\boldsymbol{p_k})\subseteq\triangle_s$ is general, and not restricted to additive properties as in the one-dimensional Smoluchowski equation. The relation

$\boldsymbol{p_{1+2}}(\boldsymbol{p_j}, \boldsymbol{p_k})$ is governed by Eq. (4.2). The weights W_s are defined in order to conserve a priori $\boldsymbol{Q}$ properties: mass, porosity and number of the newborn created particle ($\boldsymbol{Q} = [1, m, \phi]$). If the vertexes of a given triangle involved in the redistribution process are denoted with $\boldsymbol{Id} = [Id(1), Id(2), Id(3)]$ and property of the newborn particle as $\overline{\boldsymbol{Q}}$ (i.e. $\overline{\boldsymbol{Q}} = [1, M_{1+2}, \phi_{1+2}]$), the weight is given as:

$$\sum_{i=1}^{3} W_{Id(i)}\left(\boldsymbol{p_{1+2}}, \boldsymbol{p}_{Id(i)}\right) \cdot \; Q_j\left(\boldsymbol{p}_{Id(i)}\right) = \bar{Q}_j \quad \text{for } j = 1, 2, 3 \tag{4.6}$$

As an example of application of Eq. 4.6, let us assume that the triangle of the secondary grid involved in the process of redistribution is formed from the fixed pivots: $\boldsymbol{Id} = [2, 5, 8]$. The aggregate to be redistributed has internal properties M_{1+2} and ϕ_{1+2}. Equation 4.6 becomes:

$$\begin{cases} W_2 + W_5 + W_8 = 1 \\ W_2 \cdot M_2 + W_5 \cdot M_5 + W_8 \cdot M_8 = M_{1+2} \\ W_2 \cdot \phi_2 + W_5 \cdot \phi_5 + W_8 \cdot \phi_8 = \phi_{1+2} \end{cases} \tag{4.7}$$

The evaluation of weights W_s for the *i*-esim fixed pivot is performed only once in the code. It requires a searching algorithm in order to identify the triangular element that contains the point of coordinates $\boldsymbol{p_{1+2}}$. In this work we use the Matlab built-in function *pointLocation*, alternative algorithms for the implementation in different computing languages can be found in Krause and Rank (1996).

4.3 Porosities of volcanic ash aggregates

The porosity of an aggregate is defined as the ratio of voids of volume V_V with respect to the total volume of the object V_A (Manger, 1963)

$$\phi = \frac{V_V}{V_A} = 1 - \frac{V_S}{V_A} \tag{4.8}$$

Where V_S indicates the volume of the skeleton structure.

The related density of an object with total mass M_{tot} and n_c components of densities $\rho_{c1}, \rho_{c2}, \dots, \rho_{cnc}$ can be written as follows:

$$\rho_A = \frac{M_{tot}}{\sum_{i=1}^{nc} \frac{m_i}{\rho_{ci}}} \cdot (1 - \phi) \tag{4.9}$$

In this work we assume for simplicity that the initial population of particles is characterised with a unique density ρ_0 and zero porosity. This is an approximation; for example, Bagheri et al. (2016) has shown that within the same aggregate observed at Mount Sakurajima, Japan, during the fallout of August 2013, the densities of the components may vary from a maximum of 2700 kg/m^3 for 64 μm size particles to 2300 kg/m^3 for millimetric ash. Under this simplification, Eq. (4.9) can be expressed as:

$$\rho_A = \rho_0 \cdot (1 - \phi) \tag{4.10}$$

As outlined earlier, the most delicate part in defining an arbitrary internal parameter is the mathematical relationship that relates the final product to the original ones. In the following section we discuss existing and alternative solutions to this problem.

4.3.1 Existing theories for fractal geometries

A great majority of non-volcanological studies that report the evolution of porosity as aggregation occurs are based on the assumption of *fractal geometry* (Isella et al., 2008; Matthews et al., 2007; Matthews and Hyde, 2004; Min et al., 2006; Ormel et al., 2007; Richardson, 1995; Suyama et al., 2008). The fractal hypothesis has been adopted in many different contexts to describe the packing of a bunch of monomers, i.e. particles with unique size d_0. In volcanology this assumption has been used to describe the formation of ash aggregates by Costa et al. (2010) and recently applied to the study of the 26th of April eruption of La Soufrière St. Vincent, West Indies (Poret et al., 2017). The fundamental scaling law that links the number of monomers N_p and the characteristic length of an aggregate d_A is (Kostoglou and Konstandopoulos, 2001):

$$N_p = k_f \left(\frac{d_A}{d_0}\right)^{D_F} \tag{4.11}$$

Where $k_f \approx 1$ is the constant pre-factor and D_f is the fractal exponent. A possible explanation of Eq. (4.11) is given as follows: if we consider two interacting water droplets that merge together the final volume of the resulting sphere is $d_A = d_0 \cdot (2)^{1/3}$. Posing $N_p = 2$, Eq. (4.11) gives a value of $D_F = 3$. This is somehow expected, since water droplets fill completely the available space (*coagulation*). If however $D_F < 3$ two objects will occupy a larger volume than in a coagulation problem. In other words, the parameter D_F quantifies the degree of difference between a Euclidean geometry ($D_F = 3$) and a fractal geometry $D_F < 3$. In practical terms the main advantage of a fractal law is the possibility to relate the global geometry of an aggregate to its basic components. For example this allows the treatment of objects with different densities. The density of a fractal aggregate is expressed as (Isella et al., 2008):

$$\rho_A = \rho_0 \left(\frac{d_A}{d_0}\right)^{D_F - 3} \tag{4.12}$$

If an initial population of monomers evolve under the assumption of fractal packing it is thus possible to have two different densities ρ_{A1} and ρ_{A2} for objects with sizes d_{A1} and d_{A2} respectively.

One of the most exhaustive models to describe the evolution of grains porosity as aggregation occurs is described by Ormel et al. (2007). The authors condense previous studies on aggregation in protoplanetary disks to provide a simplified formula valid only for fractal geometries. In their theoretical framework, porosities are expressed in terms of the enlargement factors $\chi = \frac{1}{1-\phi}$, defined as the amount of extra volume of an aggregate if compared to its compact state. The final internal properties are:

$$\begin{cases} M_{1+2} = M' + M'' \\ \phi_{1+2} = \dfrac{\chi_{1+2} - 1}{\chi_{1+2}} \end{cases} \tag{4.13}$$

Where the conservation of mass is explicitly expressed and the value of the final enlargement factor given by:

$$\chi_{1+2} = \frac{m_1\chi_1 + m_2\chi_2}{m_1 + m_2} \cdot \left(1 + \frac{m_2\chi_2}{m_1\chi_1}\right)^{0.425} \quad \text{with} \quad m_1 \geq m_2 \tag{4.14}$$

We will refer to this set of equations for final porosities as the *Ormel scheme*.

4.3.2 New investigations of particle aggregation using virtual reality

Despite the fact that Eq. (4.14) represents a closed-form expression for the evolution of aggregates porosities, it is strictly limited to fractal geometries. However, field observations during the 2010 Eyjafjallajökull eruption, Iceland, and during the July-August 2013 eruption at Mount Sakurajima, Japan, reveal how the assumption of fractal geometries for ash aggregates structure is not generally verified (Bagheri et al., 2016; Bonadonna et al., 2011; Taddeucci et al., 2011). In particular, the presence of a large core in the inner structure of particle clusters invalidates Eq. (4.11), where a population of monomers is assumed. As an example, we report two histograms relative to the volume percentage and the number of particles present in the aggregate 27_SK_21 observed the 3rd of August 2013 at Mount Sakurajima, Japan (Fig. 4.2). Histograms Fig.4.2b and Fig.4.2c suggest that the population within volcanic aggregates may significantly vary and that any simplification may result in a biased and arbitrary description of their structure. These results are supported by other real-time field observations, e.g. (Bonadonna et al., 2011; Bonadonna et al., 2002; Sorem, 1982; Taddeucci et al., 2011).

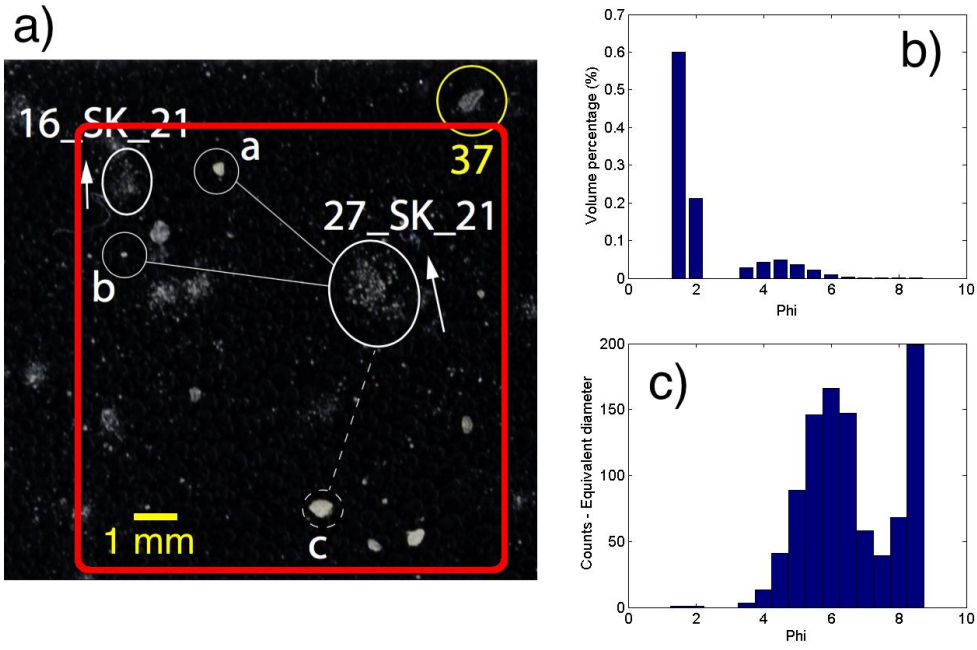

Figure 4.2 Example of observed cored aggregates at Mount Sakurajima, Japan, during the field campaign of July-August 2013. The aggregate 27_SK_21 has been related to the cores (a) and (b) in figure (a). SEM analyses of the population within the aggregate are reported in figure b) and c). Due to the large difference in size between coating and cores, the volume percentage of the entire aggregate is dominated by the cores (a) and (b), despite the large number of particles involved in the coating (fig. c).

Aggregate porosities have been experimentally studied by Lane et al. (1993). In their work the authors assume spheres of equal size and they define as the external volume of the structure a sphere with a diameter equal to the largest aggregate dimension. An alternative approach to the problem of the interaction of objects of different porosities relies on the use of virtual reality (Richardson, 1995). By this term we define a methodology based on the creation of virtual objects and the numerical study of their disposition in an imaginary volume. Porosity is a key quantity that, together with mass, contributes to determine the drag coefficient of an aggregate and in the end its residence time in the atmosphere. It is thus clear how in this context the drag coefficient is the most important aspect. Complex objects such as volcanic aggregates depend on many variables and some simplifications are needed. However, the theorem of Hill and Power (1956) states that the drag coefficient of an irregular particle in a Stokes regime is mathematically bounded by the drag exerted on the inscribed and circumscribed bodies. Bagheri and Bonadonna (2016) applied this theorem to demonstrate that the drag of an irregular object is always bounded between the drag of two ellipsoids, one internal and the other external to the body of interest. This idea suggests that the maximum drag of an aggregate is close to that of an ellipsoid that fits the external surface. The more spherical the aggregate shape, the closer will be this assumption. The total volume of our virtual aggregates will be thus defined as the ellipsoid that fits the most external components of the structure. This criterion is in agreement with that adopted by Lane et al. (1993). The algorithm for the creation of virtual objects is discussed in detail in Appendix (D.1). Some examples of different structures that can be realized are reported in Fig (4.3).

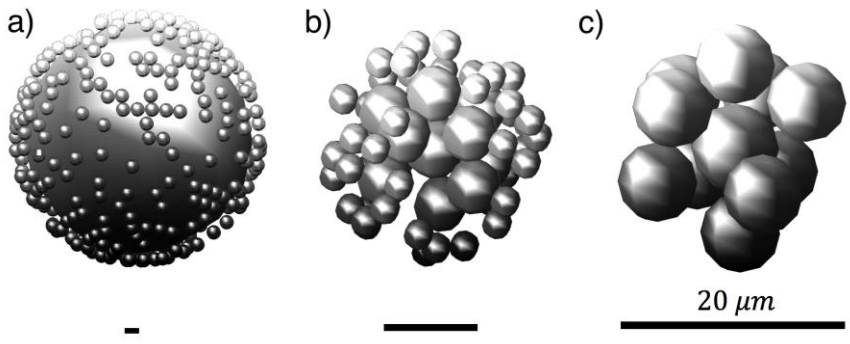

Figure 4.3 Example of different geometries that can be reproduced using the algorithm detailed in appendix D.1. Cored clusters (a), particles clusters (b), fractal objects (c)

Two examples of ellipsoids applied to the external components of virtual aggregates are reported in Fig. (4.4).

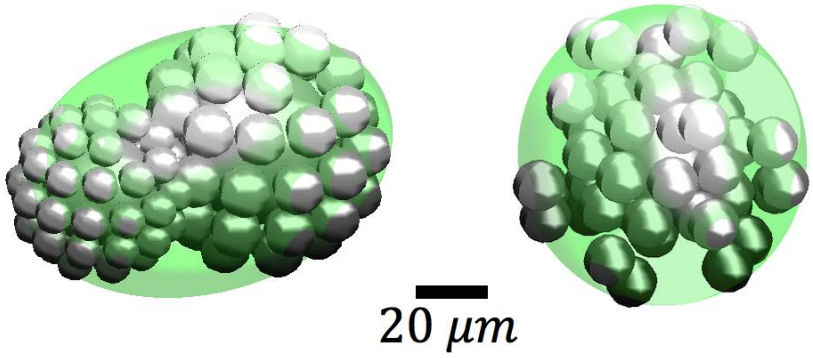

Figure 4.4 Example of fitted external volumes to two different types of aggregates.

A typical evolution of the internal porosity for an aggregate made of 20 μm particles with final fractal dimension 2.73 is reported in Fig. (4.5) as a function of ratio of d_A/d_{core} (similar to the formation of ash clusters, PC1, and poorly structured aggregates, AP1 of Brown et al., (2012)). The value of d_A is given by the diameter of a sphere with equivalent volume of the ellipsoid. The red line indicates the maximum theoretical porosity for cored structures ($\phi_{max} = 1 - (\frac{d_A}{d_{core}})^{-3}$).

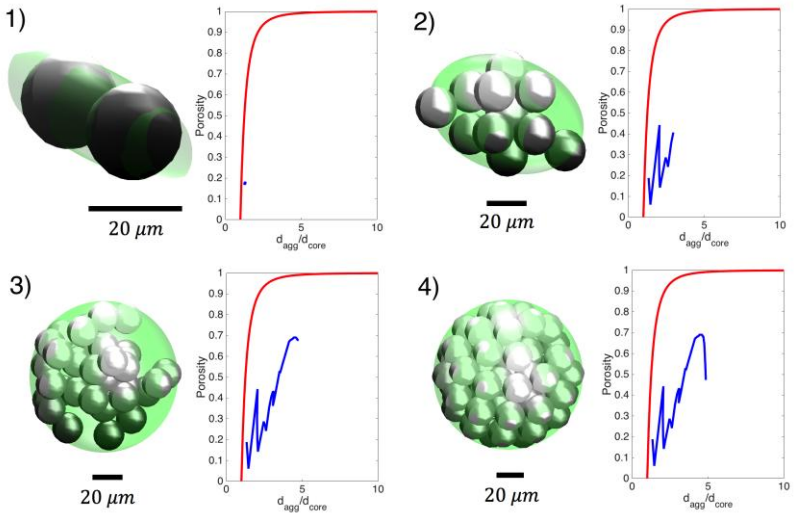

Figure 4.5 Evolution of aggregate porosity as the object changes its structure from (1) to (4). All particles are of 20 μm size. The red curve indicates the theoretical maximum porosity for a cored structure. The blue line indicates the measured aggregate porosity expressed as a function of the ratio between the aggregate diameter and inner core diameter.

It is worth noticing that in the case of unique sizes of the components, the numerical estimation of the porosity ϕ_{num} coincides within 2% with the theoretical porosities calculated using Eq. 5 in Lane et al. (1993). Another example of how porosity evolves as the aggregate is formed is reported in Fig. (4.6) (similar to the generation of coated particles, PC2, and cored particle clusters, PC3 of Brown et al., (2012) and Bagheri et al. (2016)). In this case a cored particle cluster is considered, with $d_{core} = 100\ \mu m$ and diameter of the coating particles $d_{coating} = 20\ \mu m$. Here we recall that PC2 and PC3 mostly differ because of the thicker coating on PC3 as observed with high speed camera during aggregate fallout (Bagheri et al. (2016); Taddeucci et al. (2011)). Bagheri et al. (2016) suggest that most PC1 and PC2 observed in previous studies (Brown et al., 2012) are, in fact, the remains of PC3 that broke on impact with the sticky paper used for real-time sampling.

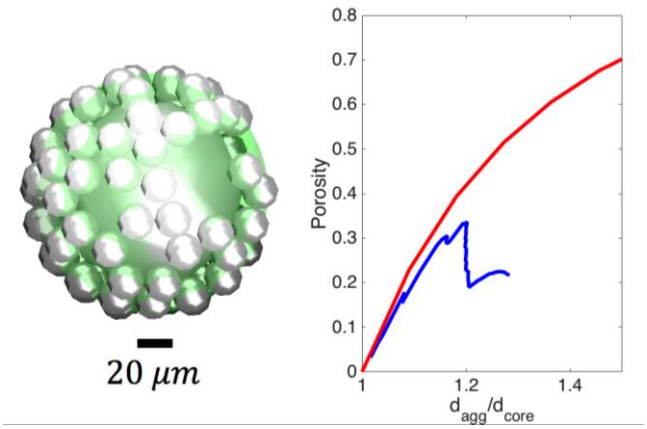

Figure 4.6 Example of final porosity for a cored object with internal diameter of 100 μm and coating particles of 20 μm. The red curve indicates the maximum theoretical porosity. The blue line indicates the measured aggregate porosity expressed as a function of the ratio between aggregate diameter and inner core diameter.

In the research of a mathematical expression for the final porosity ϕ_{1+2}, we notice that a primary role in Eq. (4.14) is played by the mass ratio $\frac{m_2}{m_1}$ of the colliding structures, where $m_1 \geq m_2$. In other words according to Ormel et al. (2007), the final porosity of the aggregates is conditioned by the mass ratios of the colliding objects more than from the absolute values of masses and porosities. This is somehow expected since more mass implies a larger object, under the assumption of equal densities for the initial population of particles. It is thus reasonable that the porosity of a larger object is less modified by interaction with a much smaller aggregate. According to this view, we indicate with

$\Lambda_m = \frac{m_2}{m_1}$ the mass ratio and with $\Lambda_\phi = \frac{\phi_2}{\phi_1}$ the porosity ratio of the colliding objects, where without loss of generality $m_1 \geq m_2$. The final form of the unknown mathematical function $\phi_{1+2} = g(\phi', \phi'', M', M'')$ is thus expressed as $\phi_{1+2} = g(\Lambda_\phi, \Lambda_m)$. Numerical simulations of the interaction of 30,000 different pairs of aggregates are performed in order to determine $\phi_{1+2} = g(\Lambda_\phi, \Lambda_m)$. The range of sizes considered in the simulations is reported in detail in appendix D.1. Results are displayed in Fig. (4.7), where ϕ_{1+2} has been expressed in terms of a relative increase/decrease with respect to the porosity ϕ_1 of the more massive object (i.e. $\phi_{rel} = \frac{\phi_{1+2} - \phi_1}{\phi_1}$). Despite the use of virtual aggregates can be applied to all the typologies of objects, in this chapter we limit our attention to the interaction of aggregates, i.e. we do not apply this methodology to single particles with zero porosity.

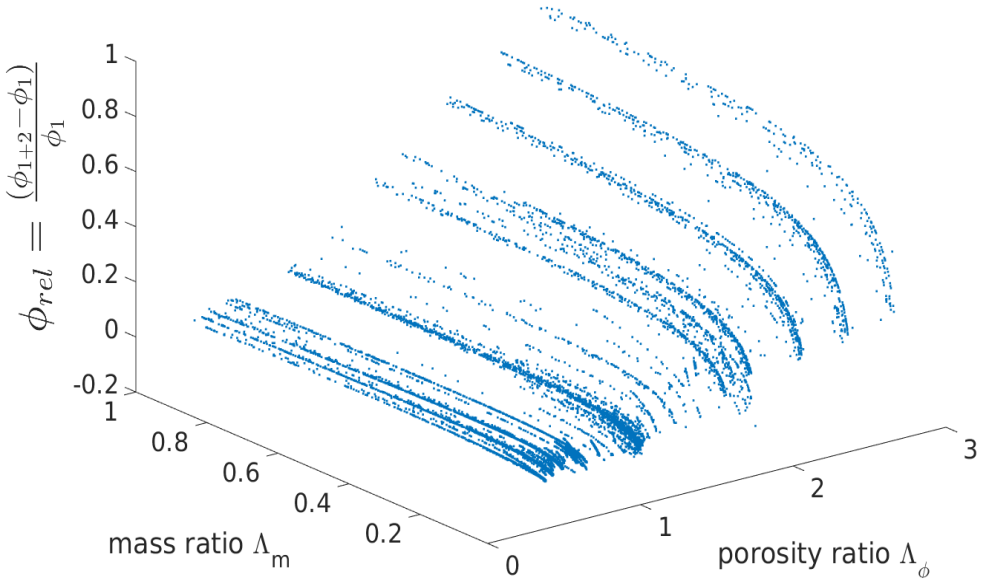

Figure 4.7 Final porosities for 30.000 aggregates as a result of the collision of two objects respectively with masses m_1 and m_2 and porosities ϕ_1 and ϕ_2. We assume that the most massive particle is always labelled with subscript "1". The final aggregate porosity, ϕ_{1+2}, is here expressed as a fraction of the initial porosity of the most massive particle (ϕ_1). On the x and y axes are reported the respectively the porosity ratio $\Lambda_\phi = \frac{\phi_2}{\phi_1}$ and mass ratio $\Lambda_m = \frac{m_2}{m_1}$.

Important considerations can be made about Fig. (4.7). First, regions with porosity ratio $\Lambda_\phi < 1$ are characterized by a final porosity ϕ_{1+2} that is generally similar to ϕ_1 (i.e. the relative difference is $\approx 10\%$), regardless of the mass ratio Λ_m. This plateau can be explained as follows: if the object with larger mass is also the most porous, aggregation

with an additional structure, smaller and more compact, does not modify dramatically the packing of the resulting sum. Second, the trend is completely different for $\Lambda_\phi > 1$, where the relative difference between ϕ_{1+2} and ϕ_1 can reach values up to $\approx 100\%$ if the object with less mass is much more porous than ϕ_1. Third, all the curves tend to collapse to zero or negative values of ϕ_{rel} if $\Lambda_m \to 0$, as also pointed out by Ormel et al. (2007). This means that aggregation of large objects with significantly smaller ones does not significantly alter the original porosity ϕ_1. It interesting to notice that the negative values for ϕ_{rel} observed in this limit indicate a partial filling of the internal structure of ϕ_1, with a consequent decrease in the porosity of the object with larger mass. Finally, for a fixed value of Λ_ϕ, the maximum of ϕ_{rel} occurs always at $\Lambda_m = 1$, i.e. when the two colliding objects are equal. The set of data displayed in Fig. (4.7) allows deriving an explicit mathematical formulation for the final porosity, expressed in terms of ϕ_{rel}. Here we adopt a simplified procedure that will be improved in future works. Points are fitted with a third order polynomial in the variable Λ_ϕ and fifth order in the variable Λ_m using a least square procedure. The choice of two different exponents for the polynomial fit is imposed by the asymmetry of data, clearly visible in Fig. (4.7). The final form of the expression for $g(\Lambda_\phi, \Lambda_m)$ states as follows:

$$\begin{aligned} g(\Lambda_\phi, \Lambda_m) = {} & p_{00} + p_{10}\,\Lambda_\phi + p_{01}\,\Lambda_m + p_{20}\,\Lambda_\phi^2 + p_{11}\,\Lambda_\phi\,\Lambda_m + p_{02}\,\Lambda_m^2 \\ & + p_{30}\Lambda_\phi^3 + p_{21}\Lambda_\phi^2\,\Lambda_m + p_{12}\,\Lambda_\phi\,\Lambda_m^2 + p_{03}\Lambda_m^3 + p_{31}\Lambda_\phi^3\,\Lambda_m \\ & + p_{22}\Lambda_\phi^2\,\Lambda_m^2 + p_{13}\Lambda_\phi\,\Lambda_m^3 + p_{04}\,\Lambda_m^4 + p_{32}\Lambda_\phi^3\,\Lambda_m^2 + p_{23}\Lambda_\phi^2\,\Lambda_m^3 \\ & + p_{14}\Lambda_\phi\,\Lambda_m^4 + p_{05}\,\Lambda_m^5 \end{aligned} \tag{4.15}$$

We will refer to this set polynomial formulation as *the Rossi scheme* for final porosities. Fit parameters for $g(\Lambda_\phi, \Lambda_m)$ are reported in Tab. (4.1) and the resulting surface is displayed in Fig (4.8).

Parameters for $g(\Lambda_\phi, \Lambda_m)$					
$p_{00} = -0.016$	$p_{10} - 0.076$	$p_{01} = 1.283$	$p_{20} = 0.17$	$p_{11} = -0.9906$	$p_{02} = -6.613$
$p_{30} = -0.024$	$p_{21} = 1.550$	$p_{12} = -1.23$	$p_{03} = 18.27$	$p_{31} = -0.2265$	$p_{22} = -1.968$
$p_{13} = 5.060$	$p_{04} = -22.870$	$p_{32} = 0.18$	$p_{23} = 0.7321$	$p_{14} = -3.177$	$p_{05} = 10.13$

Table 4.1 Fit parameters for the polynomial expression of $g(\Lambda_\phi, \Lambda_m)$ (Eq. 4.15).

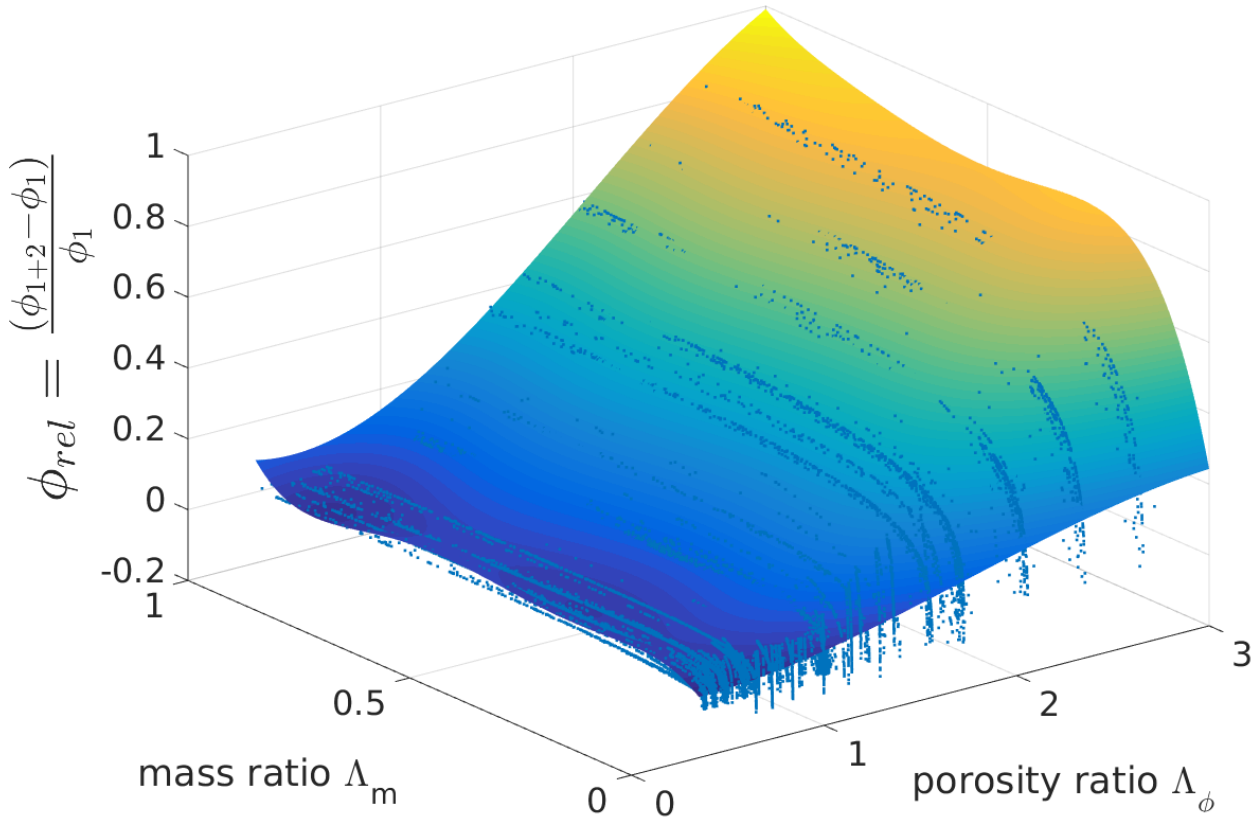

Figure 4.8 Fitted surface of the 30.000 simulations points obtained in different conditions using the algorithm of appendix D.1.The analytical expression of $g(\Lambda_\phi, \Lambda_m)$ allows relating each combination of colliding aggregates with a resulting value of the final porosity.

Eq. (4.15) can be seen as an alternative to Eq. (4.13) for aggregates of non-fractal geometries. The extremes of sizes considered are reported in detail in Appendix D.1. The explicit relationship for final porosities completes the set of equations needed in the GFPT. The next step is the combination of the previous theoretical framework inside the one dimensional steady state plume model in order to quantify the evolution of the population of aggregates within the eruptive column.

4.4 Plume modelling

Even if the GFPT can been applied to more sophisticated plume models (Kuenzli et al., *in prep.*), a good compromise between computational efficiency and accuracy in the

description of the phenomenon is achieved by coupling aggregation equations (Eq. 4.4, Eq. 4.5) with a one-dimensional steady state plume model. In the steady state approximation the conservation of fundamental quantities such as mass, momentum and total energy is derived for a control volume (Davidson, 1986a; Morton et al., 1956). The assumption that time variations are negligible when the eruption is at regime and an explicit formulation for the air entrainment, allows expressing a closed form system of ODEs in the independent variable z, height of the plume, or s, curvilinear coordinate of the central axis (if wind is considered). A large amount of models based on these assumptions are present in literature. An interesting overview can be found in Costa et al. (2016).

As outlined in the introduction, a key aspect in sticking processes is played by water. It is thus essential that plume equations adequately consider the entrainment of water vapour, its condensation threshold and possible changes in phase from liquid water to ice. In this work we combined plume models of Woods (1993) and Woodhouse et al. (2013) with the description of a liquid water to ice transition present in Folch et al. (2016). This class of models assumes that the plume remains in a saturated state if the vapour pressure inside the column equals its saturation value (over liquid water or ice). According to the assumption that in a volcanic eruption a large amount of condensation nuclei are available, no supersaturation is permitted. From Folch et al. (2016) we also derive the methodology for coupling aggregation and plume equations. The authors express the mass flux conservation for the solid phases as a sum of different contributions for each class of particles considered.

However differently from their work where aggregates are described with a unique class, we will extend this procedure to each of the total number of cells N_c in the bidimensional plane *mass-porosity*. It is worth noticing that the birth B_i and death D_i terms of Eq. (4.4, 4.5) appear explicitly in the mass flux equations for solid particles. An assumption of the air entrainment is required in order to close the system of equations. The entrained velocity is assumed to be function of a coefficient α_{entr} along the axis of the plume and a coefficient β_{entr} along the radial direction. (Bursik, 2001; Hoult and Weil, 1972)

$$U_{entr} = \alpha_{entr}|U_{th} - U_{wind}\, cos\theta| + \beta_{entr}|U_{wind}\, sin\theta| \tag{4.16}$$

Where U_{th} is the top-hat profile of the upward plume velocity, U_{wind} is the atmospheric wind at the center of the plume axis, and θ is the bending angle of the column. According to Devenish et al. (2010), $\alpha_{entr} = 0.1$ and $\beta_{entr} = 0.5$. The governing equations of the one dimensional steady state plume model are (Woodhouse et al., 2013; Woods, 1993):

$$\text{Total mass flux: } \frac{d}{ds}(Q_{tot}) = 2\pi\, R_{th}\, \rho_{atm}\, U_{entr} \tag{4.17}$$

$$\text{Dry air mass flux: } \frac{d}{ds}(Q_d) = (1 - q_{sh}) \cdot \frac{d}{ds}(Q_{tot}) \tag{4.18}$$

$$\text{Water mass flux: } \frac{d}{ds}(Q_w) = q_{sh} \cdot \frac{d}{ds}(Q_{tot}) \tag{4.19}$$

$$\text{Solid } i - \text{esim cell: } \frac{d}{ds}(Q_s \cdot X_i) = m_i\, \pi\, R_{th}^2\, \cdot \xi_2\, \cdot (B_i - D_i) \tag{4.20}$$

$$\text{s} - \text{momentum: } \frac{d}{ds}(J) = \pi\, R_p^2\, g \sin\theta\, (\rho_a - \rho_B) + U_{wind} \cos\theta \frac{d}{ds}(Q_{tot}) \tag{4.21}$$

$$\text{r} - \text{momentum: } \frac{d\,\theta}{ds} = \frac{\pi\, R_{th}^2\, g \cos\theta\, (\rho_a - \rho_B)\, - v_{wind} \sin\theta \frac{d}{ds}(Q_{tot})}{J} \tag{4.22}$$

$$\text{Energy: } \frac{d}{ds}(E) = \left(c_a\, T_a + g\, z + \frac{1}{2} U_{entr}^2\right) \frac{d}{ds}(Q_{tot}) + L_l\, \frac{d}{ds}(Q_l) + L_i\, \frac{d}{ds}(Q_i) \tag{4.23}$$

$$\text{x} - \text{coordinate: } \frac{d}{ds}(x) = \cos(\theta) \tag{4.24}$$

$$\text{z} - \text{coordinate: } \frac{d}{ds}(z) = \sin(\theta) \tag{4.25}$$

Where $Q_{tot} = Q_d + Q_v + Q_s + Q_l + Q_i$ is the total mass flux of the mixture, $Q_d = \pi\, R_{th}^2\, \rho_B n_d U_{th}$ the mass flux of dry air, $Q_w = \pi R_{th}^2\, \rho_B n_w U_{th}$ the mass flux of water vapor,

$Q_s = \pi R_{th}^2 \, \rho_B n_s U_{th}$ the mass flux of solid particles, $Q_l = \pi R_{th}^2 \, \rho_B n_l U_{th}$ the mass flux of liquid water, $Q_i = \pi R_{th}^2 \, \rho_B n_i U_{th}$ the mass flux of ice water, $Q_l = \pi R_{th}^2 \, \rho_B n_l U_{th}$ the mass flux of liquid water and $Q_i = \pi R_{th}^2 \, \rho_B n_i U_{th}$ the mass flux of iced water. The mass fractions X_i associated to the N_c cells of the plane *mass-porosity* verify $\sum_{i=1}^{N_c} X_i = 1$ at each step of the integration. The number concentration N_i that appears in Eq. (4.4) is given as $N_i = \frac{\rho_B \, n_s \, X_i}{m_i}$. It is worth mentioning that we assumed from the beginning a discretized TGSD. This means that the population under analysis is considered discrete and composed only by particles belonging to pivotal sizes, i.e. sizes at the central width of each bin. All the definitions for the quantities used in the plume-aggregation scheme can be found in appendix D.7. The coupling of plume model, topography and meteorological data is totally analogous to what presented in chapter 5. We refer to that chapter for further details.

The bulk density of the mixture ρ_b is given by (Folch et al., 2016):

$$\rho_b = \left[\frac{n_d + n_v}{\rho_{gas}} + \frac{n_l}{\rho_l} + \frac{n_i}{\rho_i} + \frac{n_s}{\rho_s} \right]^{-1} \tag{4.26}$$

The density of the gas phase (i.e. the dry air and water vapour) is evaluated from the equation of state of a perfect gas:

$$\rho_{gas} = \frac{P_{atm}}{R_g \, T_B} \tag{4.27}$$

Where R_g is a function of the gas constants of the two distinct phases, R_d and R_v, and their mass fractions n_d and n_v:

$$R_g = \frac{n_v \, R_v}{(n_v + n_d)} + \frac{n_d \, R_d}{(n_v + n_d)} \tag{4.28}$$

The gaseous fraction of the whole mixture inside the column is composed of dry air and water vapor. If we define the quantity *w* as:

$$w = \frac{n_v}{n_v + n_d} \tag{4.29}$$

The partial pressure of vapor inside the plume is (Woodhouse et al., 2013):

$$P_v = \frac{w\, P_{atm}}{w + (1 - w)\, \varepsilon} \tag{4.30}$$

Where $\varepsilon = \frac{R_d}{R_v} \approx 0.622$. Woods (1993) assumes that the large amount of fine ash in a volcanic column acts as Cloud Condensation Nuclei (CCN) in the atmosphere. This allows for a rapid conversion of the supersaturated fraction of water vapour in liquid water. It is worth noticing that these assumptions do not allow capturing the contemporary coexistence of liquid water and ice inside the eruptive column (i.e. volcanic hail). As soon as the vapour pressure P_v exceeds its saturation pressure e_{sl}, the vapour in excess is converted in the right amount of liquid water necessary to recover the equilibrium $P_v = e_{sl}$. Folch et al. (2016) extended the same procedure for saturation respect to ice ($P_v = e_{si}$). The values of the saturation pressure respect to liquid water and ice as a function of the temperature can be found in Murphy and Koop (2005). Two values of relative humidity are thus possible in a volcanic column: relative humidity respect to liquid water, $RH_l = \frac{P_v}{e_{sl}}$, and relative humidity respect to ice, $RH_i = \frac{P_v}{e_{si}}$. The conservation equation Eq. (4.19) is defined for the mass fraction of water n_w in the volcanic plume. However, the distinct phases n_v(vapour), n_l(liquid water) and n_i (ice) are required in order to constrain the physical processes that determine the sticking efficiency.

Fixing the values of $T_1 = 273.15\ K$ and $T_2 = 373\ K$, we define four different scenarios within the eruptive column.

- **Undersaturation with respect to liquid water**: $RH_l < 1$ and $T_1 < T_B < T_2$. If verified at a given position s in the column, the mass fraction of water n_w is totally attributed to water vapour:

$$\text{Subdivision of } n_w: \begin{cases} n_v = n_w \\ n_l = 0 \\ n_i = 0 \end{cases} \tag{4.31}$$

- **Saturation respect to liquid water**: $RH_l = 1$ and $T_1 < T_B < T_2$.

$$\text{Subdivision of } n_w: \begin{cases} n_v = \varepsilon \cdot \frac{e_{sl}(T_B) \cdot n_d}{P_{atm} - e_{sl}(T_B)} \\ n_l = n_w - n_v \\ n_i = 0 \end{cases} \tag{4.32}$$

- **Undersaturation respect to ice**: $RH_i < 1$ and $T_B \leq T_1$:

$$\text{Subdivision of } n_w: \begin{cases} n_v = n_w \\ n_l = 0 \\ n_i = 0 \end{cases} \tag{4.33}$$

- **Saturation respect to ice**: $RH_i = 1$ and $T_B \leq T_1$:

- Subdivision of n_w: $$\begin{cases} n_v = \varepsilon \cdot \frac{e_{si}(T_B) \cdot n_d}{P_{atm} - e_{si}(T_B)} \\ n_l = 0 \\ n = n_w - n_v \end{cases} \tag{4.34}$$

The set of equations Eq. 4.20 states that the GFPT acts as a birth and a sink term in the mass flux rate for each of the *i* cell of the plane *mass-porosity*. Eq. 4.4 and Eq. 4.5, combined with Eq. 4.13 or Eq. 4.15, allows simulating the evolution of ash aggregates once the collision rates and the sticking efficiency of the collisional processes are provided. The next sections will be dedicated to a rigorous formalization of these two quantities. In Fig. (4.9) it is possible to observe the final result coupling of aggregation and plume equations for the eruption of 18th of May 1980 at Mount Saint Helens, US. We used a constant kernel $K = 10^{-10}\ m^3 s^{-1}$ and a combination of *the Ormel scheme* and *Rossi scheme* for final porosities (Eq. 4.13, 4.14). In detail, single particles are described with the Ormel scheme ($\phi < 1\%$), aggregates with Rossi scheme ($\phi \geq 1\%$). The initial Total Grain Size Distribution (TGSD) is equal to that of the Mount Saint Helens 1980, US (Mastin et al., 2016). The TGSD with initial zero porosity evolves towards less dense aggregates. Fine ash at 4500 m of height a.s.l. appears in the form of aggregates with a median porosity of 0.4 (1500 $kg^3 m^{-1}$).

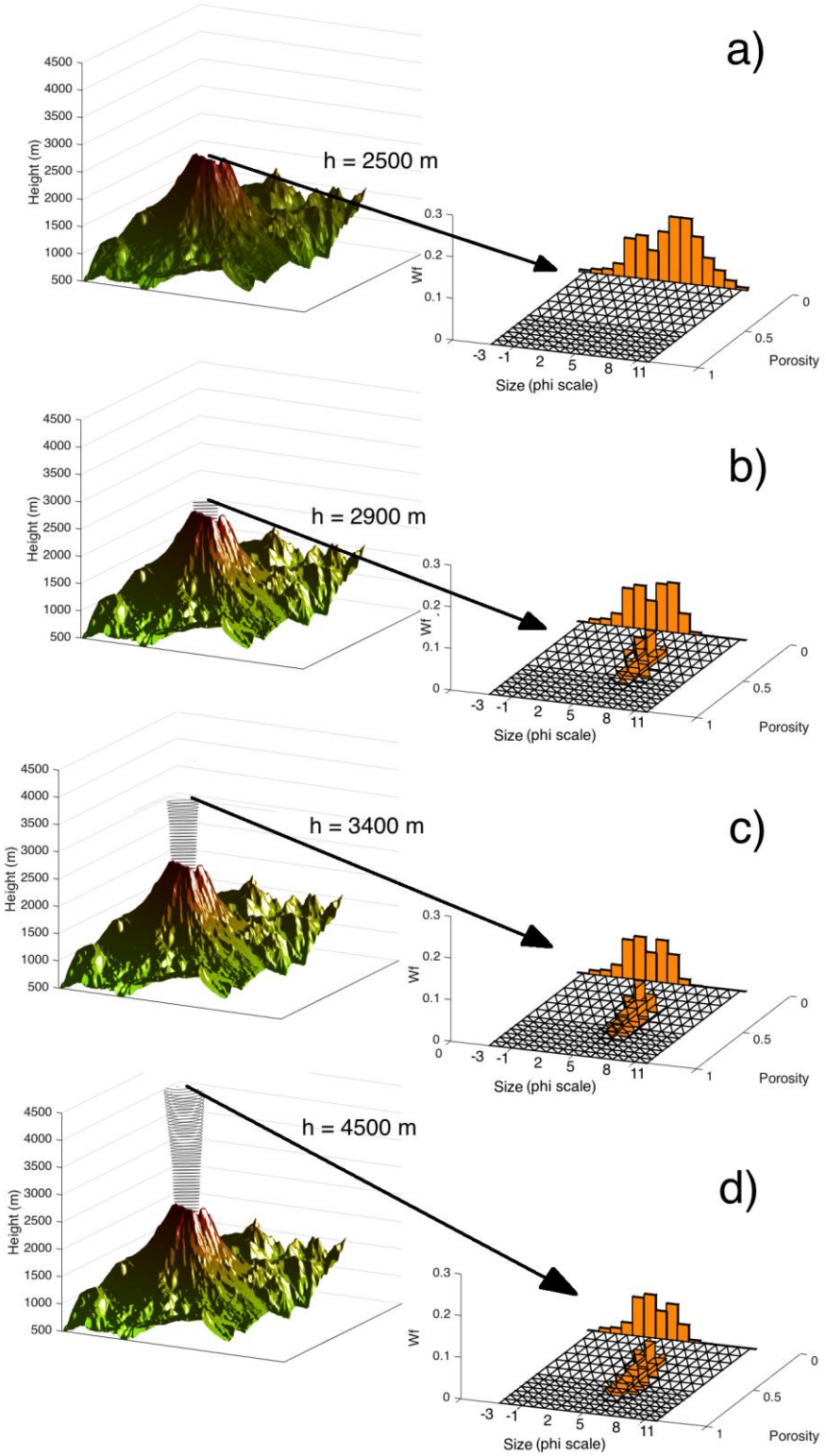

Figure 4.9 Example of application of the GFPT into a steady state plume model for aggregation with a constant aggregation kernel $K = 10^{-10}\ m^3 s^{-1}$. A combination of the Ormel and Rossi scheme has been used. The different plots, from (a) to (d), show the expected population at different heights above the vent. The initial TGSD is displayed in (a), with a null porosity. As the eruption starts, most of the fine ash occupies a position in the plane mass-porosity. Large particles are less affected to this process due to the reduced number of particles respect to fine ash.

4.5 Collision kernels

Collision kernels describe the average rate at which pairs of particles collide in any given aggregation process. A poor constraint of collision kernels has dramatic consequences on the accuracy and reliability of the final results. The aim of this chapter is to clarify what are the main processes that must be considered in order to well constrain collision kernels for a volcanic plume. In this chapter we denote every collision mechanism between two particles *i* and *j* with the Greek letter β_{ij}^{P}, with upper capital letter *P* dependent on the process. As a general rule, β_{ij}^{P} is always proportional to the product of the cross section *A* of the two colliding objects times the mean of the component of their relative velocity projected along the direction that connects the centres of the two particles (in this paragraph we refer to this term as the *radial velocity,* $\langle|U_r|\rangle$, as explained in section 4.5.1.1):

$$\beta_{ij}^{P} \propto A \cdot \langle|U_r|\rangle \cdot E_c \tag{4.35}$$

Where β_{ij}^{P} units are $[L^3T^{-1}]$. In many cases this product is weighted taking into account the collision efficiency of the process E_c, which describes the capability of small particles to avoid collisions following the streamlines of the fluid. In this case the effective cross section of the collision is reduced by the collision efficiency ($E_c \leq 1$). In this chapter $E_c \approx 1$ if not differently specified. Differently from other papers, we always report β_{ij}^{P} as an explicit function of cross section and relative velocity associated with a given process. This choice has two main advantages: first, it shows clearly the different contributions of velocity and cross section to the kernel; second, it provides the expression of mean relative radial velocities associated with different collisional processes. The second aspect is fundamental quantifying the sticking efficiency of aggregation, as we will see later. As a matter of fact, aggregation is a result of the dissipation of the kinetic energy of the collision, which is ultimately related to the relative velocity of colliding objects. Thus, expressions for relative velocities derived for the collision kernels will be also used in the section where we discuss the concept of sticking efficiency. Volcanic eruptions are predominantly turbulent environments. However, turbulence itself does not imply that particles will have significant collisions. In addition, gravity can overcome the turbulent motion and lead to the sedimentation of particles. The main aspects that will be addressed in this section can be here summarised:

- Main processes occurring in a volcanic plume that control particle aggregation are: turbulence and gravitational differential settling. Brownian motion, diffusiophoresis, thermophoresis and the role of the electric charges on the collisions are neglected due to their relatively small relevance for the sizes involved (Jacobson, 2005).

- The effect of turbulence is dominated by the *turbulent differential coupling* β_{ij}^{TDC}, a process that affects particles with a size between the smallest (*Kolmogorov length* η_{KO}) and the largest scales of turbulence (*integral length* L). The so-called *Saffman-Turner limit* seems to play a secondary role in particles aggregation.

- β_{ij}^{TDC} is a function of a particle's capacity to follow a turbulent flow (Stokes number). The final effect of turbulent eddies can be divided between class I vortexes, larger than particle sizes, and class II eddies, smaller.

- The gravitational collection mechanism β_{ij}^{GDS} matters when the drag exerted by the upward plume velocity is no longer sufficient to balance the weight of an object.

- The relative importance of β_{ij}^{TDC} and β_{ij}^{GDS} must be evaluated at each height within the column.

4.5.1 Effects of turbulence on the collision kernel

In a volcanic plume, large spatial scales (i.e. the radius of the plume) and velocities result in an enormous Reynolds number (Re), that not infrequently reaches the remarkable value of $Re \approx 10^{11}$ (Kieffer and Sturtevant, 1984). The interest here is to analyse how particles are influenced by such a high degree of turbulence. Particles with different sizes will react differently to the surrounding eddies. Some eddies will produce negligible effects; others will transfer remarkable amount of energy to the objects. The final result is a net relative velocity between particles that produces a collision rate. This process is here defined as the *turbulent differential coupling* kernel β_{ij}^{TDC}. However two mathematical limits of the problem are historically of great importance: the *Saffman-*

Turner limit, valid for particles completely coupled with the fluid; the *Abrahamson limit*, valid for large uncorrelated particles. The Saffman-Turner limit presents an additional collision mechanism, the shear effect, which is not included in the turbulent differential coupling. Both limits will be presented in some detail later. The main difficulty in quantifying β_{ij}^{TDC} comes from the estimation of relative velocities between two objects. In order to determine this quantity we will use the semi-analytical model of Ormel and Cuzzi (2007). An extensive discussion of their methodology is presented in Appendix (D.2). A brief summary of the main fluid dynamics quantities required to describe turbulence is instead reported in Appendix (D.3). It is somehow significant to notice that despite its relevance, the turbulent differential coupling has never been applied to a volcanic plume before. Previous approaches considered uniquely the Saffman-Turner limit. However it will be shown as in a volcanic eruption the conditions of applicability for this limit are rarely satisfied.

4.5.1.1 The turbulent differential coupling

In the present work we use the approach of Ormel and Cuzzi (2007), which is based on the previous works of Volk et al. (1980) and Markiewicz et al. (1991). This class of models, often named *Volk-type models*, attribute the correlation of two particles uniquely to their relative sizes with respect to the turbulent eddies. In the Volk-type models, vortexes are grouped in two distinct families according to their sizes: class I eddies are usually larger than the particle and they drive their motion; class II eddies are smaller and contribute as random fluctuation to the trajectory of the object. Before defining the collision kernel due to turbulent motion, we define for clarity the different definitions of relative velocities used in the text :

- $\langle U_m \rangle$: mean value of the total relative velocity between two particles, i.e. considering the differences along all the axes of the system of reference.
- $\langle U_r \rangle$: mean value of the relative velocity between two particles along the direction that connects the centres of the two objects. We refer to this quantity as the *radial relative velocity*
- $\langle |U_r| \rangle$: mean value of the modulus of the radial relative velocity
- $\langle U_m^2 \rangle^{\frac{1}{2}}$: root mean square value of the total relative velocity.

- $\langle U_r^2 \rangle^{1/2}$: root mean square of the radial relative velocity.

Volk-type models usually provide $\langle U_m^2 \rangle^{\frac{1}{2}}$. This quantity is then converted in $\langle U_r^2 \rangle^{1/2}$ assuming that the turbulence is isotropic along the three Cartesian axes:

$$\langle U_r^2 \rangle^{1/2} = \frac{1}{\sqrt{3}} \langle U_m^2 \rangle^{1/2} \tag{4.36}$$

However, as outlined in (Pan and Padoan, 2014), collision kernels should use the mean value of the *absolute* relative radial value $\langle |U_r| \rangle$, more than its root mean square $\langle U_r^2 \rangle^{1/2}$. This aspect is fully discussed in section (4.6.1), where the concept of relative velocity and its statistical distribution are crucial for the sticking efficiency of a collision. Here we limit to report the final averages of the absolute values of the radial velocities. These quantities will form the nucleus of the collision kernels for turbulent processes in this work. One of the main advantages of the methodology proposed by Ormel and Cuzzi (2007) is that the analytical solution of the problem results in a great computational efficiency. The complete theory and its limitations are explained in Appendix (D.3). Here we provide their final results, dependent on five main quantities: particle Stokes numbers St_{TL1} and St_{TL2}, threshold Stokes number St_{12}^*, Reynolds number of the fluid Re and its large-scale turbulent velocity fluctuation U_g (for the definition of the above quantities refer to appendix D.2). The final form of the turbulent differential coupling β_{ij}^{TDC} can be expressed as (Marshall and Li, 2014; Pan and Padoan, 2014):

$$\beta_{ij}^{TDC} = 2\pi \, g_{clust} (r_i + r_j)^2 \langle |U_r| \rangle = g_{clust} \, (8\pi/3)^{1/2} \, (r_i + r_j)^2 \, \langle U_m^2 \rangle^{1/2} \tag{4.37}$$

Where g_{clust} is a parameter that takes into account the clustering effect (Pumir and Wilkinson, 2016). Clustering effect is a relatively new concept in collision kernels. It is a particular aspect of the more general concept of particles segregation in a turbulent fluid (Calzavarini et al., 2008; Gustavsson et al., 2012; Meneguz and Reeks, 2011). It takes into account the enhanced local concentration caused by the radial drift of particles towards the edge of the vortexes. It can be demonstrated that in a rotating system the centrifugal force overcomes the inward action of the pressure gradient if particles density is higher

than the flow (Marshall and Li, 2014). It results in a drift motion towards the edge of the eddy and a local increase in concentration that can enhance aggregation. The clustering effect is a function of the particle Stokes number St_{TL} and its maximum usually occurs for particles of the same size and in general at $St_{TL} \approx 1$ (Pan and Padoan, 2014). Large Eddy Simulations evidence the actual presence of the clustering effects in a volcanic plume. Cerminara et al. (2016) show that for a low Mass Eruption Rates (MER), i.e. $MER \approx 10^6 \frac{kg}{s}$ this effect can lead to a maximum factor $g_{clust} \simeq 5$ in proximity of the central axis of the plume for particles with $St_{TL} \approx 5$. In the present work we will neglect this aspect, i.e. we will assume a homogeneous distribution of particles ($g_{clust} \approx 1$). This simplification will tend to underestimate the collision rate for larger sizes ($St_{TL} \geq 1$), but it should not be determinant for smaller sizes. However future work is needed to improve this aspect. Ormel and Cuzzi (2007) calculate the r.m.s. of the relative velocity among particles as:

$$\langle U_m^2 \rangle^{1/2} = \sqrt{U_{m\_I}^2 + U_{m\_II}^2} \tag{4.38}$$

If we denote the two particles with indexes 1 and 2, the contribute from class I eddies is:

$$U_{m\_I}^2 = U_g^2 \frac{St_{TL1} - St_{TL2}}{St_{TL1} + St_{TL2}} \left(\frac{St_{TL1}^2}{St_{12}^* + St_{TL1}} - \frac{St_{TL1}^2}{1 + St_{TL1}} - (1 \leftrightarrow 2) \right) \tag{4.39}$$

Where $St_{TL1} \geq St_{TL2}$ and the symbol $(1 \leftrightarrow 2)$ means the exchange of indexes from 1 to 2. The contribution from class II eddies is:

$$U_{m\_II}^2 = U_g^2 \left(\left(St_{12}^* - Re^{-\frac{1}{2}} \right) + \frac{St_{TL1}^2}{St_{TL1} + St_{12}^*} - \frac{St_{TL1}^2}{St_{TL1} + Re^{-\frac{1}{2}}} + (1 \leftrightarrow 2) \right) \tag{4.40}$$

The r.m.s. relative velocity is thus expressed as a function of basic properties of the flow and the two particles. The last missing quantity, St_{12}^*, is defined as $St_{12}^* = \tau_{12}^*/\tau_L$ where $\tau_{12}^* = \max(\tau_1^*, \tau_2^*)$ and τ_1^* and τ_2^* describe the threshold between class I and class II eddies for each object. The determination of τ_1^* and τ_2^* requires the use of numerical methods to solve the following equation for each particle:

$$\frac{2}{3}\frac{\tau^*}{\tau_p}\left(\frac{\tau^*}{\tau_p}-1\right)^2-\frac{\tau_p}{\tau_p+\tau^*}=-\frac{1}{1+St_{TL}^{-1}} \tag{4.41}$$

Once that τ_1^* and τ_2^* are known, τ_{12}^* can be calculated and consequently St_{12}^* and $\Delta U_{rel\_rms}^2$. The conversion of the r.m.s. relative velocity into its average value provides the mean relative velocity between two particles in a turbulent flow:

$$\langle|U_r|\rangle=\left(\frac{2}{3\pi}\right)^{\frac{1}{2}}\langle U_m^2\rangle^{1/2}=\left(\frac{2}{3\pi}\right)^{\frac{1}{2}}(U_{m\_I}^2+U_{m\_II}^2)^{1/2} \tag{4.42}$$

4.5.1.2 The Saffman-Turner limit

Historically it represents one of the first attempts of extension of the Smoluchowski theory to the cloud physics. It has been applied to the coalescence of cloud droplets, under the hypothesis of small sizes if compared with the Kolmogorov scale of turbulence. Therefore its application to the volcanic context is valid only for fine ash or low turbulence. This range describes particles with $St_{TKO}\ll 1$ and $d_p\ll\eta_{KO}$, i.e. objects smaller than the Kolmogorov scale. Saffman and Turner (1956) introduced two different collision mechanisms at this scale: the collision kernel β_{ij}^{SH}, describing the shear effect for particles moving with the turbulent fluid; the collision kernel β_{ij}^{TI}, relating the interaction of particles due to their inertia. The shear mechanism produces a collision frequency parameterized as follows:

$$\beta_{ij}^{SH}=2\pi\,(r_1+r_2)^2\,\langle|U_r|\rangle=\left(\frac{8\pi\,\varepsilon}{15\,\nu}\right)^{1/2}\left(r_i+r_j\right)^3 \tag{4.43}$$

The relative velocity associated with the shear process is:

$$\langle|U_r|\rangle=(r_1+r_2)\left(\frac{2\varepsilon}{15\,\pi\nu}\right)^{1/2} \tag{4.44}$$

The inertial mechanism β_{ij}^{TI} is instead a function of the relaxation times τ_{pi} of the two objects. If the radii of the two particles are denoted with r_i and r_j, the inertial kernel is:

$$\beta_{ij}^{TI} = \pi\,(r_i + r_j)^2 \langle |U_r| \rangle = 1.3\,\cdot\,(r_i + r_j)^2 \left(\frac{8\pi}{9}\,\frac{\varepsilon^3}{\nu}\right)^{\frac{1}{2}} (\tau_{pi} - \tau_{pj})^2 \tag{4.45}$$

Where the relative velocity associated with this process is:

$$\langle |U_r| \rangle = 1.3\,\cdot \left(\frac{8}{9\pi}\,\frac{\varepsilon^3}{\nu}\right)^{\frac{1}{2}} (\tau_{pi} - \tau_{pj})^2 \tag{4.46}$$

4.5.1.3 The Abrahamson limit

Despite this limit will be treated as a particular case of the turbulent differential coupling, it is worth describing here the Abrahamson kernel as a separate process. In fact it has been independently derived from the gas kinetic theory by Abrahamson (1975) under the assumption of particles with high Stokes numbers ($St_{TL} \gg 1$). Such mechanism of collision, here named β_{ij}^{AB}, is usually appropriate for particles larger than $1\,mm$ under particular conditions of turbulence. From an historical point of view it represents the opposite extreme to the Saffman-Turner range. Practically, the expression of β_{ij}^{AB} can be derived from Eq. (4.42) imposing the condition of heavy particles ($\tau_{12}^* = \tau_L$). In this circumstance all eddies are class II and $\Delta U_I^2 \longrightarrow 0$. In other words all eddies contribute as a background of random noise and there is no way to incorporate the particles. In this limit the turbulent differential coupling kernel β_{ij}^{TDC} tends to the Abrahamson kernel β_{ij}^{GK}:

$$\beta_{ij}^{AB} = (8\pi/3)^{1/2}\,(r_1 + r_2)^2\,(U_{r\_i}^2 + U_{m\_j}^2)^{1/2} \tag{4.47}$$

Where $U_{r\_rms\_i}^2 = U_g/\sqrt{1 + St_{TLi}}$ (see Appendix (D.3)).

4.5.2 The differential gravitational settling kernel

Gravitational settling is defined as the downward motion of particles due to the effect of gravity, which brings objects to fall at a constant velocity. In their fall, particles will tend to move at their own terminal velocity U_{si} that in general will be different for objects of different size and density. The differential settling will thus produce a net relative

velocity among them and the necessary condition to collide. This mechanism is described by the differential settling kernel β_{ij}^{GDS}:

$$\beta_{ij}^{GDS} = f_G\, E_c\, \pi\, (r_i + r_j)^2 \left| U_{si} - U_{sj} \right| \tag{4.48}$$

Where E_c denotes the collision efficiency. Wallace and Hobbs (2006) show that particles of 50 μm have $E_c \approx 0.7$, a value that rapidly approaches the unity for sizes larger than 60 μm. However for particles within $10 - 20$ μm values of $E_c \approx 0.1$ are not infrequent. In this work we assume $E_c \approx 1$ for particles larger than 60 μm and interpolated values for smaller sizes according to figure 6.20 of (Wallace and Hobbs, 2006). f_G is a number between zero and one introduced to take into account the effective importance of gravitational settling along the radial axis in a volcanic plume. In previous works it is implicitly $f_G = 1$ (Folch et al., 2016), but here we relax this condition. A detailed analysis of f_G is discussed in the following section. For gravitational settling collection, relative velocities between two objects are simply given by the differences in terminal velocity. It follows that particles of the same size and density cannot collide ($\beta_{ij}^{GDS} = 0$). The terminal velocity is given by:

$$U_{si} = \sqrt{\frac{4}{3} \frac{\rho_p\, d_p\, g}{\rho_f C_d}} \tag{4.49}$$

Where ρ_p is the particle density, d_p the diameter, ρ_f the fluid density and C_d the drag coefficient. In this work we use the drag coefficient proposed for non irregular particles by Bagheri and Bonadonna (2016).

4.5.3 Dominant collision mechanisms in a volcanic plume

All the different collision mechanisms and their range of applicability are summarised in Tab. (4.2). However it is not clear yet where these mechanisms occur within the eruptive column, how they change as the gas mixture rises and which is the prevailing one. The aim of this section is to clarify all these aspects and provide a final constraint on the correct use of the model. The following points will be discussed here: a) which turbulent mechanism should be applied for an arbitrary pair of particles along the plume. b) The

relative importance of gravity compared to the local turbulent accelerations. c) The relative importance of terminal velocities compared to the upward mean flow.

a) The application of the turbulent differential coupling is very general, since it does not constrain the particle Stokes numbers involved in the collision. However, as the Saffman-Turner limit is reached, the shear effect β_{ij}^{SH} should also be taken into account. Moreover β_{ij}^{TI} tends to β_{ij}^{TDC} (even if the contrary is not true). The Saffman-Turner limit requires that particles have $d_p \ll \eta_{KO}$ and $St_{TKO} \ll 1$, where η_{KO} is the Kolmogorov scale and St_{TKO} the turbulent Stokes number associated with the Kolmogorov scale. The way in which the smallest scale η_{KO} evolves is not trivial at all, as seen in Fig. 4.10 for two different eruptions. The change in Reynolds number modifies the smallest eddy seen by an object moving with the plume. As a consequence, it is expected that eruptions with higher MER will be characterized by smaller Kolmogorov scales. However, according to Fig. 4.10, the condition $St_{TKO} \ll 1$ seems to pose the major limitation to the use of the Saffman-Turner kernels in a volcanic context. Without any claim of generality, Fig. 4.10 suggests that the Saffman-Turner limit is no longer valid for particles larger than $\approx 50\mu m$ for small eruptions and larger than $\approx 10\mu m$ for major eruptions. These values are in good agreement with the analysis of Textor and Ernst (2004). It follows that the two kernels β_{ij}^{SH} and β_{ij}^{TI} are actually active only for small particles sizes in a volcanic plume. In our model β_{ij}^{SH} and β_{ij}^{TI} are applied if and only if both colliding objects are within the Saffman-Turner limit (St_{TKO} and η_{KO} are calculated along the column axis).

Table 4.2 Main different processes involved in aggregation of volcanic ash in an eruptive column.

Collision mechanism	Symbol	Range of applicability for particle *i*
Gravitational differential settling	β_{ij}^{GDS}	$U_{si} \gtrsim kU_p$ and $f_G > 0$ (see later)
Turbulent differential coupling	β_{ij}^{TDC}	No limitations
Saffman-Turner shear effect	β_{ij}^{SH}	$St_{TKO} \ll 1$ and $d_p \ll \eta_{KO}$
Saffman-Turner inertial motion	β_{ij}^{TI}	$St_{TKO} \ll 1$ and $d_p \ll \eta_{KO}$
Turbulent coupling for uncorrelated particles (Abrahamson limit)	β_{ij}^{AB}	$St_{TL} \gg 1$

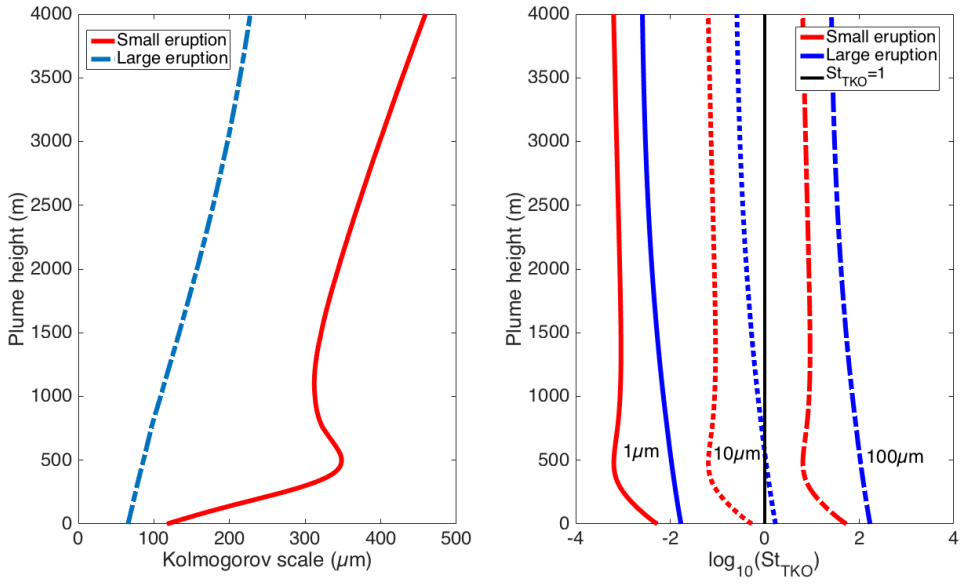

Figure 4.10 (Left): Kolmogorov scale in a volcanic plume plotted as a function of the plume height for two eruptive scenarios. Small scenario: vent radius 30 m, initial plume velocity 80 m/s. Large scenario: vent radius 200 m, initial plume velocity350 m/s. (Right): Stokes number associated with the smallest eddy size in the same eruptive conditions for three particles size: 1 μm, 10 μm and 100 μm. Both figures are obtained using the formulae of appendix D.2, relatively Eq. D.6 for Kolmogorov scale and Eq. D.10 for Stokes numbers.

b) The comparison of the gravitational acceleration with the turbulent acceleration is a first preliminary step to understand the relative importance of these collision mechanisms. Accelerations are independent of particle sizes and velocities and their ratio results in a physically meaningful dimensionless quantity (Shaw and Oncley, 2001). Outside the Saffman-Turner limit for a given eddy characterised with a size l and overturn velocity U_k the acceleration a_k can be defined as follows:

$$a_k \approx \frac{U_k^2}{l} = 2U_0^2 \frac{L^{-2/3}}{l^{1/3}} \tag{4.50}$$

Where we used the parameterization for U_k adopted in Ormel and Cuzzi (2007). Fig. (4.11) shows a sensitivity analysis for a_k with $L \subseteq [1\ m, 1000\ m]$, $U_0 \subseteq [0.1\ m/s, 30\ m/s]$, $U_0 \subseteq [\eta_{KO}, L]$. It shows that gravitational acceleration is usually larger than turbulent accelerations, except when the largest scale of turbulence is less than $\approx 50\ m$. This implies that particles larger than few tens of microns will generally dominated by the gravitational acceleration in most of the plume. Large accelerations connected with smallest scales of turbulence confirm the analysis reported in Shaw and Oncley (2001) and Textor and Ernst (2004).

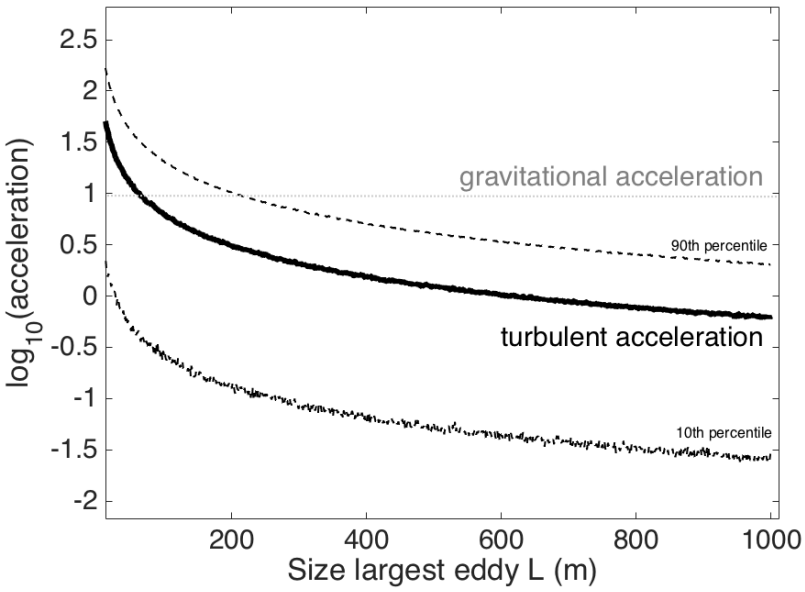

Figure 4.11 Possible different values of the turbulent acceleration a_k expressed as a function of maximum eddy sizes. The acceleration in the logarithm is normalized to $1\ m/s^2$. The range of values used in the sensitivity analysis is: L$\subseteq [1\ m, 1000\ m]$, $U_0 \subseteq [0.1\ m/s, 30\ m/s]$, $U_0 \subseteq [\eta_{KO}, L]$.

c) The relative importance of gravitational settling should also take into account the superposition of the mean upward flow U_p over the turbulent fluctuation U_0. There will be regions inside the plume where the drag exerted by the mean flow is sufficiently high to prevent particles to settle outside the plume, regardless the intensity of the turbulent fluctuation. But in practice it is hard to identify these regions with a simplified 1D steady state model. Cerminara et al. (2016) present interesting results about the preferential concentration of coarse ash (500 μm) and fine ash (16 μm) in plumes with high MER. In their work the authors show how the ratio R_{CF} of coarse to fine ash along most of the column is $R_{CF} \approx 1$ within 20 km, it descends to $R_{CF} \approx 0.8$ between 20 km and 35 km, and it drops to $R_{CF} \approx 0.1$ at 40 km, the top of the plume. This suggests that for most of the column, coarse and fine ash is still coupled with flow and thus no remarkable sedimentation is present. In this work we try to combine the observations contained in Cerminara et al. (2016) with concepts presented by Carey and Sparks (1986). The aim of the following discussion is to introduce a simple parameter that allows controlling the role of sedimentation on aggregation in different scenarios. Our analysis starts from the model of the *clast support envelope* adopted by Carey and Sparks (1986). Here it is interpreted as a measure of the relative importance of upward drag with respect to gravitational force. Clast support envelopes are defined as those regions inside volcanic columns where the Gaussian profile of the upward velocity along the radial direction of the plume equals the terminal velocity U_{si} of the objects. In this work we assume that at a given height the closer the envelope to the plume radius, the lower the role of sedimentation. The underlying idea is that sedimentation dominates if at a given height the envelope radius R_{env} is *smaller* than plume radius R_{th}. As a matter of fact, $R_{env} \ll R_{th}$ implies that the vertical drag exerted by the mean upward flow is no longer sufficient to prevent particles of a given size to sediment. We adopt this concept to quantify the relative importance of gravitation respect to turbulence. If we define $\gamma_U = \frac{U_{si}}{U_p}, \gamma_R = \frac{R_{env}}{R_{th}}$ and re-arrange the equations of Carey and Sparks (1986), the following condition holds:

$$\gamma_U \approx 2\, e^{-2{\gamma_R}^2} \tag{4.51}$$

The critical value for γ_R at which sedimentation starts to play a role is fixed a priori according to the scenario under analysis. The above relation can be used as a criterion to consider the effectiveness of the gravitational settling for a particle. For example, if we consider the start of sedimentation at $\gamma_R = 0.9$ (i.e. the envelope radius is 9/10 the plume radius), $\gamma_U = 0.4$, or alternatively, $U_{si} = 0.4\, U_{th}$. With this value of γ_R, the gravitational differential settling β_{ij}^{GDS} is supposed to be present only if $U_{si} \geq 0.4\, U_{th}$. The three different values of γ_R used as initial threshold for sedimentation are summarized in Tab. 4.3. The case $\gamma_R = 0.5$ is derived from figure 14 of Cerminara et al. (2016) for $R_{CF} \approx 0.5$. Once that the condition $U_{si} \geq \gamma_U \cdot U_{th}$ is verified, the gravitational differential settling β_{ij}^{GDS} is supposed to be present for all the collisions that involve the i-esim particle. However, a weight f_G is applied to β_{ij}^{GDS} in order to take into account the actual region of the plume where the sedimentation occurs. According to the Gaussian profile of plume velocity, the weight can be expressed as:

$$f_G = 1 - \frac{\int_0^{R_{env}} e^{-\frac{r^2}{b^2}}\, dr}{\int_0^{\infty} e^{-\frac{r^2}{b^2}}\, dr} = 1 - \mathrm{erf}(\sqrt{2}\,\gamma_R) \tag{4.52}$$

Once that sedimentation starts, Eq. (4.51) can be inverted to determine γ_R knowing γ_U. In the limit $\gamma_R \to 0$, the envelope has a no extension and this means that all along the radial coordinate the sedimentation process has its maximum ($f_G = 1$). Vice versa, for $\gamma_R = 1$ no sedimentation is present ($f_G = 0$). It is worth noticing that if only the i-esim particle is sedimenting, the relative velocity between collector and collected ash is assumed to be equal to the terminal velocity of the i object. If both particles are sedimenting, the relative velocity is equal to the differences of terminal velocities.

Ratio of envelope radius respect to plume radius (γ_R)	Ratio of envelope radius respect to plume radius (γ_U)	Ratio of envelope radius respect to plume radius U_{si}	f_G
0	2	$>2\ U_{th}$	1
0.5	1.2	$>1.2 \cdot\ U_{th}$	0.55
1	$2e^{-1}$	$>0.74 \cdot\ U_{th}$	0

Table 4.3 Different parameterizations of how gravitational settling is taken into account in the model. For $\gamma_R = 0$, gravitational collection has its maximum ($f_G = 1$) and it is applied when $U_{si} > 2U_{th}$. No effect due to gravitational settling is considered when $\gamma_R = 1$ ($f_G = 0$).

4.6 Sticking efficiency

In a previous paragraph the collision rate of volcanic particles has been presented. However not all the collisions will result in a process of sticking. Some of the impacts will produce a rebound, others an aggregate. Many aspects contribute to the determination of the final outcome of a collision and some assumptions and simplifications are required. In this section we present an exhaustive theoretical approach to the problem of the determination of the sticking probability of two objects in different environmental conditions. An intuitive way to determine the outcome of a collision is to evaluate whether the two-particle system is able to dissipate the kinetic energy of the collision. The total kinetic energy T_K of a two particles system is given by

$$T_K = \underbrace{\frac{1}{2}(m_1 + m_2)\, U_{CM}^2}_{\substack{kinetic\ energy \\ of\ the\ center\ of\ mass}} + \underbrace{\frac{1}{2}\frac{m_1 m_2}{m_1 + m_2} U_r^2}_{\substack{kinetic\ energy \\ of\ the\ collision}} \tag{4.53}$$

Where U_{CM} and U_r are the velocity of the center of mass and the relative velocity between the two particles respectively. $M = m_1 + m_2$ is the total mass of the system, $M_\mu = \frac{m_1 m_2}{m_1 + m_2}$ is the *reduced mass*. The first term represents the *kinetic energy of the center of mass*; the second term the kinetic energy relative to the center of mass. It is worth noticing that for an observer moving with the center of mass, v_{CM} drops to zero

and the net kinetic energy actually available in the collision is just given by the second term of Eq. (4.53). We will refer to this term as the *collision kinetic energy* T_{coll}. If we assume all mass is conserved and that the collision time is small enough to neglect the change in the momentum given by external forces, then the first term is conserved during collision. Therefore, the kinetic energy dissipated during collision is only a function of the initial and final collision kinetic energies:

$$\Delta T_{K\,(before-after)} = \frac{1}{2} M_{\mu} \left(U_{r\_Before}^2 - U_{r\_After}^2 \right) \tag{4.54}$$

If the internal forces acting during the collision are conservative, the collision is called *elastic* and no dissipation occurs:

$$\Delta T_{K\,(before-after)} = 0 \rightarrow U_{r\_after} = U_{r\_before} \tag{4.55}$$

If collision forces are not conservative, the collision is called *inelastic* and some energy is dissipated. For inelastic collisions, the final relative velocity is:

$$\Delta T_{K\,(before-after)} > 0 \quad \rightarrow U_{r\_after} = \sqrt{U_{r\_Before}^2 - \frac{2\Delta T_{K\,(before-after)}}{M_{\mu}}} \tag{4.56}$$

If collision forces are sufficient to dissipate all the available collision kinetic energy, the relative velocity of the two objects after the collision is zero. We define this condition as *particle sticking*. If we indicate with T_{diss} the amount of energy that the system is able to dissipate, we can write the sticking criterion as follows:

$$T_{coll} \leq T_{diss} \tag{4.57}$$

Eq. (4.57) states a unequivocal condition on the relative velocities of two colliding particles in order to stick:

$$U_r \leq \sqrt{\frac{2T_{diss}}{M_{\mu}}} = U_{crit} \tag{4.58}$$

The quantity U_{crit} indicates the *critical velocity* below which a sticking process happens. This result indicates that in order to determine the outcome of a collision, the relative velocity of two colliding object must be compared with the critical velocity. From Eq. (Eq. 4.58) it derives that in the limiting case of $U_{crit} \rightarrow 0$, no sticking process is possible

(no dissipation is present). Vice versa, for $U_{crit} \to \infty$ all the collisions result in a sticking process. For the sake of clarity, we summarize here the three main concepts required in order to describe the sticking outcome of a collision:

a. Evaluation of the relative velocities between particles. Relative velocity can be expressed as a single value (the average) or a distribution function.
b. Evaluation of the critical velocity associated with a given dissipation mechanism.
c. Comparison of relative and critical velocities: if the indicator chosen for the critical velocity is greater than the relative velocities, the collision results in a sticking event.

4.6.1 Relative velocities between particles in a volcanic plume

Expected values of the collision velocities between ash particles in a volcanic plume are presented in section (4.4.3). Here we briefly summarize the main concepts. Three collision mechanisms were considered:

I. Relative velocities generated by the different interactions/coupling with the turbulent eddies.
II. Relative velocities created by the turbulent shear for particles within the Kolmogorov scale.
III. Relative velocities generated by the different terminal velocities between objects of different size and density.

It is important to clarify here that the turbulent models used in section (4.4) assume a priori that the distribution of relative *radial* velocities U_r in a turbulent flow is described with a normal distribution with zero mean $\mu = 0$ and variance σ^2 (i.e. $f(U_r) = N(0, \sigma^2)$). These models provide the root mean square $\langle U_r^2 \rangle^{1/2}$ of this distribution, which at the end coincides with σ parameter ($\sigma = \langle U_r^2 \rangle^{1/2}$). However, the quantity commonly used in the definition of a collision kernel is not U_r, but its absolute value $|U_r|$. This is justified from the fact that the collision rate does not depend on the sign of the velocities, but only on their absolute values. The distribution function of the absolute values of $|U_r|$ is obtained mirroring around the y-axis the negative values of U_r contained in $f(U_r)$. The final result is that the distribution function of the absolute values of the relative radial velocities is

described with a *half-normal distribution* $q(|U_r|)$, also called *folded normal distribution*. The half-normal distribution is derived from a normal distribution, mirroring the negative values of the independent variables around the y-axis. The distribution function $q(|U_r|)$ can be written in terms of the variance $\sigma^2$of $f(U_r)$:

$$q(|U_r|) = \frac{\sqrt{2}}{\sigma\sqrt{\pi}} \exp\left(-\frac{U_r^2}{2\sigma^2}\right) \qquad with\ U_r \geq 0 \tag{4.59}$$

It is worth noticing that the mirroring process results in $q(|U_r|) = 2\, f(U_r)$. In this chapter we use both the mean value of $\langle|U_r|\rangle$ and the complete distribution $q(|U_r|)$ in order to define different sticking criteria. For a half-normal distribution the average value $\langle|U_r|\rangle$ is related to the quantity σ as follows:

$$\langle|U_r|\rangle = \sqrt{\frac{2}{\pi}}\,\sigma = \sqrt{\frac{2}{\pi}}\,\langle U_r^2\rangle^{1/2} \tag{4.60}$$

In other words, it is possible to fully describe $q(|U_r|)$ and its mean value using the root mean square values provided in section (4.4.1.1).

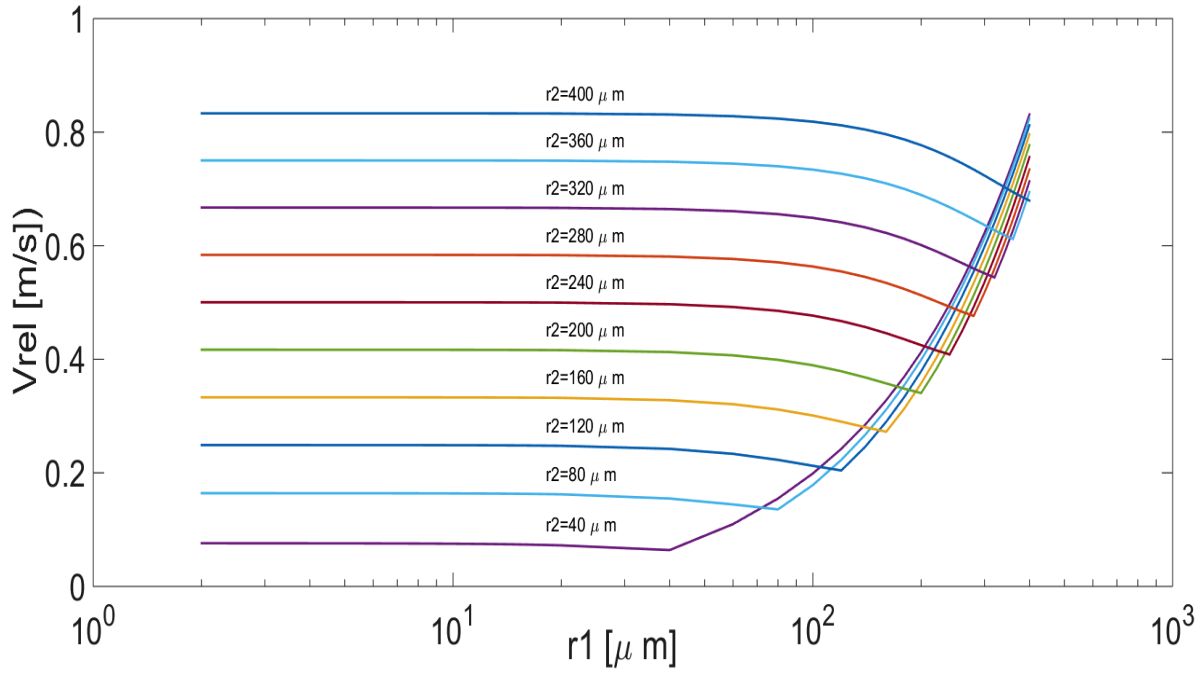

Figure 4.12 Example of relative velocities between two particles of different sizes for a plume velocity of 100 m/s. On the x axis the size of the collector, on the coloured lines the size of the collected particle. The size of the largest eddy is 1000 m, a reasonable order of magnitude for typical values of plume radius in a volcanic eruption.

4.6.2 Critical velocities

The critical velocity is defined as the maximum relative velocity that two sticking particles can have before collision. Such a velocity depends on the ability of the system to dissipate collision energy as shown in Eq. (4.58). Two different models of estimation of critical velocities are here presented:

i) A model for *wet aggregation* here denoted as *Ennis model* (Ennis et al., 1991). In Ennis model a macroscopic liquid layer on the surface of each colliding particle provides the viscous forces necessary to the energy dissipation.

ii) A model for *dry aggregation* here denoted as *Chen mode*l (Chen et al., 2015). The sticking criterion provided in Chen model assumes that energy dissipations are given both by the Van Der Waals adhesion forces interchanged during the contact phase and by viscoelastic forces associated with particle deformation. It is applicable for particles that are not surrounded by any macroscopic liquid water layer.

It is worth noticing that the presence of ice or electrostatic charges on particle surfaces can be treated as a limit case of Chen model, substituting the adhesion forces with those of ice or the resulting ones due to presence of net electrostatic charges. However, in this theoretical framework no dissipation due to the rearrangement or breaking of the ice structure is considered.

4.6.2.1 Critical velocity: wet aggregation

Ennis model (Ennis et al., 1991) is one of the main models currently used in literature for what concerns wet aggregation processes in industrial granulators. In this model, the authors consider the collision between two spherical particles surrounded by a thin liquid layer compared to particles size. The phases of a head-on collision are shown in Figure (4.13). When the water layers of the two particles get in touch, a liquid bridge is quickly formed between the particles. At this point, two forces arise: the *capillary force*, which pulls the particles towards each other, and the *viscous force*, which acts against the motion. The capillary force depends on particles size, liquid-gas surface tension and geometry of the liquid bridge. The viscous force is instead directly proportional to the

fluid viscosity, particles equivalent radius, particles relative velocity and it is inversely proportional to the gap distance between the spheres. As soon as particles surfaces get in contact with relative velocity u_0, they undergo deformation and then they bounce back at a velocity given by $e_0 \cdot u_0$, where e_0 is the dry coefficient of restitution between the particles. While bouncing back, both the capillary force and the viscous force act against the motion. In general, energy dissipation occurs in phase b), c), and d) (see Fig. 4.13). As far as only phases b) and d) are taken into account, the unique contribution to energy dissipation is given by viscous force, which always acts against the motion. In these phases capillary forces are not taken into account because the energy added to the system in the approach phase is equal to the energy dissipated during the rebound phase, provided that the geometry of the liquid bridge is symmetrical in the two phases. The amount of energy dissipated during the contact phase c), described by the coefficient of restitution, depends on particles incoming velocity and on their mechanical properties.

For a perfectly elastic collision ($e_0 = 1$), energy is conserved while particle deforms. In general, however, $e_0 < 1$ due to the viscoelastic behavior of the material. Moreover, for particularly high approach velocities, particles might overcome the elastic limit and undergo plastic deformation, dissipating a much higher amount of energy.

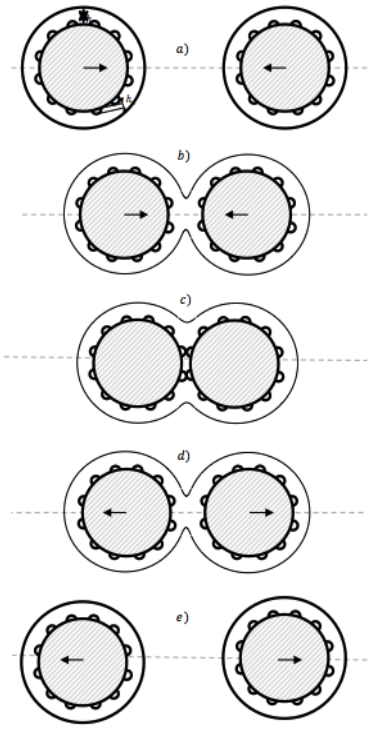

Figure 4.13 Different stages for two approaching particles in Ennis model. a) Approach stage b) Liquid bridge formation: a liquid bridge is formed when the liquid layers are in touch. Capillary forces pull particles towards each other while viscous forces act against the motion. c) Contact and particles deformation. Energy dissipation, mainly due to viscoelastic forces in this phase, is described by the dry coefficient of restitution e_0. d) Liquid bridge separation: particles surfaces detach and they move away from each other. The liquid bridge is still present. Both capillary and viscous forces act against the motion. e) Moving away stage: particles continue to move away from each other, after breakage of the liquid bridge.

The viscous force must be expressed explicitly in order to derive a condition on the critical velocity U_{crit}. For two colliding spheres of radius r, if we define μ_l the fluid viscosity, γ the fluid interfacial tension, U the incoming velocity of each object, and h_0 the half-distance of the spheres, the viscous force is expressed as:

$$F_{vis} = \frac{3}{4}\frac{\mu_l U}{\gamma}\frac{r}{h_0} \tag{4.61}$$

Ennis derives a sticking criterion for the force balance. According to this criterion, particles will stick if the collision Stokes number St_v is lower than the critical Stokes number St_{cr}. The two quantities are defined as follows:

$$St_v = \frac{8\,\rho\,R_{eq}\,U_r}{9\,\mu} \tag{4.62}$$

$$St_{cr} = \left(1 + \frac{1}{e_0}\right) ln\left(\frac{h}{h_a}\right) \tag{4.63}$$

where ρ_0 is the granule density, $R_{eq} = \frac{r_1 r_2}{r_1 + r_2}$ the effective radius, U_r the relative velocity of particles along their radial direction, e_0 the restitution coefficient for dry particles (set constant $e_0 = 0.7$), h the thickness of the liquid layer, and h_a the characteristic height of surface asperities. The final value of the critical velocity is:

$$U_{crit} = \frac{9}{4} \frac{\mu}{\rho_0 R_{eq}} \left(1 + \frac{1}{e_0}\right) ln\left(\frac{h}{h_a}\right) \tag{4.64}$$

In Fig. (4.14), the critical velocity U_{crit} is plotted as a function of particle sizes r_1 and r_2, for a density of 2500 $\frac{kg}{m^3}$ ambient temperature of 25 C and a relative humidity (RH) of 95%. The surface asperities of each particle are set to 1 nm. At a RH = 95% the expected layer thickness is of $\approx 10\ nm$ (see later in this section). Fig. 4.14 shows that reducing the size of one of the two colliding objects the critical velocity increases significantly. In other words small particles are easier to stick, since they are characterised by higher values of critical velocities. For example, when a 5 μm particle collides with objects of decreasing dimensions, its critical velocity passes from 1 m/s when the size of the second particle is 1000 μm up to 1.5 m/s when the size is 10 μm. It is worth noticing that all the curves of Fig. (4.14) are characterized by a plateau that increases only when the sizes of the colliding objects are comparable. The presence of a plateau region indicates that the smallest size involved in a collision determines the value of the critical velocity, regardless the size of the largest object.

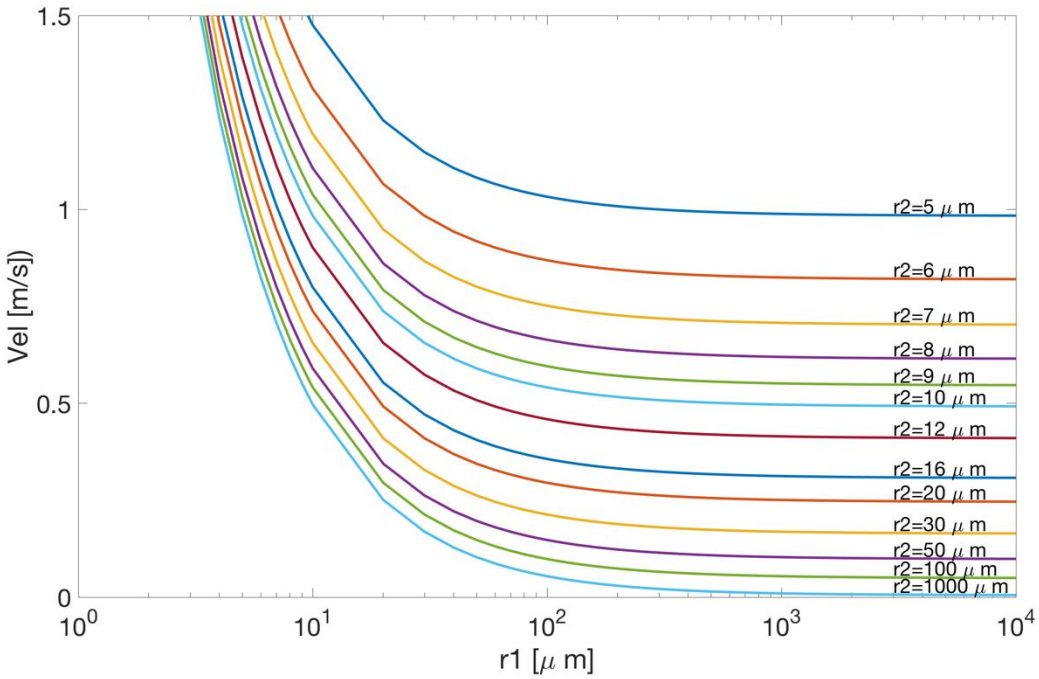

Figure 4.14 Critical velocities for colliding objects of sizes r1 and r2 applying Ennis model for wet aggregation in case of layer thickness of 10 nm and surface asperities of 1 nm (95% RH). The nature of the water layer taken into account in this plot is due to the effect of hygroscopy.

4.6.2.2 Critical velocity: dry aggregation

Chen model (Chen et al., 2015) is based on a set of simulations of collisions between viscoelastic adhesive particles using the Discrete Element Method (DEM). Three different forces are assumed to be acting on the objects: the *adhesive force*, the *elastic force* and the *viscoelastic force*. The results of their simulations have been examined a posteriori in order to provide a final recipe for the sticking of adhesive viscoelastic particles. According to the JKR model for the adhesion force (Johnson et al. 1971) the force F_C that is needed to pull apart two adhesive spheres in contact is:

$$F_C = 3\pi\gamma R_{eq} \tag{4.65}$$

Where γ is the surface tension of the material. If we consider for example two silica spheres with radius $r_1 = r_2 = 20\ \mu m$ and $\gamma = 15 \cdot 10^{-3}\frac{J}{m^2}$, we find that $F_C = 1.4 * 10^{-6}\ N$.

However in Chen model the adhesive and elastic forces are combined into a unique term that modifies F_C as follows:

$$F_{ad+el} = \left(4\left(\frac{a}{a_0}\right)^3 - 4\left(\frac{a}{a_0}\right)^{\frac{3}{2}}\right)F_c \tag{4.66}$$

Where a indicates the radius of the contact circle generated between the surfaces of two particles during the collision i.e. variable during the process. a_0 denotes the radius of the contact circle at equilibrium, when the adhesive force (attractive) is counterbalanced by the elastic force (repulsive). This quantity is not variable and it can be expressed as:

$$a_0 = \left(\frac{9\pi\gamma {R_{eq}}^2}{E_{eq}}\right)^{\frac{1}{3}} \tag{4.67}$$

a_0 uniquely depends on the equivalent radius R_{eq}, the surface tension γ and the equivalent Young modulus $E_{eq} = \frac{E_1 E_2}{E_1 + E_2}$. The total contribution of the adhesive and the elastic forces varies with the contact radius a. Therefore, it continuously changes during the collision. For two silica spheres with radius $r_1 = r_2 = 20\ \mu m$, $\gamma = 15 \cdot 10^{-3}\ \frac{J}{m^2}$, $E = 2 \cdot 10^{-8} Pa$, we find $a_0 = 7.5 * 10^{-7} m$, which is 7.5% of the particle radius. In case of a contact radius 10 times greater than the equilibrium radius ($a = 10\ a_0$) the order of magnitude of the force is $F_{(ad+el)} = 3873 F_C = 5.4 \cdot 10^{-3} N$.

The viscoelastic force is assumed to be proportional to the velocity of deformation, which is internally computed by the DEM method:

$$F_{vis} = \eta_{vis} \frac{d\delta_N}{dt} \tag{4.68}$$

Where η_{vis} is the normal dissipation coefficient $[N\ s]$, defined in literature (Tsuji et al., 1992) and δ_N $[m]$ is the deformation of particles surface. Once that the forces are defined, Chen et al. (2015) solve the equation of motion for two colliding objects using a DEM technique. For sake of clarity the complete procedure is summarized in appendix (D.5), together with a discussion on the role of the forces not taken into account by the model (electrical and aerodynamic forces).

Here we simply report the final expression for the critical velocity expressed as a function of the size ratio Λ_r and the critical velocity for head-on collisions U_{crit0} (see appendix D.5):

$$U_{crit} = \frac{1 + \Lambda_r^3}{(1 + \Lambda_r^2) \cdot \Lambda_r} \cdot U_{crit0} \tag{4.69}$$

In figure (Fig. 4.15), the procedure of Chen for critical velocity is computed for silica particles of several sizes. Comparing Fig. (4.15) with figure Fig. 4.14 it emerges how typical values for critical velocities due to dry sticking are much lower than wet aggregation, even in presence of a nanometric layer due to hygroscopy.

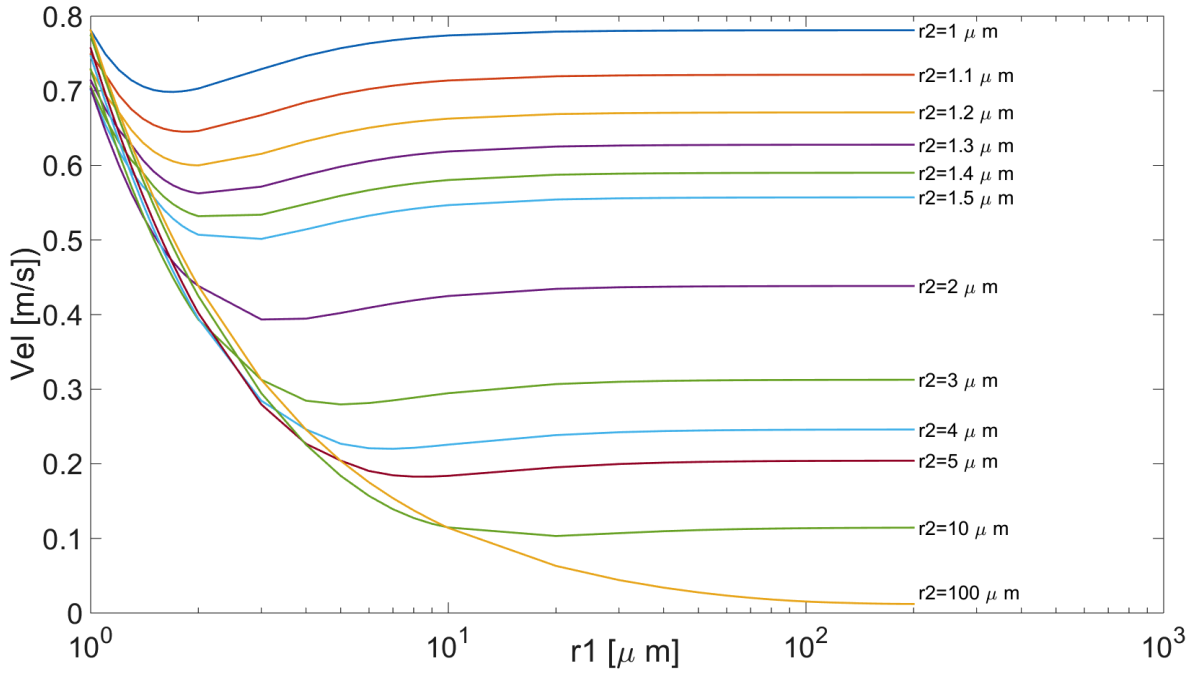

Figure 4.15 Critical velocities for colliding objects of sizes r1 and r2 applying the Chen model for dry aggregation of silica particles.

4.6.2.3 Critical velocities in a volcanic plume

Two models have been presented in the previous sections in order to evaluate the critical velocities for wet and dry environments. However the application of these methodologies in a volcanic plume still needs to be clarified. In particular in this section we will define under which conditions a given model should be considered as dominant in the eruptive column and how it can be practically implemented. Ennis model takes

into account the presence of a liquid layer on particle surfaces. This is the leading mechanism of energy dissipation if compared with dry critical velocities. Despite its importance a micrometer-size water layer is possible only when supersaturated vapour is present, or an environment with water droplets has been formed in the past from a previous state of supersaturation (here we ignore the liquid water entrained from the atmosphere). However, Fig. (4.14) shows that also a nanometric water film in an undersaturated environment can significantly increase the critical velocities. This kind of layer is a result of the hygroscopic properties of ash, not of the moisture saturation. It is of a primary role in volcanic plumes, since the external environmental conditions where it is applicable are more easily verified. From these considerations it is evident how the prediction of the presence of a water layer and its quantification is crucial to constrain the critical velocities of particles in a volcanic plume and ultimately their sticking efficiencies. Four different cases are considered in the present work:

Case I: $T_b \in [273\ °K;\ 373\ °K]$ and $RH < 100\%$

In this regime the water vapour in the volcanic gas mixture is absorbed by the hygroscopic behaviour of ash. The water layer for unsaturated conditions can be computed using the so-called Frankel-Halsey-Hill model (FHH) (Kumar et al., 2009). In the FHH model the surface coverage S_c, which quantifies the hygroscopic growth, is given by:

$$S_c = \left(-\frac{A_{FHH}}{\ln(RH)}\right)^{\frac{1}{B_{FHH}}} \tag{4.70}$$

Where A_{FHH} and B_{FHH} are experimental parameters. The surface coverage S_c is expressed as a function of the final diameter D, the initial diameter of the dry particle D_d and the diameter of a water molecule $d_{mol} = 0.275 \cdot 10^{-9}$:

$$S_c = \frac{d_w - d_d}{2d_{mol}} \tag{4.71}$$

The system of equations Eq. (4.70) and Eq. (4.71) can be solved for the unknown value d_w, once that A_{FHH} and B_{FHH} are known. Lathem et al. (2011) quantify the range of values for A_{FHH} and B_{FHH} in case of different samples of volcanic ash as: $A_{FHH} = 2.41\ \pm$

0.93 and $B_{FHH} = 1.31 \pm 0.12$. In this work we assume that all the water adsorbed by the objects remains as a liquid phase on their surface. This is of course an upper limit for their sticking capacity. However the presence of absorbed water inside an object does not exclude an alteration of its mechanical properties, with an increase of its dissipation capacity. As a matter of fact, water can act from the interior increasing the final diameter of the object and enhancing its elasticity and consequently its viscoelastic dissipation. This is less true for porous objects as correctly outlined in (Textor and Ernst, 2004). Finally, we can express the maximum theoretical water layer on the surface of a particle due to hygroscopy, as a function of the relative humidity:

$$h = \frac{d_w - d_d}{2} = d_{mol} \cdot S_c(RH) \tag{4.72}$$

The layer thickness h is computed at each s-step in the column and it is substituted in Eq. 4.64

Case II: $T_b \in [\,273\ °K;\ 373\ °K]$ and $RH = 100\%$

Plume model equations (Eq. 4.17-4.25) assume an instantaneous condensation of water vapour in the gas mixture for supersaturated values of the relative humidity in a volcanic column. This assumption is justified on the base of the enormous amount of condensation nuclei available during a volcanic eruption (Glaze et al., 1997). By definition no supersaturation is present and thus no liquid water is deposited on the surface of particles by condensation. However the instantaneous creation of liquid water in the gas mixture produces a population of droplets that can collide with volcanic ash and produce a macroscopic liquid layer on their surfaces. We will consider droplet collision as the unique process responsible for the formation of a micrometer water film. Under the assumption that every collision results in a successful sticking and that the droplet sizes is much smaller than the size of ash, the growth rate of liquid water on the surface of a particle is (Pruppacher et al., 1997):

$$\frac{dm}{dt} = A \cdot U_r \cdot \rho_b \cdot q_m \cdot C \tag{4.73}$$

Where A is the cross sectional area of the ash, V_r is the relative velocity between particle and water droplets; ρ_b the bulk density of the mixture; q_m the mass of water present in the gas ($\frac{g}{kg}$), and C the collection efficiency. Water droplets are considered as completely coupled with the turbulent eddies. This is practically obtained assigning in Eq. (4.42) a fictitious size of 0.5 μm to water droplets in order to have a Stokes number $\ll 1$. The quantity q_m is available from meteorological data. After some algebraic manipulation, the growth rate for droplet collision of the external diameter D can be expressed in its final form as a function of the plume curvilinear coordinate s:

$$\frac{d\,(d_w)}{ds} = \frac{1}{U_p(s)} \cdot \frac{U_r(s) \cdot \rho_b(s) \cdot q_m(s) \cdot C}{2\rho_l} \tag{4.74}$$

Where ρ_l is the liquid water density and $d_w(s = 0) = d_d$.

Case III: $T_b < 273\ °K$

In this work we assume that all the liquid water around volcanic particles freezes instantaneously when temperature is lower than 273 $°K$. Any supercooled state of water is assumed, according to the hypothesis of large amount of condensation nuclei in a volcanic plume. No water layer is present in this region, only ice. The ice thickness in our model does not play an effective role in dissipation, i.e. neither viscoelastic mechanisms nor a rearranging of the structure are considered. Moreover its contribution to the total mass of the object is considered negligible. Under these assumptions no difference occurs between a frozen layer generated by hygroscopy or droplets collision. The role of ice on the sticking of volcanic ash is described using Chen model for dry particles with a surface tension equal to ice: $\gamma_{ice} = 0.065\,\frac{J}{m^2}$ (Ketcham and Hobbs, 1969).

Case IV: $T_b > 373\ °K$

For temperatures higher than 373 $°K$, no liquid water is assumed to be present around volcanic particles. In this case the critical velocities are evaluated applying Chen model with a surface tension typical of silica: $\gamma_{sil} = 0.38\,\frac{J}{m^2}$ (Wall et al., 1990).

4.6.3 Quantification of the sticking efficiencies

The quantification of the sticking efficiency α_{ij} of a collision of two particles i and j derives directly from the concepts expressed in the previous sections. In particular, once the relative velocity U_r and critical velocity U_{crit} are known, the comparison of these two quantities provides an idea of the result of a collision. As a rule of thumb, if the critical velocity is much higher than the relative velocity the outcome is a sticking process. It means that the relative kinetic energy of the impact can be dissipated by the mechanisms acting within the two objects. However several possible criteria can be introduced to formalize the outcome of a collision. Here we discuss the two chosen in this work.

- *Net threshold*: in this approach both the critical and the relative velocities are considered as single values. Critical velocities are computed as in Eq. (4.42), depending to the environmental conditions in the plume. Relative velocities in a turbulent flow are associated with their mean value $\langle|U_r|\rangle$. In case of a dominant contribute from the sedimentation kernel, the relative velocity is simply given by the absolute value of terminal velocities or their difference as described in section (4.4.3). The sticking efficiency α is determined as follows:

$$\begin{cases} \alpha_{ij} = 0 & if\ (\langle|U_r|\rangle\ or\ U_s) \geq U_{crit} \\ \alpha_{ij} = 1 & if\ (\langle|U_r|\rangle\ or\ U_s) < U_{crit} \end{cases} \tag{4.75}$$

- *Smoothed threshold*: the underlying assumption in this methodology is that relative velocities in a turbulent flow are characterised with a distribution of values, more than a single one. The distribution function $q(|U_r|)$ introduced in section (4.5.1) describes this statistical behaviour. Critical velocity is still represented with a unique value. The part of the distribution function with relative velocities greater than U_{crit} will describe particles too fast to aggregate. Therefore the sticking efficiency is given by the integral of $q(|U_r|)$ comprised between zero and the critical velocity (the distribution $q(|U_r|)$ is normalized to one).

$$\alpha_{ij} = \int_0^{U_{crit}} q(|U_r|)\, d|U_r| \tag{4.76}$$

It is important to notice that this methodology does not apply to the relative velocities associated with the sedimentation kernel, that are unique by definition.

An example of application of the net threshold criterion is reported Fig 4.16. Critical velocity and sticking velocity are plotted for different heights and several collector sizes, colliding with a fixed sized particle of 5 μm. Only the hygroscopic layer is present in this eruption. The "Z" shaped curve represents the collision velocities, and the "bow-shaped" curve the critical velocity. When the two curves intersect each other, the sticking efficiency is considered equal to one. It is clearly evident how the relative velocities created in the lower part of the plume by the turbulent column are too high to be dissipated by the nanometric water layer.

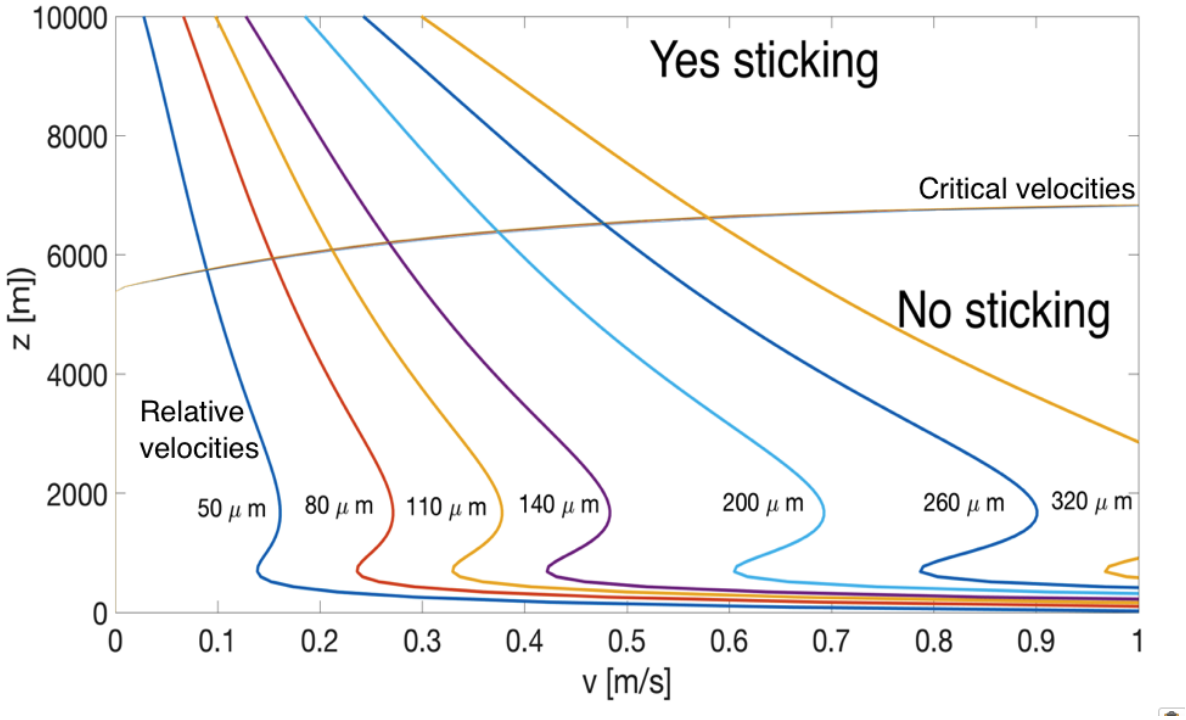

Figure 4.16 Study of the sticking efficiency due to the presence of a nanometric hygroscopic layer on the surface of volcanic ash. The plot is relative to the collision of objects of different sizes with particles of 5 μm. Both critical and relative velocities are displayed as a function of the plume height z [m]. When the relative velocities (*"Z" shaped* curves) are lower than the critical velocities (single horizontal line), particles stick together, according to the net criterion defined above.

4.7 Discussion on the methodology and conclusions

Existing theoretical models for ash aggregation in volcanic plumes are affected by significant limitations that derive both from the simplified scenario assumed in the one-dimensional Smoluchowski equations and the approximations required in order to increase the computational efficiency. Unfortunately, field observations suggest that ash aggregates are complex structures that cannot be adequately treated either as liquid droplets (i.e. as a coagulation problem) or as fractal objects. The method proposed in this chapter provides a complete set of equations and new methodologies to fully solve these limitations. The use of a multidimensional description of the problem (i.e. the GFPT) combined with existing steady state plume models, avoids the implicit ambiguity of the one-dimensional Smoluchowski equation in distinguishing porous and non-porous structures. However, the increased level of complexity requires an explicit relationship between interacting properties. A simplified algorithm has been created in order to investigate the resulting porosities of different virtual objects. Starting from the creation of coated particles, the algorithm has been extended to the interaction of two aggregates. In addition, the definition of an overall aggregate volume, i.e. the ellipsoidal fit to the external points, allows computing porosities and relating colliding and final structures. The final outcome of this stage of the work has been the realization of 30,000 Montecarlo simulations. This large dataset provided a robust number of points to be fitted. A polynomial of order three and five in the independent variables *porosity ratio* and *mass ratio* has been derived in order to provide to the aggregation equations the missing information on the final porosities of the aggregates. This pioneering approach should be considered as a first step in a new methodology for the study of ash aggregation. Several limitations are still present at this stage. The most important one concerns the non-physically based composition of the aggregates, that limits the available number of structures and that ultimately results in an overestimation of the porosities. Despite its simplicity, Fig. (4.7) shows interesting features of ash aggregation that can probably be extended to more complex algorithms and virtual structures.

The research of a rigorous definition of collisional processes in a volcanic environment has been one of the main goals of this work. Eruptive plumes show extreme conditions and the use of standard approaches developed for meteorological sciences can lead to a biased overview. A large part of section 4 has been dedicated to the rigorous definition

of collision kernels in a volcanic plume. The main aspect is the introduction of a new mechanism for collisions in a turbulent cloud that has been named the *turbulent differential coupling*. In this process, particles of different size and density react differently to the surrounding cascade of turbulent eddies. This results in a quantification of a key aspect of collision, which in past works, e.g. (Costa et al., 2010; Textor et al., 2006; Veitch and Woods, 2001), was not adequately constrained: the relative velocity between a generic pair of particles. The relative velocity is expressed as a fraction of the largest scale turbulent fluctuation. Moreover, the computation of relative velocities in a collision allows having a new parameterization of the sticking efficiency. In the present work the sticking efficiency is calculated in terms of the maximum kinetic energy that a system can dissipate. The dissipation is phenomenon-dependent, but it can always be defined in terms of a critical velocity. The critical velocity represents the maximum kinetic energy that a dissipative mechanism can deplete. Two main dissipation mechanisms have been considered: wet sticking, where the dissipation is given by the action of a water layer on the surface of the particles; dry sticking, where the dissipation is given by the adhesive-viscous forces present on the objects. Specific equations for both these two cases are provided in this chapter and solved simultaneously in the plume model, as the growth layer rate of Eq. (4.74).

The final methodology results in a combination of advanced mathematical tools and an exhaustive physical explanation of the collisional interactions in a volcanic plume. The expected improvements respect to existing models are: i) A more realistic description of the nature of ash aggregation. As a matter of fact, the fractal approximation cannot be used in this context. Moreover, the a priori assumption of a unique size for ash aggregates (Cornell et al., 1983; Costa et al., 2010) is a compromise for increasing the computational efficiency of the simulations, but it is substantially far from field observations. The use of a bidimensional description of the problem implicitly resolve these limitations, since the initial population of particles has different porosities respect to aggregates; ii) Volcanic plumes are mostly turbulent (Kieffer and Sturtevant, 1984) and they require ad hoc equations in order to adequately take into account the collision rate. Any derivation of collision kernels from scientific fields where different phenomena are important, results in a biased view of the problem. Concepts as Brownian diffusion and Saffman-Turner limit seems to not be important in volcanic ash aggregation (Textor and Ernst, 2004). The collision kernels presented in this chapter are

derived from contexts where highly turbulent environments dominate the dynamics of the collisions. Moreover the introduced definitions of relative velocities between particles in a volcanic plume is completely new and it expected to provide a more realistic constrain on the relative kinetic energies of a collision; iii) The available information on the relative kinetic energy provides an important quantification of the energy that must be dissipated in a collision in order to provoke a sticking process. Previous approaches assumed a biased quantification of the relative velocities involved in an impact. This resulted in a inaccurate prediction of the phenomenon. iv) The two dissipation mechanisms considered in this chapter (i.e. wet and dry sticking) are rigorously coupled with the thermodynamic state of the plume. A new important aspect is that a set of ODEs governs the growth rate of the water layer. The combination of the relative velocities of a collision and the exact quantification of the dissipation mechanisms allows constraining the sticking efficiency with a degree of accuracy not explored in the past.

However, the numerical combination of the aggregation scheme, plume equations and wet/dry sticking is the most challenging part that and it still requires further improvements. In particular, three main problems still need to be fully solved: the stiffness and the discontinuities of the resulting ODEs, and the computational efficiency of the code. The first two aspects are somehow related and they depend on the nature of aggregation. Aggregation of large amount of particles result in fast timescales that can be completely different from the advection processes of the plume. The presence of different timescales in the phenomenon under analysis results in stiff equations. The second aspect depends on the definition of sticking efficiency α for different couples of particles. The presence of net transitions between regions where $\alpha = 0$, into regions where $\alpha = 1$, generates huge problems to the standard ODE solvers. These aspects require both smooth transitions in the quantities within the eruptive column and different numerical techniques in the solvers. For what concerns the computation efficiency of the whole software package, we found that with 300 cells on the plane mass-porosity the time needed for the simulation of Fig. (4.9) is less than half a minute. However, the use of constant aggregation kernels avoids all the problems highlighted about stiffness and discontinuities, which seem to pose the largest constrain on the efficiency of the scheme. Test simulations with more complex kernels show a computation time of the order of ten minutes. Moreover, if higher accuracy is required in

detecting porosities, the number of cells can increase rapidly, reducing the performances.

In conclusion, a new methodology has been presented for the study of ash aggregation in volcanic plumes that poses its attention on the complexity of aggregate structures. In particular, the sedimentation in atmosphere is enormously influenced by their density. Ash aggregates thus require a more complex description to be fully characterized. The new numerical scheme uses a bidimensional solution of the GFPT in order to track the evolution of a population of particles in a volcanic plume according to their mass and porosity. A particular attention has been posed in rigorously quantifying the main processes that define a collision and a sticking process in a volcanic plume. This methodology wants to be the first stage of a new class of models and a new perspective on the potentialities of combining virtual reality, field observation and laboratory observations. The concepts formalized in this chapter will form the theoretical basis for future and challenging studies on ash aggregation.

4.8 Acknowledgements

The research leading to these results has received funding from the European Union Seventh Framework Programme (FP7/2007-2013) under the project NEMOH, grant agreement n° 289976. The authors would like to thank G. Bagheri for his precious help.

4.9 Author's contribution

E. Rossi contributed to the complete formalization of the theoretical framework and the codes that perform the computations contained in this chapter. The author partially contributed to the section on the sticking efficiency.

Appendix

D.1 Algorithm for creation of virtual aggregates

The algorithm created for the determination of aggregates porosities is based on a simple geometrical relationship between a central sphere of diameter D and its coating shell composed of smaller spheres of diameter d_0. All shells added to the aggregate are formed of particles of the same size. Before starting a new shell, the previous one must be completed, i.e. when no residual space is available for an additional sphere. Referring to Fig. (D1), the main steps followed by the program are:

1. Definition of a spherical system of coordinates centered at the origin $(x_0 = 0, y_0 = 0, z_0 = 0)$. We identify the polar angle as ϕ and the azimuthal angle as θ.
2. Definition of the number of shells.
3. Definition of the sizes of particles per each shell.
4. Generation of a sphere with diameter D_c and centre $P_c = (x_0, y_0, z_0)$. We refer to this particle as *central sphere* or *core*.
5. Generation of spheres within a single shell. Each sphere of the coating is attributed to a combination of angles (ϕ_i, θ_i) and angle extensions $(\Delta\phi, \Delta\theta)$. The first sphere is located at a random position along the northern axis of the core $(\phi_{last} = 0, \theta_{last} = \theta_{rand})$ at a distance from $L = \frac{D_c}{2} + \frac{d_0}{2}$ from P_c (see fig. D1).
6. Collocation of the next sphere at $(\phi_{next} = \phi_{last}, \theta_{next} = \theta_{last} + \Delta\theta)$, with $\Delta\theta$ expressed as a function of the polar angle:

$$\begin{cases} \Delta\theta = 2\,\mathrm{asin}\left(\dfrac{d_0}{(d_0 + D_c)\ \cdot\ \sin(\phi)}\right) & \textbf{if} \quad \phi > \mathrm{asin}\left(\dfrac{d_0}{d_0 + D_c}\right) \\ \Delta\theta = 2\,\mathrm{atan}\left(\dfrac{d_0}{(d_0 + D_c)\ \cdot\ \sin(\phi)}\right) & \textbf{if} \quad \phi \le \mathrm{asin}\left(\dfrac{d_0}{d_0 + D_c}\right) \end{cases} \tag{D.1}$$

7. Update the azimuthal angle $\theta_{last} = \theta_{next}$.
8. Repetition of step 6 n_1 times, until the condition $\Delta\theta\ \cdot \sum_{i=1}^{n_1} i = 2\pi$ is reached.

9. The ring is completed. Step number 5 is repeated, locating the first sphere of the new ring at ($\phi_{last} = \phi_1 + \Delta\phi, \theta_{last} = \theta_{rand}$), where:

$$\Delta\phi = 2\,\mathrm{asin}\left(\frac{d_0}{d_0 + D_c}\right) \tag{D.2}$$

   Check if $\phi_{last} < \pi$.

10. If $\phi_{last} > \pi$, the construction of the shell is completed and $D_c = 2L$.
11. Repeat steps 5 to 9, if more shells are still present.
12. Locate the most external points of the virtual aggregate.
13. Fit the most external points using a generic ellipsoid surface (using a specific Matlab function made available on the Matlab utility site. This function has been created by Yury Petrov, 2015).

In case of a collision of two aggregates with external diameters D_{c1} and D_{c2}, the previous steps are repeated for a second object with centre situated at $P_{c2} = (x_0 + \frac{D_{c1}}{2} + \frac{D_{c2}}{2}, y_0, z_0)$, as shown in figure (D1). This algorithm represents a first attempt to study ash porosity using virtual reality. It is clear how the simplicity of the scheme only captures the main features of the process. Further improvements are needed to make the code more general. However despite its approximations, this procedure has been successfully applied in paragraph (4.3.2). The initial conditions used for the 30.000 simulations are here summarized:

- Initial values of D_{c1} and D_{c2} are randomly picked within the interval: $[10, 300]$
- The number of shells n_s is randomly chosen, picking a single integer i number within the interval: $[1, 7]$. An additional Boolean random factor is introduced at this stage to increase the number of combinations analysed. A true or false random parameter establishes if the shell will be unique and composed of particles of size D_c/i or multiple and composed of i layers of particles sizes: $[\frac{D_c}{1}, \frac{D_c}{2}, \dots, \frac{D_c}{i}]$.

It is important to notice that the dimensionality of the spheres is not needed, since the virtual spheres are defined as a ratio between central sphere and coating. For simplicity we assume all the sizes in micrometers.

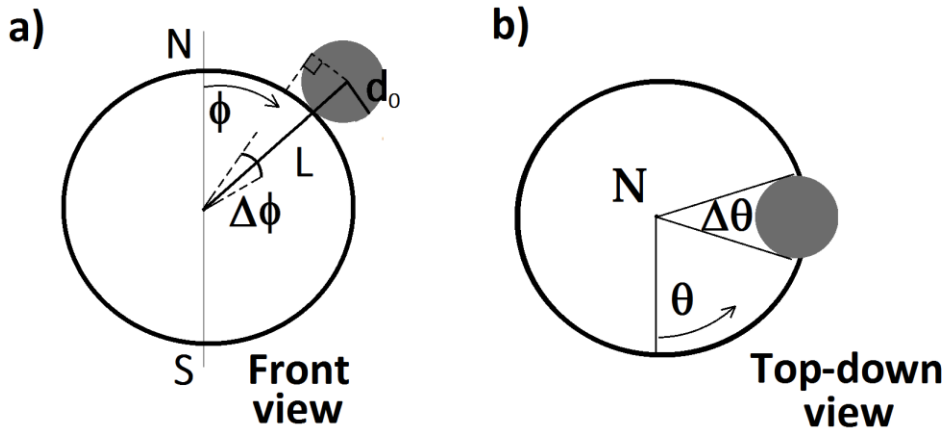

Figure D1 Scheme of the frontal view (a) and top-view (b) of a coating particle (dark grey) added to the central sphere.

D.2 General definitions for turbulence

According to Kolmogorov, turbulence can be seen as an energy cascade process from the largest eddy to the smallest one, usually named *Kolmogorov length*. Energy is transferred from larger eddies to smaller ones, but the process arrests for smallest scale beyond that viscosity and heat dissipation become dominant and turbulence is dumped. The Kolmogorov length η_{KO} can be parameterised as follows (Marshall and Li, 2014):

$$\eta_{KO} = \left(\frac{\nu^3}{\epsilon}\right)^{1/4} \tag{D.3}$$

Where ν is the kinematic viscosity and ϵ is the dissipation rate of turbulent kinetic energy per unit mass. The parameter ϵ is controlled by the large-scale flow. If the largest eddy size is denoted with L and the velocity fluctuations of the fluid respect to the mean flow with U_g, the dissipation rate of turbulent kinetic energy is (Marshall and Li, 2014):

$$\epsilon = C_1 \frac{U_g^3}{L} \tag{D.4}$$

Where the constant C_1 is of the order of unity. We refer to the largest eddy L and its related quantities as the *integral scale* of the turbulent flow. If U_{th} refers to the plume velocity along the central, we assume of $U_g \approx 0.1 \cdot U_{th}$, according to Kotsovinos (1977); Papanicolaou and List (1988). This assumption is necessary to introduce the effects of turbulence inside the 1D steady state plume model. The Reynolds number based on the largest scale of the turbulent flow is defined as:

$$Re = \frac{L U_g}{\nu} \tag{D.5}$$

For a volcanic plume this definition of the Reynolds number gives values in agreement with Kieffer and Sturtevant (1984) and it allows relating the Kolmogorov micro-scale η_{KO} and Kolmogorov time-scale τ_{KO} to the integral scale of the turbulence (Ormel and Cuzzi, 2007; Textor and Ernst, 2004):

$$\eta_{KO} = Re^{-3/4}\, L \tag{D.6}$$

$$\tau_{KO} = Re^{-1/2}\, \tau_L \tag{D.7}$$

Where $\tau_L = \frac{L}{U_0}$ is the overturn time of the largest eddy. A quantity that will play a major role is the spatial frequency k associated with a generic eddy of size l. It is defined as the reciprocal of the size of the vortex $k = \frac{1}{l}$. Particle will not follow instantaneously the fluid motion due to its inertia. It requires a certain amount of time to follow the changes in the external fluid. The relaxation time, τ_p, describes the capability of an object to adapt to changes in the surrounding fluid. Under the assumption of a Stokes regime it is defined as:

$$\tau_p = \frac{\rho_p\, d_p^2}{18\, \nu\, \rho_f} \tag{D.8}$$

The turbulent Stokes number St_{Tl} describes the degree of coupling between a generic eddy of size l and particles. It is commonly parameterized relatively to the relaxation time of the particle τ_p. High values of St_{Tl} indicate that the influence of eddies on ash is negligible. As a matter of fact, in the extreme case where $St_{Tl} \approx \infty$ no eddy is seen by the object. Vice versa, in the limit $St_{Tl} \approx 0$, particles will follow perfectly the trajectory of

the eddy. However, St_{Tl} is not uniquely defined in a vigorous turbulent flow since many eddy sizes are present. In general, for an eddy with size l and velocity u_l, the turbulent Stokes number is:

$$St_{Tl} = \tau_p \frac{u_l}{l} \tag{D.9}$$

It can be derived that $St_{Tl} \sim l^{-2/3}$, which means that large eddies have smaller turbulent Stokes numbers for a fixed particle size (Marshall and Li, 2014). Or alternatively that the coupling of a particle with the turbulent flow increases as the size of the eddy increases. In particular two Stokes numbers are of great importance in defining the effect of turbulence on particles. The Stokes number associated with the Kolmogorov scale, St_{TK}, and the Stokes number St_{TL} associated with the integral scale:

$$St_{TKO} = \frac{\tau_p}{\tau_{KO}} = \frac{\rho_p \, d_p^2}{18 \, \nu \, \rho_f} \frac{Re^{1/2}}{\tau_L} \tag{D.10}$$

$$St_{TL} = \frac{\tau_p}{\tau_L} \tag{D.11}$$

D.3 Root mean square relative velocity between two particles in a turbulent flow

In the research of a closed expression for relative velocities between particles it is of primary importance to clarify the meaning of the quantities that we will derive. In this context *velocity* have a meaning root-mean-square values. The root mean square particle velocity is defined as:

$$U_{p\_rms} = \langle {U_p}^2 \rangle^{1/2} = \langle \delta \boldsymbol{u}^2 \rangle^{1/2} = \langle (\boldsymbol{u} - \langle \boldsymbol{u} \rangle)^2 \rangle^{1/2} \tag{D.12}$$

The root mean square relative value of the absolute velocity between two grains is:

$$\langle U_m^2 \rangle^{1/2} = \langle (\Delta_{12} \delta \boldsymbol{u})^2 \rangle^{1/2} = \langle (\boldsymbol{u_2} - \boldsymbol{u_1} + \langle \boldsymbol{u_1} \rangle - \langle \boldsymbol{u_2} \rangle)^2 \rangle^{1/2} \tag{D.13}$$

In this appendix we introduce in some detail the methodology developed by Ormel and Cuzzi (2007) to calculate the relative velocities between two particles of sizes greater than the Kolmogorov scale in a turbulent flow. Three main assumptions are present in the model:

- Turbulent flow can be seen as a cascade of vortexes from the largest scale to smallest.
- The energy spectrum of the flow follows a Kolmogorov scaling.
- The correlation between particles depends uniquely on the ratio of their sizes respect to the scales of the vortexes.

The third assumption has significant implications on the accuracy of the predictions that will be discussed later. According to Kolmogorov's theory of turbulence, the energy spectrum depends on the spatial frequency k of eddies as $E(k) \propto k^{-5/3}$. The total energy per unit mass associated with the turbulent velocity U_g is given by:

$$\frac{U_g^2}{2} = \int_{k_L}^{k_\eta} dk \; E(k) \tag{D.14}$$

The next step of the methodology is to evaluate the velocity of a particle of size d_p respect to the turbulent flow. Volk et al. (1980) introduced the concept of "eddy classes". Class I eddies vary slowly enough to give time to the particle to adapt to it. Particles will forget their initial conditions and will adapt to the eddy. Class II eddies fluctuate faster than the relaxation time of the particle τ_p. Thus, only a small perturbation of the initial conditions of the grain is obtained. These concepts are formalized as follows. A specific eddy, with an associated wavenumber k, is characterized by a proper velocity U_k and overturn time $\tau_k = \frac{1}{k\, U_k}$. The eddy crossing timescale is $\tau_{cross} = l/U_{vg}$, where U_{vg} is the relative velocity between a grain and a single vortex. Therefore the condition for an eddy to be of class I and class II becomes:

$$\begin{cases} Class\ I\ eddy: \tau_k\ and\ \tau_{cross} \gg \tau_p \\ Class\ II\ eddy: \tau_k\ and\ \tau_{cross} \ll \tau_p \end{cases} \tag{D.15}$$

The boundary between these two classes is associated with a specific k, or τ_k, named respectively k^* and τ^*.

$$\frac{1}{\tau_p} = \frac{1}{\tau^*} + \frac{1}{\tau_{cross}} = \frac{1}{\tau^*} + k^*\, U_{vg}(k^*) \tag{D.16}$$

The important point here is that k^* is a function of the relaxation time τ_p. In other words, the boundary separating the two classes is different for each particle size. The averaged absolute particle velocity is:

$$U_{p\_rms}^2 = \int_{k_L}^{\max(k^*,k_L)} dk\ 2E(k)(1-\Gamma^2) + \int_{\max(k^*,k_L)}^{k_{\eta_{KO}}} dk\ 2E(k)(1-\Gamma)\,[g(\psi) + \Gamma\, \mathrm{h}(\psi) \tag{D.17}$$

Where: $\Gamma = \frac{\tau_p}{\tau_p+\tau_k}$, $\psi = \Gamma\tau_k k U_{rel}(k)$, $g(\psi) = \psi\, tan^{-1}(\psi)$ and $h(\psi) = \frac{1}{1+\psi^2}$. Ormel and Cuzzi assume that $\mathrm{h}(\psi) = \mathrm{g}(\psi) \approx 1$ for all particles sizes with a consequent maximum error on the final results of about the 10%. This is verified also in the present context as discussed later on in this appendix. This approximation allows having an analytical solution of the problem in a closed form and it represents one of the most important advantages of the method. Expression (D.17) can be explained as follows: the velocity of a particle is a result of two different contributions from the turbulent flow. The first integral on the r.h.s. describes the effects of turbulent eddies larger than the particle size d_p. The second integral is instead related to the contribution of eddies smaller than d_p but larger than the Kolmogorov scale η_{KO}. It is worth mentioning that the simpler form of the first integral respect to the second one is due to the absence of relative velocity between large eddies and the particle ($U_{vg}(k) = 0$). Both integrals are weighted comparing the lifetime of a vortex (τ_k) with the relaxation time (τ_p) of the particle. Eddies with lifetimes much shorter than τ_p will not produce a significant influence on the velocity of the particle ($\Gamma \approx 1$). On the contrary, long lasting eddies compared to τ_p tend to transfer all their energy $E(k)$ to the particle ($\Gamma \approx 0$). The eddy lifetime is related to its autocorrelation function as explained by Volk et al. (1980). Equation (D.17) finally provides the velocity of the particle respect to the turbulent velocity U_g as a function of the Reynolds number Re and the particle Stokes number St_{TL} associated with the largest eddy.

$$U_{p\_rms}^2 = \int_{k_L}^{k_\eta} dk\ 2E(k)(1-\Gamma^2) = {U_g}^2 \left(1 - \frac{{St_{TL}}^2 \left(1 - \mathrm{Re}^{-\frac{1}{2}}\right)}{(St_{TL}+1)\left(St_{TL} + \mathrm{Re}^{-\frac{1}{2}}\right)} \right) \tag{D.18}$$

It is important to realize that for highly turbulent flows and large particles $U_p \approx U_g/\sqrt{1+St_{TL}}$. This result coincides with Eq.8 of Abrahamson (1975) and it represents the limit case of relatively uncorrelated with the local fluid field (Marshall and Li, 2014). Once evaluated the relative r.m.s. velocity of a particle respect to the flow, the next step in the derivation is to calculate the relative r.m.s. velocity between two arbitrary particles. This quantity is given by (Markiewicz et al., 1991):

$$\langle U_m^2 \rangle^{1/2} = U_{p1\_rms}^2 + U_{p2\_rms}^2 - 2\,\overline{U_{p1\_rms}\,U_{p2\_rms}} \tag{D.19}$$

The last term $2\,\overline{U_{p1\_rms}\,U_{p2\_rms}}$ is the correlation term between the two particles due to their partial coupling with the turbulent flow. It is worth stressing that this term is zero for the limit case of uncorrelated particles, which coincides with the work of Abrahamson (1975). In this process of derivation we keep the dependency from the spatial wavenumber k. Later on it will be shown that every step can be expressed as a function of the eddy decay time t_k. Markiewicz et al. (1991) expresses the correlation term as:

$$2\,\overline{U_{p1\_rms}\,U_{p2\_rms}} = U_{c1\_rms}^2 + U_{c2\_rms}^2 \tag{D.20}$$

Where:

$$U_{ci\_rms}^2 = \frac{2\tau_i}{\tau_1+\tau_2} \left(\int_{k_L}^{\min(k_1^*,k_2^*)} E(k)\ dk - \int_{k_L}^{\min(k_1^*,k_2^*)} E(k) \left(\frac{1}{1+\tau_k/\tau_i} \right) dk \right) \tag{D.21}$$

Alternatively, the above integrals can be expressed as a function of the time that an eddy needs to decade, τ_k. The two differentials dk and $d\tau_k$ are related using the above relationships between τ_k and k. We obtain:

$$E(k)dk = \frac{1}{2}\,\frac{U_g^2}{\tau_L}\,d\tau_k \tag{D.22}$$

The solution of Eq. (D.21), combined with Eq. (D.19), allows obtaining the final expression for the root mean square relative velocity between two particles:

$$\langle U_m^2 \rangle^{1/2} = \Delta U_I^2 + \Delta U_{II}^2 \tag{D.23}$$

Where the term ΔU_I^2 describes the effect of class I (slow) eddies and the term ΔU_{II}^2 the effect of class II eddies.

$$\begin{aligned} \Delta U_I^2 &= \frac{U_g^2}{\tau_L} \frac{\tau_2 - \tau_1}{\tau_1 + \tau_2} \left[\frac{\tau_1^2}{\tau_1 + \tau_k} \right]_{\tau_k = \tau_{12}^*}^{\tau_k = \tau_L} + (1 \leftrightarrow 2) \\ &= U_g^2 \frac{St_{TL1} - St_{TL2}}{St_{TL1} + St_{TL2}} \left(\frac{St_{TL1}^2}{St_{12}^* + St_{TL1}} - \frac{St_{TL1}^2}{1 + St_{TL1}} - (1 \leftrightarrow 2) \right) \end{aligned} \tag{D.24}$$

$$\begin{aligned} \Delta U_{II}^2 &= \frac{U_g^2}{\tau_L} \left[\tau_k + \frac{\tau_1^2}{\tau_1 + \tau_k} \right]_{\tau_k = \tau_\eta}^{\tau_k = \tau_{12}^*} + (1 \leftrightarrow 2) \\ &= U_g^2 \left(\left(St_{12}^* - Re^{-\frac{1}{2}} \right) + \frac{St_{TL1}^2}{St_{TL1} + St_{12}^*} - \frac{St_{TL1}^2}{St_{TL1} + Re^{-\frac{1}{2}}} + (1 \leftrightarrow 2) \right) \end{aligned} \tag{D.25}$$

Where St_{12}^*, defined as $St_{12}^* = \tau_{12}^*/\tau_L$ and $\tau_{12}^* = \max(\tau_1^*, \tau_2^*)$. τ_1^* and τ_2^* can be calculated solving numerically the following equation for each particle:

$$\frac{2}{3} \frac{\tau^*}{\tau_p} \left(\frac{\tau^*}{\tau_p} - 1 \right)^2 - \frac{\tau_p}{\tau_p + \tau^*} = -\frac{1}{1 + St_{TL}^{-1}} \tag{D.26}$$

The solution of τ_1^* and τ_2^* are known, τ_{12}^* allows having a complete set of equations for $\Delta U_{12\_rms}^2$. This quantity can then be converted into the mean relative radial velocity according to Pan and Padoan (2014):

$$\langle |U_m| \rangle = \left(\frac{2}{3\pi} \right)^{\frac{1}{2}} \langle U_m^2 \rangle^{1/2} \tag{D.27}$$

An additional aspect still requires to be discussed. Ormel and Cuzzi (2007) assume that the approximation $\mathrm{h}(\psi) = \mathrm{g}(\psi) \approx 1$ holds for their problem. Since their model is derived for astrophysical applications, it is worth asking if this assumption is still valid in a volcanic context. We remember here that: $\Gamma = \frac{\tau_p}{\tau_p + \tau_k}$, $\psi = \Gamma \, \tau_k \, k \, V_{rel}(k)$,

$g(\psi) = \psi\, tan^{-1}(\psi)$ and $h(\psi) = \frac{1}{1+\psi^2}$. Assuming characteristic values for volcanic eddies $k \subseteq [1\ m, 1000\ m]$ and fixing the size of some test particles is possible to compare their figure A.1 with our results. In Fig. (D2) an example for function $g(\psi)$is reported (the same results are found for $h(\psi)$). It seems that in a volcanic context the approximation $g(\psi) \approx 1$ holds for larger values of k than in the original work. This justifies even more the use of the assumption $h(\psi) = g(\psi) \approx 1$.

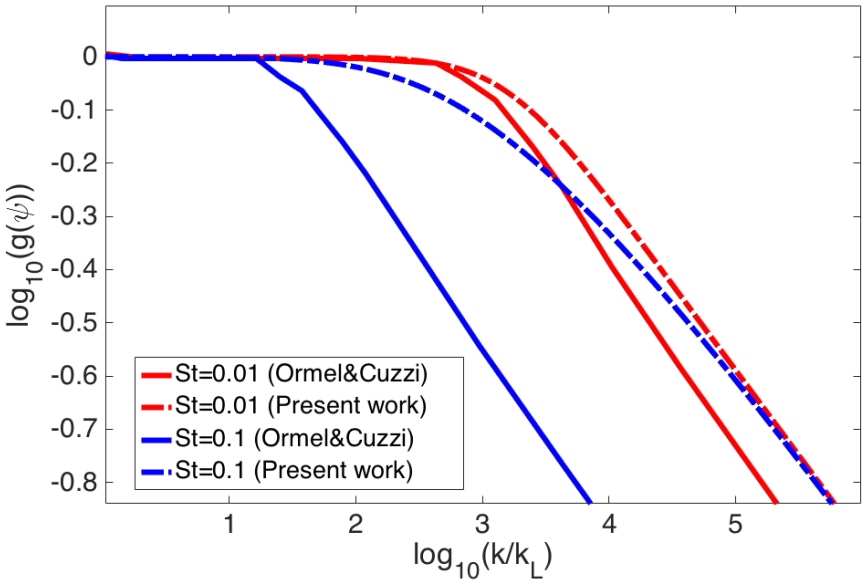

Figure D2 Comparison of function $g(\psi)$ reported in figure A.1 of Ormel et al., 2007 with $g(\psi)$ evaluated in the present work for two Stokes numbers St = 0.01 and St = 0.1 .

D.4 Correction factors for top-hat values

The 1-D steady state plume model presented in this work assumes top-hat profiles for quantities related to the volcanic mixture such as the plume temperature and density. However field observations and experiments suggest that a Gaussian profile would be a more accurate description of the problem. It is worth asking which are the consequences expected if a top-hat profile for particles concentration C_{th} is used instead of a Gaussian C_g. The problem arises since particles concentration appears in Eq. 4.20 as a power of 2, but it is not a priori verified that $C_{th}^2 \stackrel{?}{=} C_g^2$ (Folch et al., 2016). In this appendix we investigate the role of the correction factor ξ_2, defined as $C_{th}^2 = \xi_2\, C_g^2$. For a Gaussian concentration of mass inside a volcanic plume we have:

$$C_g = C_0\, e^{-\frac{r^2}{b^2}} \tag{D.28}$$

The top-hat value of the concentration is related to the Gaussian profile as follows (Davidson, 1986b) in the limit of $R \longrightarrow \infty$:

$$C_{th} = \langle C \rangle = \frac{1}{\pi R^2} \int_0^R 2\pi r\, C_g\, dr \tag{D.29}$$

It is important to notice that the factor 2 in the integral guarantees the consistency of Eq. (D. 29) in case of $C_g = C_{th}$. The solution is:

$$C_{th} = \frac{C_0}{2} \tag{D.30}$$

The value of C_g^2 is instead given by:

$$C_g^2 = \langle C^2 \rangle = \frac{1}{\pi R^2} \int_0^R 2\pi r\, {C_g}^2\, dr \tag{D.31}$$

The solution of Eq. (D.31) is:

$$C_g^2 = \frac{{C_0}^2}{4} \tag{D.32}$$

Comparing C_g^2 with C_{th}^2 we observe that no correction term should be introduced in Eq. (4.20) due to the use of top-hat values.

$$C_g^2 = \xi_2\, C_{th}^2 \rightarrow \frac{{C_0}^2}{4} = \xi_2\, \frac{{C_0}^2}{4} \;\rightarrow\; \xi_2 = 1 \tag{D.33}$$

It is interesting to notice that the equivalence of the Gaussian and top-hat profiles is not general and it disappears for exponents greater than two. For example, if concentration has appeared as the power of three in Eq. (4.20), the correction term ξ_3 should have been:

$$C_g^3 = \xi_3\, C_{th}^3 \rightarrow \frac{{C_0}^3}{6} = \xi_3\, \frac{{C_0}^3}{8} \;\rightarrow\; \xi_3 = \frac{4}{3} \tag{D.34}$$

D.5 Computation of critical velocity in Chen model

Some preliminary notions are required to fully understand the procedure. These concepts are introduced here.

- *Equilibrium radius* a_0: when two deformable adhesive particles are in contact with each other, elastic repulsion and adhesive attraction are present at the same time. The two surfaces generate a contact circle with a variable radius a that reaches equilibrium at a_0, when the adhesive force (attractive) is counterbalanced by the elastic force (repulsive). The equilibrium radius a_0 of the contact area is expressed as:

$$a_0 = \left(\frac{9\pi\gamma R^2}{E}\right)^{\frac{1}{3}} \tag{D.35}$$

  Where γ is the surface tension of the material, $R_{eq} = \frac{R_1 R_2}{R_1 + R_2}$ is the equivalent radius and $E = \frac{E_1 E_2}{E_1 + E_2}$ is the equivalent Young Modulus. If we consider as representative example two silica spheres with radius $R_1 = R_2 = 20\,\mu m$, $\gamma = 15 \cdot 10^{-3}\,\frac{J}{m^2}$, $E = 2 \cdot 10^{-8} Pa$, the radius $a_0 = 7.5 * 10^{-7} m$ which is 7.5% of the particle radius.

- *Critical overlap* δ_c: the quantity δ_c describes the final compression along the centers of the two spheres when particles reach the equilibrium. It can be calculated as:

$$\delta_c = \frac{{a_0}^2}{2 * 6^{\frac{1}{3}} * R} \tag{D.36}$$

  For the quantities involved in the previous example, the critical overlap is $\delta_c = 1.55 * 10^{-8}$m, which is 1.5% of particles radius.

To compute the critical velocity for normal collisions, Chen et al (2015) have proposed the following procedure:

1. The critical velocity at first contact U_{C1} for purely adhesive particles is:

$$U_{C1} = \left(\frac{14.18}{m^*}\right)^{\frac{1}{2}} \left(\frac{w^5 R^4}{E^2}\right)^{\frac{1}{3}} \tag{D.37}$$

2. The critical velocity just after the rebound phase U_{C2} is given by:

$$U_{C2} = \sqrt{\omega \cdot (m \cdot k_N)^{\frac{1}{2}} \cdot U_{C1} \cdot \delta_C + {U_{C1}}^2} \tag{D.38}$$

where $k_N = \frac{4}{3} E a_0$.

3. The final critical velocity U_{C0} for particles of the same radius r_p can be computed solving numerically the following equation:

$$U_{C0} - U_{C2} = H {U_{C0}}^{\frac{4}{5}} \tag{D.39}$$

where the parameter H is given by: $H = 3.43\, \omega\, m^{-\frac{1}{10}} R^{\frac{2}{15}} E^{-\frac{1}{15}} \gamma^{\frac{1}{6}}$ and ω can be computed from the coefficient of restitution e_0 with the following equation:

$$\omega = 1.2728 - 4.2783 e_0 + 11.087 {e_0}^2 - 22.348 {e_0}^3 + 27.467 {e_0}^4 - 18.022 {e_0}^5 + 4.8218\, {e_0}^6$$

4. In order to find the final critical velocity U_{crit} between two particles of different sizes, U_{C0} needs to be multiplied by $\phi(r_p, \Lambda_r)$, where r_p is the radius of the smaller particle and Λ_r is the ratio between the radii of the colliding spheres.

$$U_{crit} = \phi(r_p, \Lambda_r) \cdot U_{C0} = \underbrace{\frac{r_{p0}}{r_p} \frac{1 + \Lambda_r^3}{(1 + \Lambda_r^2) \cdot \Lambda_r}}_{\phi(r_p, \Lambda_r)} \cdot U_{C0} \tag{D.40}$$

Notice that even though U_{C0} is a function of r_{p0}, U_{crit} does not depend on r_{p0} as the product $r_{p0} \cdot U_{C0}$ is a constant.

D.6 Electrical and aerodynamic forces: some considerations

As already underlined in section (4.5.2), Chen model for dry aggregates does not take into account the effects of net charges on the surface of particles and the aerodynamic forces acting in a real environment. Here we discuss some implications related with these assumptions. Before starting it is important to notice that Van der Waals forces are considered as part of the adhesion forces and thus they are considered.

Electrical forces

If we assume that no charge is exchanged between two colliding elastic particles, in case particle carry opposite charges, the energy added to the system during the approach phase is equal to the energy subtracted to the system after rebound. In case particles carry charges of the same sign, energy is subtracted during the approach phase, and it is added to the system during rebound. In any case, no dissipation occurs due to electrical forces for perfectly elastic particles. For viscoelastic particles, the simultaneous action of electrical and viscoelastic forces during contact may result in a different dissipation compared to neutral particles. In this work, however, we assume that the charge is low enough for its effect during contact to be neglected. The assumption of a negligible charge is even more applicable in highly humid environments (Schella et al., 2017).

Aerodynamic forces

The determination of the aerodynamic force acting on particles is strongly related to the fluid condition. However, an estimation of the drag acting on a sphere in a steady flow gives a first order quantification of the role of aerodynamic forces. If we define the Reynolds number of a particle as:

$$Re = \frac{\rho_f \, d_p U}{\mu_f} \tag{D.41}$$

For air density $\rho_f = 1.225 \, \frac{kg}{m^3}$, particle diameter $d_p = 20 \, \mu m$; particle velocity respect to the fluid $U = 0.1 \, m/s$ and air dynamic viscosity $\mu_f = 1.81 * 10^{-5} Pa$, we get: $Re \approx 0.27$. The Drag coefficient can be calculated using the following formula:

$$C_D = \frac{24}{Re}(1 + 0.15 Re^{0.687}) \tag{D.42}$$

It results $C_D \approx 90$, for a size of 20 μm. The drag force F_D is defined as:

$$F_D = \frac{1}{2}\rho_f C_D A\, U^2 \tag{D.43}$$

Where A refers to the cross-sectional area of the particle. For the particles under analysis we get $F_D = 1.41 * 10^{-5} N$. Comparing this value with the total contribution of the adhesive and the elastic force $F_{(ad+el)}$ calculated in Eq. (4.66) we notice that the drag force is two orders of magnitudes lower than this force. Even though this result does not guarantee that aerodynamic forces do not play any role for irregular particles, it suggests that aerodynamic loads might be of secondary importance respect to elastic forces during particle-particle contact. However, further investigation is required in order to take into account for unsteady flow effects as well.

D.7 List of symbols used in chapter 4

Table 4.4 List of symbols used in chapter 4

Symbol	Definition	Unit
a	Variable radius of the contact circle in a collision	m
A	Cross-section of two colliding objects	m^2
a_k	Turbulent acceleration	$m\, s^{-2}$
A_{FHH}	Experimental coefficient for hygroscopic water layer	-
a_0	Radius of the contact circle at equilibrium	m
B_{FHH}	Experimental coefficient for hygroscopic water layer	-
B_i	Birth term for the GFPT	$m^{-3}s^{-1}$
C_d	Drag coefficient	-
C_g	Particles concentration along a Gaussian profile	m^{-3}
C_{th}	Particles concentration along a top-hat profile	m^{-3}
C_0	Particles concentration at the central line for a Gaussian profile	m^{-3}
d_A	External diameter of an aggregate	m
d_d	Diameter of a dry particle	m

D_F	Fractal exponent	-
D_i	Death term for the GFPT	$m^{-3}s^{-1}$
d_{mol}	Diameter of a water molecule	m
d_w	Total diameter of a wet particle	m
d_0	Diameter of a monomer in a fractal aggregate	m
E	Total energy per unit mass	J kg^{-1}
E_c	Collection efficiency for the collision kernel	-
E_{eq}	Equivalent Young modulus	Pa
e_{si}	Saturation pressure of vapour respect to ice	Pa
e_{sl}	Saturation pressure of vapour respect to liquid water	Pa
e_0	Restitution coefficient	-
F_{ad+el}	Adhesive and elastic force	N
F_c	Adhesive force	N
f_g	Weight factor for gravitational collection settling	-
F_{vis}	Viscous force	N
g	Gravitational acceleration	$m\ s^{-2}$
$g(\psi) = \psi\ tan^{-1}(\psi)$	First correlation term for the contribute of a generic eddy of size l	-
g_{clust}	Correction factor for the clustering effect	-
h	Thickness of the liquid layer	m
H	parameter require by Chen's model for the determination of the final critical velocity	-
$h(\psi) = \frac{1}{1+\psi^2}$	Second correlation term for the contribute of a generic eddy of size l	-
h_a	Characteristic height of surface asperities	m
J	J Momentum mass flux	
k	Spatial wavelength associated with an eddy of size l	m^{-1}
K	Aggregation kernel	m^3s^{-1}
k^*	Spatial wavelength of the boundary eddy between	m^{-1}

	class I and II	
k_f	Fractal prefactor for fractals ($k_f \approx 1$)	-
k_L	Spatial wavelength associated with the largest eddy L	m^{-1}
k_η	Spatial wavelength associated with the smallest eddy	m^{-1}
L	Largest size for a turbulent eddy	m
$M'\ \phi'\ M''\ \phi''$	Interacting properties of a collision M mass ϕ porosity	$M = kg$ $\phi = -$
m_i	Mass associated with the i-esim cell	kg
M_{tot}	Total mass in an aggregate	kg
M_{1+2}	Final mass of the product of a collision	kg
M_μ	Reduced mass of two-particle system	kg
N_c	Total number of cells in the *mass-porosity* plane	-
n_d	Mass fraction of dry air in the mixture	-
n_i	Mass fraction of ice water in the mixture	-
N_i	Particles concentration for object of the i-esim class	m^{-3}
n_l	Mass fraction of liquid water in the mixture	-
N_p	Number of particles contained in a fractal aggregate	-
n_s	Mass fraction of solids in the mixture	-
n_w	Mass fraction of water in the mixture (all the phases)	-
$\boldsymbol{p}$	Bidimensional vector of the internal properties	
P_{atm}	Atmospheric pressure	Pa
P_v	Partial pressure of water vapour	Pa
Q	Preserved properties in the weights definition	-
Q_d	Mass flux of dry air in the plume	$kg\ s^{-1}$
Q_l	Mass flux of liquid water in the plume	$kg\ s^{-1}$
q_m	Mass of water relatively to the mass of gas	$g\ kg^{-1}$
Q_s	Mass flux of solid particles in the plume	$kg\ s^{-1}$

q_{sh}	Mass fraction of water in the entrained ambient air (specific humidity)	$kg\ kg^{-1}$
Q_{tot}	Total mass flux entering in the control volume	$kg\ s^{-1}$
Q_v	Mass flux of water vapour in the plume	$kg\ s^{-1}$
Q_w	Mass flux of water (all phases) in the plume	$kg\ s^{-1}$
R_{CF}	Ratio of coarse to fine ash along the plume	-
R_d	Gas constant of dry air	J $kg^{-1}\ K^{-1}$
Re	Reynolds number	-
R_{eq}	Effective radius	m
R_g	Gas constant of dry air and vapour inside the gas mixture	J $kg^{-1}\ K^{-1}$
RH	Relative humidity	-
r_i	Radius of the *i*-esim particle	m
R_{th}	Top-hat radius of the plume	m
R_v	Gas constant of water vapour	J $kg^{-1}\ K^{-1}$
r_1	Radius of particle one in a binary collision	m
r_2	Radius of particle two in a binary collision	m
S_c	Surface coverage	-
St_{cr}	Critical Stokes number in Ennis model	
St_{KO}	Stokes number associated to the smallest eddy	
St_{Tl}	Turbulent Stokes number	
St_{TL}	Stokes number associated to the largest eddy	
St_v	Collision Stokes number	
T_B	Bulk temperature of the gas mixture	K
T_{coll}	Collision kinetic energy of two particles	J
T_{diss}	Maximum kinetic energy that a system can dissipate	J
T_K	Total kinetic energy of two particles system	J
T_1	Temperature value for ice formation	$T_1 = 273.15\ K$
T_2	Temperature value for water boiling	$T_2 = 373\ K$

U_{CM}	Velocity of the center of mass of two particles	$m\ s^{-1}$
U_{crit}	Critical velocity for sticking	$m\ s^{-1}$
U_{C0}	Final critical velocity for particles of the same radius in Chen model	$m\ s^{-1}$
U_{C1}	Critical velocity at first contact in Chen model	$m\ s^{-1}$
U_{C2}	Critical velocity after the rebound in Chen model	$m\ s^{-1}$
U_{entr}	Entrainment velocity of atmospheric air in the plume	$m\ s^{-1}$
U_g	Velocity of the macroscopic turbulent fluctuations in the fluid	$m\ s^{-1}$
U_k	Velocity associated to the *k* size eddy	$m\ s^{-1}$
$\langle \lvert U_m \rvert \rangle$	Mean of the absolute value of the modulus of relative velocity	$m\ s^{-1}$
$U_{p\_rms} = \langle U_m^2 \rangle^{1/2}$	Root mean square of the modulus of the relative velocity	$m\ s^{-1}$
$\langle \lvert U_r \rvert \rangle$	Mean of the absolute value of the radial relative velocity	$m\ s^{-1}$
$\langle U_r^2 \rangle^{1/2}$	Root mean square value of the relative radial velocity	$m\ s^{-1}$
U_{si}	Terminal velocity for the object *i*	$m\ s^{-1}$
U_{th}	Top-hat plume velocity	$m\ s^{-1}$
U_{vg}	Relative velocity between a grain and an eddy of size k	$m\ s^{-1}$
U_{wind}	Wind velocity	$m\ s^{-1}$
V_A	External volume of an aggregate	m^3
V_s	Volume of the skeleton structure in an aggregate	m^3
$w = \frac{n_v}{n_v + n_d}$	Mass fraction of vapour respect to gas phase	-
W	Weights for the redistribution of particles in the GFPT	-
x	Horizontal coordinate	m
X_i	Mass fraction attributed to the *i*-esim cell in the mass-porosity plane $\sum_{i=1}^{N_c} X_i = 1$	-
z	Height above sea level	m

α	Sticking efficiency	-
α_{entr}	Coefficient for axis entrainment	-
β_{entr}	Coefficient for radial entrainment	-
β_{ij}^{AB}	Collision efficiency associated to the Abrahamson limit	$m^3 s^{-1}$
β_{ij}^{GDS}	Collision efficiency associated to gravitational settling collection	$m^3 s^{-1}$
β_{ij}^{P}	Collision efficiency between two particles i and j for a particular process P	$m^3 s^{-1}$
β_{ij}^{SH}	Collision efficiency associated to turbulent shear	$m^3 s^{-1}$
β_{ij}^{TDC}	Collision efficiency associated to the turbulent differential coupling	$m^3 s^{-1}$
β_{ij}^{TI}	Collision efficiency associated to turbulent inertial collections	$m^3 s^{-1}$
γ	Fluid interfacial tension	J m^{-2}
γ_{ice}	Ice interfacial tension	J m^{-2}
$\gamma_R = \frac{R_{env}}{R_{th}}$	Ratio between envelope radius and top-hat plume radius	-
γ_{sil}	Silica interfacial tension	J m^{-2}
$\gamma_U = \frac{U_{si}}{U_p}$	Ratio between the terminal velocity and upward plume velocity	
$\Gamma = \frac{\tau_p}{\tau_p + \tau_k}$	Auxiliary parameter defined in Ormel and Cuzzi (2007)	
δ_N	Deformation of particle surface	m
$\varepsilon = \frac{R_d}{R_v}$	Gas constant ratio ($\varepsilon = 0.622$)	-
ϵ	Dissipation rate of turbulent kinetic energy	$m^2 s^{-3}$
η_{vis}	Normal dissipation coefficient	$N\ s$
η_{KO}	Kolmogorov length	m
θ	Tilting angle of the eruptive column	rad
Λ_m	$\Lambda_m = \frac{m_2}{m_1}$, where $m_1 > m_2$	-

Λ_ϕ	$\Lambda_\phi = \frac{\phi_2}{\phi_1}$, where ϕ_1 is associated with the more massive body	-
μ	Dynamic viscosity of the air	$Pa\ s$
μ_l	Dynamic viscosity of the liquid on the surface of the object	$Pa\ s$
ν	Kinematic viscosity	$m^2 s^{-1}$
ξ_2	Correction factor for top-hat distribution of particle concentration	$kg\ m^{-3}$
ρ_A	Aggregate density	$kg\ m^{-3}$
ρ_{air}	Atmospheric air density	$kg\ m^{-3}$
ρ_B	Bulk density of the gas mixture	$kg\ m^{-3}$
ρ_f	Density of the fluid	$kg\ m^{-3}$
ρ_{gas}	Density of the gas phase (dry air and water vapour)	$kg\ m^{-3}$
ρ_i	Density of ice	$kg\ m^{-3}$
ρ_l	Density of liquid water	$kg\ m^{-3}$
ρ_s	Density of solid particles $\rho_s = \rho_0 = 2500\ kg\ m^{-3}$	$kg\ m^{-3}$
ρ_0	Density of the single components in an aggregate $2500\ kg\ m^{-3}$	$kg\ m^{-3}$
σ	Variance of the Normal distribution of relative velocities	$m\ s^{-1}$
τ^*	Overturn time associated with the boundary eddy between class I and II	s
τ_k	Overturn time for eddy of size k	s
τ_{KO}	Kolmogorov time-scale	s
τ_L	Overturn time for the largest eddy	s
τ_p	Relaxation time of a particle	s
ϕ	Aggregate/particle porosity	-
ϕ_{1+2}	Final porosity of the product of a collision	-
$\phi_{rel} = \frac{\phi_{1+2} - \phi_1}{\phi_1}$	Relative final porosity respect to the more massive body	-

χ	Enlargement factor according to Ormel et al. (2007)	
χ_{1+2}	Final enlargement factor	-
ψ	$\psi = \Gamma\ \tau_k\ k\ U_{vg}$ independent variable for the correlations terms of l-size eddies	-
ω	Parameter required by Chen's model for the computation of H as a function of the restitution coefficient e_0	-

Chapter 5

A new strategy for the estimation of plume height from clast dispersal in various atmospheric and eruptive conditions[4]

5.1 Introduction

Determining eruptive source parameters (e.g. erupted volume, plume height, mass eruption rate) and evaluating the associated uncertainties is crucial to the characterization of eruption dynamics and the assessment of associated hazards (e.g. Bonadonna et al. 2015 and references therein). The increasing availability of plume and dispersal models and real-time measurements have resulted in a better description of volcanic phenomena and of their impact. Nevertheless, in many circumstances (e.g. past eruptions with no direct observations) field data represent the only means to reconstruct the eruptive source parameters. Unlike the determination of erupted volume, which has been addressed by several authors (e.g. Bonadonna and Costa, 2012; Bonadonna and Houghton, 2005; Burden et al., 2013; Fierstein and Nathenson, 1992; Nathenson, 2017; Pyle, 1989; Sulpizio, 2005), the determination of plume height from field data is still mostly based on the methodology introduced by Carey and Sparks (1986), hereafter *CS86,* and revised by Burden et al. (2011), hereafter *BPH11*. CS86 provides a set of plots, referred to as nomograms, that allows deriving plume height and wind speed from the downwind and crosswind ranges of isopleth contours associated with clast sizes between 8 and 64 mm and clast densities between 250 and 2500 $\frac{kg}{m^3}$. CS86 is based on the definition of the clast support envelope, a region of the plume where particles of a specific size may no longer be suspended within the plume and, thus, settle out. The simple application has made CS86 the most widely used method for the calculation of plume height within the community (e.g. BPH11 and references therein).

[4] Under revision in: *Earth and Planetary Science Letters* ; Rossi E., Bonadonna C., Degruyter W., *"A new strategy for the estimation of plume height from clast dispersal in various atmospheric and eruptive conditions"*

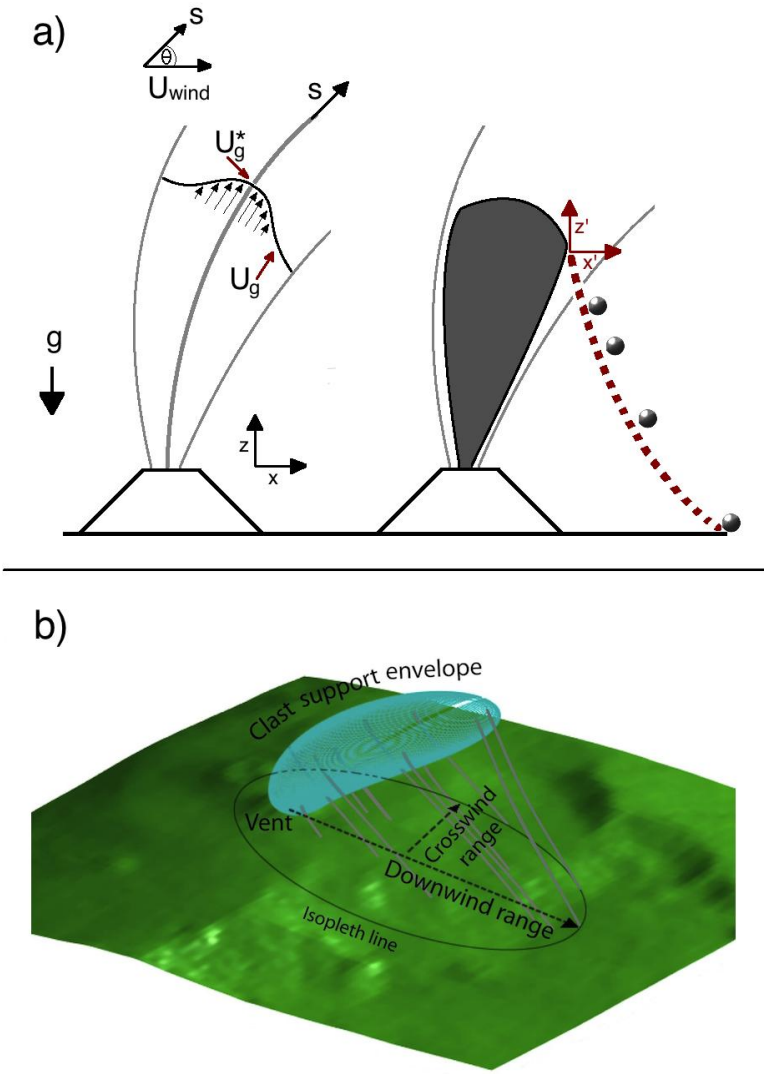

Figure 5.1: (a) Diagram of the coordinate system used to describe plume rise and particle sedimentation from the clast support envelope, shown in grey shaded colour; (b) Example of clast support envelope produced by the model with particle trajectories in the atmosphere and definition of downwind and crosswind range following CS86.

However, the methodology introduced by CS86 is associated with important issues, some of which have already been addressed by BPH11 by: i) using a plume model to avoid empirical relations for volume and temperature changes of the gas mixture along the column; ii) quantifying the associated uncertainties; iii) describing the radial velocities above the Neutral Buoyancy Level (NBL) based on a gravity current model, and iv) using more realistic wind profiles for the sedimentation of volcanic clasts in the atmosphere. Despite these important implementations, additional fundamental processes still need to be addressed. The main goal of this work is to take into account

the key role of wind in defining clast support envelopes along the downwind direction. This results in a methodology for the determination of plume height from clast dispersal applicable under a large range of eruptive and atmospheric conditions. Moreover, we have implemented a new parameterization of the gravity current for distances smaller than the radius of the plume and the influence of both particle shape and tropopause height on the final isopleth contours. Finally, we provide a new set of nomograms that can be applied to a wide range of eruptive conditions. A Matlab script for detailed analysis of specific eruptions and for the computation of theoretical isopleth contours in case of eruptions with known wind field and topography is also provided.

5.2 New modelling strategy

Following CS86, our model requires two fundamental steps: first, the definition of a clast support envelope within the volcanic plume; second, the determination of the trajectories of falling particles released from the envelope margins. Clast support envelopes are regions within the eruptive column where the upward velocity of the plume equals the terminal velocity of a given clast. CS86 assume empirical approximations of volume and temperature changes in the gas mixture within the column that introduce a significant uncertainty. The revised methodology proposed by BPH11 improves this aspect, using a more sophisticated plume description based on the model of Woods (1988). However, in both these models, wind advection only affects clast sedimentation but not the rising plume. According to Degruyter and Bonadonna (2012), the influence of atmospheric wind with a height-averaged velocity $\bar{V}_{wind}$ can be quantified with the parameter $\Pi \propto k \frac{\bar{N} H}{\bar{V}_{wind}} \left(\frac{\alpha_e}{\beta_e}\right)^2$, in which α_e and β_e are the radial and wind entrainment coefficients, $\bar{N}$ the height-averaged buoyancy frequency, H the maximum height of the plume centreline, and k a constant. Values of $\Pi \gg 1$ characterize *strong plumes*, i.e. eruptions dominated by the vertical plume rise, while values of $\Pi \ll 1$ imply a dominant influence of wind on plume rise (i.e. weak plumes), with a consequent effect on the shape of the clast support envelopes and, therefore, on the particle sedimentation distance (Fig. 5.1).

Once clasts are released from the envelope region, their deposition strongly depends on the wind velocity fields. Simplified sedimentation models are both present in CS86 and in BPH11. However, a more realistic trajectory for centimetric particles, i.e.

characterized by Stokes number $St > 1$, is obtained solving the equation of motion for each particle (section 5.2.3), without assuming that the horizontal velocities of the clasts are equal to the external velocity fields. As indicated in Fig. 5.2, we provide two ways to determine plume height: i) from a compilation of nomograms in various eruptive and atmospheric conditions or ii) from a direct calculation of the model using better constrained eruption and atmospheric conditions (Fig. 5.2). The first approach is of easier application and is based on the use of dedicated plots; the second approach requires the use of a dedicated Matlab package for the consideration of specific atmospheric and topographic data (available on GitHub.).

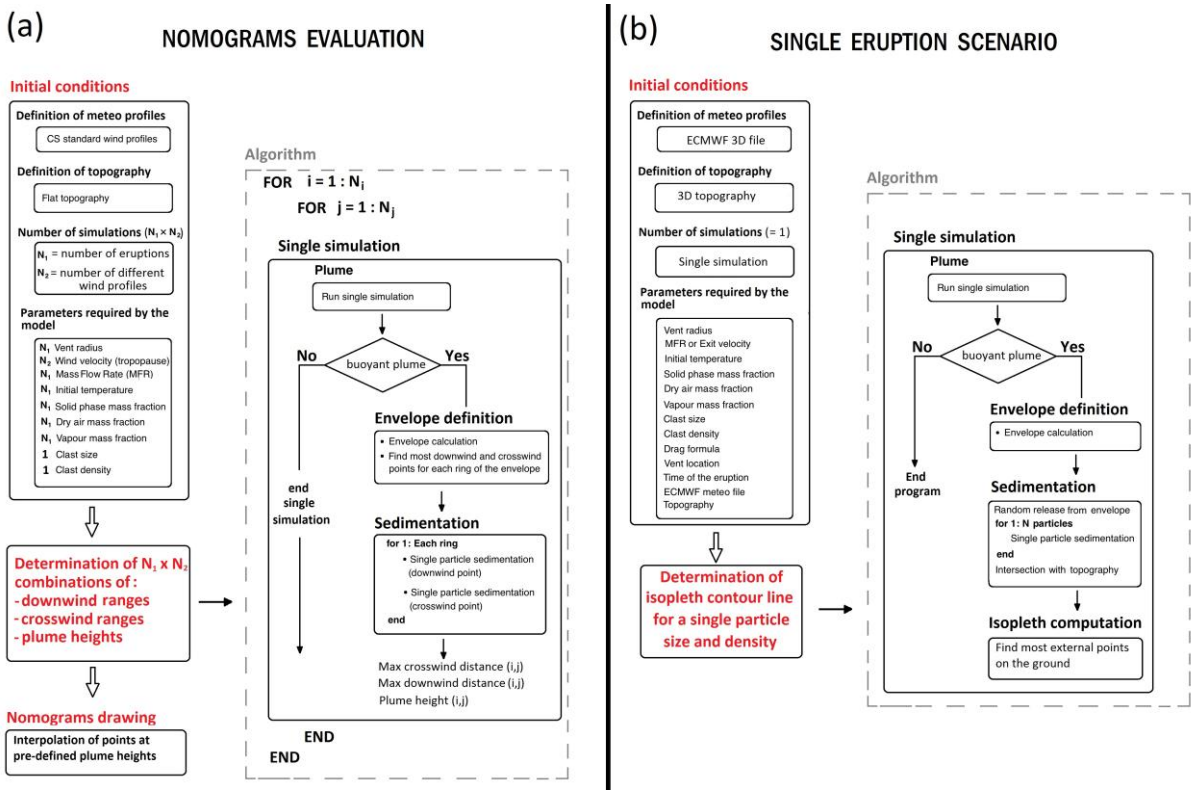

Figure 5.2: Flowchart of the two main applications of the model: (a) Compilation of nomograms: this approach is used to compile the nomograms: the model is run several times in a Montecarlo approach varying the initial eruptive conditions and the maximum wind at the tropopause. The final set of points relates the height of the plume with the maximum downwind and crosswind ranges obtained in each simulation. Nomograms are derived by interpolating the information at pre-defined plume heights (i.e. 5, 10, 15, 20, 25, 30 km). (b) The second approach allows the user to run single simulations with complete topography and three dimensional meteorological data. The final result is the computation of the isopleth map for a given particle size and density.

5.2.1 Plume velocity field

To define a clast support envelope within a volcanic plume as prescribed in CS86, we first require the knowledge of the plume centreline velocity and the Gaussian cross-plume velocity profile. We first calculate the plume centreline velocity using the integral plume model of Degruyter and Bonadonna (2012, 2013), which assumes a top-hat profile. We then convert the cross-plume velocity to an equivalent Gaussian profile using the considerations of Davidson (1986). The governing equations of the integral model consider the balance of mass, momentum, and heat flow rates within a control volume. The model accounts for the effect of wind, which we expand to include variations in wind direction in the azimuthal plane following Folch et al. (2016).

Gaussian and top-hat velocities, denoted by U_g and U_{th}, respectively, are related through averaging over the plume circular cross-sectional area:

$$U_{th} = \frac{1}{\pi R^2} \int_0^R U_g \, 2\pi r \, dr \tag{5.1}$$

with r the cross-plume radial distance from the plume centreline and R the top-hat radius. Following Davidson (1986), for a plume in an external constant wind field of value V_{wind} it holds that:

$$U_g(s,r) = V_{wind}(s,r)\cos\big(\theta(s)\big) + U_g^*(s)\, e^{-\frac{r^2}{b(s)^2}} \tag{5.2}$$

where s is the curvilinear coordinate along the trajectory, θ is the bending angle with respect to the horizontal axis, U_g^* is the velocity at the centre of the plume and b is the cross-plume radial distance at which the Gaussian velocity profile decays to $1/e$ of the centreline value. This expression defines the velocity difference between plume and wind along the central axis as a Gaussian function. In a real environment, the wind varies along r. We assume that V_{wind} is locally constant along the radial coordinate and equal to the value at the centre of the plume, i.e. $V_{wind}(s,r) = V_{wind}(s,0)$. The wind velocities at a given height z are interpolated from the closest points available in the atmospheric profile.

The characteristic width of the Gaussian velocity profile, b, can be expressed in relation to the top-hat radius R according to the following assumption (Davidson, 1986):

$$\frac{R^2}{b^2} = 2 \tag{5.3}$$

Therefore, using Eq. (5.2) and Eq. (5.3) inside equation Eq. (5.1), Gaussian velocities can be expressed in terms of their relative top-hat values:

$$U_g^*(s) = \frac{2\ (U_{th}(s) - V_{wind}(s)\cos\theta(s)\ )}{1 - e^{-\frac{R^2}{b^2}}} \approx 2\ (U_{th}(s) - V_{wind}(s)\cos\theta(s)\ ) \tag{5.4}$$

where the approximation is commonly used in the literature (Davidson, 1986; Sparks, 1986). However, it is worth mentioning that this expression is exact only for integration over an infinite radius. If the integration is made over the radius R, the approximation is associated with a relative error on the value of U_g^* of about 14% with respect to the full equation.

5.2.2 Clast support envelope

The criterion used to define clast support envelopes can be considered as follows. A single clast falling at terminal velocity will experience no net motion if the surrounding air has an upward flow of equal magnitude. This equilibrium suggests that an upward flux generating a velocity field greater than the clast terminal velocity will exert sufficient drag such that the clast will approximately follow the same trajectory as the plume. When the terminal velocity of the particle is equal to the plume velocity, clasts are no longer coupled with the gas mixture and they start to sediment. The expression for the terminal velocity U_{tv} is:

$$U_{tv} = \sqrt{\frac{4}{3}\frac{\rho_c d\ g}{\rho_f C_d}} \tag{5.5}$$

where g is the gravitational acceleration, d particle diameter, ρ_c clast density, C_d is the drag coefficient and ρ_f is the density of the plume mixture to be evaluated at each height. Given their dependence on C_d, terminal velocities are calculated iteratively equating the gravity force and the drag force (see Appendix E.1). The buoyant force is neglected due to the large difference in density between clasts and surrounding gas. Thus, the clast support envelope is defined as the three-dimensional surface where the

vertical component of the plume velocity field equals the terminal velocity U_t of the clast (Fig. 5.1). Solving the equation $U_t = U_g \cdot \sin(\theta)$ for the unknown radius R_{env} at a given height z, we find:

$$R_{env} = b \cdot \sqrt{-\ln\left\{\frac{1}{U_g^*}\left[\frac{U_{tv}}{\sin(\theta)} - V_{wind} \cdot \cos(\theta)\right]\right\}} \tag{5.6}$$

As shown in Fig. 5.1, atmospheric winds strongly affect the shape of the envelope.

5.2.3 Particle sedimentation

Depending on the use of the model, i.e. for nomogram compilation (inversion mode) or for running single eruption scenarios (forward mode) (see Fig. 5.2), particles are respectively released from selected points (the most downwind and crosswind locations on each envelope ring) or from random points uniformly distributed on the surface of the envelope. We determine the maximum deposition distance along the downwind and crosswind axes. Initial velocities are set equal to zero and each trajectory is described in a fixed (inertial) frame of reference with the origin situated on a release point on the support envelope and the axes oriented as shown in Fig. 5.1.

A Lagrangian tracking is applied to determine clast trajectories in the atmosphere. The second law of motion is solved considering the effects of drag and gravity:

$$m_c \frac{d\vec{U}_c^i}{dt} = \vec{F}_{drag} + \vec{F}_g \tag{5.7}$$

where $\vec{F}_{drag} = \frac{1}{2}\,\rho_f\,A\,|\vec{U}_c^i - \vec{U}_f|(\vec{U}_c^i - \vec{U}_f)\,C_d$, $\vec{F}_g = m_c\vec{g}$, A is the projected area of the clast with a diameter d_c ($A \approx \frac{\pi}{4}d_c^2$), $\vec{U}_c^i$ is the velocity of clast i, $\vec{U}_f$ is the velocity of the surroundings and m_c is the mass of the object. At each time step, the drag vector is evaluated and then decomposed along the Cartesian axes in order to solve the motion in three-dimensional space. A more detailed analysis of the global forces acting on a clast in the atmosphere can be found in de' Michieli Vitturi et al. (2010). We can assume that the forces that depend on the density ratio between solid particles and air (buoyancy and virtual mass term) and on the history of the trajectory (*Basset force*) are negligible. The solution of Eq. (5.7) requires an expression for the drag coefficient C_d and the

surroundings $\vec{U}_f$ along the particle trajectory. The drag coefficient is specified from the parameterization proposed by Bagheri and Bonadonna (2016) for non-spherical particles, which ensures a reduced average error of about ~ 10% with respect to the observed data (see Appendix E.1). The velocity field outside the volcanic column and umbrella cloud is determined by the atmospheric wind. Within the umbrella cloud, there is the additional contribution of gravitational spreading. Following CS86 and BPH11, we constrain the umbrella cloud region between the NBL and the top of the plume. The alternative description of gravity current spreading around NBL, e.g. between a minimum and maximum height of $\approx 0.8\, H_{NBL}$ and $\approx 1.2\, H_{NBL}$ (Bonadonna and Phillips, 2003) was also tested with no significant difference in the resulting sedimentation distances. For consistency with CS86, two distinct regions of sedimentation are defined: sedimentation above the NBL (where the radial velocity field of the gravity current dominates over wind advection; see section 2.4); sedimentation below the NBL (where the atmospheric wind is the only component contributing to clast lateral transport; see section 5.2.5). The resulting set of Ordinary Differential Equations (ODEs) is solved using the Matlab solver ode45, an explicit Runge-Kutta algorithm of 4th-5th order (Shampine and Reichelt, 1997).

5.2.4 Gravity current above the Neutral Buoyancy Level (NBL)

In the region around the NBL (i.e. the umbrella cloud) the density difference between the volcanic mixture and the atmosphere produces radial spreading as a gravity current (e.g. Johnson et al. (2015). For large eruptions, there is a first-order contribution of the gravity current to the total spreading rate of the umbrella cloud especially for proximal distances (Costa et al., 2013). The parameterization of the velocity of the gravity current U_{gc} is commonly based on the mass conservation of the incoming mass per unit time from the volcanic column and the consequent spreading of the current (Sparks, 1986). In addition, a relationship between the thickness h_{gc} and velocity of the gravity current can be defined based on scaling arguments (Bonadonna and Phillips, 2003). In both cases, this is mathematically consistent for distances greater than the plume radius at the NBL. For smaller distances, this approach overestimates the gravity-current velocity, and diverges to infinity when the distance approaches zero (Fig. 5.3). This aspect has

some impact on plume modelling that follows the approach of CS86, since clasts are often released from regions inside the plume and above the NBL. We propose a solution that comes from balancing the actual Mass Flow Rate Q^{NBL} (MFR) entering a given section at the NBL. For an object located inside the plume radius, the radial velocity at a distance r is generated by the actual MFR entering in a cross section πr^2, which tends to zero for $r \to 0$. If we assume that the velocity of the front of the gravity current scales as a function of the atmospheric buoyancy frequency N and a correction factor $\lambda \approx 1$ ($U_{gc} = \lambda N h_{gc}$) (Bonadonna and Phillips, 2003), we obtain:

$$U_{gc} = \left(\frac{\lambda N V_{wind}}{2} \cos(\theta)\, r + \frac{U_g^* \lambda N R^2}{4} \frac{(1 - e^{-\frac{r^2}{b^2}})}{r} \right)^{\frac{1}{2}} \quad with \quad 0 \leq r \leq \infty \tag{5.8}$$

Eq. (5.8) represents a generalization of gravity currents for a Gaussian profile of the plume velocity and for any distance. A comparison of equation Eq. (5.8) with those presented in Sparks (1986) and Bonadonna and Phillips (2003) is shown in Fig. 5.3. The unrealistic high velocities commonly present in the previous works for small distances are replaced with a curve that drops to zero corresponding to a null radius. For $r = R_{NBL}$ the velocity calculated with Bonadonna and Phillips (2003) differs by about 7% from equation Eq. (5.8). This discrepancy tends rapidly to zero for increasing distances (Fig. 5.3).

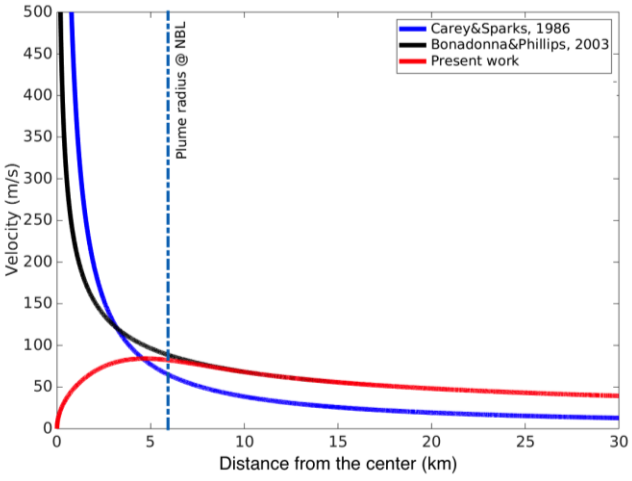

Figure 5.3: Velocity of the gravity current as a function of the distance from the center of the umbrella cloud, according to CS86, Bonadonna and Phillips (2003) and the present work (Eq. (11)). Outside the NBL the parameterization of Bonadonna and Phillips (2003) and our model are the same, with the exception of an initial 7% of difference in correspondence of the NBL. The formula proposed in the present work avoids the mathematical singularity for a null distance.

5.2.5 Meteorological data

We use a flexible structure for the accurate description of atmospheric conditions that can easily be modified. In the standard mode of operation, the code reads an Era-Interim dataset provided by the European Centre for Medium-Range Weather Forecasts (ECMWF) (Dee et al., 2011). This dataset can be easily downloaded using a modified version of the software *TephraProb* (Biass et al., 2016). This mode of operation is used for all situations where complete meteorological information is available, namely for all eruptions that occurred later than 1979 (see Biass et al., 2016 for a more detailed description on the application of ECMWF data to volcanic eruptions). For all other cases, e.g. past and future eruptions, a default wind profile provided in CS86 is applied. This profile assumes zero velocity on the ground and a linear increase up to the tropopause height, where it has its maximum value V_{wind}^{max}. It decreases linearly down to 0.75 V_{wind}^{max} in the stratosphere at a height H_S (Fig. 5.4b). Standard values of V_{wind}^{max} are chosen following CS86. A default value of 20 km is attributed to H_S. However, a variation of H_S between 14 km and 20 km does not affect significantly the final nomograms (the change in downwind ranges is less than 1%).

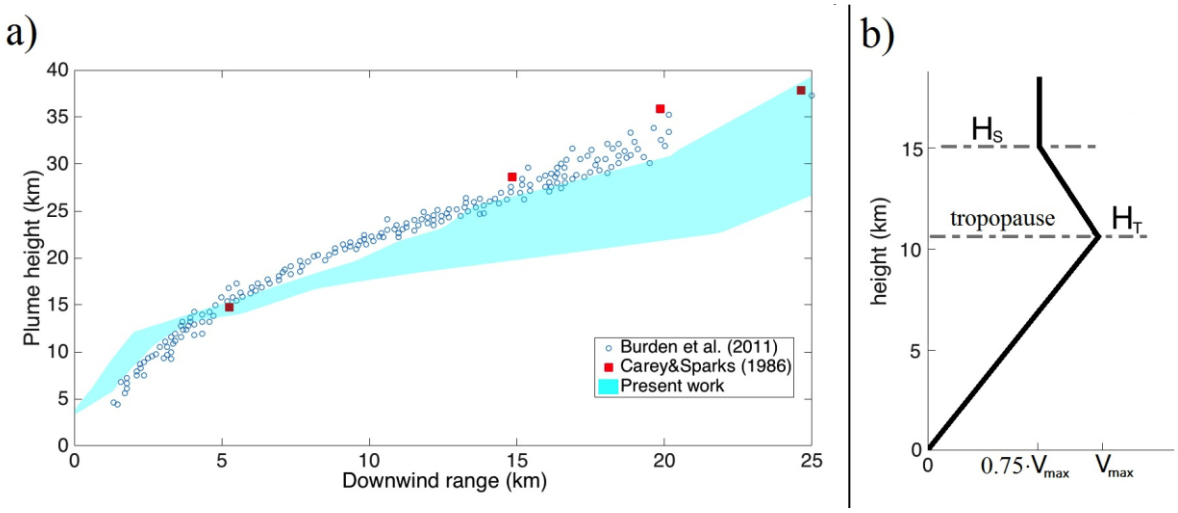

Figure 5.4: Comparison of our model with the models of CS86 and BPH11 for the same initial eruptive conditions and a no wind case. Initial conditions are the same of table 1 in BPH11. Red dots are points extrapolated from the nomograms of CS86, while the blue circles represent data of BPH11; the shadowed area in the plot describes the space of possible outcomes according to the present model. Particle size is 0.8 cm and particle density is 2500 kg/m^3. (b) Typical wind profile used in the nomograms. H_T is the height of the tropopause and H_S is the height at which the wind profile is constant. V_{max} defines the maximum value of the wind at the tropopause.

5.3 Comparison with existing models and field observations

5.3.1 Comparison with existing dispersal models

Our new model is compared against the results of BPH11 (cf. Fig. 5.2 of BPH11) (Fig. 5.4). The maximum plume centreline height is expressed as a function of the maximum downwind range for particles with a diameter of 0.8 cm, a density of 2500 kg/m^3, and no wind. The ranges of parameters investigated covers the same ranges as in BPH11 (cf. their Table 1). Four quantities are varied: initial radius, gas mass fraction, initial velocity and temperature. Particles are released from the entire column with no preferential release point on the envelope. Fig. 5.4 shows a general agreement between our model and previous works, with two main differences: slightly smaller downwind distances for plume heights less than $\approx 15\ km$ and a wider variability of the heights for a fixed downwind distance. In our model, this last aspect can be explained due to the complex combination of radial spreading above the NBL and the effect of the initial radius on the exit velocity of the column. As a result, an envelope wider in horizontal extension but smaller in height can produce the same downwind distance as a much higher, but narrower, plume. This variability can be strongly reduced if eruptive scenarios are identified, so that eruptions with very different initial radii are not clustered together (see following section).

5.3.2 Comparison with field data

The comparison with field data is carried out based on two different procedures. First, isopleth contours computed with our new model for a given size and density are compared with field observations (i.e. values of the largest clasts) of selected tephra deposits. Second, we compare observed plume heights for selected eruptions with the plume height predicted by our new nomograms.

5.3.2.1 Comparison between computed isopleth contours and field observations

Three eruptions with different values of Π have been selected to explore the effect of wind intensity on the sedimentation process. In particular, the eruption of Pinatubo 1991, Philippines (Rosi et al., 2001) was characterized by both intermediate winds and strong plume ($\Pi \approx 0.5$); the 1980 eruption of Mount St Helens, USA (Carey et al., 1990) was characterized by strong wind and a transitional plume ($\Pi \approx 0.3$); the 2011 eruption of Shinmoedake, Japan, was characterized by a strong wind and a weak plume ($\Pi \approx 0.04$) (Maeno et al., 2014). For all the three cases, we have used ECMWF meteorological data that are closest in time to the recorded date of the eruption. ECMWF provides data at 6-hour intervals (Dee et al., 2011). In this section, computed isopleth contours are compared with ground locations of the observed largest clasts. Ideally, we would expect computed isopleth contours associated with a given size to be outside (i.e. to contain) all locations of the observed largest clasts of the same size or larger and the maximum downwind and crosswind distances to match with the theoretical ones. However, a probabilistic approach is necessary since the maximum travelled distance of a clast is very sensitive to fluctuations in the eruptive parameters that are poorly constrained. Initial conditions are randomly picked from a uniform distribution within a given range (see table E.4.1 in *appendix E*) and the values of MFR are chosen to recreate the plume heights reported in the literature. This probabilistic approach allows confidence intervals to be defined in the explored parameter space. Two thresholds of 5% and 95% are identified to compare independent field data and computed isopleth contours. Particle sizes used in the simulations are specific for each eruption.

Mount Pinatubo 1991, strong plume

The 1991 eruption of Mount Pinatubo, Philippines, is one of the largest eruptions that occurred in the 20th century (Holasek et al., 1996). During the 15th-16th of June, the plume reached the height of about 40 km above sea level (a.s.l.) (Rosi et al. 2001). This climactic phase is an example of a strong plume since the wind did not significantly affect the rise of the volcanic column. The range of initial conditions and parameters used for this set of simulations are reported in Table S1. Three sizes of lithic clasts are

considered: 0.8, 1.6 and 3.2 cm to compare with the published data based on the average of the maximum dimension of the five largest clasts (Rosi et al., 2001). Fig. 5.5 shows a good agreement between modelled isopleth contours and field data. In particular, particles of 0.8 cm and 1.6 cm are all contained within their own confidence interval, which suggests a correct estimation of the downwind and crosswind distances. Results for the 3.2 cm particles tend to overestimate the sedimentation distance with respect to observations. The discrepancy can be due to the fact that the height of the clast support envelope for 3.2 cm particles matches the height at which wind abruptly changes direction. In the probabilistic approach, the simulations with a clast support envelope above the height of change in wind direction smooth this sharp threshold. As a result, the strong wind shear produces a mismatch between model and observations for this particular size.

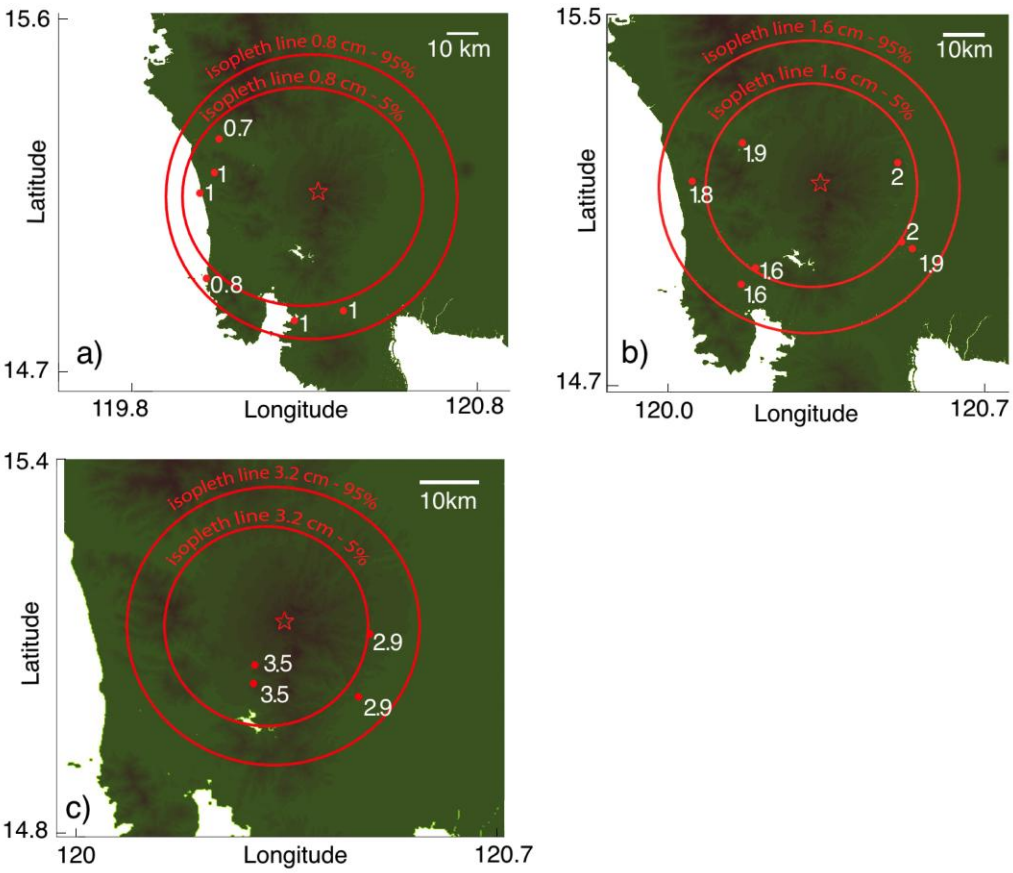

Figure 5.5: Mount Pinatubo, 1991: comparison of field data points (in cm; red dots) with computed isopleth contours (red lines) with confidence levels of 5% and 95%. Isopleth contours are computed for the following lithic sizes: a) 0.8 cm b) 1.6 cm c) 3.2 cm.

Mount St Helens 1980, transitional plume

On 18 May 1980, a Plinian eruption occurred at Mount St Helens (USA), (Carey et al., 1990). Four distinct phases were identified for the entire eruption: B1 and B2 phases associated with Plinian fallout; B3 phase, characterized by a pyroclastic density current (PDC) and associated co-PDC plumes; and B4 phase, characterized by a Plinian column up to 19 km a.s.l. (Carey et al., 1990). The comparison of our model is done with the lithic clasts (1 cm in diameter) of the B2 phase as reported in (Carey et al., 1990) (associated plume height of 17 km a.s.l.). This value is used as a reference for the simulations, leading to a reasonable MFR between $0.7 - 3 \times 10^8 \frac{kg}{s}$ (Degruyter and Bonadonna, 2012; Pouget et al., 2013). Fig. 5.6 shows a good agreement between computed isopleth contours for 1 cm sizes and field data with all the particles smaller than 1 cm plotting outside the confidence region.

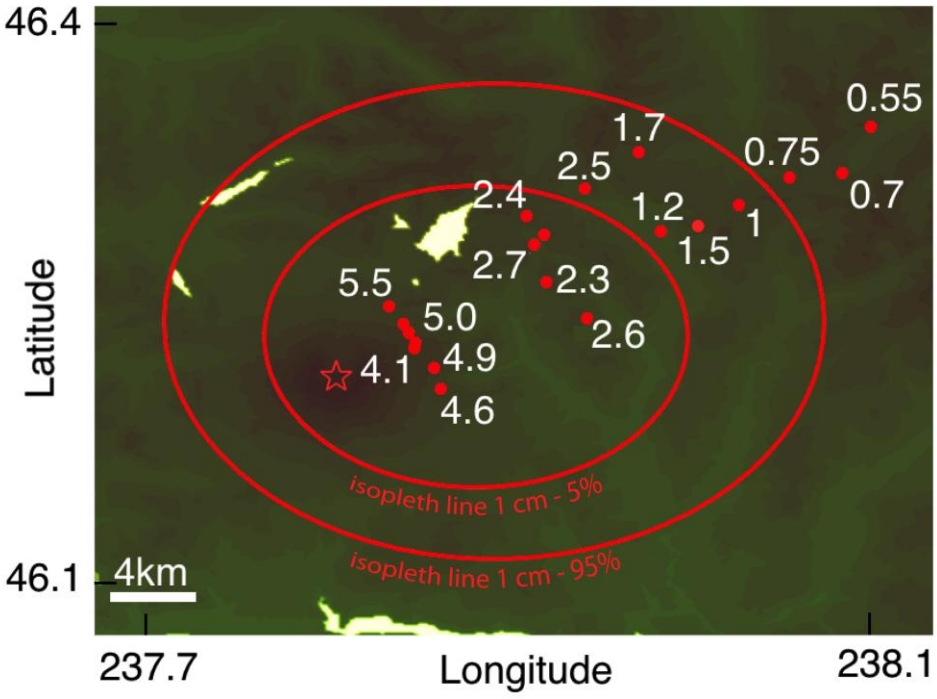

Figure 5.6 : Mount Saint Helens, 1980: comparison of field data points from the B2 phase (in cm; red dots) with computed isopleth contours (red lines) with confidence levels of 5% and 95%. Isopleth lines are computed for lithics with 1 cm of diameter.

Shinmoedake 2011, weak plume

Three sub-Plinian eruptions occurred at Mount Shinmoedake, Japan, at 2.30 pm (LT) of the 26th January 2011, at 2 am (LT) of the 27th January 2011 and at 3.40 pm (LT) of the 27th January 2011 (Maeno et al., 2014). During each of the three eruptions, the volcanic column reached an observed height of about 7 km above the vent (Maeno et al., 2014). The wind blew strongly towards southeast with a maximum intensity of 70 m/s at the tropopause (Suzuki and Koyaguchi, 2013). A sequence of meteorological profiles has been used to cover the time span from the onset to the end of the eruptive period. The observed largest clasts were determined based on the average of the 3 dimensions of the five largest clasts in a depositional plane of 0.5 m^2 at each outcrop (Maeno et al., 2014). The rapid increase of the eastward component of wind with height, combined with a major role of the gravity current for larger eruptions, results in a complex shape of the isopleth lines. However, the computed contours are generally in good agreement with field observations (i.e. pumice clasts of 0.9 cm in diameter; Fig. 5.7).

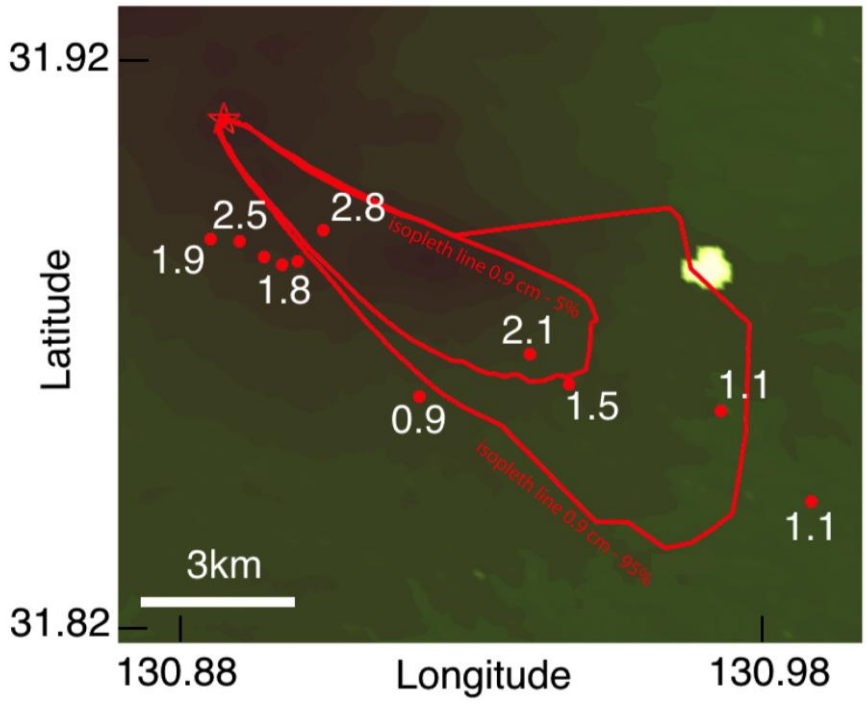

Figure 5.7: Shinmoedake, 2011: comparison of field data points for the three eruptions of 26th-27th of January 2011 (in cm; red dots) with computed isopleth contours (red lines) with confidence levels of 5% and 95%. Isopleth lines are computed for lithics with 0.9 cm diameter.

5.3.2.2 Comparison with observed plume heights based on the new nomograms

Following CS86, the resulting 3D plot showing downwind range vs. crosswind range vs. plume height is summarized in a 2D plot, i.e. the nomogram, where predefined height values are identified interpolating and extrapolating the information from the existing points (see Table S2 for eruptive conditions). Following CS86, meteorological parameters are described as a function of tropopause height and a default wind profile is expressed as a function of the maximum velocity at the tropopause. Four values of the wind velocity at the tropopause (V_{wind}^{max}) have been investigated: 0, 10, 20 and 30 m/s. Four sizes are initially considered for particles with a density of 2500 $\frac{kg}{m^3}$: 0.8 cm, 1.6 cm, 3.2 cm and 6.4 cm (and aerodynamic equivalent for different particle densities).

Particles are assumed to be spherical, i.e. with flatness and elongation equal to one. We also consider the standard atmospheric profile, i.e. with a tropopause height of 11 km, a surface temperature of 288 K and an average adiabatic lapse rate of the temperature in the troposphere of $-6.5\ K/km$ (Champion K. S. W., 1985). However, we discuss the effects particle shape and of arctic and tropical atmospheric profiles on the final nomograms in Appendices E.1 and E.2. Three main eruptive scenarios are defined for the compilation of nomograms mostly based on MFR and initial plume radius: *low intensity*, with radii less or equal to 50 meters; *intermediate intensity*, with radii comprised between 50 and 200 meters; *high intensity*, with radii comprised between 200 and 500 meters (see Table E.4.1 in *Appendix E* for more details). The choice of these three scenarios is in line with the three case studies considered: the *low intensity scenario* can be applied to events similar (or smaller) in MFR and boundary conditions to the 2011 eruption of Shinmoedake volcano, Japan; the *intermediate intensity scenario* can be applied to events similar to 1980 eruption of Mount St Helens, USA; the *high intensity scenario* can be applied to events similar or larger than the 1991 eruption of Mount Pinatubo, Philippines. The identification of plume scenarios helps differentiate eruptions associated with similar downwind and crosswind ranges but different initial conditions (i.e. mostly plume radius and MFR). As a matter of fact, the final deposition distance is a complex function of the shape of the clast support envelope and the sedimentation trajectory above and below the NBL. Two eruptions with different MFR and vent radii can be characterized by different envelopes but not necessarily by

different downwind and crosswind distances, if the effects of the gravity currents and the wind are considered. The use of three nomograms (associated with the three scenarios of initial eruptive conditions) for each particle size reduces considerably the uncertainties associated with the identification of plume height, if some constraints on the eruption are a priori known, such as expected intensity (small, intermediate or high) based on geometry and extension of isopleth and isopach maps. The comparison between the results obtained with the new nomograms, the CS86 nomograms, and observed heights is summarised in Table 1. In general, observed and predicted values show a good agreement: the relative differences between observed plume heights above the vent and predicted values are between a maximum value of 40%-50% for Shinmoedake and a minimum value of $< 1\%$ for Mount St Helens, with an average value of 16%. We refer to this last value as an indicator of the global uncertainty of the model. However, it is worth stressing that nomograms are compiled with no topography. If the difference in height Δ_v between vent location and collected field data is not negligible with respect to the column height, this would result in an overestimation of the predicted plume height using nomograms. In fact, a higher plume is required to produce the same sedimentation distance. We can notice that adding Δ_v to the plume height relative to the vent considerably reduces the relative error for Shinmoedake to 20-30%. For a fixed intensity scenario, nomograms are obtained averaging the outcomes of simulations with different initial plume radii, as in Table E.3.1 (Appendix E). This process unavoidably produces a set of different plume heights for a given pair of downwind and crosswind ranges in the nomogram. We quantified this variability evaluating the average, the minimum and the maximum plume heights for several pairs of downwind and crosswind ranges. The difference of maximum and minimum heights has been normalized to the average. Finally, we took the median of all the relative differences as a good unbiased indicator of the variability in a nomogram. We found that low intensity scenarios have smaller values of variability ($\approx 6\%$) respect to intermediate ($\approx 17\%$) and large intensity ones ($\approx 25\%$). A crucial aspect is that plume height computed with the new nomograms are lower between 8% and 30% than those obtained with CS86 (Tab. 5.1). As expected, this is due to the contribution of the tilted envelope on the sedimentation distances. Tilted envelopes can produce significant sedimentation distances even for small plume heights. However, in CS86 remarkable values of downwind ranges are uniquely associated with remarkable plume heights. Any

contribution of the initial position along the downwind axis for clast released from a tilted envelope is not taken into account. For most eruptions the intermediate scenario produces the best result. This is not surprising since this scenario spans a range of vent radii that is typical for most steady, explosive volcanic eruptions. The observed plume height for Mount Pinatubo ($z_{max} \approx 39\ km$ a. s. l.) is in between the predictions of the intermediate scenario ($z_{max} = 37\ km$ a. s. l.) and the large one ($z_{max} = 42\ km$ a. s. l.). Consequently, we can deduce that the large scenario is representative of very large events (e.g. ultra-Plinian eruptions), even larger than the 1991 Pinatubo eruption. This consideration should facilitate the practical use of the nomograms of Figures 5.8 and 5.9 (i.e. the intermediate scenario could be applied in most cases).

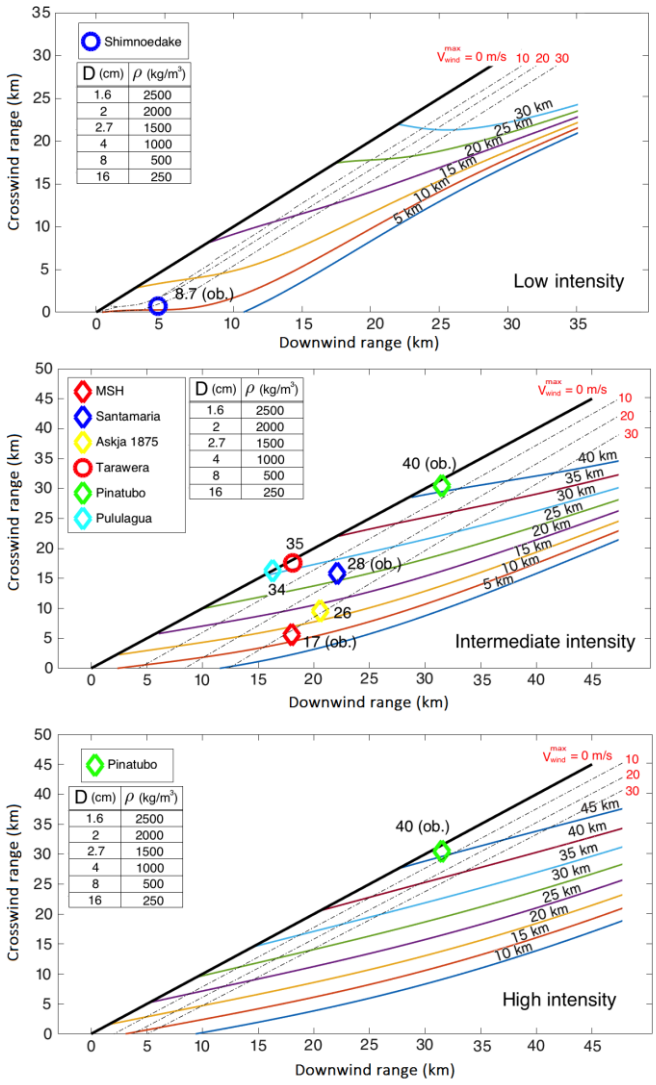

Figure 5.8: Nomograms for lithics of 1.6 cm of diameter and aerodynamically equivalent combinations of size and densities for 3 eruptive scenarios: low, intermediate and high intensity. Dashed lines represent pairs of points characterized with same values of maximum wind at the tropopause (V_{wind}^{max}).

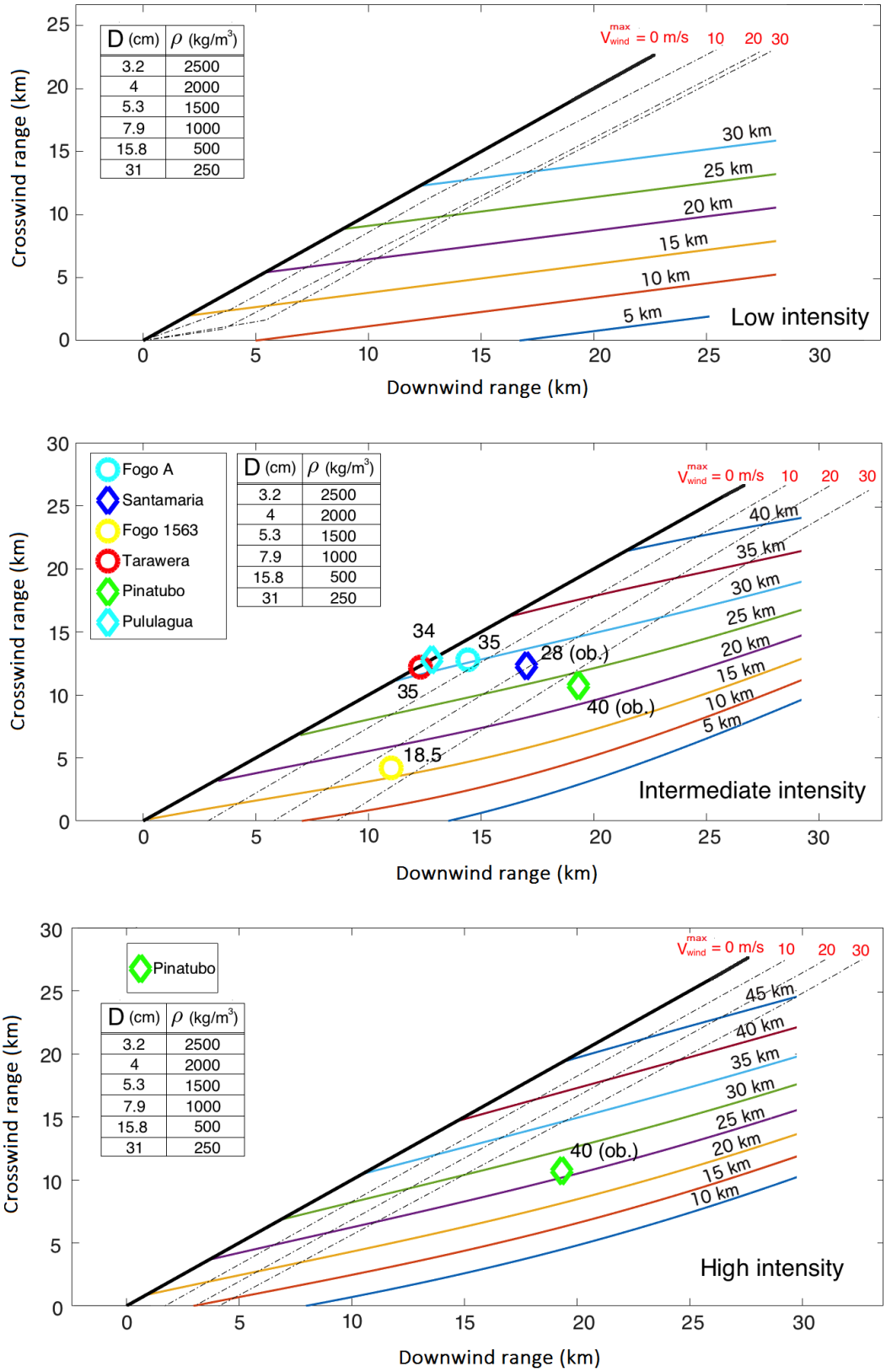

Figure 5.9: Nomograms for lithics of 3.2 cm of diameter and aerodynamically equivalent combinations of size and densities for 3 eruptive scenarios: low, intermediate and high intensity. Dashed lines represent pairs of points characterized with same values of maximum wind at the tropopause (V_{wind}^{max}).

5.4 Discussion

5.4.1 Advantages of the new model

The approach presented in this paper proposes a step forward in the methodologies of CS86 and BPH11. The first significant advantage is the use of tilted envelopes in presence of weak and transitional plumes (see Degruyter and Bonadonna (2012) and Bonadonna et al. (2015) for more detail on the characterization of weak and transitional plumes). If we compare the nomograms calculated in this study with those of CS86, we notice that the straight lines representing plumes with a fixed height are now replaced by bent curves that rise as the downwind range increases. Eruptions characterized by downwind range larger than the crosswind range are generally attributed to lower heights with respect to CS86. However, weak and transitional plumes are characterized by a non-negligible bending of the column along the wind direction. Therefore, particles may be released from the plume at a significant distance from the vent. As a result, large downwind ranges could be erroneously attributed to significantly higher plumes if the effect of the wind on the column is ignored. Second, both the computation of particle sedimentation trajectories and the coupling with complex meteorological data are novel implementations. In the new model, the full equation of motion is solved for each particle, i.e. sedimenting particles do not immediately move at their terminal velocity. In addition, for eruptions that occurred after 1979, the model can take advantage of three-dimensional meteorological profiles, time and space dependent. For historical eruptions, a standard wind profile is adapted to the entire grid following CS86. This implementation allows also for the description of dynamic wind profiles for long-lasting eruptions (e.g. 2011 Shinmoedake eruption; Fig. 5.7). Third, even though the nomograms have been compiled for spherical particles, the new model can also account for the effect of particle shape on settling velocity. In particular, the description of the drag coefficient used in the new model allows for the description of particle flatness and elongation as specified in Bagheri and Bonadonna (2016). In their work the authors show that for a given particle Reynolds number the drag of non-spherical particles is generally higher than an equivalent sphere. Therefore, non-spherical clasts are expected to have lower terminal velocities and longer sedimentation distances along the downwind and crosswind axes with respect to spheres. However, an exhaustive

discussion on the role of particle shape on the computation of isopleth contours is outside the aims of the present work. A brief example of the effects of different values of flatness and elongation is discussed in Appendix E.1. Finally, the new theoretical framework has been implemented as a Matlab package. The user can visualise the envelopes, the sedimentation paths, and isopleth contours. The input parameters are the initial eruptive conditions and the number of particles of a selected released size. The downwind and crosswind distances used for the compilation of nomograms are determined from the modelled isopleth contours. CS86 is prevalently used to invert the plume height based on crosswind and downwind distances. However, the model can have multiple applications. As an example, a forward use of the model allows for the compilation of probability maps required in hazard assessments (e.g. Osman et al. 2018).

5.4.2. Using the nomograms

Isopleth maps are compiled based on the distribution of the largest clasts observed at various distances from the vent. The two most common statistical strategies used to characterize the largest clasts are the average of the five largest clasts and the median value of a given population (e.g. Bonadonna et al. 2013). Osman et al. (2018) have shown that modelled isopleth contours as those presented here and in CS86 can be better compared with the arithmetic average of the geometric mean of the three axes of the five largest clasts. In addition, the collection of sub-spherical clasts is recommended for the application of standard nomograms, as they have been compiled based on the assumption of spheres. We present nomograms for a temperate climate zone, six densities, and three eruptive scenarios. However, eruptions may occur at almost any latitude and the characteristics of the clasts may not coincide with those considered in the nomograms. In Appendix E.2, we show how the application of nomograms of Fig. 5.8 and 5.9 to different latitudes can bring up to 20% additional error in the estimation of height. For higher accuracy, it is recommended to apply the provided Matlab package to specify more appropriate topography, meteorological profiles, particle density and particle shape.

Eruption	Observed plume height above the vent (km)	Observed plume height relatively to the altitude of the downwind range location (km)	Predicted plume height (this work) (km)	Predicted plume height (CS86) (km)
Calbuco 2015	15 (1)	16.5	17 (7)	18 (7)
Mount Saint Helens 1980	15 (3)	17 (B2 phase)	15	21
Pinatubo 1991	39 (4)	40	37-42	>43
Santamaria 1902	24-26 (5)	26-28	27	34
Shinmoedake 2011	7.3 (6)	8.4	10-11	8.6
Askja 1875	-	-	17-22	26
Fogo A	-	-	30.5	35
Fogo 1563	-	-	16	18.5
Pululagua 2450 BP	-	-	31	34
Tarawera 1886	-	-	30	34

Table 5.1: Comparison between observed plume height and prediction using our new nomograms and those of CS86. The observed plume height in the third column is considered relatively to the altitude of the extreme point of the downwind range (which is comparable to the height predicted by the nomograms). Observation techniques and references for observed plume heights: (1)(2) Radar observation, Vidal et al., (2017) (observations related to the 1st plume of Calbuco 2015, i.e. corresponding to Layer 1 of Castruccio et al. 2016); (3) Radar observations, Carey et al. (1990); (4) Satellite observation, Holasek et al. (1996); (5) Visual estimation, Anderson (1908); (6) Satellite observation, Maeno et al. (2014); (7) This prediction is based on the isopleth contour of 5 cm scoria clasts with a density of 1350 kg/m^3 (Castruccio et al., 2016; Layer 1) and our nomogram for particles with 5.3 cm and density of 1500 kg/m^3. The Calbuco 2015 eruption was not reported in the nomograms since clast size and density from field data do not perfectly match the combinations available in the plots. In this situation the methodology provides an upper or lower limit of the expected plume height, depending on the difference between the terminal velocities of the clast in the nomogram and the clast collected in the field.

5.4.3 Caveats

The main caveats of the presented model need to be discussed in order to assure a current application of the proposed methodology. First, the assumption that the effects of the atmospheric winds on the umbrella cloud are negligible compared to the gravity current leads to an overestimation of the upwind axis of the isopleth contours and an underestimation of the downwind distance. This approximation holds for large eruptions, where the velocity of the radial spreading is higher, but it is not necessarily verified for small ones (i.e. plume height < 10 km). However, the role of the gravity current on the sedimentation process with respect to the role of wind in the free atmosphere becomes less important as the plume height h_p decreases, given that the thickness of gravity current scales as $h_{gc} \sim 0.3\, h_p$ (Bonadonna and Phillips 2003). Second, the value of the wind V_{wind} in Eq. (5.2) (taken at the central axis of the plume) is assumed to depend only on the height z and not on the radial coordinate r. We can quantify the error that this assumption brings into Eq. (5.4). For a linear expansion of wind around its value along the central axis ($V_{wind} \approx c_1 \times r + c_0$), our approximation neglects the term $K_1 = \frac{2}{3} c_1 \times \cos(\theta) \times R$ in Eq. (5.4). For example, if we consider a typical wind profile as in CS86, the relative importance of the variation of wind velocity along the radial axis can be quantified as $\approx \frac{R\cos(\theta)}{z}$. From this relationship, it follows that our approximation is exact when $\theta \approx 90°$ (strong plumes and the initial part of weak plumes). However, by definition, weak plumes are characterized by lower exit velocity at the vent, a reduced radial entrainment and thus a slower increase of the radius respect to strong plumes for a fixed height. This produces $\frac{R}{z} < 1$ in most parts of the volcanic column for a weak plume, as also confirmed by the simulations with the one-dimensional plume model. We can thus deduce that our approximation holds for the most part of the column, with the exception of the upper part for weak plumes.

Finally, the drag formula of Bagheri and Bonadonna (2016) is derived under the assumption of laminar conditions in the upstream flow. We found that its application in a turbulent environment, i.e. inside the plume region, leads to an underestimation of the final maximum sedimentation distances of about 5% for low intensity scenarios, 3% for intermediate and less than 1% for large ones.

5.5 Conclusions

The present work introduces a new versatile and comprehensive methodology to determine plume height and wind speed from the distribution of the largest clasts around the volcano. The original approach of CS86 has been revised, generalised and modified to include important aspects of plume dynamics and particle sedimentation:

1. The effect of wind advection on the shape of the clast support envelope.
2. A new parameterization of the radial spreading of the umbrella cloud to avoid unrealistic velocities for distances smaller than the plume radius (which is where clast support envelopes are constructed).
3. The effect of the atmospheric structure at different latitudes on plume dynamics.
4. The effect of particle shape on particle sedimentation (clasts are described in terms of their flatness and elongation).
5. Three-dimensional ECMWF meteorological fields for eruptions after 1979.
6. Three-dimensional topography that allows tracing realistic isopleth contours on the ground.
7. The uncertainties related to the use of the nomograms are quantified.

For complex eruptive conditions and atmospheric conditions, the reader is recommended to apply the provided Matlab script to determine the associated plume height. However, for an easy application of the strategy, a set of 6 nomograms for three eruptive scenarios (low, intermediate and high intensity scenarios), 2 particle sizes (1.6 and 3.2 mm), density of 2500 kg/m^3, temperate latitude and spherical particle shape are presented. A set of aerodynamical equivalent sizes are also indicated for densities between 250-2500 kg/m^3. Discrepancies associated with tropical and arctic latitudes (between 7-20%) are also discussed in Appendix E.2.

Based on our analysis, we can conclude that:

1. Wind advection on plume rise results in bent clast-support envelopes, and, therefore, in a non-linear relationship between plume height and particle sedimentation, which requires the introduction of three eruptive scenarios for the compilation of nomograms.

2. For a given downwind distance, neglecting the role of the wind on clast-support envelops overestimates the plume height. Due to the effect of bent columns, heights of weak plumes estimated with the new nomograms are generally lower than those calculated with the CS86.
3. The effect of particle shape on particle sedimentation results in downwind distances 36 to 70% larger than the equivalent spheres.
4. The effect of atmospheric structure at different latitudes on plume dynamics is more significant for weak and transitional plumes than for strong plumes; discrepancies between plume height estimates at tropical and arctic latitudes with respect to temperate latitudes are between 7% and 20%.

5.6 Acknowledgments

The research leading to these results has received funding from the European Union Seventh Framework Programme (FP7/2007-2013) under the project NEMOH, grant agreement n° 289976. The authors would like to thank Sebastien Biass for his help in handling meteorological data. L. Mastin and D. Jassop are also thanked for their thorough review that largely improved the manuscript.

5.7 Author's contribution

E. Rossi contributed to the complete formalization of the theoretical framework and the codes that perform the computations contained in this chapter.

Appendix E.1 – Effects of clast shape on the computation of isopleth contours

The nomograms of section 5.3.2.2 are evaluated assuming spherical particles. However, the Matlab package associated with this study allows the use of non-spherical shapes in the evaluation of terminal velocities and thus in the final isopleth lines. The aim of this appendix is to provide an example of the influence of clast shapes on the downwind and crosswind ranges. We adopted the drag coefficient for irregular particles provided by Bagheri and Bonadonna (2016) that takes into account the effect of flatness and elongation on the drag. The form factors *flatness fl* and *elongation el* are expressed as a function of the longest (L), the intermediate (I) and the shortest (S) length of the particle ($fl = \frac{S}{I}$; $el = \frac{I}{L}$). These three parameters can be measured with the low operator-dependent error following the so-called *projection area protocol* (Bagheri et al., 2015). The drag coefficient is expressed as:

$$C_d = \frac{24}{Re_p}\, k_S \left(1 + 0.125 \cdot \left(Re_p \frac{k_N}{k_S}\right)^{2/3}\right) + \frac{0.46\, k_N}{1 + 5330/(Re_p \cdot k_N/k_S)} \qquad \text{(Eq.E.1.1)}$$

The drag coefficient is a function of the particle Reynolds number Re_p and two numbers associated with the shape of the objects: the Newton's drag correction $k_N = 10^{[0.45 \cdot (-\log(F_N)^{0.99})]}$ and the Stokes' drag correction $k_S = \frac{1}{2}\left(F_S^{1/3} + F_S^{-1/3}\right)$. We use simplified expressions to relate F_S and F_N with the flatness and elongation of the particle. Using Table 8 in Bagheri and Bonadonna (2016), we have $F_S = fl \cdot el^{1.3}$ and $F_N = fl^2 \cdot el$. As an example, we discuss the application to the tephra deposit associated with the 1980 eruption of Mt St Helens. Initial parameters are fixed and selected from one of the combinations reported in Table E.3.1 (see *appendix E.3*). We consider particles with a geometric diameter of 1 cm and four different shapes: spherical ($fl = el = 1$), disk-like ($fl = 0.1; el = 1$), needle-like ($fl = 1; el = 0.1$) and intermediate ($fl = el = 0.5$). According to Fig. E.1.1, the sedimentation of non-spherical particles results in larger downwind and crosswind ranges with respect to the sedimentation of spherical particles. In particular, needle-like and disk-like shapes can have downwind distances that are 36% and 70% larger than those of spheres, respectively. Given that, for simplicity, nomograms can only be constructed based on the

spherical assumptions, particular attention should be given when applied to very irregular clasts. As a rule of thumb, the flatter the clast the larger the distance travelled, and plume height could be underestimated. For best results in the determination of plume height, we recommend collecting sub-spherical clasts for the compilation of isopleth maps (e.g. Bonadonna et al. 2013). Alternatively, in case most available clasts are irregular, the direct use of the proposed script (where particle flatness and elongation can be specified) is recommended instead of using nomograms.

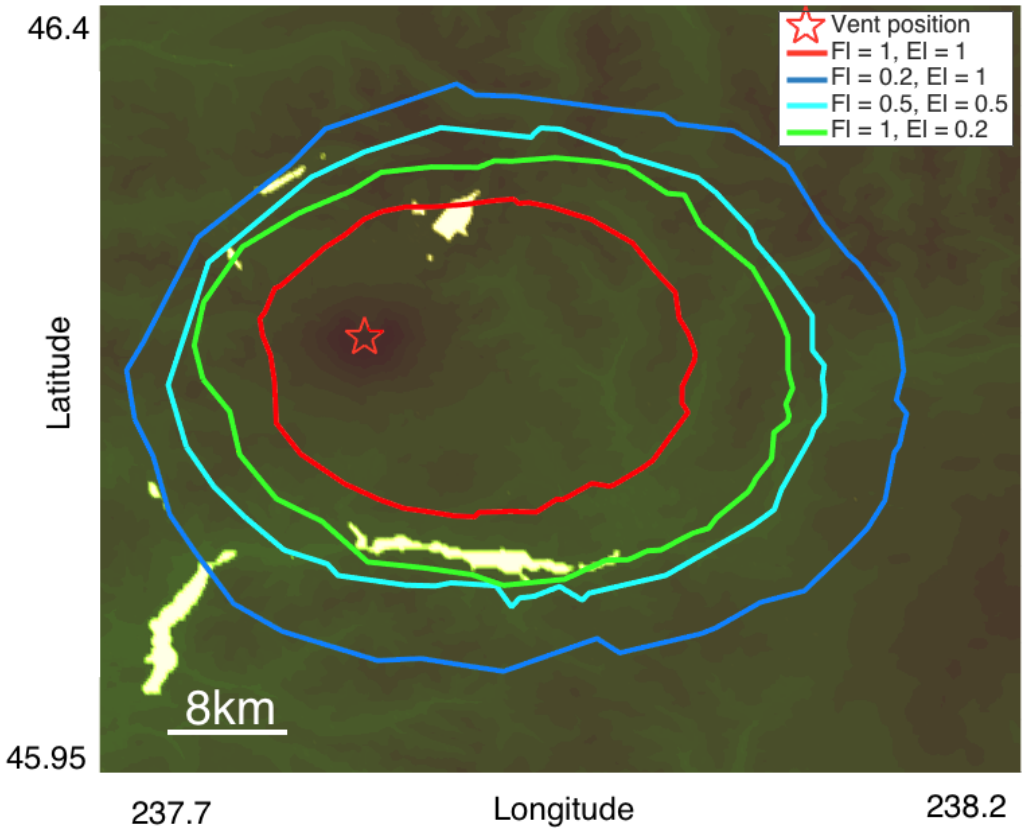

Figure E.1.1: Effect of particle shape on the sedimentation distances for lithics with a diameter of 1 cm. Four different shapes are investigated: spheres (fl = el =1), disk-like (fl =0.1; el =1), needle-like (fl =1, el =0.1) and intermediate (fl = el =0.5).

Appendix E.2 – Effects of different climate zones on the use of the nomograms

Plume rise depends on the density differences between the gas mixture and the atmosphere and thus, ultimately, on the atmospheric temperature. Different atmospheric profiles, notably different tropopause heights and temperature profiles, will affect both plume dynamics and sedimentation processes. This appendix provides an estimation of the error associated with using the nomograms provided in this study, evaluated for a temperate profile, for eruptions characterized by different atmospheric profiles. We tested two alternatives: a *tropical profile*, defined for latitudes between the 23rd parallels north and south of the equator with a tropopause height of 15 km, a surface temperature of 293 K and a moist adiabatic lapse rate in the troposphere of $-5.7\ K/km$. An *arctic profile*, defined for latitudes situated poleward from the 66th parallel, with a tropopause height of 8 km, a surface temperature of 273 K and a moist adiabatic lapse rate in the troposphere of $-8\ K/km$. Tropopause heights as a function of the latitude are reported in Shapiro et al. (1987). Assuming the same wind profile as in CS86, for a maximum wind velocity at the tropopause of 30 m/s the increase of wind velocities with height in the tropopause is faster in the Arctic region ($0.003\ s^{-1}$) than in the tropical one ($0.002\ s^{-1}$). Tests show that for the same initial conditions the arctic profile generally produces lower plume heights with respect to the standard and tropical profiles. However, the broader shape of the envelope under arctic conditions results in slightly larger sedimentation distances. In the following discussion, we refer to the heights provided by the plume model as the *model height* (h_{pb}) and those evaluated with the nomograms as the *nomogram height* (h_{pp}). The match between the model and the nomogram height provides an indication of the error associated in using nomograms with different atmospheric profiles with respect to the standard temperate. Tables E.2.1 and E.2.2 show the differences Δ_h in percentage between the benchmark and the predicted height for the arctic and tropical profile, respectively ($i.e. \Delta_h = 100 \times \left|\frac{h_{pp}-h_{pb}}{h_{pb}}\right|$). We notice that high intensity scenarios are less affected by the choice of the atmospheric profile ($\Delta_h = 7\%$) than low and intermediate intensity scenarios ($\Delta_h = 7 - 20\%$). The large MFR and initial radii reduce the relative importance of the atmosphere on the plume rise height. It is worth stressing that the uncertainties

introduced by atmospheric conditions should be added to the intrinsic uncertainties associated with the model if nomograms are used for eruptions not located at a temperate latitude.

Size (mm)	**Intensity scenario**	Δ_h (%)			
		Wind @ tropopause(m/s)			
		0	**10**	**20**	**30**
16	Low/Intermediate	8%	10%	16%	12%
16	High	5%	6%	5%	7%
32	Low/Intermediate	18%	18%	20%	20%
32	High	5%	5%	6%	5%

Table E.2.1 Arctic atmospheric profile. Differences between plume height predicted using the nomograms of Figures 5.8 and 5.9 and plume heights computed with the integral plume model, expressed in terms of the quantity Δ_h.

Size (mm)	**Intensity scenario**	Δ_h (%)			
		Wind @ tropopause (m/s)			
		0	**10**	**20**	**30**
16	Low/Intermediate	13%	12%	16%	20%
16	High	7%	7%	6%	7%
32	Low/Intermediate	9%	11%	13%	16%
32	High	8%	7%	7%	8%

Table E.2.2 Tropical atmospheric profile. Differences between plume heights predicted using the nomograms of Figures 5.8 and 5.9 and plume heights computed with the integral plume model, expressed in terms of the quantity Δ_h.

Appendix E.3 – Range of initial conditions used for the comparison

The validation process of the model is based on the comparison between field data and computed isopleth lines. However, the determination of the isopleth lines is strongly influenced by the actual maximum Mass Flow Rate (MFR) of an eruption. This value depends on the fluctuations that occur during the eruption and thus it can differ from the MFR reported in the literature. Moreover, several additional parameters influence the shape of the clast support envelope and clast sedimentation, such as the initial plume radius, the initial mass fraction of solid particles, plume temperature, the shape of particles. All these values are usually not easily constrained and a probabilistic approach is preferred in order to span the outcome of a given eruption. In table E.3.1 we report the range of initial conditions used for the validation of the model. Three eruptions are used in this phase: the 1991 Pinatubo eruption, Philippines; the 1980 Mount St Helens eruption, USA; the 2011 Shinmoedake eruption, Japan.

Table E.3.1 – Range of initial conditions used for the validation of the model.

Eruption	MFR (Kg/s)	Plume temperature (K)	Elongation or Flatness	Particles density (kg/m^3)	Mass fraction solid (%)	Radius (m)	N Simulations
Pinatubo	0.8-1.2 1e9	1100 - 1400	0.5-1	2600-2700	95-97	200-500	200
MSH	0.7-1 1e8	1100 - 1400	0.5-1	2600-2700	95-97	50-200	200
Shinmoe-dake	1-4 1e6	1100 - 1400	0.5-1	1100-1300	95-97	25-50	100

Appendix E.4 – Definition of the eruptive scenarios

Scenario	Radius
Low intensity	$r \leq 50\ m$
Intermediate intensity	$50\ m \leq r \leq 200\ m$
Large intensity	$200\ m \leq r \leq 500\ m$

Table E. 4.1. Definition of the three eruptive scenarios applied to the compilation of the nomograms of Figures 5.8 and 5.9

Appendix E.5 – List of mathematical symbols of chapter 5

Table E. 5.1. Definition of mathematical symbols used in chapter 5

Symbol	Definition	Unit
A	Projected area ($A \approx \frac{\pi}{4} d^2$) of a single clast	m^2
b	Gaussian width parameter $\frac{R^2}{b^2} = 2$	m
c_a	Specific heat capacity of the air	$J\ kg^{-1}K^{-1}$
c_b	Specific heat capacity of the mixture	$J\ kg^{-1}K^{-1}$
C_d	Drag coefficient	-
c_0	Zero-order coefficient of the Taylor series expansion for wind velocity as a function of the radial coordinate r	$m\ s^{-1}$
c_1	First-order coefficient of the Taylor series expansion for wind velocity as a function of the radial coordinate r	s^{-1}
d_c	Clast diameter	m
E_{tot}^{NBL}	Volumetric flow rate	$m^3\ s$
el	Clast elongation $el = \frac{I}{L}$	-

$\vec{F}_{drag}$	Drag force	N
$\vec{F}_g$	Gravitational force	N
fl	Clast flatness $fl = \frac{S}{I}$	-
g	Gravitational acceleration	$m\ s^{-2}$
h_{gc}	Height of the gravity current	m
H_{NBL}	Height of the Neutral Buoyancy Level (NBL)	m
h_{pb}	Maximum height of the plume used as benchmark for testing the effect of different latitudes	m
h_{pp}	Maximum plume height predicted by the nomograms	m
H_S	Height in the stratosphere where the CS86 wind profile assumes the constant value of $0.75\ V_{wind}^{max}$	m
H_T	Height of the tropopause	m
I	Intermediate length of the clast	m
K_1	Error in the Gaussian velocity profile of Eq.5.4 assuming a wind profile that not depends on r. K_1 holds under the hypothesis of a linear relation for wind velocity and radial coordinate, i.e. $V_{wind} \approx c_1 \cdot r + c_2$	$m\ s^{-1}$
k_N	Newton's drag correction factor	-
k_S	Stokes' drag correction factor	-
L	Longest length of the clast	m
m_c	Mass of a single clast	kg
N	Atmospheric buoyancy frequency	s^{-1}
n_d	Mass fraction of dry gas component	-
n_s	Mass fraction of solid component	-
n_v	Mass fraction of water vapour component	-
P_{atm}	Atmospheric pressure	Pa
P_{sat}	Saturation pressure of water vapour	Pa
Q_d	Mass flux of dry air	$kg\ s^{-1}$
Q_s	Mass flux of solid phase	$kg\ s^{-1}$

Q_{tot}	Total mass flux $Q_{tot} = Q_d + Q_v + Q_s$	$kg\ s^{-1}$
Q_v	Mass flux of water vapour	$kg\ s^{-1}$
r	Radial coordinate along plume radius	m
r_h	Relative humidity	-
R	Top-hat radius of the plume	m
R_d	Gas constant of dry air	$J\ kg^{-1}\ mol^{-1}$
R_{env}	Radius of the clast support envelope	m
Re_p	Particle Reynolds number	-
R_g	Gas constant of the mixture	$J\ kg^{-1}\ mol^{-1}$
R_v	Gas constant of waer vapour	$J\ kg^{-1}\ mol^{-1}$
s	Curvilinear coordinate along the center-line of the plume	m
S	Shortest length of the clast	m
T_b	Plume temperature	K
$\vec{U}_c^i$	Velocity of the *i-esim* sedimenting clast	$m\ s^{-1}$
U_{entr}	Velocity of the entrained atmospheric air	$m\ s^{-1}$
$\vec{U}_f$	Velocity of the surrounding fluid for a sedimenting particle	$m\ s^{-1}$
U_g	Gaussian profile of plume velocity	$m\ s^{-1}$
U_g^*	Maximum value of plume velocity at the center line	$m\ s^{-1}$
U_{gc}	Velocity of the radial spreading of the umbrella cloud	$m\ s^{-1}$
U_{tv}	Terminal velocity of an object	$m\ s^{-1}$
U_{th}	Top-hat profile of plume velocity	$m\ s^{-1}$
V_{wind}	Modulus of wind velocity	$m\ s^{-1}$
$\bar{V}_{wind}$	Modulus of wind velocity	$m\ s^{-1}$
V_{wind}^{max}	Maximum value of the modulus of wind velocity at the tropopause	$m\ s^{-1}$
x	East-ward coordinate in the Cartesian system of reference	m
y	North-ward coordinate in the Cartesian system of reference	m
w_a	Mass ratio of water vapor to air in the atmosphere	-

w_s	Mass ratio of water vapor to air under saturated conditions	-
z	Vertical coordinate in the Cartesian system of reference	m
z_{max}	Maximum plume height	m
α_e	Entrainment coefficient along the axis of the plume	-
β_e	Entrainment coefficient along the radial component of the plume	-
Δ_h	Difference between the benchmark and the predicted height, normalized to the height of the benchmark, expressed as a percentage	%
Δ_v	Difference in height between vent altitude and the altitude of the field location at the downwind range	-
θ	Angle of the plume central axis respect to the ground	rad
λ	Geometrical correction factor for the gravity current $\lambda \approx 1$	-
ρ_{atm}^{d}	Density of dry air	$kg\ m^{-3}$
ρ_{atm}^{v}	Density of water vapour	$kg\ m^{-3}$
ρ_b	Bulk density of the plume mixture	$kg\ m^{-3}$
ρ_c	Density of the clast	$kg\ m^{-3}$
ρ_f	Density of the fluid surrounding the clast	$kg\ m^{-3}$
ρ_{gas}	Density of the gas phase	$kg\ m^{-3}$
ρ_s	Density of the solid phase inside the plume model	$kg\ m^{-3}$
Φ_a	Azimuthal wind angle	rad

Chapter 6

Concluding remarks

In this thesis new methodologies for the study of ash sedimentation are presented, with a specific attention to particle aggregation and to the characterization of large clasts dynamics. First, a discrete solution of the one-dimensional Smoluchowski equation applied to a thermal plume model is discussed (chapter 2). Second, a complete mathematical description is introduced (chapter 3), where the solution of aggregation problems has been obtained in a general form. Third, this new theoretical framework was combined with a 1-D steady state plume model in order to provide an exhaustive and versatile tool of investigation of ash aggregation processes within the eruptive column (Chapter 4). Finally, in chapter 5 an improved methodology for the study of large clasts sedimentation and their associated hazard assessment is presented.

6.1 Application of a discretized solution of Smoluchowski equation to the study of a real eruption

In chapter 2 a numerical solution of the one-dimensional Smoluchowski equation is combined with the equations governing time evolution of a thermal plume model. The main goal is to compare specific outputs of the model with observed quantities from field observations for weak Vulcanian eruptions occurred at Mount Sakurajima, Japan, between July and August 2013. The observations used in this chapter are reported in Bagheri et al. (2016). The internal parameter *mass* is sampled over a discrete set of values according to the Fixed Pivot technique (FP) (Kumar and Ramkrishna, 1996). The continuous Smoluchowski coagulation equation is discretized according to these bins and then coupled with the equations governing the solid phases mass flux inside the thermal. It results in a set of Ordinary Differential Equations (ODEs) that can be solved simultaneously to the plume equations. Sensitivity tests are performed in order to investigate the role of disaggregation in the gas thrust region, several mass fractions for

the each initial gas phase, the role of sticking efficiency on the final distribution. The sticking efficiency is assumed to follow the parameterization of Costa et al. (2010). As expected, it results that aggregation is very sensitive to the initial value of the mass fraction of the solid phase, since it influences particles concentration. Moreover, considering aggregation in the first parts of the plume leads to a sensitive overestimation of the number of the aggregates in the larger sizes. As a matter of fact disaggregation should also occur in this highly energetic region. However, the importance of this effect decreases rapidly with the distance from the vent. A key aspect of the study is represented by the timescale governing aggregation processes in a volcanic plume. This parameter is defined as the time a population needs to not evolve further due to aggregation processes and it can be easily compared with observed values. The initial TGSD assumed in this test has been set equal to the TGSD of a weak Vulcanian eruption occurred at Montserrat on the 18 of July 2008 (Cole et al., 2014). For the eruption under analysis, the time needed for the observed aggregates to form is about 180 s (Bagheri et al., 2016). The timescales t_s estimated from our model are reported in table 2.2 for four eruptive scenarios. Since the computed timescale is relative to all the possible aggregation events in the thermal, we can conclude that scenarios 1 to 3 are all a priori possible. A larger number of observations along the dispersal axis of the cloud are needed to better constrain the most realistic scenario. However this simplified approach demonstrates the possibility to successfully use the fixed pivot technique to study aggregation in volcanic environments.

6.2 The Generalized Fixed Pivot Technique

An innovative methodology to treat aggregation of complex objects is presented in chapter 3. We named this approach the *Generalized Fixed Pivot Technique* (GFPT). The GFPT is an extension of the Fixed Pivot method (FP) (Kumar and Ramkrishna, 1996) that allows treating aggregation of arbitrary properties. As a matter of fact, the original Smoluchowski Coagulation Equation (SCE) is based on a mass conservation balance (Smoluchowski, 1916). Only one single internal parameter is treated, mass. However, solid aggregates with the same mass may have different properties, such as their density. The need to characterize sedimentation processes in volcanic eruptions has led

to the creation of the GFPT. In the GFPT the population under analysis is described in terms of multiple arbitrary properties $\boldsymbol{p} = \{p_1, p_2, \dots, p_n\}$, internal properties of the final objects $\boldsymbol{p_{1+2}}$ and the balance equations are discretized following the FP procedure. The space of the internal parameters is subdivided in n-dimensional elements of arbitrary shape (*cells*), identified with a single internal point (*pivot*). The position of the pivots is rigorously fixed. The rigorous mathematical demonstration of chapter 3 states that the GFPT can be applied both to additive properties, such as mass, as well as to non additive ones, like density, porosity, colours. The final Ordinary Differential Equation (ODE) that governs the creation of objects in a given cell i can be written according to the GFPT as:

$$\frac{\partial N_i(t)}{\partial t} = B_i - D_i \tag{6.1}$$

$$B_i = \frac{1}{2}\sum_{j=1}^{N_c}\sum_{k=1}^{N_c}\sum_{\boldsymbol{p_{1+2}}(\boldsymbol{p_j},\boldsymbol{p_k})\subseteq\Delta_s} W_s(\boldsymbol{p_{1+2}}(\boldsymbol{p_j},\boldsymbol{p_k}),\boldsymbol{p_i})\; K(\boldsymbol{p_j},\boldsymbol{p_k})\, N_j N_k \tag{6.2}$$

$$D_i = N_i \sum_{k=1}^{N_c} K(\boldsymbol{p_i},\boldsymbol{p_k})\, N_k \tag{6.3}$$

The multidimensional matrix $K(\boldsymbol{p_j},\boldsymbol{p_k}) = \alpha(\boldsymbol{p_j},\boldsymbol{p_k}) \cdot \beta(\boldsymbol{p_j},\boldsymbol{p_k})$ indicates the aggregation kernel, α the sticking efficiency, β the collision frequency. The quantities $W_s(\boldsymbol{p_{1+2}}(\boldsymbol{p_j},\boldsymbol{p_k}),\boldsymbol{p_i})$ are necessary to attribute newborn particles to the existing network of pivots. The definition of $W_s(\boldsymbol{p_{1+2}}(\boldsymbol{p_j},\boldsymbol{p_k}),\boldsymbol{p_i})$ is based on the a-priori conservation of $n+1$ properties Q, where usually $Q(1)$ is the number of particles and $Q(2), \dots, Q(n+1) = \boldsymbol{p}$.

$$\sum_{i=1}^{N_p} W_{Id(i)}\left(\boldsymbol{p_{1+2}},\boldsymbol{p_{id(i)}}\right) \cdot\; Q_j(\boldsymbol{p_{Id(i)}}) = Q(\boldsymbol{p_{1+2}}) \tag{6.4}$$

In chapter 3 two examples of application of the GFPT are discussed: the interaction of liquid paint droplets and the sedimentation in a vertical laboratory column. These

examples are thought to underline the great versatility and the high degree of abstraction of our formalism.

6.3 Aggregation in volcanic plumes

In chapter 4 the GFPT has been applied to the study of ash aggregation in volcanic plumes, where particle concentrations is thought to have its maximum value (Veitch and Woods, 2001). The main goal is to provide a coherent theory to describe the problem of aggregates with different densities. The strategy adopted can be summarised as follows:

- Definition of mass and porosity as two internal parameters.
- Definition of a bi-dimensional grid in the space of the internal parameters.
- Evaluation of the weights $W_s(\boldsymbol{p_{1+2}}(\boldsymbol{p_j}, \boldsymbol{p_k}), \boldsymbol{p_i})$ (Eq.6.4).
- Definition of a relationship between the porosities of two colliding objects and the porosity of the resultant object. A simplified code to simulate virtual aggregates has been created. Literature formulae for the specific case of fractal objects are also provided.
- Definition of one-dimensional steady-state equations for plume model. The scheme adopted in this work is a combination of (Woods, 1993), Woodhouse et al. (2013) and Folch et al. (2016). These schemes allows for an approximated parameterization of the relative humidity inside the plume.
- Definition of the atmospheric profile and topography.
- Modification of the mass fraction of the solid phase in order to take into account the creation of objects in the GFPT cell i:

$$\frac{d}{ds}(Q_{si}) = m_i \, \pi \, R_p^2 \cdot (B_i - D_i) \tag{6.5}$$

  Where B_i and D_i are given by Eq. (6.1), (6.2)

Then for each s-step in the plume rise we evaluate:

- Computation of the collisional velocity associated with each cell i that defines the quantity β in Eq. (6.2).
- Computation of the sticking process in action as a function of the temperature and the relative humidity. This stage defines the quantity α in Eq. (6.2).

The above procedure is a complete and innovative recipe for the study of ash aggregation in volcanic plumes.

We found that in a volcanic plume the main collision mechanism should be associated with the different reactions of particles to the turbulent vortexes. This mechanism, named the *turbulent differential coupling*, has been applied for the first time to volcanic plumes. As a matter of fact, the common description based on Saffman-Turner limit seems to be not easily verified in a volcanic context (Textor and Ernst, 2004). Moreover an alternative formulation of the gravitational collection kernel has been introduced in order to take into account the effect of the upward plume velocity as in Carey and Sparks (1986). Two main models for aggregate sticking have been adopted: a model for wet sticking (Ennis et al., 1991), and a model for dry sticking (Chen et al., 2015). As expected the dissipation mechanisms associated with wet sticking are at least one order of magnitude more efficient than those associated with dry sticking (i.e. adhesion and viscoelastic forces). The role of hygroscopy in ash aggregation has been taken into account as a possible mechanism to explain aggregation in sub-saturated plumes. It results that a hygroscopic water layer for a relative humidity of 95% ($thickness \approx nm$) can dissipate twice the collision kinetic with respect to dry aggregation.

6.4 Sedimentation of large clasts

A new strategy for the estimation of plume height based on the ground deposition of large clasts is presented in chapter 5. Our approach consists in a revised version of the methodology introduced by Carey and Sparks (1986) (here named *CS method*), where the effect of the wind on the eruptive column is now taken into account. Particles are released from the clast support envelope, internal regions of the plume where the terminal velocity of the objects equals the upward plume velocity. Their trajectories are then computed solving the full Newton's second law. The complete procedure is implemented in a Matlab code that can be applied to single eruptions with a three dimensional topography and meteorological data. Running thousands of simulations with different meteorological conditions is then possible to relate the maximum downwind and crosswind distances with the height of the plume. This information is stored in a set of plots, *nomograms*, that allows for inverse process: determining the

height of the plume based on isopleth contour dimensions. One of the main limitations of the original CS method is that, neglecting the effect of wind advection on plume rise, it can rigorously be applied only to *strong plumes*. The new model avoids this restriction and it can be applied to all plumes, i.e. *weak*, *transitional* and *strong* plumes. Moreover three intensity scenarios are defined according to the initial plume radius r_0 and the Mass Eruption Rate (MER): *low intensity* ($r_0 \leq 50\,m$; $MER \leq 1e6$), *intermediate intensity* ($50\,m \leq r \leq 200\,m$; $1e6 < MER \leq 5e8$) and *high intensity* ($200\,m \leq r \leq 500\,m$; $MER > 5e8$). This choice increases the accuracy of the predictions and is necessary because the effect of wind on plume rise makes the function between plume height and clast deposition non-linear. The most important outcome of the model is a new set of nomograms that can be used for every eruptive and meteorological condition. Table 5.2 shows that for increasing wind velocities the height associated with eruption is smaller, if compared with the CS nomograms. This interesting result is explained taking into account that part of the downwind distance of an object is now attributed to the tilted plume.

Additional aspects are also investigated in chapter 5: the role of particle shape on sedimentation distance, a new parameterization of the gravity current, and the effect of latitude on atmospheric profiles. Extreme particle shapes, such as needle-like and disk-like, are characterized by downwind distances that can be up to 36% and 70% larger than those evaluated for spheres, respectively. For high intensity scenarios, we also estimated a relative error of 7% when using for high and low latitudes a nomogram calibrated for middle latitudes. However, the relative error rises up to a 20% for small or intermediate scenarios. This result reflects the property of large eruptions to be relatively less affected from the surrounding atmospheric profiles, if compared to smaller ones. A final consideration is the possibility to use newly developed Matlab code to compile probability maps for the assessment of hazard associated with the sedimentation of large clasts. A recent application of this strategy for the hazard assessment at Mount Etna, Italy, can be found in (Osman et. al, submitted).

6.5 Future perspectives

Even though new comprehensive models have been presented for the characterization and parameterization of both particle aggregation and large clast sedimentation, more

investigations are required to have an exhaustive description of particle fallout during explosive volcanic eruptions. Relatively to the methodologies presented in this thesis, we cite five aspects that require further attention in the future. First, the theoretical framework for ash aggregation presented in this thesis is only a preliminary step towards a better understanding of ash aggregation. In order for this framework to be used operationally, it still needs to be validated, systematically tested and combined with additional field observations. In particular, dedicated field and laboratory experiments need to be set up in order to produce ad hoc data for model validation. Second, a more general algorithm is required in order to fully simulate aggregate porosities. Algorithms based on the minimization principles could be applied to the construction of more realistic virtual objects. Without the limitation of the basic algorithm presented here, the real population of particles observed on the surface of cored aggregates could be applied to virtual objects. This would result in a more reliable relationship between collisions and associated porosities. Third, a more efficient solution of the multidimensional aggregation equations is probably required for an operational use of the model. The increase in the dimensionality p of the problem scales as N^p, where N is the number of cells considered in the GFPT. This means that the use of more than three variables is practically impossible. An alternative solution can be derived from the method of moments (Marchisio and Fox, 2005). This methodology is based on the solution of bulk properties of the multidimensional distribution of particles f. This results in a tremendous speed up of the entire solution. The price is the loss of information on the details of density function f. Fourth, experimental investigations are needed to support the theoretical description of collisional frequencies and sticking efficiency adopted in this thesis. The experimental investigation should be focused in detail on the validation of Ennis and Chen models. Fifth, further extensions of the nomograms elaborated in this work should be proposed for particle shapes. We found that for extreme shaped objects the sedimentation distance are affected tremendously.

Under a more general perspective, if we consider the future challenges associated with ash aggregation, a key aspect that emerges from this thesis is the importance of a multidisciplinary approach of the investigation techniques. In fact, field observations of cored aggregates at Sakurajima have been the main motivation to extend the theoretical framework into a multi-dimensional description. However, field observations require advanced techniques in order to capture an unbiased reconstruction of the phenomena.

In the recent past, the contemporary use of high-speed cameras and ash collectors revealed to be a promising tool of investigation for aggregation. Improvements can regard the addition of ash concentrations measurements in the cloud, using Optical Particles Counters (OPC), drones or aerostatic balloons, and a better way to preserve the structure of collected aggregates avoiding disaggregation. A better observation of natural phenomena results in a more defined constrain for theoretical models, improving their predictions. In turn, theoretical models can suggest new field and experimental investigations. As a matter of fact, one of the key points addressed in this thesis is the link between sticking processes and environmental parameters. The concept of dissipation of relative kinetic energy in a collision is as crucial as tricky to assess in field campaign. Laboratory experiments are the perfect tool to recreate observed conditions in controlled environments and to simplify the intrinsic natural complexities.

These considerations show how the future of tephra investigations is thus related to a synergic approach between field, laboratory and theoretical studies. A multidisciplinary view of the problems triggers a virtuous circle, which in turn stimulates the progress in research and helps society in reducing the consequences of volcanic eruptions. The fragile coexistence of billions of people over a live and active planet requires the scientific community to be ready to measure up with new challenges, from new perspectives.

Bibliography

Abel, J.S., Stangle, G.C., Schilling, C.H. and Aksay, I.A., 1994. Sedimentation in flocculating colloidal suspensions. J. Mater. Res., 9(2): 451-461.

Abrahamson, J., 1975. Collision rates of small particles in a vigorously turbulent fluid. Chem. Eng. Sci., 30(11): 1371-1379.

Armienti, P., Macedonio, G. and Pareschi, M.T., 1988. A numerical model for simulation of tephra transport and deposition - Applications to May 18, 1980, Mount-St-Helens eruption. Journal of Geophysical Research-Solid Earth and Planets, 93(B6): 6463-6476.

Bagheri, G. and Bonadonna, C., 2016. On the drag of freely falling non-spherical particles. Powder Technol., 301: 526-544.

Bagheri, G., Rossi, E., Biass, S. and Bonadonna, C., 2016. Timing and nature of volcanic particle clusters based on field and numerical investigations. J. Volcanol. Geotherm. Res., 327: 520-530.

Bagheri, G.H., Bonadonna, C., Manzella, I. and Vonlanthen, P., 2015. On the characterization of size and shape of irregular particles. Powder Technol., 270: 141-153.

Biass, S., Bonadonna, C., Connor, L. and Connor, C., 2016. TephraProb: a Matlab package for probabilistic hazard assessments of tephra fallout. Journal of Applied Volcanology, 5(1): 10.

Biass, S., Scaini, C., Bonadonna, C., Folch, A., Smith, K. and Hoskuldsson, A., 2014. A multi-scale risk assessment for tephra fallout and airborne concentration from multiple Icelandic volcanoes - Part 1: Hazard assessment. Nat. Hazards Earth Syst. Sci., 14(8): 2265-2287.

Bonadonna, C. and Costa, A., 2012. Estimating the volume of tephra deposits: A new simple strategy. Geology, 40(5): 415-418.

Bonadonna, C., Genco, R., Gouhier, M., Pistolesi, M., Cioni, R., Alfano, F., Hoskuldsson, A. and Ripepe, M., 2011. Tephra sedimentation during the 2010 Eyjafjallajokull eruption (Iceland) from deposit, radar, and satellite observations. J. Geophys. Res.-Solid Earth, 116: 20.

Bonadonna, C. and Houghton, B.F., 2005. Total grain-size distribution and volume of tephra-fall deposits. Bulletin of Volcanology, 67(5): 441-456.

Bonadonna, C., Macedonio, G. and Sparks, R.S.J., 2002. Numerical modelling of tephra fallout associated with dome collapses and Vulcanian explosions: application to hazard assessment on Montserrat. Geological Society, London, Memoirs, 21(1): 517.

Bonadonna, C. and Phillips, J.C., 2003. Sedimentation from strong volcanic plumes. J. Geophys. Res.-Solid Earth, 108(B7): 28.

Brown, R.J., Bonadonna, C. and Durant, A.J., 2012. A review of volcanic ash aggregation. Phys. Chem. Earth, 45-46: 65-78.

Burden, R.E., Chen, L. and Phillips, J.C., 2013. A statistical method for determining the volume of volcanic fall deposits. Bulletin of Volcanology, 75(6): 10.

Burden, R.E., Phillips, J.C. and Hincks, T.K., 2011. Estimating volcanic plume heights from depositional clast size. J. Geophys. Res.-Solid Earth, 116: 13.

Burns, F.A., Bonadonna, C., Pioli, L., Cole, P.D. and Stinton, A., 2017. Ash aggregation during the 11 February 2010 partial dome collapse of the Soufriere Hills Volcano, Montserrat. J. Volcanol. Geotherm. Res., 335: 92-112.

Bursik, M., 2001. Effect of wind on the rise height of volcanic plumes. Geophysical Research Letters, 28(18): 3621-3624.

Calzavarini, E., Cencini, M., Lohse, D., Toschi, F. and Int Collaboration Turbulence, R., 2008. Quantifying turbulence-induced segregation of inertial particles. Phys. Rev. Lett., 101(8): 4.

Carey, S., Sigurdsson, H., Gardner, J.E. and Criswell, W., 1990. Variations in column height and magma discharge during the may 18, 1980, eruption of Moun St. Helens. J. Volcanol. Geotherm. Res., 43(1-4): 99-112.

Carey, S. and Sparks, R.S.J., 1986. Quantitative models of the fallout and dispersal of tephra from volcanic eruption columns. Bulletin of Volcanology, 48(2-3): 109-125.

Carey, S.N. and Sigurdsson, H., 1982. Influence of particle aggregation on deposition of distal tephra from the May 18, 1980, eruption of Mount St-Helens volcano. Journal of Geophysical Research, 87(NB8): 7061-7072.

Cerminara, M., Ongaro, T.E. and Neri, A., 2016. Large Eddy Simulation of gas-particle kinematic decoupling and turbulent entrainment in volcanic plumes. J. Volcanol. Geotherm. Res., 326: 143-171.

Chakraborty, J. and Kumar, S., 2007. A new framework for solution of multidimensional population balance equations. Chem. Eng. Sci., 62(15): 4112-4125.

Champion K. S. W., C.A.E., Kantor A. J., 1985. Standard and reference atmospheres. Handbook of geophysics and the space environment.

Chen, S., Li, S.Q. and Yang, M.M., 2015. Sticking/rebound criterion for collisions of small adhesive particles: Effects of impact parameter and particle size. Powder Technol., 274: 431-440.

Chiney, A. and Kumar, S., 2012. On the solution of bivariate population balance equations for aggregation: Pivotwise expansion of solution domain. Chem. Eng. Sci., 76: 14-25.

Cole, P.D., Smith, P.J., Stinton, A.J., Odbert, H.M., Bernstein, M.L., Komorowski, J.C. and Stewart, R., 2014. Chapter 5 Vulcanian explosions at Soufrière Hills Volcano, Montserrat between 2008 and 2010. Geological Society, London, Memoirs, 39(1): 93-111.

Cornell, W., Carey, S. and Sigurdsson, H., 1983. Computer-simulation of transport and deposition of the Campanian Y-5 ash. J. Volcanol. Geotherm. Res., 17(1-4): 89-109.

Costa, A., Folch, A. and Macedonio, G., 2010. A model for wet aggregation of ash particles in volcanic plumes and clouds: 1. Theoretical formulation. J. Geophys. Res.-Solid Earth, 115: 14.

Costa, A., Folch, A. and Macedonio, G., 2013. Density-driven transport in the umbrella region of volcanic clouds: Implications for tephra dispersion models. Geophysical Research Letters, 40(18): 4823-4827.

Costa, A., Suzuki, Y.J., Cerminara, M., Devenish, B.J., Ongaro, T.E., Herzog, M., Van Eaton, A.R., Denby, L.C., Bursik, M., Vitturi, M.D., Engwell, S., Neri, A., Barsotti, S., Folch, A., Macedonio, G., Girault, F., Carazzo, G., Tait, S., Kaminski, E., Mastin, L.G., Woodhouse, M.J., Phillips, J.C., Hogg, A.J., Degruyter, W. and Bonadonna, C., 2016. Results of the eruptive column model inter-comparison study. J. Volcanol. Geotherm. Res., 326: 2-25.

Davidson, G.A., 1986a. A discussion of Schatzmann integral plume model from a control volume viewpoint. Journal of Climate and Applied Meteorology, 25(6): 858-867.

Davidson, G.A., 1986b. Gaussian versus top-hat profile assumptions in integral plume models. Atmospheric Environment, 20(3): 471-478.

de' Michieli Vitturi, M., Neri, A., Ongaro, T.E., Lo Savio, S. and Boschi, E., 2010. Lagrangian modeling of large volcanic particles: Application to Vulcanian explosions. J. Geophys. Res.-Solid Earth, 115: 18.

Dee, D.P., Uppala, S.M., Simmons, A.J., Berrisford, P., Poli, P., Kobayashi, S., Andrae, U., Balmaseda, M.A., Balsamo, G., Bauer, P., Bechtold, P., Beljaars, A.C.M., van de Berg, L., Bidlot, J., Bormann, N., Delsol, C., Dragani, R., Fuentes, M., Geer, A.J., Haimberger, L., Healy, S.B., Hersbach, H., Holm, E.V., Isaksen, L., Kallberg, P., Kohler, M., Matricardi, M., McNally, A.P., Monge-Sanz, B.M., Morcrette, J.J., Park, B.K., Peubey, C., de Rosnay, P., Tavolato, C., Thepaut, J.N. and Vitart, F., 2011. The ERA-Interim reanalysis: configuration and performance of the data assimilation system. Q. J. R. Meteorol. Soc., 137(656): 553-597.

Degruyter, W. and Bonadonna, C., 2012. Improving on mass flow rate estimates of volcanic eruptions. Geophysical Research Letters, 39(16): n/a-n/a.

Degruyter, W. and Bonadonna, C., 2013. Impact of wind on the condition for column collapse of volcanic plumes. Earth and Planetary Science Letters, 377-378: 218-226.

Devenish, B.J., Rooney, G.G., Webster, H.N. and Thomson, D.J., 2010. The Entrainment Rate for Buoyant Plumes in a Crossflow. Bound.-Layer Meteor., 134(3): 411-439.

Dioguardi, F., Mele, D. and Dellino, P., 2018. A new one-equation model of fluid drag for irregularly-shaped particles valid over a wide range of Reynolds number. Journal of Geophysical Research: Solid Earth: n/a-n/a.

Durant, A.J., Rose, W.I., Sarna-Wojcicki, A.M., Carey, S. and Volentik, A.C.M., 2009. Hydrometeor-enhanced tephra sedimentation: Constraints from the 18 May 1980 eruption of Mount St. Helens. J. Geophys. Res.-Solid Earth, 114: 21.

Ennis, B.J., Tardos, G. and Pfeffer, R., 1991. A microlevel-based characterization of granulation phenomena. Powder Technol., 65(1-3): 257-272.

Fierstein, J. and Nathenson, M., 1992. Another look at the calculation of fallout tephra volumes. Bulletin of Volcanology, 54(2): 156-167.

Fisher, R.V., 1961. Proposed classification of volcanic clast, sediments and rocks. GSA Bulletin, 72(9): 1409-1414.

Folch, A., 2012. A review of tephra transport and dispersal models: Evolution, current status, and future perspectives. J. Volcanol. Geotherm. Res., 235: 96-115.

Folch, A., Costa, A., Durant, A. and Macedonio, G., 2010. A model for wet aggregation of ash particles in volcanic plumes and clouds: 2. Model application. J. Geophys. Res.-Solid Earth, 115: 16.

Folch, A., Costa, A. and Macedonio, G., 2016. FPLUME-1.0: An integral volcanic plume model accounting for ash aggregation. Geoscientific Model Development, 9(1): 431-450.

Ganser, G.H., 1993. A rational approach to drag prediction of spherical and nonspherical particles. Powder Technol., 77(2): 143-152.

Gilbert, J.S. and Lane, S.J., 1994. The origin of accretionary lapilli. Bulletin of Volcanology, 56(5): 398-411.

Gilbert, J.S., Lane, S.J., Sparks, R.S.J. and Koyaguchi, T., 1991. Charge measurements on particle fallout from a volcanic plume. Nature, 349: 598.

Glaze, L.S., Baloga, S.M. and Wilson, L., 1997. Transport of atmospheric water vapor by volcanic eruption columns. J. Geophys. Res.-Atmos., 102(D5): 6099-6108.

Gustavsson, K., Meneguz, E., Reeks, M. and Mehlig, B., 2012. Inertial-particle dynamics in turbulent flows: caustics, concentration fluctuations and random uncorrelated motion. New J. Phys., 14: 18.

Haider, A. and Levenspiel, O., 1989. Drag coefficient and terminal velocity of spherical and nonspherical particles. Powder Technol., 58(1): 63-70.

Hanna, S.R., Oceanic, U.S.N., Administration, A. and Organization, W.M., 1981. Handbook on Atmospheric Diffusion Models. National Oceanic and Atmospheric Administration, reproduced by U.S. Department of Commerce.

Hashimoto, A., Shimbori, T. and Fukui, K., 2012. Tephra Fall Simulation for the Eruptions at Mt. Shinmoe-dake during 26-27 January 2011 with JMANHM. SOLA, 8: 37-40.

Hill, R. and Power, G., 1956. Extremum principles for slow viscous flow and the approximate calculation of drag. The Quarterly Journal of Mechanics and Applied Mathematics, 9(3): 313-319.

Hobbs, P.V., Radke, L.F., Eltgroth, M.W. and Hegg, D.A., 1981. Airborne studies of the emissions from the volcanic eruptions of Mount St. Helens. Science, 211(4484): 816-818.

Hoffman, J.D., 2001. Numerical methods for scientists and engineers.

Holasek, R.E., Self, S. and Woods, A.W., 1996. Satellite observations and interpretation of the 1991 Mount Pinatubo eruption plumes. J. Geophys. Res.-Solid Earth, 101(B12): 27635-27655.

Hoult, D.P. and Weil, J.C., 1972. Turbulent plume in a laminar cross flow. Atmospheric Environment, 6(8): 513-&.

Isella, L., Giechaskiel, B. and Drossinos, Y., 2008. Diesel-exhaust aerosol dynamics from the tailpipe to the dilution tunnel. J. Aerosol. Sci., 39(9): 737-758.

Jacobson, M.Z.U.h.b.g.c.b.i.w., 2005. Fundamentals of Atmospheric Modeling. Cambridge University Press.

James, M.R., Gilbert, J.S. and Lane, S.J., 2002. Experimental investigation of volcanic particle aggregation in the absence of a liquid phase. J. Geophys. Res.-Solid Earth, 107(B9): 13.

James, M.R., Lane, S.J. and Gilbert, J.S., 2003. Density, construction, and drag coefficient of electrostatic volcanic ash aggregates. J. Geophys. Res.-Solid Earth, 108(B9): 12.

Johansen, A., Brauer, F., Dullemond, C., Klahr, H. and Henning, T., 2008. A coagulation-fragmentation model for the turbulent growth and destruction of preplanetesimals. Astronomy & Astrophysics, 486(2): 597-611.

Ketcham, W.M. and Hobbs, P.V., 1969. An experimental determination of the surface energies of ice. The Philosophical Magazine: A Journal of Theoretical Experimental and Applied Physics, 19(162): 1161-1173.

Kieffer, S.W. and Sturtevant, B., 1984. Laboratory studies of volcanic jets. Journal of Geophysical Research, 89(NB10): 8253-8268.

Kostoglou, M. and Konstandopoulos, A.G., 2001. Evolution of aggregate size and fractal dimension during Brownian coagulation. J. Aerosol. Sci., 32(12): 1399-1420.

Kotsovinos, N.E., 1977. Plane turbulent buoyant jets. 2. Turbulence structure. J. Fluid Mech., 81(JUN9): 45-&.

Krause, R. and Rank, E., 1996. A fast algorithm for point-location in a finite element mesh. Computing, 57(1): 49-62.

Kumar, J., Peglow, M., Warnecke, G., Heinrich, S. and Morl, L., 2006. Improved accuracy and convergence of discretized population balance for aggregation: The cell average technique. Chem. Eng. Sci., 61(10): 3327-3342.

Kumar, P., Nenes, A. and Sokolik, I.N., 2009. Importance of adsorption for CCN activity and hygroscopic properties of mineral dust aerosol. Geophysical Research Letters, 36: 6.

Kumar, S. and Ramkrishna, D., 1996. On the solution of population balance equations by discretization .1. A fixed pivot technique. Chem. Eng. Sci., 51(8): 1311-1332.

Kumar, S. and Ramkrishna, D., 1997. On the solution of population balance equations by discretization - III. Nucleation, growth and aggregation of particles. Chem. Eng. Sci., 52(24): 4659-4679.

Lane, S.J., Gilbert, J.S. and Hilton, M., 1993. The aerodynamic behavior of volcanic aggregates. Bulletin of Volcanology, 55(7): 481-488.

Lathem, T.L., Kumar, P., Nenes, A., Dufek, J., Sokolik, I.N., Trail, M. and Russell, A., 2011. Hygroscopic properties of volcanic ash. Geophysical Research Letters, 38: 4.

Liu, E.J., Cashman, K.V. and Rust, A.C., 2015a. Optimising shape analysis to quantify volcanic ash morphology. GeoResJ, 8(Supplement C): 14-30.

Liu, Y.J., Xu, C.X., Fan, D. and He, Y., 2015b. Efficient Construction and Simplification of Delaunay Meshes. ACM Trans. Graph., 34(6): 13.

Maeno, F., Nagai, M., Nakada, S., Burden, R.E., Engwell, S., Suzuki, Y. and Kaneko, T., 2014. Constraining tephra dispersion and deposition from three subplinian explosions in 2011 at Shinmoedake volcano, Kyushu, Japan. Bulletin of Volcanology, 76(6): 16.

Manger, G.E., 1963. Porosity and Bulk Density of Sedimentary Rocks. U.S. Government Printing Office.

Marchisio, D.L. and Barresi, A.A., 2009. Investigation of soot formation in turbulent flames with a pseudo-bivariate population balance model. Chem. Eng. Sci., 64(2): 294-303.

Marchisio, D.L. and Fox, R.O., 2005. Solution of population balance equations using the direct quadrature method of moments. J. Aerosol. Sci., 36(1): 43-73.

Markiewicz, W.J., Mizuno, H. and Volk, H.J., 1991. Turbulence induced relative velocity between two grains. Astronomy & Astrophysics, 242(1): 286-289.

Marshall, J.S. and Li, S.U., 2014. Adhesive Particle Flow. Cambridge University Press.

Mastin, L.G., Van Eaton, A.R. and Durant, A.J., 2016. Adjusting particle-size distributions to account for aggregation in tephra-deposit model forecasts. Atmos. Chem. Phys., 16(14): 9399-9420.

Matthews, L.S., Hayes, R.L., Freed, M.S. and Hyde, T.W., 2007. Formation of cosmic dust bunnies. IEEE Trans. Plasma Sci., 35(2): 260-265.

Matthews, L.S. and Hyde, T.W., 2004. Effects of the charge-dipole interaction on the coagulation of fractal aggregates. IEEE Trans. Plasma Sci., 32(2): 586-593.

Meneguz, E. and Reeks, M.W., 2011. Statistical properties of particle segregation in homogeneous isotropic turbulence. J. Fluid Mech., 686: 338-351.

Min, M., Dominik, C., Hovenier, J.W., de Koter, A. and Waters, L., 2006. The 10 mu m amorphous silicate feature of fractal aggregates and compact particles with complex shapes. Astronomy & Astrophysics, 445(3): 1005-1014.

Moore, J.G. and Peck, D.L., 1962. Accretionary Lapilli in Volcanic Rocks of the Western Continental United States. The Journal of Geology, 70(2): 182-193.

Morton, B.R., Taylor, G. and Turner, J.S., 1956. Turbulent gravitational convection from maintained and instantaneous sources. Proceedings of the Royal Society of London Series a-Mathematical and Physical Sciences, 234(1196): 1-&.

Mueller, S.B., Kueppers, U., Ametsbichler, J., Cimarelli, C., Merrison, J.P., Poret, M., Wadsworth, F.B. and Dingwell, D.B., 2017. Stability of volcanic ash aggregates and break-up processes. Sci Rep, 7: 11.

Mueller, S.B., Kueppers, U., Ayris, P.M., Jacob, M. and Dingwell, D.B., 2016. Experimental volcanic ash aggregation: Internal structuring of accretionary lapilli and the role of liquid bonding. Earth and Planetary Science Letters, 433: 232-240.

Murphy, D.M. and Koop, T., 2005. Review of the vapour pressures of ice and supercooled water for atmospheric applications. Q. J. R. Meteorol. Soc., 131(608): 1539-1565.

Nathenson, M., 2017. Revised tephra volumes for Cascade Range volcanoes. J. Volcanol. Geotherm. Res., 341: 42-52.

Okuzumi, S., Tanaka, H. and Sakagami, M.-a., 2009. Numerical Modeling of the Coagulation and Porosity Evolution of Dust Aggregates. The Astrophysical Journal, 707(2): 1247-1263.

Ormel, C.W. and Cuzzi, J.N., 2007. Closed-form expressions for particle relative velocities induced by turbulence (Research Note). Astronomy & Astrophysics, 466(2): 413-420.

Ormel, C.W., Spaans, M. and Tielens, A., 2007. Dust coagulation in protoplanetary disks: porosity matters. Astronomy & Astrophysics, 461(1): 215-232.

Pan, L. and Padoan, P., 2014. Turbulence-induced relative velocity of dust particles. IV. The collision kernel. Astrophys. J., 797(2): 18.

Papanicolaou, P.N. and List, E.J., 1988. Investigations of round vertical turbulent buoyant jets. J. Fluid Mech., 195: 341-391.

Patrick, M.R., 2007. Dynamics of Strombolian ash plumes from thermal video: Motion, morphology, and air entrainment. Journal of Geophysical Research, 112(B6).

Pollack, M., Salenbauch, S., Marchisio, D.L. and Hasse, C., 2016. Bivariate extensions of the Extended Quadrature Method of Moments (EQMOM) to describe coupled droplet evaporation and heat-up. J. Aerosol. Sci., 92: 53-69.

Poret, M., Costa, A., Folch, A. and Martí, A., 2017. Modelling tephra dispersal and ash aggregation: The 26th April 1979 eruption, La Soufrière St. Vincent. J. Volcanol. Geotherm. Res., 347(Supplement C): 207-220.

Pouget, S., Bursik, M., Webley, P., Dehn, J. and Pavolonis, M., 2013. Estimation of eruption source parameters from umbrella cloud or downwind plume growth rate. J. Volcanol. Geotherm. Res., 258: 100-112.

Pridmore, R.W., 2011. Complementary Colors Theory of Color Vision: Physiology, Color Mixture, Color Constancy and Color Perception. Color Res. Appl., 36(6): 394-412.

Pruppacher, H.R., Klett, J.D. and Springer, 1997. Microphysics of Clouds and Precipitation. Springer.

Pumir, A. and Wilkinson, M., 2016. Collisional Aggregation Due to Turbulence. In: M.C. Marchetti and S. Sachdev (Editors), Annual Review of Condensed Matter Physics, Vol 7. Annual Review of Condensed Matter Physics. Annual Reviews, Palo Alto, pp. 141-170.

Pyle, D.M., 1989. The thickness, volume and grainsize of tephra fall deposits. Bulletin of Volcanology, 51(1): 1-15.

Richardson, D.C., 1995. A self-consistent numerical treatment of fractal aggregate dynamics. Icarus, 115(2): 320-335.

Rose, W.I. and Durant, A.J., 2011. Fate of volcanic ash: Aggregation and fallout. Geology, 39(9): 895-896.

Rosi, M., Paladio-Melosantos, M.L., Di Muro, A., Leoni, R. and Bacolcol, T., 2001. Fall vs flow activity during the 1991 climactic eruption of Pinatubo Volcano (Philippines). Bulletin of Volcanology, 62(8): 549-566.

Saffman, P.G. and Turner, J.S., 1956. On the collision of drops in turbulent clouds. J. Fluid Mech., 1(1): 16-30.

Schella, A., Herminghaus, S. and Schroter, M., 2017. Influence of humidity on tribo-electric charging and segregation in shaken granular media. Soft Matter, 13(2): 394-401.

Schumacher, R., 1994. A reappraisal of Mount St. Helens' ash clusters - depositional model from experimental observation. J. Volcanol. Geotherm. Res., 59(3): 253-260.

Schumacher, R. and Schmincke, H.-U., 1995. Models for the origin of accretionary lapilli. Bulletin of Volcanology, 56(8): 626-639.

Scrope, P., 1829. On the volcanic district of Naples. Geol. Soc. London Trans., v.2: 337-352.

Shampine, L.F. and Reichelt, M.W., 1997. The MATLAB ODE suite. SIAM J. Sci. Comput., 18(1): 1-22.

Shapiro, M.A., Hampel, T. and Krueger, A.J., 1987. The arctic tropopause fold. Mon. Weather Rev., 115(2): 444-454.

Shaw, R.A. and Oncley, S.P., 2001. Acceleration intermittency and enhanced collision kernels in turbulent clouds. Atmos. Res., 59: 77-87.

Smoluchowski, M.V., 1916. Drei Vorträge über Diffusion, Brownsche Molekularbewegung und Koagulation von Kolloidteilchen. Physik. Z., 17: 557-585.

Sorem, R.K., 1982. Volcanic ash clusters - Tephra rafts and scavengers. J. Volcanol. Geotherm. Res., 13(1-2): 63-71.

Sparks, R.S.J., 1986. The dimensions and dynamics of volcanic eruption columns. Bulletin of volcanology, 48: 3-15.

Sparks, R.S.J. and Wilson, L., 1982. Explosive volcanic-eruptions. 5. Observations of plume dynamics during the 1979 Soufriere eruption, St. Vincent. Geophysical Journal of the Royal Astronomical Society, 69(2): 551-570.

Sulpizio, R., 2005. Three empirical methods for the calculation of distal volume of tephra-fall deposits. J. Volcanol. Geotherm. Res., 145(3-4): 315-336.

Sulpizio, R., Folch, A., Costa, A., Scaini, C. and Dellino, P., 2012. Hazard assessment of far-range volcanic ash dispersal from a violent Strombolian eruption at Somma-Vesuvius volcano, Naples, Italy: implications on civil aviation. Bulletin of Volcanology, 74(9): 2205-2218.

Suyama, T., Wada, K. and Tanaka, H., 2008. Numerical simulation of density evolution of dust aggregates in protoplanetary disks. I. Head-on collisions. Astrophys. J., 684(2): 1310-1322.

Suzuki, Y.J. and Koyaguchi, T., 2013. 3D numerical simulation of volcanic eruption clouds during the 2011 Shinmoe-dake eruptions. Earth Planets Space, 65(6): 581-589.

Taddeucci, J., Scarlato, P., Montanaro, C., Cimarelli, C., Del Bello, E., Freda, C., Andronico, D., Gudmundsson, M.T. and Dingwell, D.B., 2011. Aggregation-dominated ash settling from the Eyjafjallajokull volcanic cloud illuminated by field and laboratory high-speed imaging. Geology, 39(9): 891-894.

Telling, J. and Dufek, J., 2012. An experimental evaluation of ash aggregation in explosive volcanic eruptions. J. Volcanol. Geotherm. Res., 209: 1-8.

Textor, C. and Ernst, G.G.J., 2004. Comment on "Particle aggregation in volcanic eruption columns'' by Graham Veitch and Andrew W. Woods. J. Geophys. Res.-Solid Earth, 109(B5): 6.

Textor, C., Graf, H.F., Herzog, M., Oberhuber, J.M., Rose, W.I. and Ernst, G.G.J., 2006. Volcanic particle aggregation in explosive eruption columns. Part I: Parameterization of the microphysics of hydrometeors and ash. J. Volcanol. Geotherm. Res., 150(4): 359-377.

Tsuji, Y., Tanaka, T. and Ishida, T., 1992. Lagrangian numerical simulation of plug flow of cohesionless particles in a horizontal pipe. Powder Technol., 71(3): 239-250.

Vale, H.M. and McKenna, T.F., 2005. Solution of the population balance equation for two-component aggregation by an extended fixed pivot technique. Ind. Eng. Chem. Res., 44(20): 7885-7891.

Van Eaton, A.R., Mastin, L.G., Herzog, M., Schwaiger, H.F., Schneider, D.J., Wallace, K.L. and Clarke, A.B., 2015. Hail formation triggers rapid ash aggregation in volcanic plumes. Nat. Commun., 6: 7.

Van Eaton, A.R., Muirhead, J.D., Wilson, C.J.N. and Cimarelli, C., 2012. Growth of volcanic ash aggregates in the presence of liquid water and ice: an experimental approach. Bulletin of Volcanology, 74(9): 1963-1984.

Vanni, M., 2000. Approximate population balance equations for aggregation-breakage processes. J. Colloid Interface Sci., 221(2): 143-160.

Veitch, G. and Woods, A.W., 2001. Particle aggregation in volcanic eruption columns. J. Geophys. Res.-Solid Earth, 106(B11): 26425-26441.

Volk, H.J., Jones, F.C., Morfill, G.E. and Roser, S., 1980. Collisions between grains in a turbulent gas. Astronomy & Astrophysics, 85(3): 316-325.

Wall, S., John, W., Wang, H.C. and Goren, S.L., 1990. Measurements of kinetic-energy loss ofr particles impacting surfaces. Aerosol Sci. Technol., 12(4): 926-946.

Wallace, J.M. and Hobbs, P.V.U.h.b.g.c.b.i.H.Z.w.o., 2006. Atmospheric Science: An Introductory Survey. Elsevier Science.

Woodhouse, M.J., Hogg, A.J., Phillips, J.C. and Sparks, R.S.J., 2013. Interaction between volcanic plumes and wind during the 2010 Eyjafjallajökull eruption, Iceland. Journal of Geophysical Research: Solid Earth, 118(1): 92-109.

Woods, A.W., 1988. The fluid-dynamics and thermodynamics of eruption columns. Bulletin of Volcanology, 50(3): 169-193.

Woods, A.W., 1993. Moist convection and the injection of volcanic ash into the atmosphere. J. Geophys. Res.-Solid Earth, 98(B10): 17627-17636.

Wright, H. and Ramkrishna, D., 1993. Upper critical dimension for aggregation processes. Phys. Rev. E, 47(5): 3225-3230.